Durham E-Theses

TIME-CONSERVATIVE FINITE-VOLUME METHOD WITH LARGE-EDDY SIMULATION FOR COMPUTATIONAL AEROACOUSTICS

AYBAY, ORHAN

TIME–CONSERVATIVE

FINITE–VOLUME METHOD

WITH

LARGE–EDDY SIMULATION

FOR

COMPUTATIONAL AEROACOUSTICS

Orhan Aybay

School of Engineering

Durham University

A thesis submitted to Durham University

for the degree of Doctor of Philosophy in Engineering

January 2010

Abstract

This thesis presents a time–conservative finite–volume method based on a modern flow simulation technique developed by the author. Its applicability to technically relevant aeroacoustic applications is demonstrated. The time–conservative finite–volume method has unique features and advantages in comparison to traditional methods. The main objectives of this study are to develop an advanced, high–resolution, low dissipation second–order scheme and to simulate the near acoustic field with similar accuracy as higher–order (e.g., 4th–order, 6th–order, etc.) numerical schemes. Other aims are to use a large–eddy simulation (LES) technique to directly predict the near–field aerodynamic noise and to simulate the turbulent flow field with high–fidelity.

A three–dimensional parallel LES solver is developed in order to investigate the near acoustic field. Several cases with wide ranges of flow regimes have been computed to validate and verify the accuracy of the method as well as to demonstrate its effectiveness. The time–conservative finite–volume method is efficient and yields high–resolution results with low dissipation similar to higher–order conventional schemes. The time–conservative finite–volume approach offers an accurate way to compute the most relevant frequencies and acoustic modes for aeroacoustic calculations. Its accuracy was checked by solving demonstrative test cases including the prediction of narrowband and broadband cavity acoustics as well as the screech tones and the broadband shock–associated noise of a planar supersonic jet.

The second–order time–conservative finite–volume method can solve practically relevant aeroacoustic problems with high–fidelity which is an exception to the conventional second–order schemes commonly regarded as inadequate for computational aeroacoustic (CAA) applications.

To my parents

and

my brother

Prof. Dr. Cemalettin Aybay

Acknowledgements

Declaration

The work in this thesis is based on research carried out at the Computational Fluid Dynamics Group, School of Engineering, Durham University, United Kingdom. No part of this thesis has been submitted elsewhere for any other degree or qualification and it all my own work unless referenced to the contrary in the text.

Contents

List of Tables

List of Figures

Nomenclature

Latin Letters

c_p	Specific heat capacity at constant pressure
C_p	Pressure coefficient
C_R	Subgrid–scale model constant
C_I	Compressibility correction constant in the subgrid–scale model
c	Speed of sound
dB	Decibel
e	Total energy per unit volume
f	Arbitrary variable; Frequency
$\overline{f}$	Large–scale component of variable f
f'	Small–scale component of variable f
$\mathbf{F}, \mathbf{G}, \mathbf{H}$	Convective flux vectors
$\mathbf{F}_v, \mathbf{G}_v, \mathbf{H}_v$	Diffusive flux vectors
$\mathbf{h}$	Total space–time flux
k	Wavenumber; Thermal conductivity coefficient
l_k	Smallest eddy length scale
L	Characteristic length scale
M	Mach number
p	Pressure
Pr	Prandtl number
Pr_t	Turbulent Prandtl number

q_x, q_y, q_z	Components of the diffusive thermal fluxes
Re	Reynolds number
$\tilde{S}_{ij}$	Favre–filtered strain rate tensor
$\tilde{S}_M$	Magnitude of the Favre–filtered strain rate tensor
St	Strouhal number
t	Time
T	Temperature
T_{ij}	Lighthill's stress tensor
$\mathbf{U}$	Vector of the conservative variables
x, y, z	Cartesian coordinates

Greek Letters

Δ	Grid spacing
δ_{ij}	Kronecker delta
μ	Dynamic viscosity
μ_{ref}	Reference viscosity
μ_t	Subgrid–scale eddy–viscosity
τ_{ij}	Shear stress tensor
σ_{ij}	Normal stress tensor
ρ	Fluid density
γ	Specific heat ratio

Subscripts

$(\cdot)_{m,x}$	Spatial derivative of $(\cdot)$ in the x–direction
$(\cdot)_{m,y}$	Spatial derivative of $(\cdot)$ in the y–direction
$(\cdot)_{m,z}$	Spatial derivative of $(\cdot)$ in the z–direction
$(\cdot)_{m,t}$	Temporal derivative of $(\cdot)$

Superscripts

$+$	Non–dimensional quantity scaled to wall variables
$'$	Time level at n; Fluctuation
$''$	Time level at $n + 1/2$
$*$	Solution point

Abbreviations

1–D	One–Dimensional
2–D	Two–Dimensional
3–D	Three–Dimensional
2D	Two Dimensions
3D	Three Dimensions
ADM	Approximate Deconvolution Model
AGARD	Advisory Group for Aerospace Research and Development
CAA	Computational Aeroacoustics
CE	Conservation Element
CFD	Computational Fluid Dynamics
CFL	Courant–Friedrichs–Lewy Number
CV	Control Volume
DES	Detached–Eddy Simulation
DDES	Delayed Detached–Eddy Simulation
DNS	Direct Numerical Simulation
FWH	Ffowcs Williams–Hawkings
LES	Large–Eddy Simulation
MILES	Monotonically Integrated Large–Eddy Simulation
MPI	Message Passing Interface
NASA	National Aeronautics and Space Administration
PSD	Power–Spectral–Density
RANS	Reynolds Averaged Navier–Stokes
RMS	Root–Mean–Square
SE	Solution Element
SEM	Synthetic–Eddy–Method
SGS	Subgrid–Scale
SPL	Sound Pressure Level
URANS	Unsteady Reynolds Averaged Navier–Stokes
WALE	Wall–Adapting Local–Eddy Viscosity

List of Publications

1) Aybay, O. and He, L. (2007) Time–Conservative Finite–Volume Method for Large–Eddy Simulation, *Proc. of the World Congress on Engineering 2007*, **2**, pp. 1198–1203.

2) Aybay, O. and He, L. (2008) Development of a High–Resolution Time–Conservative Finite–Volume Method for Large–Eddy Simulation, *Engineering Letters*, **16**(1), pp. 96–103.

3) Aybay, O. and He, L. (2008) Development of Time–Conservative Finite–Volume Method for Large–Eddy Simulation, *Current Themes in Engineering Science 2007*, (ed.) Korkunsky, A.M., American Institute of Physics, pp. 31–41.

4) Aybay, O., Breuer, M., and He, L. (2009) Large–Eddy Simulation of Three–Dimensional Cavity Flow Using a Time–Conservative Finite–Volume Method, *New Results in Numerical and Experimental Fluid Mechanics VII* (eds.) Dillmann, A., Heller, G., Klass, M., Kreplin, H.–P., Nitsche, W. and Schröder, W., Notes on Numerical Fluid Mechanics and Multidisciplinary Design, Vol. 112, Springer, 2010. (Presented at 16. DGLR Symposium of STAB, RWTH Aachen University, Nov. 3–4, Germany).

5) Aybay, O., Breuer, M., and He, L. (2009) Large–Eddy Simulation of Cavity Aeroacoustics Based on a Time–Conservative Finite–Volume Method, *EUROMECH–Colloquium 504: Large–Eddy Simulation for Aerodynamics and Aeroacoustics*, Technical University of Munich, March 23–25, Germany.

Chapter 1

Introduction

1.1 Background

Sound can be described as pressure fluctuations which travel through a medium (i.e, solid, liquid or gas) from its point of origin and reach our ears as longitudinal waves. Sound generation and propagation by a vibrating plate (see Fig. 1.1) can be explained as follows. Consider that the plate is moving in the positive x–direction. The molecules are squashed or compressed together due to the movement of the air molecules, causing an increase in the pressure of the air. Since the pressure in the compression region is greater than in the undisturbed zone, the air molecules tend to move rightward into this region and transmit the pressure impulse to the adjacent layer and so on. On the other hand, when the vibrating plate is moving in reverse direction (i.e., in the negative x–direction), the opposite effect occurs. The molecules are pulled apart, which decreases the pressure to a value below that of the undisturbed zone. Hence, the air molecules tend to move leftward in the negative x–direction and a rarefaction occurs (Raichel, 2006). Consequently, sound will be generated by the vibration of the air molecules and propagate due to the compression and rarefaction impulses.

In Fig. 1.1, the compression and rarefaction of air molecules are depicted with the fundamental components of sound waves (i.e., amplitude and wavelength). Sound travels in different media at different rates based on a characteristic speed of the medium. Sound is generated due to the movement of molecules, without movement

there could be no sound. Therefore, acoustic signals cannot travel through a vacuum. Sound velocities are greater in solids than in liquids. However, sound travels more slowly in gases than it does in liquids. Sound waves contain energy and this energy can be changed into other forms of energy, e.g., electrical energy. The vibrating molecules are merely moved back and forth without changing their positions under the influence of the transmitted waves. The distances of these particles move about their respective equilibrium positions are referred to as displacement amplitudes (see Fig. 1.1). The strength of an acoustic signal directly relates to the magnitudes of the displacement amplitudes as well as variations in the density and velocity of the fluid. Small displacement of the amplitude produces quiet sounds, whereas large displacements produce loud ones. The distance between two successive compressions is called the wavelength and the rate of oscillation is described as the frequency. An acoustic signal may or may not be audible to the human ear, based on its frequency content and intensity. The human ear can detect an acoustic signal in the frequency range of approximately between 20 Hz and 20 kHz.
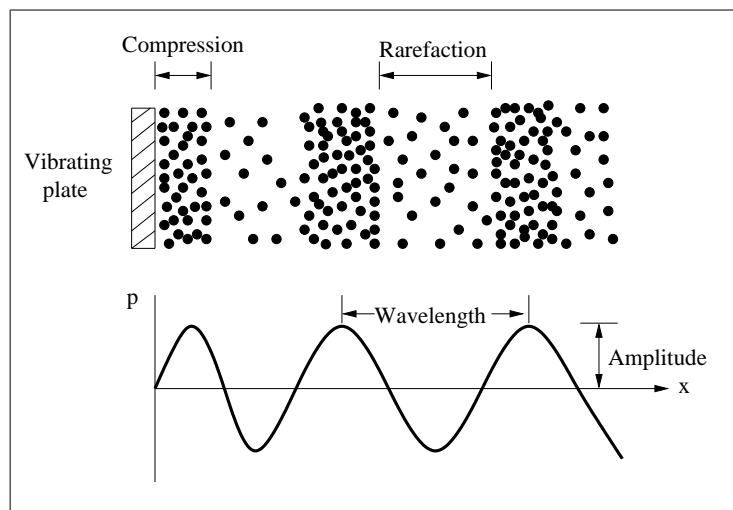
Figure 1.1: Schematic view of compression and rarefaction of air molecules

Noise conveys the definition of *unwanted sound* and it can be considered as a form of environmental pollution. There is no doubt that noise has negative effects on human beings, both physiologically and psychologically. Excessive levels of sound is a major issue for the urban communities due to increasing air and road traffic. Therefore, significant noise reduction in airplanes, trains, and cars is mandatory.

Table 1.1: Sound pressure levels chart and corresponding pressures of various sound sources

Common sound source	SPL (dB)	p (Pa)
Rocket launching pad	180	20,000
Turbojet engine	160	2,000
Jet engine at 30 m	140	200
Aircraft taking off	120	20
Subway train, Chain saw	100	2.0
Factory noise	80	0.2
Normal conversation	60	2×10^{-2}
Library	40	2×10^{-3}
Whisper at 1 m	20	2×10^{-4}
Threshold of hearing	0	2×10^{-5}

Table 1.1 illustrates the range of sound pressure level of common sound sources. For human beings, the range of hearing starts at 0 dB and is considered safe up to 70 dB (Wagner et al., 2007). Long–term exposure above that level is hazardous and can cause permanent hearing loss.

Airplane, train and car manufacturers are forced to develop and build quieter products in order to fulfill current noise regulations as well as to operate in or near cities (Ihme and Breuer, 2002). Understanding of sound generation and sound propagation are a matter of particular interest. Prediction and reduction of noise have become important design criteria for the aviation and the vehicle industries. Besides pollution of the environment by the radiated sound, intense sound tones can also lead to high dynamic loads on parts of the aircraft causing structural damage. Therefore, these industrial sectors are investing in resources which employing different strategies (e.g., theoretical, experimental and numerical) in order to reduce the sound pressure level (i.e., noise) and investigate sound generation as well as propagation mechanisms.

1.2   Motivation

For a long time, prediction of flow–induced sound was mostly based on ana-
lytical and experimental studies. In the last few decades, the world has seen a
revolution in technological achievement brought about by computers. Numerical
study of flow–induced noise and the role of *Computational Fluid Dynamics* (CFD)
in engineering applications has become more essential (Tam, 2004; Anderson, 1995)
and feasible owing to the strongly increased computer performance. The use of
numerical simulation techniques to better understand aerodynamic noise is known
as *Computational Aero–Acoustics* (CAA). CAA is a numerical tool that combines
the classical approaches of flow field with acoustics. CAA could be a useful design
tool and has become very important not only for the aviation industry but also in
many other fields such as the automotive industry, computer manufacturing indus-
try or the energy industry. Moreover, CAA methods became capable of analyzing
more complex engineering problems where no simple analytical or classical numer-
ical solutions exists. CAA could help to quantify important flow–generated noise
phenomena including the following: jet noise, high bypass–ratio ducted fans, noise
of open rotors, airframe noise of aircrafts (e.g., landing gear, high lift devices and
weapon bays) which are some examples from the aviation industry. Car sunroof,
wind noise and climate system noise are the most common examples from the ground
vehicle industry. In the future, due to the noise regulations CAA will be a stan-
dard analysis tool for industry in the design process just like CFD. One should be
aware of the fact that today there is no unique methodology existing to simulate all
kinds of acoustic problems with adequate resolution and accuracy (Kurbatskii and
Mankbadi, 2004). More sophisticated methods must be developed and investigated
to predict sound generation and propagation reliably.

There are a number of major challenges posed by the computation of flow–
induced noise relative to general CFD (Tam, 2004). CAA methodology must be ro-
bust, cost–effective and consistent with the limitations of computing capacity. CAA
focuses primarily on the time–accurate numerical simulations of flow–generated
sound and the propagation of acoustic waves. Aeroacoustic problems are time–
dependent problems. In other words, unsteady flow processes are at the core of

predicting flow–induced sound. These problems typically cover a wide range of frequencies and amplitudes that spread over a bandwidth (Loh et al., 2001a). A large length–scale disparity between sound and flow is another salient feature of aeroacoustics. The length–scale of the acoustic source is very different than the acoustic wave length (Wang et al., 2006). Simulation methods must be designed to deal with problems with greatly different length scales in different parts of the computational domain (Tam, 2001). A high fidelity modeling of the acoustic problems for industrial applications is very difficult due to the complex geometries as well as the physics of the noise generation. Separated regions, instabilities and turbulent flows are all important contributors to the sound field (Marvin, 1976). Pressure fluctuations which are radiated as sound, tend to increase in shear layers, shock cell structures and in the vicinity of sharp edges. Even loud flows radiate a small fraction of their total energy as sound (Colonius, 2004). The acoustic signals are typically much smaller than those of the mean flow variables. The sound intensity is five to six orders smaller (Tam, 2001). Moreover, small errors in the unsteady flow can ruin predictions of the noise radiation. Hence, the modeling requirements of aeroacoustic problems are substantially different from traditional fluid dynamics problems. A numerical scheme must have low dispersion and numerical dissipation to compute sound waves accurately. Consequently, many computational issues, which are essential for the CAA problem, are not so important for fluid dynamics problems. Due to these reasons, CAA has largely been developed somewhat independent of CFD.

In principle, there are two approaches to obtain accurate results for CAA problems. The first one employs standard CFD finite–volume or finite–difference methods typically of a second–order accuracy in space with much finer grid resolution. The second one employs high–order numerical schemes for direct or hybrid computation of flow–generated sound. Details of the direct and hybrid computations of flow–induced noise can be found in Section 2.2.

According to Wagner et al. (2007) the standard second–order CFD schemes (e.g. central schemes, upwind schemes) work surprisingly well for transonic problems in which the differences between aerodynamics and aeroacoustics are negligible. However, they are generally susceptible to high numerical dissipation and dispersion

errors which may result in low–quality aeroacoustic simulations (Kurbatskii and Mankbadi, 2004). The basic requirements of CFD and CAA methodologies are different from each other. To be able to compute or simulate aeroacoustic problems accurately and efficiently, standard CFD schemes are generally not adequate (Tam, 2001).

The numerical schemes should resolve acoustic waves with low dissipation and dispersion errors in order to obtain accurate predictions of sound generation and sound propagation processes. Thus, high–order numerical schemes developed by Tam and Webb (1993) as well as Lele (1992) have been widely used to investigate the aeroacoustic problems. However, they tend to have difficulties in simulating regions with high gradients or discontinuities, e.g., shock waves. The major drawbacks of high–order schemes are the lack of a shock–capturing property and the difficulty to deal with complex geometries. Spurious oscillations are frequently observed in the steep regions of the shock (Tam and Webb, 1993). An adaptive shock–capturing methodology based on selective filtering was proposed by Kim and Lee (2001) in order to remove grid–to–grid oscillations. These non–physical oscillations of the flow variables can be dampened by employing low–order numerical smoothing in the vicinity of large gradients. However, the smoothing complicates and prevents the numerical scheme from being general. Furthermore, the smoothing results in loss of accuracy (Envia et al., 2004). Another difficult aspect of high–order schemes is the application of boundary conditions. The order of the schemes tends to be reduced at the boundaries which results in more complicated boundary condition treatments and again a reduction of accuracy. For large–scale stencils associated with high–order numerical schemes, the communication at block interfaces becomes problematic, difficult and costly for parallel computing. Therefore, there is a strong need to address the issues between standard second–order and high–order schemes as carried out in the present thesis.

Engineering flows are by their nature mostly turbulent which are irregular, chaotic and fluctuating fluid motions. These motions are very complex and always three–dimensional and also affect the distribution of velocity, temperature, noise production or propagation, mixing process as well as heat and mass transfer (Rodi,

Table 1.2: Effects of turbulent flows in engineering applications

Disadvantages	Advantages
Increased skin friction	Increased heat and mass transfer
Noise production and emission	Mixing
Large energy losses	Dissipation of energy

2006). In table 1.2, negative effects of turbulent flows and advantages in certain engineering applications are summarized (Breuer, 2007). Turbulent flows with a high Reynolds number contain a broad range of spatial and temporal scales (Colonius, 2004). The interaction of the flow with the geometrical singularities produces turbulent flows resulting in turbulence noise radiation. For instance, turbulent energy is converted into acoustic energy mostly in the vicinity of sharp edges (e.g., trailing edge of airfoil) (Wagner et al., 2007). The simulation of turbulent flow still continues to present a significant problem for scientists and engineers. There is no single turbulence model which can reliably simulate all kinds of turbulent flows (Blazek, 2005). Different techniques are available to simulate turbulent flows and their effect on the aerodynamic noise generation and propagation. Each of the models has its individual advantages and disadvantages.

The Reynolds–Averaged Navier–Stokes (RANS) equations closed by statistical turbulence models are the most widely used approaches to predict the mean flow field of turbulent flows at moderate cost and engineering accuracy. Steady–state RANS calculations can provide turbulence time and length scales coupled with acoustic correlations (derived from Lighthill's analogy) (Mendonça et al., 2002). However, these steady models can only assist qualitatively by computing the location and strength of the main sound sources. Aeroacoustic problems are highly time–dependent and they often generate very complex flow fields. The sound–generating flow is inherently unsteady, which renders steady RANS models unsuitable and unsteady RANS methods generally insufficient except when the flow–induced noise is dominated by simple large–scale oscillations. It is therefore difficult to simulate the noise–generating flows

and to predict broadband noise generation as well as propagation based on RANS models alone (Wang et al., 2006).

Direct Numerical Simulation (DNS) is conceptually the simplest approach for predicting broadband noise as all details of turbulence can be obtained by solving the three–dimensional, time–dependent Navier–Stokes equations without introducing any turbulence model. However, it is computationally very expensive as all length and time scales have to be resolved numerically by a grid which has to be extremely fine. For high Reynolds number turbulent flows, the ratio of the energy containing large scales to the dissipative small scales characterized by the Kolmogorov scale (Colonius, 2004) increases with the Reynolds number so that the computing time required grows rapidly with the third power of the Reynolds number (Fröhlich and Rodi, 2002). Therefore, the application of this technique is limited to flows with a low–to–moderate Reynolds number (Pope, 2000). DNS is not a method for everyday engineering applications, since most technically relevant flows are characterized by a high Reynolds number. However, it is a very useful tool to study the details of turbulent flows and aerodynamic sound phenomena as well as to provide benchmarking results for validating lower order approximations (Rodi, 2006).

Using the Large–Eddy Simulation (LES) technique, only the contributions of the large and energy–carrying scales can be resolved on a given grid and the more homogeneous, isotropic and universal characteristics of the small scales should be modeled. Although LES requires a higher grid resolution compared to RANS models, it yields more accurate results than the RANS methods for unsteady turbulent phenomena. Furthermore, the LES technique is considerably cheaper than DNS (Blazek, 2005). Consequently, RANS models, DNS and LES techniques were developed and extensive research is still ongoing to predict turbulent flows reliably. Between these approaches, LES is the perfectly suited method to directly compute the large–scale fluctuations which are known to contribute most to the noise generation in near–field problems (Wagner et al., 2007). Hence, the LES technique can be used as a noise prediction tool in order to investigate practical aeroacoustic problems in near-field.

1.3 Objectives of the Present Study

Different aeroacoustic problems often exhibit totally different characteristics and behaviour. Due to the lack of commercial software, many companies and research institutes have developed various strategies for solving CAA problems using their specialized in–house codes with second or high–order accuracy, each with its individual strengths and weaknesses. Standard low–order methods are generally producing low–quality aeroacoustic simulations due to excessive dissipation whereas using high–order accurate schemes for industrial applications is a challenge due to their computational cost and complexity. The main question arising concerning these strategies is: Is there any numerical methodology which can address the issues (see Section 1.2) associated with standard second–order and high–order accurate schemes in order to simulate aeroacoustics problems with high–resolution and accuracy? The numerical methodology should be able to resolve the acoustic waves without introducing too much numerical dissipation and dispersion error. It should be able to capture shocks, or other non–linear phenomena, accurately without using an ad hoc method. The application of boundary conditions including the non–reflecting ones should not be complicated by using the proposed methodology as in the traditional approaches, and the limitations of computing capacity should not be a constraint in order to utilize the present CAA methodology as a noise prediction tool.

The approach taken here is to develop an advanced high–resolution, low dissipation second–order scheme, relying on a novel numerical methodology, namely, a time–conservative finite–volume method, as well as to simulate flow features similar to high–order (e.g., 4th–order, 6th–order, etc.) schemes. The time–conservative method can resolve strong shocks and acoustic waves simultaneously without using any kind of ad hoc techniques. The objectives of LES technique implementation were twofold: to directly predict the sound generation process and to simulate the turbulent flow field features with high–fidelity.

1.3.1 Development and Validation of a 3–D Navier–Stokes Solver Based on a Novel Numerical Methodology

A second–order accurate in both space and time, high–resolution, 3–D parallel LES solver based on the time–conservative finite–volume approach has been developed, aiming at the solution of complex unsteady aerodynamic and aeroacoustic problems with high accuracy.

The method is based on the space–time conservation element and solution element (CE/SE) method originally proposed by Chang (1995) at NASA Glenn Research Centre. The conservation element (CE) is equivalent to a finite control volume (i.e., cell) and the solution element (SE) can be considered as the cell interface. The original CE/SE method was extended for structured grids by Zhang, Z.C. et al. (2002). The time–conservative finite–volume method employed in the present study relies on a new definition of control volume and cell interface. Here, the methodology is based on the hexahedral mesh. The proposed scheme can be considered as an improved version of the numerical scheme given by Zhang, Z.C. et al. (2002) (see Section 4.1). To the best knowledge of the author, the time–conservative scheme was discretized for the first time in three–dimension including the addition of the viscous terms based on the new definitions of cell interface and control volume in the present study.

The time–conservative finite–volume method has unique features and advantages with respect to already mentioned traditional methods and high–order schemes in Section 1.2. For the present scheme no knowledge about the waves or the direction of wave propagation is required. A space–time staggered mesh allows for evaluation of fluxes at the cell interfaces (i.e., the face of the control volume) without solving the Riemann problem. The conservation of space–time fluxes is enforced over the surface of the control volume. In the present method, spatial and temporal discretizations are coupled to calculate the flux conservation. On the other hand, traditional methods use a separate discretization in space and time. Another unique feature of the present scheme is that it allows the use of a simple but effective non–reflecting boundary condition due to the flux–based nature of the method (see Section 4.4.1).

In contrast to that, the implementation of the non–reflecting boundary condition for traditional methods, based on the characteristic theory, can be numerically expensive. Furthermore, the time–conservative finite–volume method is a two time–level explicit scheme (see Section 4.1). The maximum permissible time step is restricted by the smallest grid cell due to stability limitations. In order to reduce the run–time requirement of the simulations and to apply on complicated geometries, the flow solver is parallelized by domain decomposition with explicit message passing via MPI. For that purpose, it is useful that the method is based on a multiblock structured grid. For simplicity, the number of grid points is taken as equal at both sides of a block interface. Hence, exchanging the physical quantities between the blocks becomes straightforward. The solver can be easily adapted for calculations in several applications with complicated geometries. The time–conservative method has been validated by calculating inviscid, viscous laminar and turbulent flows in the field of CFD. Particularly for viscous flows and highly stretched grid cells, time–step limitation results in slow convergence. In order to accelerate the convergence of the Navier–Stokes solver, the direct flux–based multigrid method is implemented (see Section 4.5.1). Several cases with a wide range of flow conditions have been computed to verify the accuracy of the method and to demonstrate its effectiveness (Aybay and He, 2007, 2008a,b). The present flow solver also has the capability to compute laminar viscous flows by replacing all filtered variables with their unfiltered forms and setting the subgrid–scale stress tensor and the subgrid–scale heat flux terms to zero (see Section 5.2). Furthermore, inviscid Euler computations are carried out by setting the viscous stress tensor to zero (see Section 5.1).

1.3.2 Implementation of Large–Eddy Simulation Technique for Direct Noise Simulation

The second aim of the present project is to use the LES technique, since it is well suited to directly predict the near–field aerodynamic noise as well as to simulate the turbulent flow field. In LES, all flow variables are decomposed into resolved and subgrid–scales. Most of the momentum and energy transport contributions are emerging from the large–scale fluctuations. In contrast, the small scales are

much weaker and also more homogeneous and isotropic. Hence, it is reasonable to directly compute the large energy–carrying structures which are contributing most to the noise generation and to model the effects of the small structures.

The subgrid–scale turbulent fluctuations are approximated by the Smagorinsky subgrid–scale (SGS) model (Smagorinsky, 1963). In this SGS model, the eddy–viscosity quantity is evaluated from algebraic relations based on equilibrium assumption (see Section 3.3.2) in order to reduce computing time. The growth of the small scales in the immediate vicinity of walls is reduced by employing Van Driest damping (Van Driest, 1956).

In order to predict the near–field aerodynamic noise, implementation of the LES technique based on the new definitions of cell interface and control volume was carried out for the first time in the present study. In order to investigate the near acoustic field three–dimensional numerical simulations of compressible flows over open cavity and a planar underexpanded jet are carried out by the 3–D parallel LES solver. (see Section 6) (Aybay et al., 2009a,b).

1.4 Overview of the Thesis

The work carried out during this thesis is presented as follows. Chapter 2 reviews different numerical approaches (already briefly introduced in the present chapter) used for the simulations of turbulent flows. Existing methods to predict flow–induced noise and the underlying theories are also provided in this chapter. Furthermore, a new methodology is presented, namely the *time–conservative finite–volume method*, based on a novel numerical framework. This chapter is concluded with the description and review of cavity noise and supersonic jet noise. Details of the governing equations and the implementation of the LES technique including the subgrid–scale modeling are explained in Chapter 3. The following chapter provides the details of the computational techniques including the discretization of the conservative variables, the convective fluxes and the diffusive fluxes as well as the space–time flux evaluation based on the new definitions of cell interfaces and control volume. The stability criterion for the time–conservative scheme is also given here. Chapter 4

ends with the description of the boundary conditions as well as the basic implementation issues of the direct–flux based multigrid method for steady state flows and the parallel computing technique. In Chapter 5, several two–dimensional test cases with a wide range of flow conditions including inviscid, viscous laminar and viscous turbulent flows, are investigated in order to verify the accuracy and illustrate the capabilities of the method. In the subsequent sections the geometry and the flow configuration are defined including the details of the grids and boundary conditions used. The near–field cavity aeroacoustics and shock–included noise by a planar underexpanded jet are of practical engineering relevance and include complex flow phenomena, as shown in Chapter 6. These flows are simulated using the three–dimensional parallel LES solver in order to demonstrate the validity and effectiveness of the developed methodology for the investigation of near–field aeroacoustics. Finally, Chapter 7 includes conclusions together with recommendations for future work.

Chapter 2

Literature Review

This chapter reviews the simulation techniques for turbulent flows as well as computational techniques to predict flow–induced noise. The emphasis is given to a time–conservative finite–volume method including the reasons for choosing LES in the present study and description of two challenging test cases, namely, near–field cavity aeroacoustics and shock–induced noise by a planar underexpanded jet. The chapter is organized as follows. First, different numerical approaches, namely, DNS, LES, RANS and hybrid LES–RANS methods are reviewed in Section 2.1 including the required number of mesh points and grid resolution for an attached boundary layer flow. Then, computational methods for aeroacoustics problems and the underlying theories are given briefly in Section 2.2. Section 2.3 provides an overview of the time–conservative finite–volume method and describes unique as well as non–traditional features of this modern flow simulation technique. The review ends with the description of cavity flow noise and supersonic jet noise which are explained in Sections 2.4 and 2.5, respectively.

2.1   Simulation of Turbulent Flows

A significant part of technically relevant fluid flows are turbulent. Turbulent flows are three–dimensional, irregular, random and chaotic (see Fig. 2.1). Turbulence consists of chaotic motion at a range of scales (i.e., eddy sizes) that increases rapidly with a Reynolds number (Rogallo and Moin, 1984). The large eddies interact with
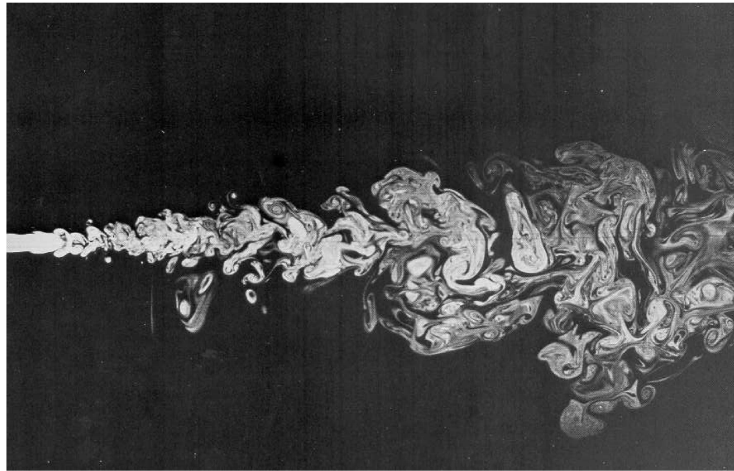
Figure 2.1: Picture of vortical structures in jet turbulence at $Re \approx 2300$, taken by Dimotakis, Lye and Papantoniou (1981) (Van Dyke, 1982)

the mean flow and extract energy from it. Furthermore, they are in the order of the flow geometry (e.g., boundary layer thickness, jet width, etc.), whereas the smallest eddies are characterized by the Kolmogorov scales (a scale of velocity, length and time), where dissipation occurs due to viscous effects. Not all of the length and time scales can be resolved with the computer capacity of today. Hence, in order to simulate turbulent flows and compute their effect on the flow–induced noise generation and propagation, different techniques (e.g., DNS, LES, RANS and hybrid LES–RANS methods) are available.

2.1.1 Direct Numerical Simulation (DNS) of Flow–Induced Noise

In order to investigate physical mechanisms of sound generation and sound propagation processes in detail, direct noise computation can be conducted using the DNS technique. The compressible Navier–Stokes equations need to be solved in order to obtain both aerodynamic and acoustic variables, without restricting hypothesis and without introducing any kind of modeling (Bogey et al., 2000b). In other words, direct simulation eliminates the need for ad hoc models (Rogallo and Moin, 1984). Both the energy containing large scales and the dissipative small scales need to be resolved in DNS (see Fig. 2.2). In addition, the time–step must be smaller than

the smallest turbulent time–scale. Nevertheless, the computational cost of such direct computations is large due to a very fine grid resolution and large memory requirements.

In the DNS, no turbulence model or empirical closure assumptions are required. It relies purely on the solution of the three–dimensional, instantaneous Navier–Stokes equations. Hence, it can be considered as the most accurate method for the simulations of turbulent flows. However, the computational effort for DNS is very high even at a moderately high Reynolds number. The ratio of the characteristic length scales of the largest (L) to the smallest (l_k) eddies can be estimated as in eq. (2.1) (Blazek, 2005; Rodi, 2006; Breuer, 2007)

$$\frac{L}{l_k} \sim Re^{3/4} \tag{2.1}$$

The computational cost for the DNS prediction of turbulent flows can be evaluated in a simple manner. Since turbulence is always a three–dimensional phenomenon, the number of grid points required to resolve all relevant scales ($l_k \leq l \leq L$) can be estimated as follows

$$\left(\frac{L}{l_k}\right)^3 \sim \left(Re^{3/4}\right)^3 = Re^{9/4} \tag{2.2}$$

Equation (2.2) clearly demonstrates how, with an increasing Reynolds number, the number of grid points strongly increases. In DNS, over 99% of the effort is devoted to the dissipation range (see Fig. 2.2) and this effort increases with the Reynolds number (Pope, 2000). With the current computational capacity DNS is only feasible for turbulent flows in simple geometries at a relatively low Reynolds number.

The first direct computation of flow–induced sound using the DNS technique was a study of the far–field sound generated by compressible co–rotating vortices on a computational domain that extends to two acoustic wavelengths in all directions (Mitchell et al., 1995). In this study, very good agreement is observed between the computed far–field sound and the predictions of the acoustic analogy proposed by Lighthill (1952), Powell (1964) and Möhring (1979).

DNS of the temporally evolving mixing layer and plane wake have been studied by Rogers and Moser (1994). Not surprisingly, it is found that the specification of appropriate initial conditions and inflow conditions are crucial. The initial condi-

tions are found to have a first–order effect on the evolution. Colonius et al. (1997) have investigated direct sound generation of a two–dimensional mixing layer using DNS. Flow field was forced at its most unstable frequency and with the first three subharmonics. The resulting flow field character was found to be regular and nearly periodic in time. Two vortex pairings, which were the main sources of the acoustic radiation, are observed at fixed streamwise locations (Bogey et al., 2000b).

The first DNS of the sound generation and propagation from a perfectly expanded supersonic jet was reported by Freund et al. (2000). The Reynolds and the Mach numbers were 2,000 and 1.92, respectively. The radiation of a Mach wave from supersonic jets was investigated. Moreover, the computed sound pressure levels were compared with experimental data and very good agreement was found. Later on, Freund (2001) simulated the first DNS of a subsonic ($M = 0.9$) turbulent jet using 25.6 million grid points, which matched the experimental conditions of Stromberg et al. (1980) and showed very good agreement with experimental data for both mean flow field and radiated sound.

The flow over an open cavity has significant industrial applications including weapon bays, landing gear wheel wells and car sun-roofs. Recently, the DNS technique has been used to analyse the two– and three–dimensional compressible flows over open cavities by Brés and Colonius (2007a,b, 2008). Simulations were performed for several different cavity configurations and flow conditions. The transient three–dimensional instabilities were found to have a frequency of about an order of magnitude lower than the two–dimensional Rossiter instabilities (Rossiter, 1964). More details can be found in Section 2.4.

Under certain operating conditions supersonic jets can form quasi periodic shock cell structures in the jet plume and have discrete frequencies, referred to as screech tones. Manning and Lele (2000) and Suzuki and Lele (2003) employed DNS in order to investigate the physical processes responsible for generating shock–associated noise. Further discussion on shock–induced noise generated by supersonic jets can be found in Section 2.5.

2.1.2 Large–Eddy Simulation (LES)

The large–eddy simulation technique is a highly promising approach. In LES, all flow variables are decomposed into resolved (large) scales and subgrid (small) scales. The large–scales are responsible for most of the momentum and energy transport. In contrast, the small scales are much weaker and also have a much more homogeneous and isotropic structure (Breuer, 2007). Hence, it is reasonable to directly compute the energy–carrying large–scales and to model the dissipative small scales.
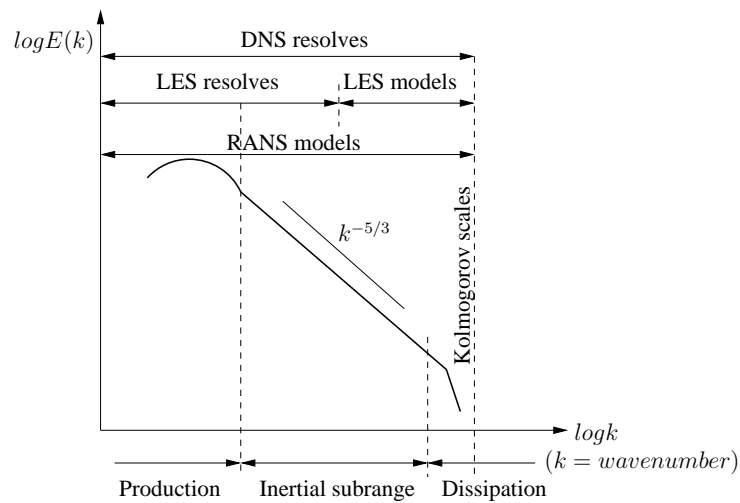
Figure 2.2: Schematic views of energy spectrum $E(k)$ of a locally homogeneous isotropic, fully developed turbulent flow (Breuer, 2007) including resolved and modeled turbulent scales by DNS, LES and RANS (Mihăescu, 2005)

Considering Fig. 2.2, in LES the desired statistics can be obtained directly from the computed scales (Rogallo and Moin, 1984) in the production range, as well as from the ones which are entering into the inertial subrange where the energy cascade takes place (Breuer, 2007). On the other hand, unclosed subgrid–scale (SGS) stress terms (corresponding energy spectrum of small–scale structures is shown in Fig. 2.2 as LES models) has to be approximated by a model. LES is expected to be more robust than RANS predictions which model all turbulent scales (Wang et al., 2006). RANS methods often have difficulties when applied to complex flows with large–scale separation and reattachment or vortex shedding (Fröhlich and Rodi, 2002). In contrast to the RANS methods, the modeling in LES is restricted to a small part of the energy spectrum of turbulent scales (see Fig. 2.2). The small–scale motions

have a more homogeneous, isotropic and universal character than the large–scale ones. Hence, the description of the small scales are much easier than the large ones (Breuer, 2007).

Much of the pioneering work on LES was motivated by meteorological applications (Smagorinsky, 1963; Lilly, 1967). In 1970, the first engineering application of LES was presented by Deardorff (1970). In the following years Schumann (1975) extended and improved Deardorff's method. During the 1980's, some important work was carried out by Bardina et al. (1980) (i.e., the scale similarity model) and Moin and Kim (1982). Numerous studies have been undertaken over the past few years. LES is increasingly applied to flows in complex geometries that occur in engineering applications including aeroacoustic problems. Examples of such problems are the sound generation by vortex pairing in plane and axisymmetric mixing layers (Bogey et al., 1999, 2000b), far–field jet aeroacoustics (Bodony and Lele, 2003, 2004; Bogey et al., 2000b; Bogey and Bailly, 2006; Uzun et al., 2002; Uzun, 2003), cavity noise (Larchevêque et al., 2003; Bertier et al., 2004; Lai and Luo, 2007; Aybay et al., 2009a,b), aeroelastic noise (i.e., aerovibroacoustics) (Vergne et al., 2002), trailing–edge noise (Howe, 2000; Ewert et al., 2003; Ewert and Schröder, 2004), blunt–body simulations (e.g., LES around the Ahmed body) (Howard and Pourquie, 2002; Hinterberger et al., 2003) and internal flows (e.g., ducted flows) (Lafon et al., 2003). The interest in LES highly increased at the beginning of the year 2000. This trend was certainly supported by the availability of low–cost and powerful computers (Blazek, 2005).

LES requires a finer grid resolution with respect to RANS calculations. However, it is considerably cheaper than DNS calculations (Kobayashi, 2006). The number of grid points required to resolve the outer layer is proportional to $Re^{0.4}$. The resolution has to be increased to $Re^{1.8}$ in the viscous sublayer. Therefore compared to $Re^{9/4}$ required by DNS, LES can be applied at Reynolds numbers at least one order of magnitude higher and yields more accurate results than the RANS methods for steady and unsteady flows (Blazek, 2005). These features make the use of LES methodology very attractive especially for the detailed analysis of noise prediction at high Reynolds numbers. Consequently, the LES technique is used in the present

study since it is a good compromise between RANS and DNS.

In most LES of compressible flows, the flow variables are Favre averaged or density–weighted (Moin et al., 1991; Erlebacher et al., 1992). In principle, there are two approaches to obtaining filtered Navier–Stokes equations. The first one employs the Favre averaging and applies one of the standard LES filtering techniques and the second one employs the LES averaging without using density weighting (Boersma and Lele, 1999). Although the non–density weighted filtering offers some numerical advantages when high–order numerical schemes are used for discretization (Colonius, 2004), their computational cost and complexity may prevent the utilization of high–order accurate schemes for industrial applications (Garnier et al., 1999). Moreover, the non–density weighted equations are more complicated than the density–weighted equations due to the appearance of an additional unsteady term in the momentum equations (Boersma and Lele, 1999). Thus, in the present study, the density–weighted sets of equations are preferred and these filtered equations are obtained by using the Favre averaging with the standard LES filtering technique (see Section 3.3.1).

The resulting LES equations (3.30) to (3.33) describe the evolution of the large eddies and contain the unresolved SGS stress tensor in the momentum (3.31) and energy (3.32) equations. The dissipative effects of the SGS stress terms can be taken into account by the SGS models. Several modeling approaches for the small scales have been proposed. The first subgrid–scale model based on an eddy–viscosity concept is proposed by Smagorinsky (1963). The eddy–viscosity describes the proportionality between the subgrid–scales and the large–scale strain rate tensor. The determination of the eddy–viscosity is purely based on an algebraic relation. Furthermore, the value of the eddy–viscosity can vary both in space and time depending on the structure of turbulence. The classical Smagorinsky model is equivalent to Prandtl's mixing length theory (Schlichting, 1979; Breuer, 2007) in the RANS approach. Nevertheless, the fundamental difference is the determination of the characteristic length scale. If the LES methodology is based on the Smagorinsky model then the characteristic length scales can be evaluated by the Smagorinsky constant and the filter width, whereas velocity scales can be estimated from the smallest re-

solved scales (Rogallo and Moin, 1984). On the other hand, for the Prandtl's mixing length theory, it is problematic and depends on the flow problem (Breuer, 2007).

In order to take into account the reduction of the subgrid–scale length in the vicinity of a wall (Breuer, 1998), SGS eddy–viscosity is usually adjusted with a damping function proposed by Van Driest (1956) (see Section 3.3.2). Despite the Smagorinsky model being extremely simple, it has several disadvantages. First of all, the value for the Smagorinsky constant is not uniquely defined. Another disadvantage of the model is that the process of energy backscattering is not modeled. Due to these shortcomings, a dynamic procedure for computing the model coefficient is proposed by Germano et al. (1991) and Moin et al. (1991). The dynamic SGS models use the same relation as the Smagorinsky model. The difference is that the Smagorinsky constant is replaced by a parameter, which evolves dynamically in space and time. The detailed formulation of the model can be found elsewhere (Germano et al., 1991; Pope, 2000; Sagaut, 2006). Improved dynamic SGS models were proposed by (Ghosal et al., 1995; Carati, 1995; Piomelli and Liu, 1995). Dynamical computation of the Smagorinsky coefficient requires approximately 50% more CPU–time in contrast to the constant–coefficient SGS model (Uzun, 2003). A more modern SGS model (i.e., Wall–Adapting Local–Eddy Viscosity (WALE) SGS model), that uses a novel form of the velocity gradient tensor was proposed by Nicoud and Ducros (1999). The main advantage of the WALE SGS model is that it does not require any form of near–wall damping. The WALE model is based on the square of the velocity gradient tensor and accounts for the effects of both the strain and the rotation rate of the smallest resolved turbulent fluctuations. This model also produces the correct scaling in the vicinity of the wall without using the local wall distance (Nicoud and Ducros, 1999; Li et al., 2007). Therefore, it is more suited to wall bounded turbulent flows. In the present LES simulations, the classical Smagorinsky model (Smagorinsky, 1963) is used, as the model is numerically cheap and easy to implement (Blazek, 2005). The model constants and approximations for the subgrid–scale stress terms are given in Section 3.3.2.

In order to improve the robustness and accuracy of LES, other approaches are also proposed including the structure function model which is an eddy–viscosity model in spectral space developed by Chollet and Lesieur (1981) and the approximate deconvolution model (ADM) was suggested by Stolz and Adams (1999). The principle of this model is based on an inverse filtering operation called *deconvolution*. All these SGS models belong to the class of explicit SGS models. Kuwahara and Komurasaki (2000) proposed an implicit SGS approach, in which no extra term is introduced into the governing equations and the truncation error of the numerical methods responsible for the withdrawal of energy in the smallest scales (Sagaut, 2006; Breuer, 2007). Boris et al. (1992) as well as Fureby and Grinstein (1999) considered the same fundamental concept based on a much more systematic level. They proposed *Monotonically Integrated Large–Eddy Simulation (MILES)*. Comparative studies between MILES approach and conventional LES predictions were carried out by Fureby and Grinstein (1999, 2000). The results achieved by the MILES concept in general are not worse than those obtained by LES using standard SGS models. However, detailed investigations on the influence of the choice of the discretization scheme are missing and the grid dependency has to be checked in more detail (Sagaut, 2006).

2.1.3 Reynolds–Averaged Navier–Stokes (RANS) and Hybrid LES–RANS Methods

The RANS approach is based on a statistical description of turbulent flows, whereas the instantaneous flow quantities are represented by the sum of mean and fluctuating values (Wilcox, 1994). In order to evaluate the mean flow field of turbulent flows, a time–averaged rate of momentum transfer (i.e., Reynolds stress tensor) needs to be described. In other words the entire spectrum of turbulent length scales in the flow has to be modeled. However, no statistical turbulence model exists, which represents the best choice for all kinds of flows (Breuer, 2007).

The simulation of complex aeroacoustics problems at high Reynolds numbers encountered in practical applications is still a challenge, particularly those with solid boundaries. Aeroacoustic applications are in most cases wall–bounded flows,

Table 2.1: Grid resolution requirements for an attached boundary layer flow using DNS and wall–resolved LES (Breuer, 2007)

		DNS	Wall–resolved LES
Streamwise	Δx^+	10–15	50–150
Spanwise	Δz^+	5	10–40
Wall–normal	Δy^+	1	1
Number of points	$0 < y^+ < 10$	3–5	3–5

whereby LES requires a number of grid points comparable to DNS due to the near–wall grid resolution requirements (Piomelli and Balaras, 2002). At high Reynolds numbers, the size of the eddies near the wall become very small and the grid resolution requirements become very strict. Extremely large velocity gradients are found in the near–wall region, which are responsible for the production of turbulent kinetic energy. In order to resolve these velocity gradients adequately a very fine grid is required, not only in the wall–normal direction, but also in all spatial directions (Breuer, 2007). The resolution in the streamwise (Δx^+) and the spanwise (Δz^+) directions are important parameters for the quality of the simulation. High resolution LES can be obtained for $\Delta x^+ \leq 50$ and $\Delta z^+ \leq 12$. On the other hand, for $\Delta x^+ \geq 100$ and $\Delta z^+ \geq 30$ the resolution is considered as poor. Hence, in many attached boundary layer flows, it is not feasible for wall–resolved LES to resolve the turbulent eddies due to a DNS–like resolution requirement. In Table 2.1, grid resolution requirements in terms of wall units are displayed for DNS and wall–resolved LES predictions (Breuer, 2007).

In order to avoid these resolution requirements and to reduce the high computational cost, the coupling of LES with statistical turbulence (RANS) or more specifically with unsteady Reynolds–averaged Navier–Stokes (URANS) models has recently been actively pursued. The main objective of hybrid methods is to combine the advantages of both approaches. In this method, the small eddies near the wall are modeled using a RANS–type model, whereas LES is performed outside the near–wall region, where large unsteady vortical structures are resolved directly (Breuer et al.,

2009). The location where the switch is made from URANS to LES is called the interface (see Fig. 2.3). An overall hybrid approach dramatically reduces the near–wall resolution requirements with the exception of the wall–normal direction (Nikitin et al., 2000).
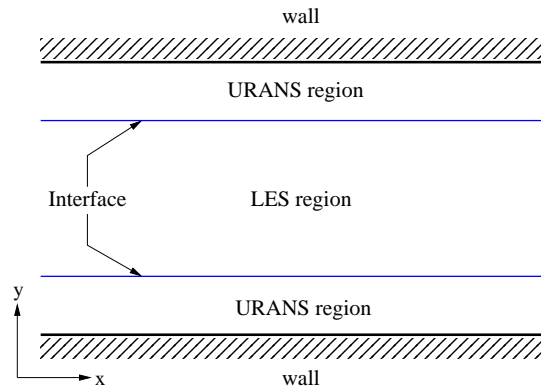
Figure 2.3: Schematic views of URANS and LES regions with interface position

The most widely known hybrid method is the detached–eddy simulation (DES) proposed by Spalart et al. (1997). DES can be easily obtained from an existing RANS code with a small modification of the turbulence model (Wang et al., 2006). The aim of the DES technique was to simulate unsteady turbulent flows with large separation regions for which RANS methods do not work properly. The DES has been employed not only to address the challenge of high–Reynolds number flows but also to predict the noise in such fields as aerospace and ground transportation, as well as in atmospheric studies (Spalart, 2009). The noise radiation from a generic airliner landing–gear truck was calculated by Hedges et al. (2002) using DES. The computed results were compared with those from unsteady RANS calculations. Transient flow fields were found to be very dissimilar. However, there was no unsteady experimental data available for a quantitative assessment of the unsteady simulation behaviour. Furthermore, DES appeared more promising for noise prediction up to some frequency limits (Hedges et al., 2002).

One main disadvantage of DES is that the LES–RANS interface position (i.e., switching) is not determined by the physics of the flow but instead controlled by the local grid spacing relative to the wall (Breuer et al., 2009). Therefore, the interface position should be predefined by the user. In this case the grid design is

crucial in order to obtain accurate simulation results. DES is not especially adapted to the challenges of modeling the near–wall region appropriately, which is another drawback of the model. A new version of DES, denoted as delayed DES (DDES), is proposed by Spalart et al. (2006) to overcome the inaccurate behaviour of DES observed for thick boundary layers. DDES is basically based on a new length scale which detects boundary layers and prolongs the full RANS model. This new length scale depends on the eddy viscosity, so that the interface position now depends on the solution. DDES results show an improvement compared to DES (Menter and Kuntz, 2002).

Lately, new kinds of hybrid methodologies have been developed, which combine the main features of both LES and RANS simulations to overcome the above–mentioned difficulties (Davidson and Peng, 2003; Hamba, 2003; Temmerman et al., 2005). The basic idea of these approaches is to avoid too expensive computational effort for the near–wall region and to achieve an automatic switching criterion which is based on physical quantities not on numerical ones such as the grid resolution (Breuer et al., 2008). A new hybrid LES–RANS methodology was proposed by Jaffrézic and Breuer (2008). The underlying idea of this new approach is based on the coupling of a near–wall explicit algebraic Reynolds stress model (EARSM) (Wallin and Johansson, 2000) with LES for the outer flow. In this method a gradual transition between URANS and LES regions is assured in order to avoid the predefinition of LES and URANS regions. The attention is particularly devoted to the interface treatment which relies on the instantaneous distribution of the modeled turbulent kinetic energy and the wall distance. The instantaneous interface position based on these physical quantities varies in space and time depending on the flow field in the vicinity of the wall. The turbulent kinetic energy is evaluated by the solution of one additional transport equation. Furthermore, synthetic or reconstructed turbulence at the interface is avoided by this dynamic interface criterion in order to assess the method in its simplest form. Further details of this hybrid approach can be found in (Jaffrézic and Breuer, 2008; Breuer et al., 2008, 2009). Well–developed hybrid methods offer an attractive alternative for the simulation of aeroacoustic problems at a high Reynolds number.

2.2 Computational Methods for Aeroacoustic Problems

The characteristics of acoustic waves and computational issues in the application of aeroacoustic theories have already been discussed in Section 1.2. Here, two main computational techniques, namely, hybrid methods and the direct computation of flow–generated sound, will be reviewed briefly. In the present study, the latter technique is employed.

In a hybrid approach, the computation of flow is decoupled from the computation of sound. The noise prediction step can be carried out in a post–processing step based on an aeroacoustic theory. Time–accurate turbulence simulation tools such as DNS, LES, and unsteady RANS methods can be used to compute unsteady flow fields, from which acoustic (sound) sources are extracted. The acoustic far–field is obtained by integral or numerical solutions of the acoustic analogy equations using the sound sources field data.

The first overall aeroacoustics theory was proposed by Sir James Lighthill, the first part of his publications was based on aerodynamically generated sound (Lighthill, 1952). The second publication (Lighthill, 1953) was focused on aerodynamic sound generation by turbulent flows. The motivation for his work was the investigation of jet noise and he introduced an aeroacoustic *analogy*.

The basic idea of Lighthill's acoustic analogy was to find the sources of sound in turbulent flows. The sound sources are generated either by the free fluid motion (e.g., turbulent jets and mixing layers) or by fluid–solid interaction (e.g., propellers). Monopoles, dipoles and quadrupoles are the fundamental sound source types. A monopole acoustic sound source is associated with the displacement of the fluid due to the acceleration of the moving surface. The sound waves generated by the monopole are spreading out spherically. Pulsating spheres, sirens and propellers are practical examples of monopole sources. The sound generated by dipoles represent force (a rotating dipole) or pressure fluctuations on a surface. The dipole acoustic source consists of two monopoles of equal source strength with opposite phases, separated by a small distance. Blowers used for air handling subsystem applications,

propellers and fans are examples of the dipoles. Quadrupole sources are generated from the fluctuations of velocity for specified volumes. The quadrupole source consists of two identical dipoles which are opposite in phase. The quadrupole sources can be categorized as the lateral and the longitudinal quadrupole sources based on the position of the dipole axes. The lateral and the longitudinal quadrupoles are associated with the shear stresses and the normal stresses, respectively. The lateral quadrupole can be found in all turbulent flows.

Lighthill derived an inhomogeneous wave equation from the conservation of mass and momentum equations for compressible flows in order to separate the linear wave operator for the density fluctuations from all nonlinear effects acting as sound sources (Kurbatskii and Mankbadi, 2004).

Lighthill's equation (Lighthill, 1952) can be expressed as;

$$\frac{\partial^2 \rho'}{\partial t^2} - c^2 \frac{\partial^2 \rho'}{\partial x_i \partial x_i} = \frac{\partial^2 T_{ij}}{\partial x_i \partial x_j} \qquad (2.3)$$

where ρ' and c are the acoustic density fluctuations and the ambient speed of sound, respectively. T_{ij} is the Lighthill's stress tensor and given as

$$T_{ij} = \rho u_i u_j + (p - c^2 \rho)\delta_{ij} \qquad (2.4)$$

where ρ, u_i, p and δ_{ij} are the density, velocity, pressure and Kronecker delta, respectively. The summation convention is used in eqs. (2.3) and (2.4).

On the right–hand side of the inhomogeneous wave equation, Lighthill's stress tensor comprises of all acoustic sources in the turbulent flow. It is also assumed that sound propagation takes place in an infinite homogeneous medium at rest. The effects of refraction due to shear and convection are therefore neglected. Moreover, the explicit knowledge of the Green's function is needed (Bogey et al., 2000b). Thus Lighthill's acoustic analogy can only be applied for simple geometries without considering the effects of solid surfaces on sound generation.

A fundamental assumption for acoustic analogy–based prediction is the one–way coupling of flow and sound, i.e., the unsteady flow generates sound and modifies its propagation, but the sound waves do not affect the flow in any significant way. Lighthill's acoustic analogy was extended in order to take into account the effect of solid boundaries on sound generation and radiation by the subsequent works of Curle

(1955). Curle's theory was later extended to include surfaces in arbitrary motion of aerodynamic surfaces by Ffowcs Williams and Hawkings (1969).

At low Mach numbers, incompressible flow solutions can be adequate for approximating acoustic source terms. Due to the high computational cost of the time–accurate simulation, there have been efforts to use a combination of k–ε turbulence model (i.e., steady RANS) calculations to generate acoustic source terms in conjunction with the acoustic analogy. In this method, only the mean turbulent flow field is calculated. Statistical source representations is combined with a turbulence closure and then they are used to predict the radiated acoustic far–field of complex turbulent flows (Bailly et al, 1997).

In contrast to hybrid methods, the direct approaches can compute both the unsteady flow and the radiated sound field by solving the compressible Navier–Stokes equations. For the direct computation of sound, high–fidelity methods such as DNS and LES can be employed. The simulation domain must be sufficiently large to include the noise–producing flow region and at least part of the acoustic near–field associated with the flow. In addition, the unsteady flow field and the sound generation process should be well represented by the selected computational mesh. In other words, care must be taken in designing the computational mesh to ensure that sufficient grid resolution is provided in order to resolve sound within some error threshold.

Different methods are available to investigate the far–field sound propagation. The simplest numerical approach is the domain extension. In the extended domain a uniform mesh can be used and a simpler set of governing equations can be employed, for example linearized Euler equations (Freund et al., 2000). Analytical methods such as Kirchhoff (Freund et al., 1996; Lyrintzis, 2003) and Ffowcs Williams and Hawkings integration (Ffowcs Williams and Hawkings, 1969) can also be utilized. The quality of the predicted far–field sound is directly related to the quality of near–field acoustic data (Colonius, 2004). In the present study, only the near acoustic field is investigated.

Implementation of the accurate boundary conditions is another essential requirement for the direct sound computation. Boundary conditions should be able to ab-

sorb flow disturbances whilst they are leaving the computational domain without causing excessive acoustic reflections (Wang et al., 2006). The time–conservative method allows the use of simple but effective non–reflecting boundary conditions due to the flux–based nature of the method (see Section 4.4.1).

2.3 Time–Conservative Finite–Volume Method

A novel numerical framework, named time–conservative finite–volume method, has several attractive features. The most important ones are already mentioned briefly in Section 1.3.1. This high–resolution and multi–dimensional numerical methodology has been built in order to solve conservation laws and was originally proposed by Chang (1995). This method can be categorized as a finite–volume method, where the conservation element (CE) refers to a finite control volume and the solution element (SE) is equivalent to the cell interface. Chang introduced solution elements, which are subdomains in the space–time coordinates. Within each solution element, any flux vector can be approximated in terms of a simple smooth function (see Section 4.1). The computational domain is divided into non–overlapping conservation elements (i.e., control volumes) where the space–time flux conservation is enforced. The fundamental idea of this method is treating space and time as one entity whilst calculating the flux balance. This idea is the key difference between the time–conservative method and traditional numerical methods. In this method, the first–order spatial derivatives of flow variables are introduced as solving variables. Independent flow variables and their spatial derivatives are solved at each grid point simultaneously. For flows in multiple spatial dimensions, no directional splitting is employed. One and multi–dimensional problems are treated in the same manner. It is substantially different in both its concept and approach from well–established methods (Chang et al., 1999).

The time–conservative scheme is second–order accurate in space and time. It uses a space–time staggered stencil structure. Due to this staggered arrangement, fluxes at the cell interface can be evaluated in a simple and consistent manner without using any interpolation or extrapolation procedure, which enables shock capturing

without using Riemann solvers (Chang, 2007). The time–conservative scheme can resolve strong shocks and small disturbances (e.g., acoustic pressure fluctuations) simultaneously (Loh et al., 2001a). The flux–based nature of the method leads to the use of flux–based boundary conditions. The implementation of a flux–based boundary condition (e.g., a non–reflecting boundary condition) is extremely simple as each control volume allows flux and the flow information to propagate into future (see Section 4.4.1).

The original time–conservative scheme was extended for solving the two and three–dimensional unsteady Euler equations using quadrilateral and hexahedral meshes by Zhang, Z.C. et al. (2002). In order to demonstrate the capability of the method, Zhang presented numerical results for several benchmark problems including oblique shock reflection, supersonic flow over a wedge, and a 3–D detonation flow. Zhang, M. et al. (2004) then proposed to solve unsteady Navier–Stokes equations in two dimensions including the details of viscous fluxes evaluation. Zhang, M. et al. (2004) showed that the first derivatives of the velocity components and the components of the viscous stress tensor can be written as a function of the flow variables and the spatial derivatives of the flow variables (see eqs. (3.19) and (3.22)). Therefore, the flow variables and their spatial derivatives are the only independent discrete variables to be solved for each grid point. In order to validate the proposed methodology Zhang, M. et al. (2004) solved a shock wave boundary layer interaction and a driven cavity flow problem and numerical results were predicted accurately. This extended method has been used in the present study to evaluate the effect of viscous fluxes (see Section 3.2).

The time–conservative method has been successfully adapted to model several different applications in unsteady flow solutions with Mach numbers from 0.0028 to 10, travelling and interacting shocks, detonation waves, cavitation, etc. (Chang, 1995; Chang et al., 1999; Chang, 2007; Zhang, Z.C. and Yu, 1999; Zhang, Z.C. et al., 2002; Zhang, M. et al., 2004; Venkatachari et al., 2008).

The scheme is capable of computing flows over a wide range of flow regimes including discontinuities and very low Mach number flows. It has very little or almost no numerical dissipation making it an ideal candidate among the many available

numerical schemes for problems involving flow instability. The time–conservative
finite–volume method is robust enough to cover the complete spectrum of inviscid
and viscous flow from linear acoustic waves up to high–speed flows with shocks,
as well as being stable for long run times. This method has been used to analyze
several CAA problems (Loh et al., 1996, 2000a,b,c; Loh, 2001; Loh et al., 2001a,b,c;
Jorgenson and Loh, 2002; Loh, 2003a, 2005; Loh and Hultgren, 2005).

Due to the above–mentioned remarkable features, time–conversation method
is a good candidate for practical aeroacoustic applications. Second–order time–
conservative finite–volume method can solve aeroacoustic problems with high–fidelity
which is an exception to the conventional second–order schemes commonly regarded
as inadequate for solving CAA problems.

2.4   Cavity Flow Noise

Strong flow field instabilities associated with acoustic resonance have been ob-
served in many engineering applications. Compressible flows over open cavities have
significant industrial applications, such as aircraft weapon bay, landing gear wheel
well and car sunroof where noise reduction and sonic fatigue are of prime concern.
Unsteady and turbulent flows are the central theme of the cavity aeroacoustics. The
flow over cavities is naturally unsteady. Although geometrically simple, cavity flows
have very complex flow fields, involving the shear layer instabilities, turbulence and
flow induced low–frequency resonance.
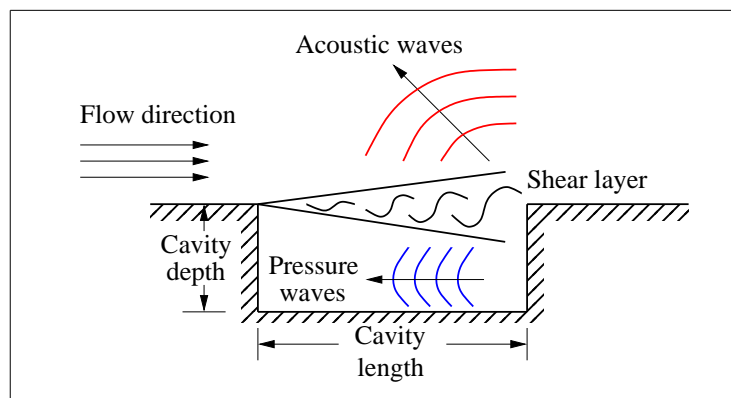
Figure 2.4: Schematic view of feedback mechanism of an open cavity

There are several different mechanisms for generating cavity flow noise. The shear layer instability and the shedding of vortices at the cavity leading edge are the main noise sources due to the interaction of the vortex shedding with the flow (Caraeni et al., 2009). Open cavity flows are governed by a feedback mechanism and this phenomenon is depicted in Fig. 2.4. First of all, vortices are generated in the free shear layer and convected from the cavity leading edge to the cavity rear wall along the shear layer. Due to the interaction between the vortices and the back wall of the cavity, strong pressure variations and acoustic waves are generated in the vicinity of the cavity rear wall. Part of the acoustic waves radiate into the far–field and the other part (i.e., pressure waves) propagate inside the cavity in the upstream direction. When the pressure waves reach the cavity leading edge they further excite vortical disturbances in the shear layer and cause the shedding of new vortices. Since these vortical structures are convected again in the streamwise direction along the shear layer, a feedback loop results. The spacing between the vortices in the shear layer and the frequency of the feedback mechanism are determined by the pressure waves. Self–sustained oscillations inside the cavity generate intense density and pressure fluctuations that may lead to strong vibrations up to structural damage as well as aerodynamic and vibroacoustic problems.

Initial investigations to understand the physics of the flow over rectangular cavities were conducted by Rossiter (1964) in 1964. A well–known semi–empirical relation to predict the frequency of the cavity tones was first proposed by him. From a structural design viewpoint, in order to minimise structural damage, it is vital to avoid the possibility of a structural–acoustic mode coinciding with a high–energy Rossiter mode. It is more desirable to design weapon bay structures to have modal frequencies outside the expected frequency range of Rossiter modes (Mendonça et al., 2003). The cavity geometry with a length–to–depth (L/D) ratio of 5 and a width–to–depth (W/D) ratio of 1 at Mach number 0.85 is taken from the M219 cavity configurations (Peshkin, 2002). The specific case was provided by AGARD (Henshaw, 2000) as a benchmark problem and experiments were carried out by QinetiQ as part of the project on Turbulence Modeling for Military Application Challenges (Peshkin, 2002).

Earlier computational studies of cavity flows were generally two–dimensional and often employed RANS models to represent turbulence effects (Zhang, X. et al, 1998; Shieh and Morris, 1999). Some successful URANS applications (Henderson et al., 2000; Inagaki et al., 2002) have been reported for modeling the narrowband Rossiter mode components of the acoustic spectra (Rossiter, 1964). According to Mendonça et al. (2003) it is widely accepted that URANS methods are currently unable to predict the broadband contribution to the acoustic spectra. This was attributed to excessive turbulent dissipation in the used turbulence models. DES of cavity flows based on Spalart–Allmaras, k–ε and SST k–ω models were performed to resolve dominant narrowband flow excitations by Allen and Mendonça (2004); Mendonça et al. (2003). In these studies, good Rossiter mode shape predictions were observed with slightly over–predicting RMS pressure and sound pressure levels. Larchevêque et al. (2003) provided appealing results using LES for a flow over a deep cavity. Larchevêque's work was extended by Bertier et al. (2004) using several unstructured and hybrid meshes demonstrating good results whilst reducing the number of cells. Lai and Luo (2007) proposed to use hybrid LES Ffowcs Williams and Hawkings (FWH) acoustic analogy to predict open cavity noise, as well as to highlight the different nature of 2–D and 3–D wave propagation. More recently, Brés and Colonius (2007a,b, 2008) performed DNS of three–dimensional cavity flows which provided fundamental insights into fluid motions and instabilities in cavities at relatively low Reynolds numbers.

In the present study, 2–D and 3–D numerical calculations are performed on the M219 swallow cavity at Mach number 0.85 (see Sections 5.3.2 and 6.1, respectively) (Aybay et al., 2009a,b). In these sections, the geometry and the flow configuration are defined including details of the grids and boundary conditions used. The resonance frequencies and acoustic modes are calculated by using the present method. LES results of the present scheme are compared with the results of high–order numerical schemes (Chen et al., 2007; Nayyar et al., 2005) as well as experimental data (Peshkin, 2002; Henshaw, 2000) for the flow over a rectangular cavity.

2.5   Supersonic Jet Noise

Supersonic jet noise is a challenging topic in computational aeroacoustics due to a high disparity of length and velocity scales. The noise characteristics of supersonic jets are quite complex and very different from those of subsonic jets (Tam, 1995). For imperfectly expanded supersonic jets, a quasi–periodic shock–cell structure is formed inside the jet plume. Screech noise is produced by the interaction of turbulent mixing layer and this shock–cell structure under certain operating conditions. A schematic view of the shock–vortex interaction with shock–induced noise radiation is depicted in Fig. 2.5. The supersonic jet noise simulation requirements may be divided into two categories. On the one hand, the numerical methodology is required to resolve the acoustic waves without introducing too much numerical dissipation and dispersion error. On the other hand, it is required to capture shocks, or other non–linear phenomena, near or in the jet plume. Jet screech noise is of importance in aeronautics (e.g., military aircraft) where very high dynamic loads associated with the intense screech tone are capable of causing structural damage and fatigue failure of aircraft components (Panda et al., 1997; Panda, 1998, 1999). The correct prediction of the acoustic field and the development of control strategies to suppress screech noise while maintaining jet thrust performance are of prime concern.
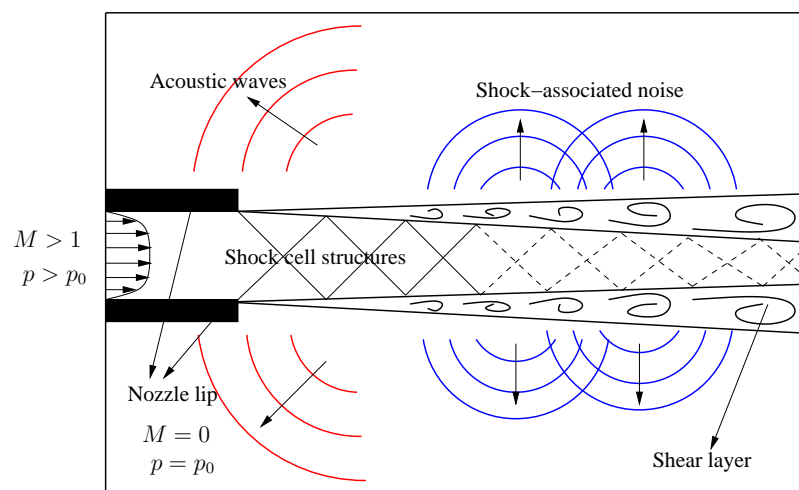
Figure 2.5: Schematic views of the interaction of shear layer and shock–cell structure with noise radiation

The noise of a supersonic jet comprises of three basic components. One has discrete frequencies, which are commonly referred to as the screech tones. The other components are the broadband shock–associated noise and the turbulent mixing noise. The dominant part of the turbulent mixing noise is generated by the large–scale turbulence structures, whilst the fine–scale turbulence structures are responsible for the background noise. The mixing noise is related to instability waves in the shear layer. Discrete frequencies (i.e., screech tones) and the broadband shock–associated noise are generated only when a quasi–periodic shock–cell structure is present in the jet plume. Oblique shocks and expansion fans generated at the nozzle lip, where there is a mismatch of the pressure inside and outside of the jet, are responsible for the formation of the shock–cell structure. The characteristics of both the screech tone frequency and the broadband shock noise rely on the quasi–periodicity of the shock–cells (Tam, 1988, 1995). According to Tam (1995) the turbulent mixing noise is the most dominant noise source in the downstream direction of the jet. On the other hand, the broadband shock–associated noise is more intense in the upstream direction. Therefore the relative intensity of noise is a strong function of the direction of observation.

In the early 1950s jet engine noise became a new research branch. According to Powell (1953) the screech tones of supersonic jets are generated by a feedback mechanism. The characteristics of this self–sustained loop were first observed by Powell (1953) and the screech tone frequencies of rectangular supersonic jets were measured by him. Physically, flow instabilities originate from the nozzle lip and are convected in the downstream direction. As the instabilities propagate downstream they extract energy from the mean flow and rapidly grow in amplitude. Due to the interaction of these instability waves in the shear layer and the shock waves of the quasi–periodic shock–cell structure, shock–induced acoustic waves are generated. The shock–vortex interaction emanates a broadband noise component. Part of the acoustic waves propagate in the upstream direction (see Fig. 2.5). Upon reaching the nozzle lip these acoustic (i.e., sound) waves excite the shear layer and regenerate the instability waves at the nozzle lip or in the vicinity of the nozzle lip and thus complete the resonant loop (Tam, 1988; Berland et al, 2007).

Since Powell's first observations, several experimental, analytical and numerical studies have been carried out on the self–sustained loop characteristics. The screech noise generation process from supersonic underexpanded jets at fully expanded Mach numbers of 1.19 and 1.42 was investigated experimentally by Panda et al. (1997); Panda (1998, 1999). Panda provided in his work detailed measurements of the shock structure, near–field pressure fluctuations and the properties of the coherent turbulent structure in the shear layer. Shen and Tam (2002) solved the fully three–dimensional jet screech modes using dispersion–relation-preserving scheme. The unsteady Reynolds averaged Navier–Stokes equations (RANS) with the k–ε turbulence model was used to calculate the jet flow. Hence, a limited bandwidth of the turbulence spectra was simulated. Rona and Zhang (2004) solved the time–dependent RANS equations using a two–equation k–ω turbulence model to reproduce the screech tones of a circular jet at Mach number 2. It was found that the time–averaged axial velocity decayed at a faster rate than in the experiments. The interaction between shock–cell modulated instability waves and the shock–expansion system which generates screech noise were found in agreement with experimental data. Computation of a shock containing planar underexpanded jet and its screech tones using LES was performed by Berland et al (2007). The computational domain was discretized by a Cartesian grid of approximately 16 million points. It was found that the upstream acoustic fields exhibit harmonic tones that compare correctly to screech tones observed on rectangular jets in terms of frequency and amplitude. Furthermore, the shock-cell spacing and the shock strength for the first three–shock–cells were compared with experimental data provided by Raman and Rice (1994). Computation of the shock–cell spacing was found to be smaller than expected and the shock strengths were overestimated particularly for the second and the third shocks. Computation of an underexpanded three–dimensional rectangular jet using an unstructured three–dimensional space–time conservation element and solution element (CE/SE) Euler solver was investigated by Loh et al. (2001c). Although the strong momentum exchange in the shear layer was not taken into account a feedback loop was likely formed in the computation. In order to achieve a more physically relevant simulation a Navier–Stokes CE/SE solver with LES or

turbulence modeling capability was required. Loh and Hultgren (2005) simulated a fully expanded supersonic circular jet of Mach number 1.4 using a three–dimensional CE/SE Navier–Stokes solver with a LES technique. It was found that time–averaged results, such as the streamwise velocity and radial density profiles agree well with the experimental data. Near–field spectral results were also in good agreement with the experiments in the expected range of lower Strouhal numbers. One may refer to the computation of 2–D axisymmetric and 3–D screech noise for circular jets by Loh et al. (2000a,b, 2001b); Loh and Hultgren (2002); Loh (2005) for further details. In order to obtain the full range of turbulence scales in the jet flow and to study the details of shock–induced noise generation, a direct numerical simulation of a supersonic jet and its acoustic field was carried out recently by Schulze et al. (2009). The computational grid contained approximately 300 million grid points with a Reynolds number of 30,000 based on the height of the jet. A finite difference compact scheme of sixth order and a spectral like method in the periodic direction were used to capture the sound generation and propagation processes. An adaptive shock–capturing filtering is implemented in order to remove grid–to–grid oscillations in the vicinity of large gradients 1020 CPU's with 0.5 TB of main memory and 15 TB of output data were used to perform the DNS of supersonic jet. The computational requirements for the direct noise computation of supersonic jets using the DNS technique are very high. Hence, in the present study, LES is used to reproduce the essential flow dynamics in the early stages of the jet plume development and to investigate the screech tone frequencies of rectangular supersonic jets. The shock–vortex interaction is also investigated without implementing any kind of ad hoc filtering method (e.g., an adaptive shock–capturing filtering (Kim and Lee, 2001)). The time–conservative finite–volume method can resolve strong shocks and acoustic waves simultaneously. In Section 6.2, the details of the flow configuration and the geometry are defined, including details on the grids and boundary conditions used. The screech tone frequency, subharmonic tones and the shock–cell spacing at Mach number 1.55 are calculated. The results of the present scheme are compared with the results of the high–order numerical scheme computed by Berland et al (2007) and the experimental data (Raman and Rice, 1994; Panda et al., 1997).

Chapter 3

Flow Governing Equations

The flow governing equations are presented in this chapter. The full set of three–dimensional time–accurate compressible Navier–Stokes equations is defined in Section 3.1. Details about modified form of the Navier–Stokes equations are given in Section 3.2. Section 3.3 provides the details of the large–eddy simulation method used for the present study including the filtered Navier–Stokes equations and the subgrid–scale modeling for compressible turbulent flows.

3.1   3–D Compressible Navier–Stokes Equations

The Navier–Stokes equations describe the exchange (flux) of mass, momentum and energy through the boundary of a control volume (Blazek, 2005). The three–dimensional Navier–Stokes equations with respect to a fixed coordinate system, with no body force or volumetric heating can be expressed in an integral form as

$$\frac{\partial}{\partial t} \int_{\Omega} \mathbf{U} d\Omega + \oint_{\partial \Omega} \left(\mathbf{W}_c - \mathbf{W}_v \right) \cdot d\mathbf{s} = 0 \qquad (3.1)$$

where $\mathbf{U}$ represents the vector of conservative variables, Ω is the finite–volume bounded by the surface $\mathbf{s}$. The vector of convective fluxes, $\mathbf{W}_c$, is related to the convective transport of quantities in the fluid. $\mathbf{W}_v$ is the vector of viscous fluxes, contains the viscous stresses and the heat diffusion. Variation of the conservative variables depends solely on the flux across the boundary of the control volume since the integral formulation of the conservation law has no volume sources (Blazek, 2005;

38

Hirsch, 2007). The components of the convective and diffusive (viscous) fluxes can be expressed in Cartesian coordinates as follows

$$(\mathbf{W}_c - \mathbf{W}_v) = (\mathbf{F}i + \mathbf{G}j + \mathbf{H}k) - (\mathbf{F_v}i + \mathbf{G_v}j + \mathbf{H_v}k) \tag{3.2}$$

where $\mathbf{U}$ is the vector of the conservative variables, $\mathbf{F}$, $\mathbf{G}$ and $\mathbf{H}$ are the convective flux vectors and $\mathbf{F_v}$, $\mathbf{G_v}$ and $\mathbf{H_v}$ are the diffusive flux vectors.

The vector of the conservative variables consists of the following five components in three dimensions

$$\mathbf{U} = \begin{bmatrix} \rho \\ \rho u \\ \rho v \\ \rho w \\ e \end{bmatrix} \tag{3.3}$$

The vectors of the convective fluxes are defined as

$$\mathbf{F} = \begin{bmatrix} \rho u \\ \rho u^2 + p \\ \rho uv \\ \rho uw \\ (e + p)\,u \end{bmatrix} \tag{3.4}$$

$$\mathbf{G} = \begin{bmatrix} \rho v \\ \rho uv \\ \rho v^2 + p \\ \rho vw \\ (e + p)\,v \end{bmatrix} \tag{3.5}$$

$$\mathbf{H} = \begin{bmatrix} \rho w \\ \rho uw \\ \rho vw \\ \rho w^2 + p \\ (e + p)\,w \end{bmatrix} \tag{3.6}$$

and one can obtain the following components for the vectors of the diffusive fluxes
in Cartesian coordinates

$$\mathbf{F_v} = \begin{bmatrix} 0 \\ \sigma_{xx} \\ \tau_{xy} \\ \tau_{xz} \\ u\sigma_{xx} + v\tau_{xy} + w\tau_{xz} - q_x \end{bmatrix} \tag{3.7}$$

$$\mathbf{G_v} = \begin{bmatrix} 0 \\ \tau_{yx} \\ \sigma_{yy} \\ \tau_{yz} \\ u\tau_{yx} + v\sigma_{yy} + w\tau_{yz} - q_y \end{bmatrix} \tag{3.8}$$

$$\mathbf{H_v} = \begin{bmatrix} 0 \\ \tau_{zx} \\ \tau_{zy} \\ \sigma_{zz} \\ u\tau_{zx} + v\tau_{zy} + w\sigma_{zz} - q_z \end{bmatrix} \tag{3.9}$$

where ρ, p, u, v and w are the density, pressure and velocity components in the x,
y and z directions, respectively.

The total energy per unit volume e is defined by

$$e = \frac{p}{(\gamma - 1)} + \frac{\rho \left(u^2 + v^2 + w^2\right)}{2} \tag{3.10}$$

where γ is the specific heat ratio.

Assuming Newtonian fluids, the normal stress tensor and the shear stress tensor
have the following Cartesian components (Hirsch, 2007)

$$\sigma_{xx} = \frac{2}{3}\mu \left(2\frac{\partial u}{\partial x} - \frac{\partial v}{\partial y} - \frac{\partial w}{\partial z}\right),$$

$$\sigma_{yy} = \frac{2}{3}\mu \left(2\frac{\partial v}{\partial y} - \frac{\partial u}{\partial x} - \frac{\partial w}{\partial z}\right),$$

$$\sigma_{zz} = \frac{2}{3}\mu \left(2\frac{\partial w}{\partial z} - \frac{\partial u}{\partial x} - \frac{\partial v}{\partial y}\right),$$

$$\tau_{xy} = \tau_{yx} = \mu \left(\frac{\partial u}{\partial y} + \frac{\partial v}{\partial x} \right),$$

$$\tau_{xz} = \tau_{zx} = \mu \left(\frac{\partial u}{\partial z} + \frac{\partial w}{\partial x} \right),$$

$$\tau_{yz} = \tau_{zy} = \mu \left(\frac{\partial v}{\partial z} + \frac{\partial w}{\partial y} \right). \tag{3.11}$$

where μ is the coefficient of the dynamic viscosity.

The components of the diffusive thermal fluxes read

$$q_x = -k\frac{\partial T}{\partial x}, \qquad q_y = -k\frac{\partial T}{\partial y}, \quad \text{and} \quad q_z = -k\frac{\partial T}{\partial z}. \tag{3.12}$$

where k stands for the thermal conductivity coefficient and T is the temperature. q_x, q_y and q_z are terms describing the work of the heat conduction on the fluid.

The ideal gas relation is given by

$$p = \rho R T \tag{3.13}$$

Sutherland's law is used to determine the dynamic viscosity as a function of temperature

$$\mu = \mu_{ref} \left(\frac{T}{T_{ref}} \right) \frac{T_{ref} + S}{T + S} \tag{3.14}$$

where R, T_{ref} and μ_{ref} are the ideal gas constant, reference temperature and reference viscosity, respectively. S is chosen as $110K$ (Uzun, 2003).

3.2   Modified Form of the Navier–Stokes Equations

The components of the conservative variables, convective and diffusive fluxes including the viscous stress tensor and the thermal flux components can be written in a modified form to construct flux conservation in both space and time. Thus the only independent discrete solution variables associated with each grid point can be written in terms of the conservative variables (U_m) and the spatial derivatives of the conservative variables (i.e., gradients) $(U_{m,x}, U_{m,y}, U_{m,z})$ where $m = 1, 2, \ldots, 5$. With known values of $(U_m, U_{m,x}, U_{m,y}, U_{m,z})$ the distribution of the conservative variables vector $(\mathbf{U})$, the convective fluxes $(\mathbf{F}, \mathbf{G} \text{ and } \mathbf{H})$, as well as the diffusive fluxes

($\mathbf{F_v}$, $\mathbf{G_v}$ and $\mathbf{H_v}$) can be fully specified for the control volume. Consequently, the modified form of Navier–Stokes equations will be depended solely on the conservative variables and the spatial derivatives of them.

The components of the conservative variables in three dimensions are defined as

$$U_1 = \rho, \qquad U_2 = \rho u,$$

$$U_3 = \rho v, \qquad U_4 = \rho w,$$

$$U_5 = \frac{p}{\gamma - 1} + \rho \frac{(u^2 + v^2 + w^2)}{2}. \tag{3.15}$$

The components of the convective fluxes in the x–direction can be written in the following modified form

$$F_1 = U_2,$$

$$F_2 = (\gamma - 1) U_5 + \frac{[(3 - \gamma) U_2^2 - (\gamma - 1)(U_3^2 + U_4^2)]}{2U_1},$$

$$F_3 = \frac{U_2 U_3}{U_1}, \qquad F_4 = \frac{U_2 U_4}{U_1},$$

$$F_5 = \gamma \frac{U_2 U_5}{U_1} - (\gamma - 1) \frac{U_2 [U_2^2 + U_3^2 + U_4^2]}{2U_1^2}. \tag{3.16}$$

Similarly, the components of the convective fluxes in the y–direction can be expressed as

$$G_1 = U_3, \qquad G_2 = \frac{U_2 U_3}{U_1},$$

$$G_3 = (\gamma - 1) U_5 + \frac{[(3 - \gamma) U_3^2 - (\gamma - 1)(U_2^2 + U_4^2)]}{2U_1},$$

$$G_4 = \frac{U_3 U_4}{U_1},$$

$$G_5 = \gamma \frac{U_3 U_5}{U_1} - (\gamma - 1) \frac{U_3 [U_2^2 + U_3^2 + U_4^2]}{2U_1^2}. \tag{3.17}$$

Lastly, the components of the convective fluxes in the z–direction are defined as

$$H_1 = U_4, \qquad H_2 = \frac{U_2 U_4}{U_1}, \qquad H_3 = \frac{U_3 U_4}{U_1},$$

$$H_4 = (\gamma - 1) U_5 + \frac{[(3 - \gamma) U_4^2 - (\gamma - 1)(U_2^2 + U_3^2)]}{2U_1},$$

$$H_5 = \gamma \frac{U_4 U_5}{U_1} - (\gamma - 1) \frac{U_4 [U_2^2 + U_3^2 + U_4^2]}{2U_1^2}. \tag{3.18}$$

The estimation of the viscous and thermal fluxes requires the calculation of the velocity and temperature gradients (Hirsch, 2007). In order to express the viscous stress tensor components as well as the diffusive thermal fluxes in terms of the conservative variables (U_m) and the spatial derivatives of the conservative variables $(U_{m,x}, U_{m,y}, U_{m,z})$, the first derivatives of the velocity components in eq. (3.11) are defined as follows (Zhang, M. et al., 2004)

$$\frac{\partial u}{\partial x} = \frac{1}{\rho}\frac{\partial (\rho u)}{\partial x} - \frac{\rho u}{\rho^2}\frac{\partial \rho}{\partial x} = \frac{U_{2,x}}{U_1} - \frac{U_2 U_{1,x}}{U_1^2},$$

$$\frac{\partial u}{\partial y} = \frac{1}{\rho}\frac{\partial (\rho u)}{\partial y} - \frac{\rho u}{\rho^2}\frac{\partial \rho}{\partial y} = \frac{U_{2,y}}{U_1} - \frac{U_2 U_{1,y}}{U_1^2},$$

$$\frac{\partial u}{\partial z} = \frac{1}{\rho}\frac{\partial (\rho u)}{\partial z} - \frac{\rho u}{\rho^2}\frac{\partial \rho}{\partial z} = \frac{U_{2,z}}{U_1} - \frac{U_2 U_{1,z}}{U_1^2}. \tag{3.19}$$

Similar expressions can be obtained for the spatial derivatives of the wall–normal (v) velocity

$$\frac{\partial v}{\partial x} = \frac{1}{\rho}\frac{\partial (\rho v)}{\partial x} - \frac{\rho v}{\rho^2}\frac{\partial \rho}{\partial x} = \frac{U_{3,x}}{U_1} - \frac{U_3 U_{1,x}}{U_1^2},$$

$$\frac{\partial v}{\partial y} = \frac{1}{\rho}\frac{\partial (\rho v)}{\partial y} - \frac{\rho v}{\rho^2}\frac{\partial \rho}{\partial y} = \frac{U_{3,y}}{U_1} - \frac{U_3 U_{1,y}}{U_1^2},$$

$$\frac{\partial v}{\partial z} = \frac{1}{\rho}\frac{\partial (\rho v)}{\partial z} - \frac{\rho v}{\rho^2}\frac{\partial \rho}{\partial z} = \frac{U_{3,z}}{U_1} - \frac{U_3 U_{1,z}}{U_1^2}. \tag{3.20}$$

The spatial derivatives of the spanwise (w) velocity can be defined as

$$\frac{\partial w}{\partial x} = \frac{1}{\rho}\frac{\partial (\rho w)}{\partial x} - \frac{\rho w}{\rho^2}\frac{\partial \rho}{\partial x} = \frac{U_{4,x}}{U_1} - \frac{U_4 U_{1,x}}{U_1^2},$$

$$\frac{\partial w}{\partial y} = \frac{1}{\rho}\frac{\partial (\rho w)}{\partial y} - \frac{\rho w}{\rho^2}\frac{\partial \rho}{\partial y} = \frac{U_{4,y}}{U_1} - \frac{U_4 U_{1,y}}{U_1^2},$$

$$\frac{\partial w}{\partial z} = \frac{1}{\rho}\frac{\partial (\rho w)}{\partial z} - \frac{\rho w}{\rho^2}\frac{\partial \rho}{\partial z} = \frac{U_{4,z}}{U_1} - \frac{U_4 U_{1,z}}{U_1^2}. \tag{3.21}$$

Then the components of the viscous stress tensor can also be written in terms of $(U_m, U_{m,x}, U_{m,y}, U_{m,z})$ by using eq. (3.19) in the following modified form

$$\tau_{xy} = \mu\left(\frac{U_{2,y}}{U_1} - \frac{U_2 U_{1,y}}{U_1^2} + \frac{U_{3,x}}{U_1} - \frac{U_3 U_{1,x}}{U_1^2}\right),$$

$$\tau_{xz} = \mu\left(\frac{U_{2,z}}{U_1} - \frac{U_2 U_{1,z}}{U_1^2} + \frac{U_{4,x}}{U_1} - \frac{U_4 U_{1,x}}{U_1^2}\right),$$

$$\tau_{yz} = \mu\left(\frac{U_{3,z}}{U_1} - \frac{U_3 U_{1,z}}{U_1^2} + \frac{U_{4,y}}{U_1} - \frac{U_4 U_{1,y}}{U_1^2}\right),$$

$$\sigma_{xx} = \frac{2}{3}\mu \left(2\frac{U_{2,x}}{U_1} - 2\frac{U_2 U_{1,x}}{U_1^2} - \frac{U_{3,y}}{U_1} + \frac{U_3 U_{1,y}}{U_1^2} - \frac{U_{4,z}}{U_1} + \frac{U_4 U_{1,z}}{U_1^2} \right),$$

$$\sigma_{yy} = \frac{2}{3}\mu \left(2\frac{U_{3,y}}{U_1} - 2\frac{U_3 U_{1,y}}{U_1^2} - \frac{U_{2,x}}{U_1} + \frac{U_2 U_{1,x}}{U_1^2} - \frac{U_{4,z}}{U_1} + \frac{U_4 U_{1,z}}{U_1^2} \right),$$

$$\sigma_{zz} = \frac{2}{3}\mu \left(2\frac{U_{4,z}}{U_1} - 2\frac{U_4 U_{1,z}}{U_1^2} - \frac{U_{2,x}}{U_1} + \frac{U_2 U_{1,x}}{U_1^2} - \frac{U_{3,y}}{U_1} + \frac{U_3 U_{1,y}}{U_1^2} \right). \tag{3.22}$$

Symmetry of the viscous stress tensor provides the following three equations

$$\tau_{yx} = \tau_{xy}, \qquad \tau_{zx} = \tau_{xz}, \quad \text{and} \quad \tau_{zy} = \tau_{yz}. \tag{3.23}$$

Similar expressions can also be obtained for the thermal fluxes

$$
\begin{aligned}
q_x =& \ \gamma\frac{\mu}{Pr}\left[\frac{U_{5,x}}{U_1} - \frac{U_5 U_{1,x}}{U_1^2} + \frac{U_2^2 + U_3^2 + U_4^2}{U_1^3}U_{1,x} \right] \\
& - \gamma\frac{\mu}{Pr}\left[\frac{U_2 U_{2,x} + U_3 U_{3,x} + U_4 U_{4,x}}{U_1^2} \right]
\end{aligned} \tag{3.24}
$$

$$
\begin{aligned}
q_y =& \ \gamma\frac{\mu}{Pr}\left[\frac{U_{5,y}}{U_1} - \frac{U_5 U_{1,y}}{U_1^2} + \frac{U_2^2 + U_3^2 + U_4^2}{U_1^3}U_{1,y} \right] \\
& - \gamma\frac{\mu}{Pr}\left[\frac{U_2 U_{2,y} + U_3 U_{3,y} + U_4 U_{4,y}}{U_1^2} \right]
\end{aligned} \tag{3.25}
$$

$$
\begin{aligned}
q_z =& \ \gamma\frac{\mu}{Pr}\left[\frac{U_{5,z}}{U_1} - \frac{U_5 U_{1,z}}{U_1^2} + \frac{U_2^2 + U_3^2 + U_4^2}{U_1^3}U_{1,z} \right] \\
& - \gamma\frac{\mu}{Pr}\left[\frac{U_2 U_{2,z} + U_3 U_{3,z} + U_4 U_{4,z}}{U_1^2} \right]
\end{aligned} \tag{3.26}
$$

The derivation of the diffusive thermal fluxes in terms of $(U_m, U_{m,x}, U_{m,y}, U_{m,z})$ may be found in Appendix A. Furthermore, the full set of the diffusive fluxes ($\mathbf{F_v}$, $\mathbf{G_v}$ and $\mathbf{H_v}$) is given in Appendix B.

The components of the convective ($\mathbf{F}$, $\mathbf{G}$ and $\mathbf{H}$) and diffusive fluxes ($\mathbf{F_v}$, $\mathbf{G_v}$ and $\mathbf{H_v}$) depend solely on the conservative variables and the spatial derivatives of the conservative variables. Consequently, the only independent discrete variables for each grid points are (U_m, $U_{m,x}$, $U_{m,y}$ and $U_{m,z}$) where $m = 1, 2, \ldots, 5$.

3.3 Large–Eddy Simulation and Filtering

The simulation of turbulent flows may be performed using three different approaches, i.e., Reynolds–Averaged Navier–Stokes equations (RANS), direct numerical simulation (DNS) and large–eddy simulation (LES). In the present study, the

LES is employed to simulate the turbulent flow field features with high–fidelity, since the LES concept is well suited to detailed studies of complex unsteady flows and flow–induced noise.

3.3.1 Filtered Navier–Stokes Equations

Large–eddy simulations are three–dimensional, time–dependent and expensive but much less costly than DNS of the same flow (Ferziger and Perić, 2002). The primary difference between DNS and LES is the filtering approach. This approach was originally suggested by Leonard (1974). Any flow quantity generally given by the variable $f(\mathbf{x}, t)$ being a function of space $\mathbf{x}$ and time t can be decomposed into the resolved–scale or a large–scale part $\overline{f}(\mathbf{x}, t)$ and the subgrid–scale or a small–scale part $f'(\mathbf{x}, t)$. The decomposition of the flow variables is defined by

$$f(\mathbf{x}, t) = \overline{f}(\mathbf{x}, t) + f'(\mathbf{x}, t) \tag{3.27}$$

The filtered variable $\overline{f}(\mathbf{x}, t)$ is obtained by filtering the entire domain using a grid filter function G as follows

$$\overline{f}(\mathbf{x}, t) = \int_D G(\mathbf{x}, \mathbf{x}', \Delta) f(\mathbf{x}', t) dV(x') \tag{3.28}$$

where D is the entire domain and Δ describes a characteristic filter width.

Filter functions which have been applied in LES include a Gaussian, a top–hat filter and a cut–off. For compressible turbulent flows the use of a Favre averaging together with one of the spatial filter functions is a common approach, since it does not alter the conservative form of the unfiltered governing equations (Moin et al., 1991; Erlebacher et al., 1992). Otherwise, using any other filtering approach would introduce more complicated subgrid–scale terms in the governing equations due to additional correlations involving density fluctuations. The filtered Navier–Stokes equations would contain products between density and other variables like velocity or temperature (Blazek, 2005). The Favre–filtered variable is given by

$$\tilde{f} = \frac{\overline{\rho f}}{\overline{\rho}} \tag{3.29}$$

where $\tilde{f}$ represents the large–scale component written in terms of a Favre–filtered.

In the time–conservative finite–volume method, the Favre averaging is combined with a top–hat filter kernel where the filter width (Δ) is chosen equal to the grid size (h), i.e., $\Delta = h$. Thus an explicit filtering operation of the velocity distribution assumed to be cell–wise constant leads to the initial distribution again. Consequently, the application of an *explicit* filtering operation can be omitted completely (Breuer, 2007). Instead, the filtering operation is *implicitly* given by the numerical method used (i.e., the grid as well as the discretization errors are assumed to define the filter G) (Blazek, 2005). The effectiveness of the implicit filtering operation was demonstrated by Rogallo and Moin (1984); De Stefano and Vasilyev (2004). The explicit filtering usually poses new difficulties for general non–equidistant grids with non–constant filter widths. One may refer to the review of Lund (1997) for further details about the weak points of the explicit filtering. The advantages of explicit filtering method in practice remain unclear. Due to the extra filtering operations, the explicit filtering approach is computationally more expensive than its implicit counterpart (Gullbrand and Chow, 2003). The implicit filtering approach is popular and in most LES methods filtering is performed implicitly, especially for practically relevant turbulent flows in complex geometries (Loh and Hultgren, 2005; Breuer, 2007; Li et al., 2007). The resulting equations have the same structure as the unsteady RANS equations with additional terms called subgrid–scale (SGS) stresses. When the Navier–Stokes equations with constant density (incompressible flow) are filtered, one obtains a set of equations very similar to the RANS equations (Ferziger and Perić, 2002).

The filtering operation (eq. (3.28)) is applied to the three–dimensional time–dependent Navier–Stokes equations in order to remove the small turbulent scales of the total flow field and to obtain the filtered conservation equations to conduct large–eddy simulations. The resulting equations describe the evolution of the resolved field and contain the subgrid–scale parts which represent the effects of the instantaneous small–scale fluctuations on the resolved field. The resulting governing equations are then solved directly for the resolved–scales whilst the subgrid–scales are computed using a subgrid–scale model. The Favre–filtered compressible Navier–

Stokes equations (Uzun et al., 2002; Uzun, 2003):

$$\frac{\partial \overline{\rho}}{\partial t} + \frac{\partial \overline{\rho} \tilde{u}_i}{\partial x_i} = 0 \tag{3.30}$$

$$\frac{\partial \overline{\rho} \tilde{u}_i}{\partial t} + \frac{\partial \overline{\rho} \tilde{u}_i \tilde{u}_j}{\partial x_j} + \frac{\partial \overline{p}}{\partial x_i} = \frac{\partial}{\partial x_j}(\hat{\tau}_{ij} - \tau_{ij}^{SGS}) \tag{3.31}$$

$$\frac{\partial \overline{e}_t}{\partial t} + \frac{\partial \tilde{u}_i(\overline{e}_t + \overline{p})}{\partial x_i} = \frac{\partial}{\partial x_j}\tilde{u}_i(\hat{\tau}_{ij} - \tau_{ij}^{SGS}) - \frac{\partial}{\partial x_i}(\hat{q}_i + q_i^{SGS}) \tag{3.32}$$

where the total energy is defined as

$$\overline{e}_t = \frac{1}{2}\overline{\rho}\tilde{u}_i\tilde{u}_i + \frac{\overline{p}}{(\gamma - 1)} \tag{3.33}$$

$\hat{\tau}_{ij}$ is the resolved stress tensor and $\hat{q}_i$ describes the resolved heat flux. Furthermore, τ_{ij}^{SGS} and q_i^{SGS} are the subgrid–scale stress tensor and the subgrid–scale heat flux, respectively. The summation convention is used in the eqs. (3.30) to (3.33). The filtered governing equations may be rearranged into a form that looks identical to URANS equations.

3.3.2 Subgrid–Scale Modeling for Compressible Turbulent Flows

In order to simulate the momentum and energy transfer between large and small eddies, the resolvable large eddies can be solved directly by the filtered conservation equations (3.30)–(3.33) whereas the subgrid–scales have to be modeled. In addition to assumptions of homogeneity and isotropy of the small scales, the assumption of equilibrium (i.e., the small scales with lower energy content have shorter time scales than the large ones since the energy contained in large eddies is transferred to the smaller ones and eventually all are dissipated into heat at the level of smallest eddies due to the molecular viscosity) is also imposed for most of the applications. Although, most of the energy transfer takes place from the large–scale structure to the small–scale structure, the reverse can also occur (e.g. backscatter), which is not taken into account by the equilibrium assumption. Consequently, the main purpose of the subgrid–scale model is to provide dissipation of energy.

The resolved viscous stress tensor is defined as

$$\hat{\tau}_{ij} = 2\tilde{\mu}(\tilde{S}_{ij} - \frac{1}{3}\tilde{S}_{kk}\delta_{ij}) \tag{3.34}$$

where δ_{ij} stands for the Kronecker delta and $\tilde{S}_{ij}$ describes the Favre–filtered strain rate tensor

$$\tilde{S}_{ij} = \frac{1}{2}\left(\frac{\partial \tilde{u}_i}{\partial x_j} + \frac{\partial \tilde{u}_j}{\partial x_i}\right) \tag{3.35}$$

In the present study the classical Smagorinsky subgrid–scale (SGS) model (Smagorinsky, 1963) is employed due to its simplicity. The subgrid–scale stress tensor is given by

$$\tau_{ij}^{SGS} = \overline{\rho}\left(\widetilde{u_i u_j} - \tilde{u}_i \tilde{u}_j\right) \tag{3.36}$$

and modeled as (Uzun, 2003; Blazek, 2005)

$$\tau_{ij}^{SGS} = -\mu_t(2\tilde{S}_{ij} - \frac{2}{3}\tilde{S}_{kk}\delta_{ij}) + \frac{2}{3}\overline{\rho}k^{SGS}\delta_{ij} \tag{3.37}$$

where μ_t is the subgrid–scale eddy-viscosity term defined as

$$\mu_t = C_R\overline{\rho}\Delta^2|\tilde{S}_M| \tag{3.38}$$

and k^{SGS} is the subgrid–scale kinetic energy and estimated as follows

$$k^{SGS} = C_I\Delta^2|\tilde{S}_M|^2 \tag{3.39}$$

where $|\tilde{S}_M|$ is the magnitude of the strain–rate tensor computed from the resolved velocity field and given by

$$|\tilde{S}_M| = (2\tilde{S}_{ij}\tilde{S}_{ij})^{1/2} \tag{3.40}$$

C_R and C_I are free parameters called the Smagorinsky model constants. All computations in this study were carried out with Smagorinsky constants of $C_R = 0.0324$ and $C_I = 0.00575$ based on previous studies (Uzun, 2003). The filter width Δ is the characteristic length scale of the smallest resolved eddies (Rogallo and Moin, 1984) and given by $(\Delta x \cdot \Delta y \cdot \Delta z)^{1/3}$ where Δx, Δy and Δz are the sizes of the control volume.

The first term appearing on the right–hand side of eq. (3.37) is the incompressible term in Smagorinsky's model (Smagorinsky, 1963) and the second term is the compressibility correction known as Yoshizawa's expression (Yoshizawa, 1986).

In order to account for the reduction of the subgrid length in the near–wall regions the value of the eddy–viscosity (μ_t) has to be reduced. Thus, the eddy–viscosity is modified based on a Van Driest damping function (Van Driest, 1956)

as

$$\mu_t = C_R \overline{\rho} \Delta^2 \left[\left(1 - e^{-y^+/25} \right)^{\gamma_1} \right]^{\gamma_2} |\tilde{S}_M| \tag{3.41}$$

The alternative values for the exponents $\gamma_1 = 3$ and $\gamma_2 = 0.5$ given by Piomelli et al. (1988) are used. However, the application of the damping function remains problematic for complex geometries (Breuer, 2007). The dimensionless wall distance is defined as

$$y^+ = \frac{u^* y}{\nu} \tag{3.42}$$

where u^* is the friction velocity computed from the instantaneous wall shear stress at the wall and ν is the kinematic viscosity.

The resolved heat flux reads:

$$\hat{q}_i = -c_p \frac{\mu}{Pr} \frac{\partial \tilde{T}}{\partial x_i} \tag{3.43}$$

where c_p, Pr and μ are the specific heat capacity at constant pressure, the Prandtl number and the dynamic viscosity, respectively.

The subgrid–scale heat flux is given by

$$q_i^{SGS} = -c_p \overline{\rho} \left(\widetilde{u_i T} - \tilde{u}_i \tilde{T} \right) \tag{3.44}$$

and it is modeled by using a temperature gradient approach (Uzun, 2003)

$$q_i^{SGS} = -c_p \frac{\mu_t}{Pr_t} \frac{\partial \tilde{T}}{\partial x_i} \tag{3.45}$$

where μ_t is the quantity of the eddy–viscosity and given by eq. (3.38). Pr_t is the turbulent Prandtl number and set to a value of 0.9 (Uzun, 2003).

In order to close the system of equations, the perfect gas relation (eq. (3.13)) and Sutherland's law (eq. (3.14)) are used.

The Navier–Stokes computations without turbulence terms can be carried out by replacing all filtered variables with their unfiltered forms and setting the subgrid–scale stress tensor and the subgrid–scale heat flux terms to zero. Furthermore, for the inviscid Euler computations the viscous stress tensor should be set to zero (Aybay and He, 2007).

Chapter 4

Numerical Methodology

This chapter is organized as follows. First, Section 4.1 provides details about the coupled spatial and temporal discretizations of the flow variables and the evaluation of fluxes. In Section 4.2 the solution procedure is discussed for the evaluation of the flow variables and the spatial derivatives of the flow variables. Section 4.3 provides details of the stability criterion for the explicit time–conservative scheme. Then, implementation of the non–reflecting boundary condition, inlet and outlet boundary conditions, the solid wall boundary condition for inviscid and viscous flows as well as the periodic boundary condition is explained in Section 4.4. Finally, the basic implementation issues of the direct–flux based multigrid technique and parallel computing are given in Section 4.5.1 and Section 4.5.2, respectively.

4.1 Coupled Spatial and Temporal Discretizations

The conservation form of the three–dimensional unsteady Navier–Stokes equations with respect to a stationary reference frame, with no external body force and heat generation can be expressed as follows

$$\frac{\partial \mathbf{U}}{\partial t} + \frac{\partial \mathbf{F}}{\partial x} + \frac{\partial \mathbf{G}}{\partial y} + \frac{\partial \mathbf{H}}{\partial z} = \frac{\partial \mathbf{F_v}}{\partial x} + \frac{\partial \mathbf{G_v}}{\partial y} + \frac{\partial \mathbf{H_v}}{\partial z} \qquad (4.1)$$

where $\mathbf{U}$ is the vector of conservative variables, $\mathbf{F}$, $\mathbf{G}$ and $\mathbf{H}$ are the convective flux vectors and $\mathbf{F_v}$, $\mathbf{G_v}$ and $\mathbf{H_v}$ are the viscous flux vectors in the x, y and z directions, respectively.

Let $x_1 = x$, $x_2 = y$, $x_3 = z$ and $x_4 = t$ be the coordinates of a four–dimensional Euclidean space E_4. Using Gauss' divergence theorem the integral form of eq. (4.1) in the space–time domain E_4 can be expressed as follows (Zhang, Z.C. et al., 2002)

$$\oint_{S(V)} \mathbf{h} \cdot d\mathbf{s} = 0 \qquad (4.2)$$

where $\mathbf{h} = (\mathbf{F} - \mathbf{F}_v, \mathbf{G} - \mathbf{G}_v, \mathbf{H} - \mathbf{H}_v, \mathbf{U})$ are the flux vectors in space–time of mass, x–momentum, y–momentum, z–momentum, energy and the vector of conservative variables. $S(V)$ is the surface of an arbitrary space–time region V in E_4 and $d\mathbf{s} = \mathbf{n}d\sigma$ where $\mathbf{n}$ is the outward unit normal vector and $d\sigma$ is the area of a surface element on $S(V)$. The time–conservative finite–volume method integrates eq. (4.2) in the four–dimensional Euclidean space to evaluate the flow variables. The equation states that the total space–time flux $\mathbf{h}$, vanishes through the surface of the arbitrary space–time region (Zhang, Z.C. et al., 2002; Loh et al., 2001a; Chang, 1995).

The time–conservative finite–volume method employed in the present study is based on a multiblock structured grid in three–dimensional space. The method was extended from the numerical scheme given by Zhang, Z.C. et al. (2002) and used here with some modifications (Aybay and He, 2007, 2008a). The discretization type given by Zhang, Z.C. et al. (2002) is depicted in Fig. 4.1. This method will be described first. Later on an improved discretization which is used in this study will be explained.
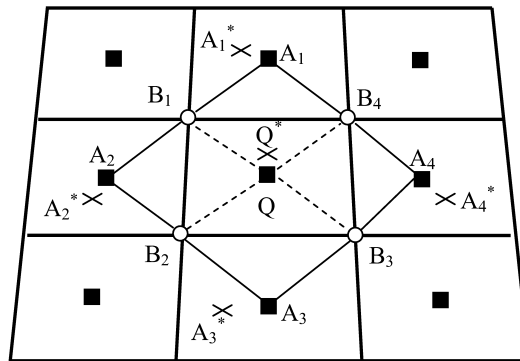
Figure 4.1: 2–D discretization type given by Zhang, Z.C. et al. (2002)

The computational domain is divided into non–overlapping convex quadrilaterals defined by $B_1 B_2 B_3 B_4$, as shown in Fig. 4.1. Any two neighboring quadrilaterals

share a common side. The centroid of each grid cell is denoted by a square symbol and the vertices of the quadrilaterals are marked by circles. Point Q is the centroid of the quadrilateral $B_1B_2B_3B_4$, whereas A_1, A_2, A_3 and A_4 are the centroids of the neighboring quadrilaterals. Furthermore, Q^* (marked by a cross) is the centroid of the polygon $A_1B_1A_2B_2A_3B_3A_4B_4$ and stands for the solution point associated with the point Q. In general, the point Q^* does not coincide with point Q for a non–uniform grid distribution. Note that A_1^*, A_2^*, A_3^* and A_4^* are the solution points associated with the points A_1, A_2, A_3 and A_4, respectively. All flow variables and their spatial derivatives are solved and stored at the solution points, i.e., Q^*, A_1^*, A_2^*, A_3^* and A_4^* (see Fig. 4.1).
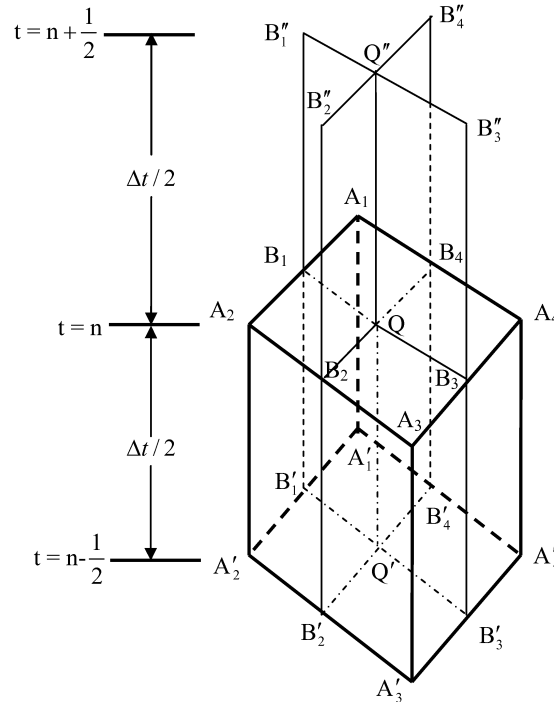
Figure 4.2: 2–D grid distribution in space and time given by Zhang, Z.C. et al. (2002)

Considering Fig. 4.2, the grid points Q, Q' and Q'' denote the points on the $(n)^{th}$, the $\left(n - \frac{1}{2}\right)^{th}$ and the $\left(n + \frac{1}{2}\right)^{th}$ time levels, respectively. The control volume is represented by the hexahedron $A_1A_2A_3A_4A_1'A_2'A_3'A_4'$ and considered for time marching from $t = n - \frac{1}{2}$ to $t = n$. First of all, the flow variables and their spatial derivatives are assumed to be known at the centroid of each grid cell (i.e., A_1', A_2', A_3' and A_4') at

time level $t = n - \frac{1}{2}$. Then, the conservation of space–time flux is enforced over the surface of the control volume $(A_1 A_2 A_3 A_4 A_1' A_2' A_3' A_4')$ to evaluate the flow variables at the solution point Q^* associated with the centre of the grid cell (i.e. Q) at time level $t = n$ (see Fig. 4.1). Finally, the corresponding spatial derivatives at the same time level are calculated based on a weighted finite–difference approach (details are provided in Section 4.2.2). The same procedure is repeated for the advancement of the simulation from time level $t = n$ to $t = n + \frac{1}{2}$.

The discretization type given by Zhang, Z.C. et al. (2002) requires the generation of dummy cells (ghost cells) that lie on the other side of the boundary in order to maintain the order of numerical accuracy as well as to ensure the flux conservation in the vicinity of the boundaries. The main disadvantage of using this approach is that the domain decomposition based on a multiblock structured grid becomes complicated for complex geometries. An improved discretization is depicted in Fig. 4.3 which relies on a new definition of cell interfaces and a new definition of control volume is displayed in Fig. 4.4. In order to prevent or deal efficiently with the problem as mentioned above these new definitions are used. Thus, the evaluation of fluxes along the boundaries is simplified and the flux conservation is ensured. To the best knowledge of the author, the numerical scheme based on these new definitions is discretized for the first time in 3D in the present study including the addition of the viscous terms and the implementation of the LES technique. The objectives of the new definitions of control volume and cell interface in comparison to Zhang's method were twofold; on the one hand, to avoid the generation of the dummy cells outside the computational domain to ensure the flux conservation in the vicinity of the boundaries; on the other hand, to generate non–overlapping subdomains during the decomposition of the computational domain in order to simplify the multiblock grid generation (see Section 4.5.2).

Time–marching for the proposed numerical scheme can be explained as follows. First of all, grid points are shown in a two–dimensional plane (i.e., the x–y plane) for the sake of simplicity. Considering Fig. 4.3, similar to Zhang's discretization (Zhang, Z.C. et al., 2002) the computational domain is divided into non–overlapping convex quadrilateral grid cells defined by $A_1 A_2 A_3 A_4$ and any two neighboring grid cells

share a common side. The four vertices of a quadrilateral (A_1, A_2, A_3 and A_4) are marked by circles which are also the grid points at $t = n - \frac{1}{2}$. Spatial projection of the grid points (Q_1, Q_2, Q_3 and Q_4) and the corresponding solution points (Q_1^*, Q_2^*, Q_3^* and Q_4^*) at $t = n$ are shown by square symbols in Fig. 4.3. Lastly, Q_1^* is the centroid of the polygon (i.e., control volume) $A_1A_2A_3A_4$ and stands for the solution point associated with the grid point Q_1. Similarly, Q_2^*, Q_3^* and Q_4^* are the centroids of neighboring polygons (control volumes)and the corresponding solution points associated with the grid points Q_2, Q_3 and Q_4, respectively. For both, a uniform grid and a non–uniform grid, the solution points (i.e., Q_1^*, Q_2^*, Q_3^* and Q_4^*) coincides with the grid points (i.e., Q_1, Q_2, Q_3 and Q_4) at $t = n$. Hence all flow variables and their spatial derivatives are solved and stored at the solution points (Q_1^*, Q_2^*, Q_3^* and Q_4^*) for time–marching from $t = n - \frac{1}{2}$ to $t = n$.
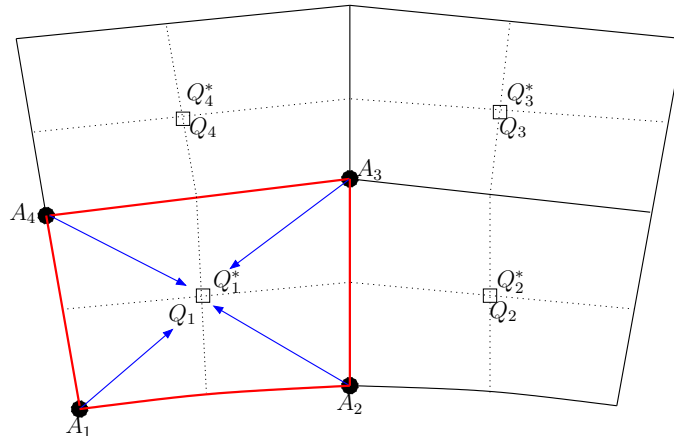
Figure 4.3: Grid points (A_1, A_2, A_3 and A_4) at $t = n - \frac{1}{2}$, spatial projection of grid points (Q_1, Q_2, Q_3 and Q_4) and the corresponding solution points (Q_1^*, Q_2^*, Q_3^* and Q_4^*) at $t = n$ in the x-y plane (without time axis)

In Fig. 4.4, the control volume represented by the hexahedron $A_1A_2A_3A_4A_1'A_2'$ $A_3'A_4'$ shows the grid arrangement in the space–time domain. The points Q_1 and Q_1' denote the grid points on the $\left(n - \frac{1}{2}\right)^{th}$ and the $(n)^{th}$ time levels, respectively. Furthermore, $Q_1^{*\prime}$ lies on the $(n)^{th}$ time level and it is the space–time solution point associated with point Q_1'. In Fig. 4.4, the spatial projections of the solution point $Q_1^{*\prime}$ and the grid point Q_1' are shown as Q_1^* and Q_1, respectively in Fig. 4.3. In the present scheme, the solution point $Q_1^{*\prime}$ and the grid point Q_1' coincide for any

kind of grid distribution (e.g., uniform or non–uniform) for the time–marching from $t = n - \frac{1}{2}$ to $t = n$. This is one of the distinctive features from the discretization given by Zhang, Z.C. et al. (2002). In order to advance the simulation in time, initially the flow variables and their spatial derivatives are assumed to be known at the vertex of each grid cell (i.e., A_1, A_2, A_3 and A_4) at time level $t = n - \frac{1}{2}$. Then, the conservation of space–time flux is enforced over the surface of the control volume in order to calculate the flow variables at the solution point $Q_1^{*\prime}$ at the time level $t = n$. Finally, the corresponding spatial derivatives for this same time level (n) are evaluated by using a weighted finite–difference approach (see Section 4.2.2).
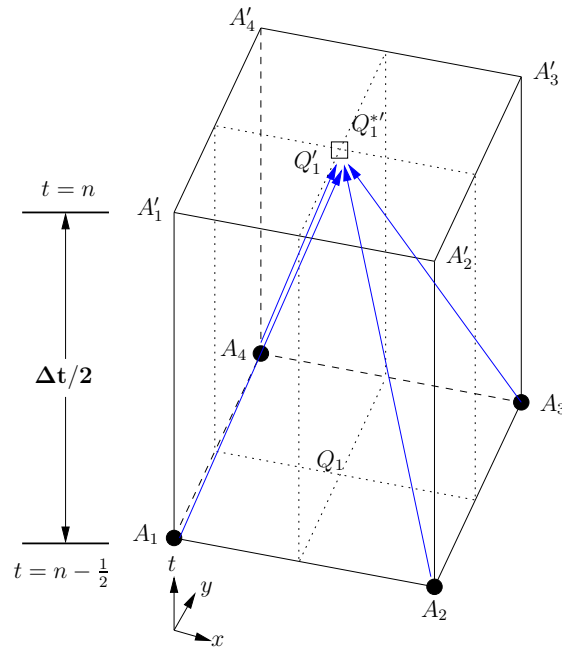
Figure 4.4: Control volume for time–marching from $t = n - \frac{1}{2}$ to $t = n$

The same procedure is repeated for the time–marching from $t = n$ to $t = n + \frac{1}{2}$. In Fig. 4.5, the grid points (Q_1', Q_2', Q_3' and Q_4') at $t = n$ are marked by squares. Spatial projections of the grid points (A_1', A_2', A_3' and A_4') and the corresponding solution points ($A_1^{*\prime}$, $A_2^{*\prime}$, $A_3^{*\prime}$ $A_4^{*\prime}$) at $t = n + \frac{1}{2}$ are shown by circles and cross symbols, respectively. Considering Fig. 4.5, $A_3^{*\prime}$ is the space–time solution point associated with the grid point A_3' and the centroid of the polygon (control volume) defined as $Q_1'Q_2'Q_3'Q_4'$. Similarly, $A_1^{*\prime}$, $A_2^{*\prime}$ and $A_4^{*\prime}$ are the centroids of neighboring polygons

(control volumes) and the corresponding solution points associated with the grid points A'_1, A'_2 and A'_4, respectively.
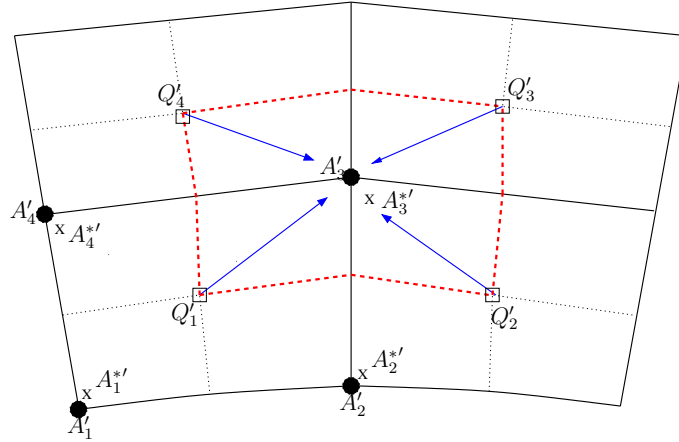
Figure 4.5: Grid points (Q'_1, Q'_2, Q'_3 and Q'_4) at $t = n$, spatial projection of grid points (A'_1, A'_2, A'_3 and A'_4) and the corresponding solution points ($A^{*'}_1$, $A^{*'}_2$, $A^{*'}_3$ $A^{*'}_4$) at $t = n + \frac{1}{2}$ in the x-y plane (without time axis)

In Fig. 4.6, the control volume for the time–marching from $t = n$ to $t = n + \frac{1}{2}$ is shown and described by $Q'_1 Q'_2 Q'_3 Q'_4 Q''_1 Q''_2 Q''_3 Q''_4$. The points A'_3 and A''_3 denote the grid points on the $(n)^{th}$ and $\left(n + \frac{1}{2}\right)^{th}$ time levels, respectively. In order to complete the two–level explicit time–marching, the values of the flow variables and the gradients from the previous time step (at Q'_1, Q'_2, Q'_3 and Q'_4) are used to enforce the conservation of space–time flux over the surface of the control volume. Hence the flow variables are evaluated at the space–time solution point $A^{*''}_3$. Spatial projections of the solution point $A^{*''}_3$ and the grid point A''_3 are shown as $A^{*'}_3$ and A'_3, respectively in Fig. 4.5. One should note that the solution point $A^{*'}_3$ and the grid point A'_3 do not coincide for a non–uniform grid distribution. Hence, when the flow variables and the gradients are evaluated at the solution points, the corresponding values should be transferred from the solution points ($A^{*'}_1$, $A^{*'}_2$, $A^{*'}_3$ and $A^{*'}_4$) to the vertices of each grid cell (A'_1, A'_2, A'_3 and A'_4) by using a first–order Taylor series expansion. The numerical scheme alternates between the cell–vertices and the cell–centres of the grid cells. As a conclusion, by using this proposed discretization the flux conservation was ensured in the vicinity of the boundaries, parallelization of the flow solver based on domain decomposition was simplified (see Section 4.5.2) and

exchanging the physical quantities between the blocks became straightforward.
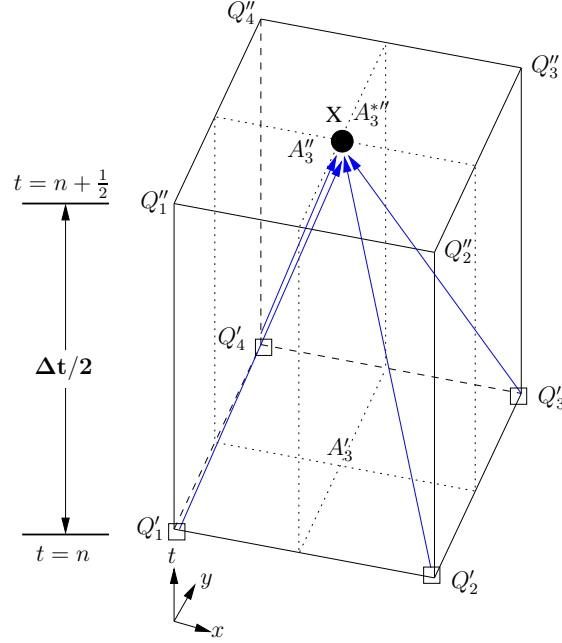
Figure 4.6: Control volume for time–marching from $t = n$ to $t = n + \frac{1}{2}$

Note that the control volumes and the grid arrangement in the space–time domain are shown in 2D up to this point, for the sake of clarity. The discretization of the conservative variables, the convective fluxes, the diffusive fluxes and the space–time flux evaluation for 3D is described here. The discretized conservative variables and the convective fluxes are assumed to be continuous and linearly distributed over the surface of control volume (CV) and they are approximated by the first–order Taylor series expansion, whereas the viscous fluxes are assumed to be constant (see eqs. (4.3) to (4.9)). For any space–time solution points $U_m(x, y, z, t)$, $F_m(x, y, z, t)$, $G_m(x, y, z, t)$, $H_m(x, y, z, t)$, $F_{vm}(x, y, z, t)$, $G_{vm}(x, y, z, t)$ and $H_{vm}(x, y, z, t)$ are approximated with the help of $U_m{}^*$, $F_m{}^*$, $G_m{}^*$, $H_m{}^*$, F_{vm}^*, G_{vm}^* and H_{vm}^*, respectively.

The conservative variables (U_m) are approximated by the first–order Taylor series expansion as follows

$$
\begin{aligned}
U_m{}^*(x, y, z, t) &= (U_m)_{Q^*} + (U_{m,x})_{Q^*}(x - x_{Q^*}) + (U_{m,y})_{Q^*}(y - y_{Q^*}) \\
&\quad + (U_{m,z})_{Q^*}(z - z_{Q^*}) + (U_{m,t})_{Q^*}\left(t^n - t^{n-\frac{1}{2}}\right)
\end{aligned}
\tag{4.3}
$$

Similarly, using the first–order Taylor series expansion the approximated convective fluxes (F, G, H) can be expressed as

$$
\begin{aligned}
F_m{}^* (x, y, z, t) \;=\; & (F_m)_{Q^*} + (F_{m,x})_{Q^*} (x - x_{Q^*}) + (F_{m,y})_{Q^*} (y - y_{Q^*}) \\
& + (F_{m,z})_{Q^*} (z - z_{Q^*}) + (F_{m,t})_{Q^*} \left(t^n - t^{n-\frac{1}{2}} \right)
\end{aligned}
\tag{4.4}
$$

$$
\begin{aligned}
G_m{}^* (x, y, z, t) \;=\; & (G_m)_{Q^*} + (G_{m,x})_{Q^*} (x - x_{Q^*}) + (G_{m,y})_{Q^*} (y - y_{Q^*}) \\
& + (G_{m,z})_{Q^*} (z - z_{Q^*}) + (G_{m,t})_{Q^*} \left(t^n - t^{n-\frac{1}{2}} \right)
\end{aligned}
\tag{4.5}
$$

$$
\begin{aligned}
H_m{}^* (x, y, z, t) \;=\; & (H_m)_{Q^*} + (H_{m,x})_{Q^*} (x - x_{Q^*}) + (H_{m,y})_{Q^*} (y - y_{Q^*}) \\
& + (H_{m,z})_{Q^*} (z - z_{Q^*}) + (H_{m,t})_{Q^*} \left(t^n - t^{n-\frac{1}{2}} \right)
\end{aligned}
\tag{4.6}
$$

where $(x_{Q^*}, y_{Q^*}, z_{Q^*}, t^n)$ shows the coordinates of the space–time solution point Q^*.

Then, the diffusive fluxes (F_{vm}, G_{vm}, H_{vm}) are assumed to be constant over the surface of the control volume and defined as

$$
F_{vm}^* (x, y, z, t) \;=\; (F_{vm})_{Q^*}
\tag{4.7}
$$

$$
G_{vm}^* (x, y, z, t) \;=\; (G_{vm})_{Q^*}
\tag{4.8}
$$

$$
H_{vm}^* (x, y, z, t) \;=\; (H_{vm})_{Q^*}
\tag{4.9}
$$

Lastly, the vector of conservative variables and the flux vectors $\mathbf{h} = (\mathbf{F} - \mathbf{F}_v, \mathbf{G} - \mathbf{G}_v, \mathbf{H} - \mathbf{H}_v, \mathbf{U})$ in space–time of mass, x, y, z–momentum and energy can be approximated as

$$
\mathbf{h}^* = \mathbf{h}
\tag{4.10}
$$

$(U_m)_{Q^*}$, $(U_{m,x})_{Q^*}$, $(U_{m,y})_{Q^*}$, $(U_{m,z})_{Q^*}$ and $(U_{m,t})_{Q^*}$, are the coefficients of the Taylor series expansion in eq. (4.3) and they are the numerical analogues of the values of U_m, $\partial U_m/\partial x$, $\partial U_m/\partial y$, $\partial U_m/\partial z$ and $\partial U_m/\partial t$ at point Q^*, respectively.

Similarly, $(F_m)_{Q^*}$, $(F_{m,x})_{Q^*}$, $(F_{m,y})_{Q^*}$, $(F_{m,z})_{Q^*}$, $(F_{m,t})_{Q^*}$, $(G_m)_{Q^*}$, $(G_{m,x})_{Q^*}$, $(G_{m,y})_{Q^*}$, $(G_{m,z})_{Q^*}$, $(G_{m,t})_{Q^*}$, $(H_m)_{Q^*}$, $(H_{m,x})_{Q^*}$, $(H_{m,y})_{Q^*}$, $(H_{m,z})_{Q^*}$ and $(H_{m,t})_{Q^*}$ are the Taylor series expansion coefficients in the equations (4.4) to (4.6). These coefficients are the numerical analogues of the values of F_m, $\partial F_m/\partial x$, $\partial F_m/\partial y$, $\partial F_m/\partial z$,

$\partial F_m/\partial t$, G_m, $\partial G_m/\partial x$, $\partial G_m/\partial y$, $\partial G_m/\partial z$, $\partial G_m/\partial t$, H_m, $\partial H_m/\partial x$, $\partial H_m/\partial y$, $\partial H_m/\partial z$ and $\partial H_m/\partial t$ at point Q^*, respectively (Zhang, Z.C. et al., 2002; Chang, 1995; Zhang, M. et al., 2004).

Let $(F_{m,l})_{Q^*}$, $(G_{m,l})_{Q^*}$ and $(H_{m,l})_{Q^*}$ be the components of the Jacobian matrices of $\mathbf{F}$, $\mathbf{G}$ and $\mathbf{H}$ associated with the solution point Q^*, respectively. The Jacobian matrices are described in Appendix C and their components can be defined as

$$(F_{m,l})_{Q^*} = \frac{\partial F_m}{\partial U_l}, \qquad (G_{m,l})_{Q^*} = \frac{\partial G_m}{\partial U_l}, \qquad \text{and} \quad (H_{m,l})_{Q^*} = \frac{\partial H_m}{\partial U_l}. \qquad (4.11)$$

for $m = 1, 2, \ldots, 5$ and $l = 1, 2, \ldots, 5$.

The spatial derivatives of $\mathbf{F}$, $\mathbf{G}$ and $\mathbf{H}$ can be expressed by using the chain rule as follows

$$(F_{m,x})_{Q^*} = \sum_{l=1}^{5} (F_{m,l})_{Q^*} (U_{l,x})_{Q^*}, \qquad (G_{m,x})_{Q^*} = \sum_{l=1}^{5} (G_{m,l})_{Q^*} (U_{l,x})_{Q^*},$$

$$(H_{m,x})_{Q^*} = \sum_{l=1}^{5} (H_{m,l})_{Q^*} (U_{l,x})_{Q^*}. \qquad (4.12)$$

$$(F_{m,y})_{Q^*} = \sum_{l=1}^{5} (F_{m,l})_{Q^*} (U_{l,y})_{Q^*}, \qquad (G_{m,y})_{Q^*} = \sum_{l=1}^{5} (G_{m,l})_{Q^*} (U_{l,y})_{Q^*},$$

$$(H_{m,y})_{Q^*} = \sum_{l=1}^{5} (H_{m,l})_{Q^*} (U_{l,y})_{Q^*}. \qquad (4.13)$$

$$(F_{m,z})_{Q^*} = \sum_{l=1}^{5} (F_{m,l})_{Q^*} (U_{l,z})_{Q^*}, \qquad (G_{m,z})_{Q^*} = \sum_{l=1}^{5} (G_{m,l})_{Q^*} (U_{l,z})_{Q^*},$$

$$(H_{m,z})_{Q^*} = \sum_{l=1}^{5} (H_{m,l})_{Q^*} (U_{l,z})_{Q^*}. \qquad (4.14)$$

Note that, by their definitions eqs. (4.12) to (4.14) are functions of U_m, $U_{m,x}$, $U_{m,y}$ and $U_{m,z}$.

In order to define the temporal coefficients of the Taylor series expansion $[(U_{m,t})_{Q^*}$, $(F_{m,t})_{Q^*}$, $(G_{m,t})_{Q^*}$ and $(H_{m,t})_{Q^*}]$ in the equations (4.3) to (4.6). Equation (4.1) can be considered without viscous flux vectors and the following expression can be obtained

$$(U_{m,t})_{Q^*} = -(F_{m,x})_{Q^*} - (G_{m,y})_{Q^*} - (H_{m,z})_{Q^*} \qquad (4.15)$$

Using equations (4.12), (4.13) and (4.14), eq. (4.15) can be written as

$$(U_{m,t})_{Q^*} = -\sum_{l=1}^{5} \left[(F_{m,l})_{Q^*} (U_{l,x})_{Q^*} + (G_{m,l})_{Q^*} (U_{l,y})_{Q^*} + (H_{m,l})_{Q^*} (U_{l,z})_{Q^*} \right] \quad (4.16)$$

Similarly, the temporal derivatives of the convective fluxes ($\mathbf{F}$, $\mathbf{G}$ and $\mathbf{H}$) can be described as follows

$$(F_{m,t})_{Q^*} = \sum_{l=1}^{5} (F_{m,l})_{Q^*} (U_{m,t})_{Q^*} \quad (4.17)$$

$$(G_{m,t})_{Q^*} = \sum_{l=1}^{5} (G_{m,l})_{Q^*} (U_{m,t})_{Q^*} \quad (4.18)$$

$$(H_{m,t})_{Q^*} = \sum_{l=1}^{5} (H_{m,l})_{Q^*} (U_{m,t})_{Q^*} \quad (4.19)$$

The viscous terms have no influence on the distribution of $(U_{m,t})_{Q^*}$ over each CV surface. However, the viscous terms ($(F_{vm})_{Q^*}$, $(G_{vm})_{Q^*}$ and $(H_{vm})_{Q^*}$) will have their contributions on the integral equation (see eq. (4.22)). The viscous fluxes are assumed to be constant within the cell interface (i.e., the surface of control volume). Due to the dissipative nature of the viscous terms, they are obtained from flow variables at the centroid of each cell interface. The viscous fluxes can be evaluated as functions of U_m, $U_{m,x}$, $U_{m,y}$ and $U_{m,z}$ using equations (3.22) to (3.26).

Consequently, the only independent discrete variables to be solved simultaneously at each grid point are the components of the conservative variables (U_m) and their spatial gradients ($U_{m,x}$, $U_{m,y}$ and $U_{m,z}$). Although the convective fluxes and the diffusive fluxes can be completely determined on the surface of CV as functions of the conservative variables (U_m) and their gradients ($U_{m,x}$, $U_{m,y}$ and $U_{m,z}$), one should note that the temporal coefficients $(F_{m,t})_{Q^*}$, $(G_{m,t})_{Q^*}$ and $(H_{m,t})_{Q^*}$ of the Taylor series expansions in the equations (4.4) to (4.6), will appear with additional time terms to evaluate the total space–time flux over the surface of CV (see eq. (4.22)).

The conservation of the space–time fluxes is enforced over the surface of CV. In the present method, spatial and temporal discretizations are coupled to calculate

flux conservation. Hence the flux conservation is not only enforced in space but also in time. Contrarily, traditional methods focus only on the conservation of the spatial fluxes and employ a separate discretization in time.

4.2 Solution Procedure

When values of $(U_m)_{Q^*}$, $(U_{m,x})_{Q^*}$, $(U_{m,y})_{Q^*}$, $(U_{m,z})_{Q^*}$ and $(U_{m,t})_{Q^*}$ are known, the distribution of the flow variables as well as the inviscid and viscous fluxes can be fully specified over the surface of CV. Unknown flow variables at the solution point can be solved by using the flux conservation equation (see eq. (4.2)).

4.2.1 Evaluation of the Flow Variables

The flux leaving each surface of the CV is equal to the scalar product between the vector of conservative variables and the flux vectors in space–time of mass, x–momentum, y–momentum, z–momentum and energy $[\mathbf{h}^* = (\mathbf{F}^* - \mathbf{F}_v^*, \mathbf{G}^* - \mathbf{G}_v^*, \mathbf{H}^* - \mathbf{H}_v^*, \mathbf{U}^*)]$, evaluated at the centroid of the surface and the surface vector $\mathbf{s}$.

Considering Fig. 4.7, for the hexahedron defined by $A_1A_2A_3A_4A_5A_6A_7A_8$, its surface vector is $s_{A_1A_2A_3A_4A_5A_6A_7A_8}$ and composed of eight sub–hexahedrons.
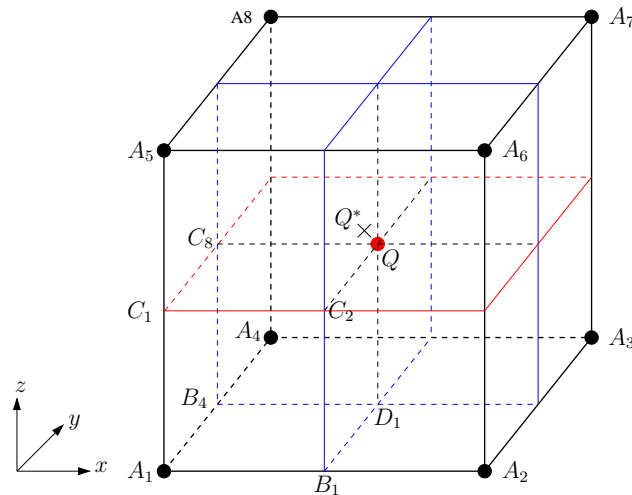
Figure 4.7: 3–D control volume without time axis

Here the flux evaluation is only shown for one of the sub–hexahedron for the time–marching from $t = n$ to $t = n + \frac{1}{2}$ for the other sub–hexahedrons the flux

evaluation can be performed in a similar way. In Fig. 4.7, the sub–hexahedron defined by $A_1B_1D_1B_4C_1C_2QC_8$ is depicted and the surface vector is defined by $s_{A_1B_1D_1B_4C_1C_2QC_8}$. The coordinates of its centroid are $(x_{q_1^*}, y_{q_1^*}, z_{q_1^*}, t^n)$. Therefore, the flux leaving the surface of the sub–hexahedron $(A_1B_1D_1B_4C_1C_2QC_8)$ can be expressed as

$$
\begin{aligned}
(FLUX_m)_{A_1B_1D_1B_4C_1C_2QC_8} = & -V_1^*[(U_m)^n_{A_1^*} + (x_{q_1^*} - x_{A_1^*})(U_{m,x})^n_{A_1^*} \\
& + (y_{q_1^*} - y_{A_1^*})(U_{m,y})^n_{A_1^*} \\
& + (z_{q_1^*} - z_{A_1^*})(U_{m,z})^n_{A_1^*}]
\end{aligned}
\tag{4.20}
$$

where $m = 1, 2, \ldots, 5$ and V_1^* is the volume of the sub–hexahedron defined by $A_1B_1D_1B_4C_1C_2QC_8$.
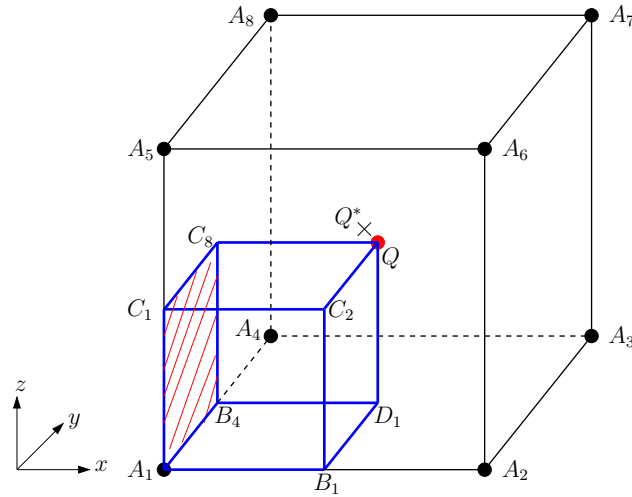
Figure 4.8: Flux evaluation on the quadrilateral defined by $A_1B_4C_8C_1$

In Fig. 4.8, the quadrilateral defined by $A_1B_4C_8C_1$ is shown. Its surface vector is defined as

$$
\begin{aligned}
s_{A_1B_4C_8C_1} = & \frac{\Delta t}{2}((y_{C_1} - y_{B_4})(z_{C_8} - z_{A_1}) - (z_{C_1} - z_{B_4})(y_{C_8} - y_{A_1}), \\
& (z_{C_1} - z_{B_4})(x_{C_8} - x_{A_1}) - (x_{C_1} - x_{B_4})(z_{C_8} - z_{A_1}), \\
& (x_{C_1} - x_{B_4})(y_{C_8} - y_{A_1}) - (y_{C_1} - y_{B_4})(x_{C_8} - x_{A_1}), 0)
\end{aligned}
\tag{4.21}
$$

and the coordinates of its centroid are $(C_{x_1}, C_{y_1}, C_{z_1}, t^n + \frac{\Delta t}{4})$.

The flux leaving the surface $A_1 B_4 C_8 C_1$ is described as follows

$$
\begin{aligned}
(FLUX_m)_{A_1 B_4 C_8 C_1} = & \frac{\Delta t}{2}[(y_{C_1} - y_{B_4})(z_{C_8} - z_{A_1}) - (z_{C_1} - z_{B_4})(y_{C_8} - y_{A_1})] \\
& [(F_m)^n_{A_1^*} + (C_{x_1} - x_{A_1^*})(F_{m,x})^n_{A_1^*} + (C_{y_1} - y_{A_1^*})(F_{m,y})^n_{A_1^*} \\
& + (C_{z_1} - z_{A_1^*})(F_{m,z})^n_{A_1^*} \\
& + \frac{\Delta t}{4}(F_{m,t})^n_{A_1^*} - F_{vm}^{A_1 B_4 C_8 C_1}] \\
& + \frac{\Delta t}{2}[(z_{C_1} - z_{B_4})(x_{C_8} - x_{A_1}) - (x_{C_1} - x_{B_4})(z_{C_8} - z_{A_1})] \\
& [(G_m)^n_{A_1^*} + (C_{x_1} - x_{A_1^*})(G_{m,x})^n_{A_1^*} + (C_{y_1} - y_{A_1^*})(G_{m,y})^n_{A_1^*} \\
& + (C_{z_1} - z_{A_1^*})(G_{m,z})^n_{A_1^*} \\
& + \frac{\Delta t}{4}(G_{m,t})^n_{A_1^*} - G_{vm}^{A_1 B_4 C_8 C_1}] \\
& + \frac{\Delta t}{2}[(x_{C_1} - x_{B_4})(y_{C_8} - y_{A_1}) - (y_{C_1} - y_{B_4})(x_{C_8} - x_{A_1})] \\
& [(H_m)^n_{A_1^*} + (C_{x_1} - x_{A_1^*})(H_{m,x})^n_{A_1^*} + (C_{y_1} - y_{A_1^*})(H_{m,y})^n_{A_1^*} \\
& + (C_{z_1} - z_{A_1^*})(H_{m,z})^n_{A_1^*} \\
& + \frac{\Delta t}{4}(H_{m,t})^n_{A_1^*} - H_{vm}^{A_1 B_4 C_8 C_1}]
\end{aligned}
\tag{4.22}
$$

where $m = 1, 2, \ldots, 5$, the viscous fluxes $F_{vm}^{A_1 B_4 C_8 C_1}$, $G_{vm}^{A_1 B_4 C_8 C_1}$ and $H_{vm}^{A_1 B_4 C_8 C_1}$ are obtained from the flow variables at the centroids of the surface $A_1 B_4 C_8 C_1$ as well as $(U_{m,x})^n_{A_1^*}$, $(U_{m,y})^n_{A_1^*}$ and $(U_{m,z})^n_{A_1^*}$. Here the descriptions of a surface vector and the flux leaving a surface are provided only for the quadrilateral defined by $A_1 B_4 C_8 C_1$. The flux evaluation on the quadrilateral defined by $A_1 B_1 C_2 C_1$ and $A_1 B_1 D_1 B_4$ with their surface vectors can be found in Appendix D.

The total flux leaving three surfaces of the sub–hexahedron defined by $A_1 B_1 D_1 B_4$ $C_1 C_2 Q C_8$ can be written as follows

$$
\begin{aligned}
(flux_m)^n_1 = & (FLUX_m)_{A_1 B_1 D_1 B_4 C_1 C_2 Q C_8} + (FLUX_m)_{A_1 B_4 C_8 C_1} \\
& + (FLUX_m)_{A_1 B_1 C_2 C_1} + (FLUX_m)_{A_1 B_1 D_1 B_4}
\end{aligned}
\tag{4.23}
$$

where $m = 1, 2, \ldots, 5$.

Similarly, the fluxes leaving the surfaces of other seven sub–hexahedrons (e.g., $A_2 B_2 D_1 B_1$ $C_3 C_4 Q C_2$) can be expressed in a similar way.

Using the fundamental principle of the time–conservative finite–volume scheme, the total space–time flux leaving a CV through the surfaces of the CV vanishes (see

eq. (4.2)). As a result, the space–time flux conservation over the CV surface can be written as

$$
\begin{aligned}
(FLUX_m)_{A_1 A_2 A_3 A_4 A_5 A_6 A_7 A_8} = \quad & -[(flux_m)_1^n + (flux_m)_2^n + (flux_m)_3^n \\
& + (flux_m)_4^n + (flux_m)_5^n + (flux_m)_6^n \\
& + (flux_m)_7^n + (flux_m)_8^n]
\end{aligned}
\tag{4.24}
$$

where $m = 1, 2, \ldots, 5$, $l = 1, 2, \ldots, 8$ and n is the time level, $(flux_m)_l^n$ stands for the evaluation of flux for each sub–hexahedron.

Consequently, sorting now all the above contributions and terms, the flow variables $(U_m)_{Q^*}^{n+\frac{1}{2}}$ at point Q^* is updated as follows

$$
(U_m)_{Q^*}^{n+\frac{1}{2}} = \frac{(flux_m)_1^n + (flux_m)_2^n + \ldots + (flux_m)_7^n + (flux_m)_8^n}{V_1^* + V_2^* + \ldots + V_7^* + V_8^*}
\tag{4.25}
$$

where $m = 1, 2, \ldots, 5$, V_l^* represents the volume of each sub–hexahedron ($l = 1, 2, \ldots, 8$).

4.2.2 Evaluation of the Gradients of the Flow Variables

A weighted finite–difference approach is employed to calculate the spatial derivatives (i.e., gradients) of the flow variables, e.g., $(U_{m,x})_{Q^*}$, $(U_{m,y})_{Q^*}$ and $(U_{m,z})_{Q^*}$. Initially, for the sake of clarity, this approach is described for the two–dimensional discretization. Then the same procedure is adapted for the three–dimensional discretization. As discussed in Section 4.1, the solution point (Q^*) and the grid point (Q) coincide for any kind of grid distribution for the time–marching from $t = n - \frac{1}{2}$ to $t = n$ (see Fig. 4.3). On the other hand, considering Fig. 4.5, these points do not coincide for a non–uniform grid distribution for the time–marching from $t = n$ to $t = n + \frac{1}{2}$. Hence, evaluation of the spatial derivatives is explained here only for the time–marching from $t = n$ to $t = n + \frac{1}{2}$. Note that the same procedure can be used for evaluation of the spatial gradients for the time–marching from $t = n - \frac{1}{2}$ to $t = n$.

In Fig. 4.5, the flow variables at $A_3^{*\prime}$ (marked by a cross symbol) are obtained from eq. (4.25) at $t = n + \frac{1}{2}$. In order to employ the weighting procedure, the flow variables at four neighboring points Q_1', Q_2', Q_3' and Q_4' are obtained by using the

first–order Taylor series expansion along the time axis from the time level $t = n$ as follows

$$(U_m)_{Q'_l}^{n+\frac{1}{2}} = (U_m)_{Q'_l}^n + \frac{\Delta t}{2}(U_{m,t})_{Q'_l}^n \tag{4.26}$$

where $m = 1, 2, \ldots, 4$ and $l = 1, 2, \ldots, 4$ denoting the points Q'_1, Q'_2, Q'_3 and Q'_4, respectively.

As a result, the spatial gradients of the flow variables can be obtained by four sets of $(U_{m,x})_{A_3^{*'}}$ and $(U_{m,y})_{A_3^{*'}}$ associated with the neighboring points $(Q'_1, Q'_2, Q'_3$ and $Q'_4)$.

The first set of $(U_{m,x})_{A_3^{*'}}$ and $(U_{m,y})_{A_3^{*'}}$ associated with the points Q'_1 and Q'_2 (see Fig. 4.5) can be evaluated as follows

$$\left(u_{m,x}^{(1)}\right)_{A_3^{*'}} = \frac{\Delta_x}{\Delta} \quad \text{and} \quad \left(u_{m,y}^{(1)}\right)_{A_3^{*'}} = \frac{\Delta_y}{\Delta} \quad (\Delta \neq 0) \tag{4.27}$$

where

$$\Delta = \begin{vmatrix} x_{Q'_1} - x_{A_3^{*'}} & y_{Q'_1} - y_{A_3^{*'}} \\ x_{Q'_2} - x_{A_3^{*'}} & y_{Q'_2} - y_{A_3^{*'}} \end{vmatrix} \tag{4.28}$$

$$\Delta_x = \begin{vmatrix} (U_m)_{Q'_1}^{n+\frac{1}{2}} - (U_m)_{A_3^{*'}}^{n+\frac{1}{2}} & y_{Q'_1} - y_{A_3^{*'}} \\ (U_m)_{Q'_2}^{n+\frac{1}{2}} - (U_m)_{A_3^{*'}}^{n+\frac{1}{2}} & y_{Q'_2} - y_{A_3^{*'}} \end{vmatrix} \tag{4.29}$$

and

$$\Delta_y = \begin{vmatrix} x_{Q'_1} - x_{A_3^{*'}} & (U_m)_{Q'_1}^{n+\frac{1}{2}} - (U_m)_{A_3^{*'}}^{n+\frac{1}{2}} \\ x_{Q'_2} - x_{A_3^{*'}} & (U_m)_{Q'_2}^{n+\frac{1}{2}} - (U_m)_{A_3^{*'}}^{n+\frac{1}{2}} \end{vmatrix} \tag{4.30}$$

The rest of the pairs $(u_{m,x}^{(2)})_{A_3^{*'}}$–$(u_{m,y}^{(2)})_{A_3^{*'}}$, $(u_{m,x}^{(3)})_{A_3^{*'}}$–$(u_{m,y}^{(3)})_{A_3^{*'}}$ and $(u_{m,x}^{(4)})_{A_3^{*'}}$–$(u_{m,y}^{(4)})_{A_3^{*'}}$ associated with the points Q'_2–Q'_3, Q'_3–Q'_4 and Q'_4–Q'_1, respectively, can be obtained in a similar way. Consequently, in Fig. 4.5 the flow gradients at the solution point $(A_3^{*'})$ can be obtained by

$$(U_{m,x})_{A_3^{*'}} = \frac{1}{4}\sum_{k=1}^{4}\left(u_{m,x}^{(k)}\right)_{A_3^{*'}} \tag{4.31}$$

$$(U_{m,y})_{A_3^{*'}} = \frac{1}{4}\sum_{k=1}^{4}\left(u_{m,y}^{(k)}\right)_{A_3^{*'}} \tag{4.32}$$

For flows with discontinuities the weighting procedure can be applied as follows

$$(U_{m,x})_{Q^*} = \begin{cases} 0, & \text{if } \theta_{mk} = 0, k = 1, 2, \ldots, 4 \\ \sum_{k=1}^{4}\frac{\left(W_m^{(k)}\right)^\alpha\left(u_{m,x}^{(k)}\right)_{Q^*}}{\left(W_m^{(k)}\right)^\alpha}, & \text{otherwise} \end{cases} \tag{4.33}$$

and

$$(U_{m,y})_{Q^*} = \begin{cases} 0, & \text{if } \theta_{mk} = 0, k = 1, 2, \ldots, 4 \\ \sum_{k=1}^{4} \dfrac{\left(W_m^{(k)}\right)^\alpha \left(u_{m,y}^{(k)}\right)_{Q^*}}{\left(W_m^{(k)}\right)^\alpha}, & \text{otherwise} \end{cases} \qquad (4.34)$$

where $\alpha \geq 0$ is an adjustable constant (usually $\alpha = 1$ or $\alpha = 2$),

$$\theta_{mk} = \sqrt{\left[\left(u_{m,x}^{(k)}\right)_{Q^*}\right]^2 + \left[\left(u_{m,y}^{(k)}\right)_{Q^*}\right]^2} \qquad (4.35)$$

and a similar definition for each k, $W_m^{(k)}$ is the product of $\theta_{m1}, \theta_{m2}, \ldots, \theta_{m4}$ excluding θ_{mk}.

The procedure explained above to evaluate the flow gradients at the solution points can be adapted for the three–dimensional discretization in a similar way. Considering Fig. 4.7, the solution point Q^* (marked by a cross symbol) and the grid point Q (marked by a circle symbol) do not coincide for a non–uniform grid distribution for the time–marching from $t = n$ to $t = n + \frac{1}{2}$ (see Section 4.1). In Fig. 4.7, flow variables at Q^* (marked by a cross symbol) are obtained from eq. (4.25) at $t = n + \frac{1}{2}$. Similarly, the flow variables at eight neighboring points $A_1, A_2, \ldots, A_8$ can be obtained by using the Taylor series expansion along the time axis from the time level $t = n$ to use the weighting procedure.

$$(U_m)_{A_l}^{n+\frac{1}{2}} = (U_m)_{A_l}^n + \frac{\Delta t}{2}(U_{m,t})_{A_l}^n \qquad (4.36)$$

where $m = 1, 2, \ldots, 5$ and $l = 1, 2, \ldots, 8$ denoting points $A_1, A_2, \ldots, A_8$, respectively.

Consequently, the flow gradients can be obtained by eight sets of $(U_{m,x})_{Q^*}$, $(U_{m,y})_{Q^*}$ and $(U_{m,z})_{Q^*}$ associated with the neighboring points $(A_1, A_2, \ldots, A_8)$.

Let,

$$\delta u_m^l = (U_m)_{A_l}^{n+\frac{1}{2}} - (U_m)_{Q^*} \qquad (4.37)$$

and

$$\delta x_l = x_{A_l} - x_{Q^*}, \qquad \delta y_l = y_{A_l} - y_{Q^*} \quad \text{and} \quad \delta z_l = z_{A_l} - z_{Q^*} \qquad (4.38)$$

can be defined for $m = 1, 2, \ldots, 5$ and $l = 1, 2, \ldots, 8$.

The first set of $(U_{m,x})_{Q^*}$, $(U_{m,y})_{Q^*}$ and $(U_{m,z})_{Q^*}$ associated with the vertex A_1 (see Fig. 4.7) can be evaluated as follows

$$\left(u_{m,x}^{(1)}\right)_{Q^*} = \frac{\Delta_x}{\Delta}, \qquad \left(u_{m,y}^{(1)}\right)_{Q^*} = \frac{\Delta_y}{\Delta} \quad \text{and} \quad \left(u_{m,z}^{(1)}\right)_{Q^*} = \frac{\Delta_z}{\Delta} \qquad (\Delta \neq 0) \quad (4.39)$$

where

$$\Delta = \begin{vmatrix} \delta x_1 & \delta y_1 & \delta z_1 \\ \delta x_2 & \delta y_2 & \delta z_2 \\ \delta x_3 & \delta y_3 & \delta z_3 \end{vmatrix} \tag{4.40}$$

$$\Delta_x = \begin{vmatrix} \delta u_m^1 & \delta y_1 & \delta z_1 \\ \delta u_m^2 & \delta y_2 & \delta z_2 \\ \delta u_m^3 & \delta y_3 & \delta z_3 \end{vmatrix} \tag{4.41}$$

$$\Delta_y = \begin{vmatrix} \delta x_1 & \delta u_m^1 & \delta z_1 \\ \delta x_2 & \delta u_m^2 & \delta z_2 \\ \delta x_3 & \delta u_m^3 & \delta z_3 \end{vmatrix} \tag{4.42}$$

and

$$\Delta_z = \begin{vmatrix} \delta x_1 & \delta y_1 & \delta u_m^1 \\ \delta x_2 & \delta y_2 & \delta u_m^2 \\ \delta x_3 & \delta y_3 & \delta u_m^3 \end{vmatrix} \tag{4.43}$$

Similarly for each $k = 2, 3, \ldots, 8$, $(u_{m,x}^{(k)})_{Q^*}$, $(u_{m,y}^{(k)})_{Q^*}$ and $(u_{m,z}^{(k)})_{Q^*}$ are defined by the procedure defined above except that the vertex A_1 is replaced by A_k.

Consequently, $(U_{m,x})_{Q^*}$, $(U_{m,y})_{Q^*}$ and $(U_{m,z})_{Q^*}$ for each $m = 1, 2, \ldots, 5$ can be evaluated by

$$(U_{m,x})_{Q^*} = \frac{1}{8} \sum_{k=1}^{8} \left(u_{m,x}^{(k)} \right)_{Q^*} \tag{4.44}$$

$$(U_{m,y})_{Q^*} = \frac{1}{8} \sum_{k=1}^{8} \left(u_{m,y}^{(k)} \right)_{Q^*} \tag{4.45}$$

$$(U_{m,z})_{Q^*} = \frac{1}{8} \sum_{k=1}^{8} \left(u_{m,z}^{(k)} \right)_{Q^*} \tag{4.46}$$

For flows with discontinuities or steep gradients, the averages in eqs. (4.44) to (4.46) can be replaced by weighted averages, i.e.,

$$(U_{m,x})_{Q^*} = \begin{cases} 0, & \text{if } \theta_{mk} = 0, k = 1, 2, \ldots, 8 \\ \sum_{k=1}^{8} \dfrac{\left(W_m^{(k)} \right)^\alpha \left(u_{m,x}^{(k)} \right)_{Q^*}}{\left(W_m^{(k)} \right)^\alpha}, & \text{otherwise} \end{cases} \tag{4.47}$$

$$(U_{m,y})_{Q^*} = \begin{cases} 0, & \text{if } \theta_{mk} = 0, k = 1, 2, \ldots, 8 \\ \sum_{k=1}^{8} \dfrac{\left(W_m^{(k)} \right)^\alpha \left(u_{m,y}^{(k)} \right)_{Q^*}}{\left(W_m^{(k)} \right)^\alpha}, & \text{otherwise} \end{cases} \tag{4.48}$$

and

$$
(U_{m,z})_{Q^*} = \begin{cases} 0, & \text{if } \theta_{mk} = 0, k = 1, 2, \ldots, 8 \\ \sum_{k=1}^{8} \dfrac{\left(W_m^{(k)}\right)^{\alpha}\left(u_{m,z}^{(k)}\right)_{Q^*}}{\left(W_m^{(k)}\right)^{\alpha}}, & \text{otherwise} \end{cases}
\tag{4.49}
$$

where $\alpha \geq 0$ is an adjustable constant (usually $\alpha = 1$ or $\alpha = 2$),

$$
\theta_{mk} = \sqrt{\left[\left(u_{m,x}^{(k)}\right)_{Q^*}\right]^2 + \left[\left(u_{m,y}^{(k)}\right)_{Q^*}\right]^2 + \left[\left(u_{m,z}^{(k)}\right)_{Q^*}\right]^2}
\tag{4.50}
$$

and a similar definition for each k, $W_m^{(k)}$ is the product of $\theta_{m1}, \theta_{m2}, \ldots, \theta_{m8}$ excluding θ_{mk}. In order to avoid dividing by zero, a small positive number (10^{-60}) is added to the denominators that appear in eqs. (4.33), (4.34), (4.47), (4.48) and (4.49).

4.3 Stability Criterion

In the solution for explicit numerical schemes, the time step size is a critical choice to obtain a consistent and stable solution. The fundamental stability condition for explicit numerical schemes is given by the Courant–Friedrichs–Lewy (CFL) condition. This condition is common to all explicit numerical methods due to the highly non–linear governing equations (Anderson, 1995; Tannehill et al., 1997). For 1–D advection–diffusion problems by using a von Neumann's stability analysis, the CFL condition can be expressed as follows;

$$
CFL = a\frac{\Delta t}{\Delta x} < 1
\tag{4.51}
$$

where a is a maximum propagation velocity, Δt is the size of a time step and Δx is the grid spacing. The maximum propagation velocity is the sum of convective velocity and the speed of sound. After eq. (4.51) is rearranged, the allowable time step is obtained as

$$
\Delta t < \frac{\Delta x}{a}
\tag{4.52}
$$

The physical interpretation of this condition is that Δt must be less than the time it takes any information is carried with the maximum propagation speed from one grid point to the next.

For the present 3–D flow, an analogous stability condition is constructed as follows;

$$\Delta t < \frac{min(\Delta x, \Delta y, \Delta z)}{a} \qquad (4.53)$$

where Δx, Δy and Δz are the grid spacing and Δt is the size of the time step.

By introducing the CFL number, the constraint on the time step size can be expressed as follows;

$$\Delta t = CFL\frac{min(\Delta x, \Delta y, \Delta z)}{a} \qquad (4.54)$$

The CFL number must stay below value of 1 for each cell in the computational domain for the stability of the present two–time level explicit scheme. Furthermore, for a steady flow solution, local time–stepping approach is used to increase the rate of convergence. In this approach, each individual grid point has its own local time step calculated based on the above equation. The flow variables at each grid point are advanced in time according to their own pace towards the steady state conditions. Steady state calculations are carried out with a CFL number of 0.8 and unsteady ones are performed with a CFL number of 0.6.

4.4 Boundary Conditions

Only a part of the real physical domain can be considered for any numerical simulation. The truncation of the domain leads to artificial boundaries where certain physical quantities (i.e., flow variables) have to be prescribed (Blazek, 2005). Implementation of the accurate boundary conditions is an essential requirement and it needs a particular care for the direct noise computation. Additionally, the technique used in implementing the boundary conditions can have a major effect on the stability and convergence speed of the numerical solution. Boundary conditions should be able to absorb flow disturbances when they are leaving the computational domain without causing excessive reflections. An improper implementation can result in an inaccurate simulation. In the present study, unlike conventional finite–volume schemes, boundary conditions are defined not only for the conservative variables (U_m) but also for their spatial derivatives ($U_{m,x}, U_{m,y}, U_{m,z}$) where $m = 1, 2, \ldots, 5$. The flux–based nature of the time–conservative finite–volume method results in use

of the flux–based boundary condition. Implementation of the flux–based boundary conditions particularly for the non–reflecting boundary condition is extremely simple since each control volume allows flux and the flow information to propagate into future. Boundary conditions have to be compatible with both physical and numerical properties of the problem to be solved. In the present study, different boundary conditions are used including the non–reflecting boundary condition, the subsonic and supersonic inlet as well as outlet boundary conditions, the inviscid and viscous wall boundary conditions and the periodic boundary condition. In the subsequent sections, implementation of these boundary conditions is provided.

4.4.1 Non–Reflecting Boundary Condition

Numerical treatment to achieve a non–reflecting boundary condition is a critical issue for unsteady flow calculations and practical aeroacoustics applications. Reflected signals from the boundaries may contaminate the flow field without an effective non–reflecting boundary condition. The non–reflecting boundary condition for the time–conservative finite–volume scheme is indeed very simple and robust such that they are applicable to subsonic, transonic and supersonic flows even in the presence of discontinuities. Various implementations of the non–reflecting boundary condition are proposed by Chang et al. (2003). The non–reflecting boundary condition treatment is based on flux conservation near the domain boundary through flux balance over the surfaces of a control volume. It was demonstrated by Chang et al. (2003); Loh (2003b); Loh and Jorgenson (2005) that only negligible reflection occurs even when a shock passes through a boundary with this type of flux–based condition (Loh et al., 2001a). The non–reflecting boundary conditions described here have been successfully applied to different aeroacoustics problems by Loh et al. (2001a,b,c); Loh (2003a, 2005); Loh and Hultgren (2005); Aybay et al. (2009a,b).

The following non–reflecting boundary conditions are adapted from Loh et al. (2001a) and employed in the present study. For a grid node (i, j, k, n) lying at the physical domain boundary where (i, j, k) is the index of the node and n stands for the time level, the non–reflecting boundary condition (Type–I) requires that

$$(U_{m,x})^n_{(i,j,k)} = (U_{m,y})^n_{(i,j,k)} = (U_{m,z})^n_{(i,j,k)} = 0 \qquad (4.55)$$

whereas $(U_m)^n_{(i,j,k)}$ is kept fixed at the initially given steady boundary value.

(Type–II) is used if there are substantial gradients in, for example, the y and z–directions. The non–reflecting boundary condition (Type–II) requires that

$$(U_{m,x})^n_{(i,j,k)} = 0 \tag{4.56}$$

whereas $(U_m)^n_{(i,j,k)}$, $(U_{m,y})^n_{(i,j,k)}$ and $(U_{m,z})^n_{(i,j,k)}$ are defined by simple extrapolation from the closest interior node and previous time step, denoted by $(i', j', k', n-1)$, using the following relations

$$(U_m)^n_{(i,j,k)} = (U_m)^{n-1}_{(i',j',k')}, \qquad (U_{m,y})^n_{(i,j,k)} = (U_{m,y})^{n-1}_{(i',j',k')},$$

$$(U_{m,z})^n_{(i,j,k)} = (U_{m,z})^{n-1}_{(i',j',k')}. \tag{4.57}$$

The proposed non–reflecting boundary conditions are remarkable for their simplicity and robust enough to allow a near–field computation without disturbing or distorting the flow acoustic fields. No characteristic theory is employed in their construction. These conditions allow even shock waves to leave the computational domain with no noticeable reflection at the boundary (Loh et al., 2001a; Chang et al., 2003).

4.4.2   Inlet and Outlet Boundary Conditions

For hyperbolic problems the number of boundary conditions required can be determined by an evaluation of the direction that information is carried by the flow characteristics. These characteristics are related to the entropy, vorticity and acoustic disturbances. The number of boundary conditions to be specified should be equal to the number of characteristics that are directed from the exterior of the region toward the physical domain. For instance, in the case of subsonic inflow there are four incoming flow characteristics (in 3D) and one outgoing flow characteristic running across the boundary. Therefore, in the present flow solver, four flow characteristics are prescribed based on the stagnation pressure, the stagnation temperature and flow angles (i.e., free stream values). One characteristic variable is extrapolated from the interior of the computational domain, then the specified quantities together with the isentropic relation are used to determine other flow variables at the inlet boundary. The situation reverses for subsonic outflow. The four outgoing

characteristic variables have to be extrapolated from the interior of the domain and the remaining incoming characteristic variable needs to be specified.

All conservative variables at the inlet boundary are determined by free stream values for the supersonic inflow boundary condition. On the other hand, the supersonic outflow boundary requires that all the flow variables be extrapolated from the interior of the domain. The supersonic inflow and the supersonic outflow boundary conditions have some similarities with the non–reflecting boundary conditions given in Section 4.4.1. The difference between the supersonic inflow boundary condition and the (Type–I) non–reflecting boundary condition is the definition of the gradients on the boundary. For the supersonic outflow case the difference is not only the flow gradients definition on the outlet boundary but also the extrapolation. The flow variables are extrapolated from the previous time level for the (Type–II) non–reflecting boundary condition (see eq. (4.57)). Therefore, in the present study, only the subsonic inflow and outflow boundary conditions are imposed to solve one problem, namely, shock capturing case for a convergent–divergent nozzle given in Section 5.1.2. The rest of the calculations are carried out as a combination of the non–reflecting boundary conditions, the solid wall boundary condition and the periodic boundary condition.

4.4.3   Solid Wall Boundary Condition

The fluid slips over the solid body for an inviscid flow case. The velocity vector must be tangent to the wall since there is no friction force. In the present flow solver no flow normal to the wall is permitted. Pressure gradients normal to the wall are assumed to be zero ($p_n = 0$). Tangential velocity components and pressures are determined by extrapolation from the interior to the boundary in the present study.

For viscous flow, the relative velocity between the wall and the fluid directly at the surface is set to zero. The Cartesian velocity components become zero (i.e., no–slip boundary condition), namely,

$$u = v = w = 0 \quad \text{at a stationary wall surface} \tag{4.58}$$

If the wall is adiabatic (i.e., no heat flux through the wall), then the following

condition for temperature is imposed

$$T_n = 0 \tag{4.59}$$

The pressure in the convective fluxes is obtained in the same way as described above for the inviscid flow.

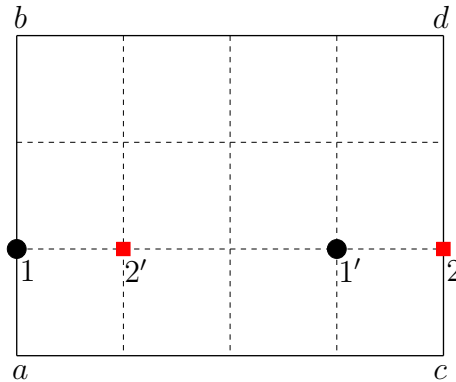### 4.4.4 Periodic Boundary Condition

In the present study, the periodic boundary condition is employed only for the three–dimensional LES applications in the spanwise direction (see Sections 6.1 and 6.2). This boundary condition is the simplest to be implemented among the other types of boundary conditions given in the previous sections. A schematic view is shown in Fig. 4.9 to illustrate the periodic boundary condition. The configuration is assumed to be periodic between the points ab and cd. The periodic boundary is implemented for the present flow solver by setting the flow variables and the spatial derivatives of the flow variables. For example,

$$(U_m)_1 = (U_m)_{1'}, \qquad (U_{m,x})_1 = (U_{m,x})_{1'},$$

$$(U_{m,y})_1 = (U_{m,y})_{1'} \quad \text{and} \quad (U_{m,z})_1 = (U_{m,z})_{1'}. \tag{4.60}$$

$$(U_m)_2 = (U_m)_{2'}, \qquad (U_{m,x})_2 = (U_{m,x})_{2'},$$

$$(U_{m,y})_2 = (U_{m,y})_{2'} \quad \text{and} \quad (U_{m,z})_2 = (U_{m,z})_{2'}. \tag{4.61}$$

Figure 4.9: Schematic view for the illustration of periodic boundary condition

4.5   Acceleration Techniques

4.5.1   Direct–Flux Based Multigrid Method

In viscous flows, to resolve thin viscous layers properly highly stretched grid cells are required in the near–wall regions. This requirement leads to employing grid cells with high aspect ratios in many flow cases. A numerical scheme produces larger truncation error when the aspect ratio of the grid cells becomes large (Tannehill et al., 1997). The run–time requirement of the simulation might be very long due the time step which is limited by the smallest grid cell. The multigrid methodology can be used in order to accelerate the solution of the Navier–Stokes equations and improve the convergence rate of viscous calculations. This technique was originally developed by Brandt (1981) and later this acceleration method was applied to the Euler equations by Jameson (1983). The fundamental idea of the multigrid method is to employ coarse grids in order to drive the solution on the finest grid faster to steady state (Blazek, 2005).

In the present study, the direct–flux based multigrid method is implemented as an acceleration technique. This multigrid method at two–level was proposed by He and Denton (1994). In this method a fine mesh is defined as the one on which the flow variables and fluxes are evaluated. On the other hand a coarse mesh is defined in a way that it can be directly obtained from those of the fine meshes. According to He and Denton (1994) the temporal integration should be formulated for the direct–flux based multigrid technique as following first the solution should march on the fine mesh up to its stability limit then on the coarse mesh using a larger time step owing to a larger control volume.

For one–level grid (i.e., single–grid), a temporal change of the flow variables on the fine mesh is defined as

$$(U_m^{n+1} - U_m^n)_f = \Delta t_f \frac{R_f}{\Delta V_f} \tag{4.62}$$

where the subscript f denotes the fine mesh, Δt_f is the permissible time step and R_f is the net flux for the finite–volume on the fine mesh.

For the two–level time integration method (two–grid) the solution is first marched

on the fine grid and then on the coarse grid. Therefore, the overall time step is much larger than the one–level temporal change and the accuracy of the solution is controlled by the fine grid (He and Denton, 1994). The temporal change of the flow variables in the fine mesh is given by

$$(U_m^{n+1} - U_m^n)_f = \Delta t_f \frac{R_f}{\Delta V_f} + \Delta t_c \frac{R_c}{\Delta V_c} \qquad (4.63)$$

where the subscript c denotes the coarse mesh, Δt_c is the permissible time step and R_c is the net flux for the finite–volume on the coarse mesh. A detailed discussion of the two–level multigrid method for unsteady flows can be found in (He and Denton, 1994). Implementation of the direct–flux based multigrid method is much easier and numerically cheaper than the conventional one. To the best knowledge of the author, in order to increase the convergence rate of the viscous flow calculations, implementation of the direct–flux based multigrid technique for the time–conservative finite–volume method was carried out for the first time in the present study. The steady state calculations are performed using the two–level multigrid method for viscous laminar flows. Influence of this multigrid method on the convergence speed of the solution scheme is presented in Sections 5.2.1 and 5.2.2.

4.5.2   Interface Between Multiblocks and Parallel Computing

The multiblock technique has been widely used for structured grid flow solvers to deal with complex geometries. In this method, the physical domain is divided into a certain number of subdomains (i.e., blocks). By doing this, a complex geometry can be divided into a sequence of simple geometries. The physical solution in a particular block will depend on the flow in neighbouring blocks (Blazek, 2005). Therefore, an exchange of information between blocks is required. The most common approaches rely on interpolation formulas that can produce artificial discontinuities in the flow variables across the boundaries (Lockard, 1999).

In the present study, a simple multiblock method is used where the grid lines match at the block interface, as shown in Fig. 4.10. Exchange of flow variables in 2D is depicted also in Fig. 4.10. The procedure consists of three steps. First of all, the
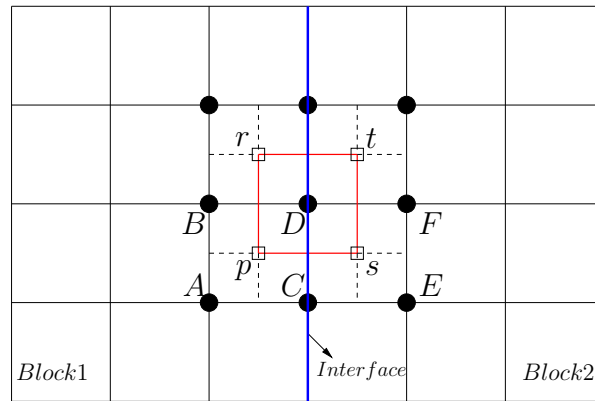
Figure 4.10: Schematic view for exchange of flow variables in 2D

flow variables at grid points s and t are transferred from $Block2$ to $Block1$. Then, in $Block1$ using the flow variables at grid points p, r, s and t flux evaluation is carried out in order to obtain the flow variables at grid point D. In the last step, the flow variables information at grid point D transferred from $Block1$ to $Block2$. The same flux evaluation method is used here as inside the physical domain along the block interfaces in order to prevent any artificial discontinuities across the boundaries. The multiblock approach is performed first for the Euler solver and used for the supersonic flow over a forward–facing step problem (see Section 5.1.3).

The multiblock technique was the basis for splitting up the computational domain for a parallel computation. The cost of performing the practical acoustic calculations is still very high. Hence, in order to reduce the run–time requirement of the simulations the Navier–Stokes flow solver is parallelized by domain decomposition with explicit message passing via MPI. The parallel Navier–Stokes solver is first used for a 2–D mixing layer problem where the computational domain is decomposed into 16 subdomains (see Section 5.3.1). 3–D direct noise computations using large–eddy simulation technique are also performed with the parallel flow solver (see Section 6.1 and 6.2). All parallel computations are carried out on an AMD Opteron based Linux Cluster (Hamilton) provided by the ITS High Performance Computing service at Durham University.

Chapter 5

Validation of the Time–Conservative Finite–Volume Method

In this chapter validation studies for the two–dimensional inviscid (Section 5.1), viscous laminar (Section 5.2) and viscous turbulent (Section 5.3) flows are carried out on different test cases with a wide range of flow regimes. The aim of this validation study was to verify the accuracy and illustrate the capabilities of the time–conservative finite–volume method as function of discretization options and grid density.

5.1 Inviscid Flows

Inviscid flows are modeled by the system of Euler equations and these equations describe flows where the influence of viscous shear stresses and heat conduction effects can be neglected (Hirsch, 2007). The Euler equations are obtained by dropping both the viscous and the heat–transfer terms from the Navier–Stokes equations (see eq. (4.1)). In two–dimensional Cartesian coordinates, the system of time–dependent Euler equations can be written as

$$\frac{\partial \mathbf{U}}{\partial t} + \frac{\partial \mathbf{F}}{\partial x} + \frac{\partial \mathbf{G}}{\partial y} = 0 \qquad (5.1)$$

where $\mathbf{U}$ is the vector of the conservative variables, $\mathbf{F}$ and $\mathbf{G}$ are the convective flux vectors. The Euler equations given by eq. (5.1) are always hyperbolic in space and time, independent of flow regime.

The Euler equations form the basis for the Navier–Stokes solutions. Therefore, the observed properties of these equations will be of critical importance when the same discretization of the convective terms is applied to viscous laminar and viscous turbulent flows. In order to investigate the accuracy and the shock–capturing capabilities of the method, numerical solutions are provided for three different inviscid test cases in the subsequent sections. Mach numbers for the test cases are higher than 0.2. Therefore compressibility effects can not be neglected. The developed method is a density–based solver (i.e., the density is based on the velocities of the previous iteration) in order to take into account the influence of compressibility.

5.1.1 Shock Reflection on a Flat Plate

The steady–state oblique shock reflection on a flat plate was proposed by Yee et al. (1983). This test case was considered by Chang et al. (1999); Zhang, Z.C. and Yu (1999); Zhang, Z.C. et al. (2002) also. Here, the accuracy and the shock–capturing capabilities of the proposed scheme based on the new definitions of cell interface and control volume (see Section 4.1) are investigated for the shock reflection on a flat plate problem.

The computational domain and the exact shock locations are depicted in Fig. 5.1. The computational domain is rectangular extending from $0 \leq x \leq 4$ and $0 \leq y \leq 1$. The inflow boundary condition is imposed on the left boundary as a supersonic flow with a Mach number of 2.9. The inflow and the upper boundary conditions at $t = 0$ are as follows (Zhang, Z.C. et al., 2002)

$$(u, v, \rho, p) = \begin{cases} (2.9, 0.0, 1.0, 0.71428) & \text{inflow boundary condition} \\ (2.6193, -0.50632, 1.7, 1.5282) & \text{upper boundary condition} \end{cases}$$

where u, v, ρ and p are the non–dimensional streamwise velocity, wall–normal velocity, density and pressure parameters, respectively. The lower boundary is a solid reflecting wall. The flow variables and the spatial derivatives of the flow variables

are defined by simple extrapolation from the interior at the outflow boundary (right–hand).
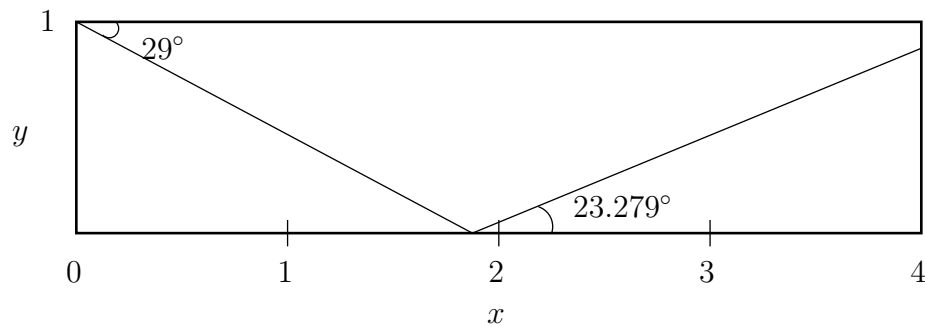
Figure 5.1: Computational domain and the shock locations of a steady–state oblique
shock problem

A quadrilateral mesh is constructed using 121 nodes in the streamwise and 41 nodes in the wall–normal directions with equal grid spacing (see Fig. 5.2). The numerical simulation is carried out for a finer mesh also. The fine mesh consists of 241×81 grid points in the streamwise and wall–normal directions, respectively.
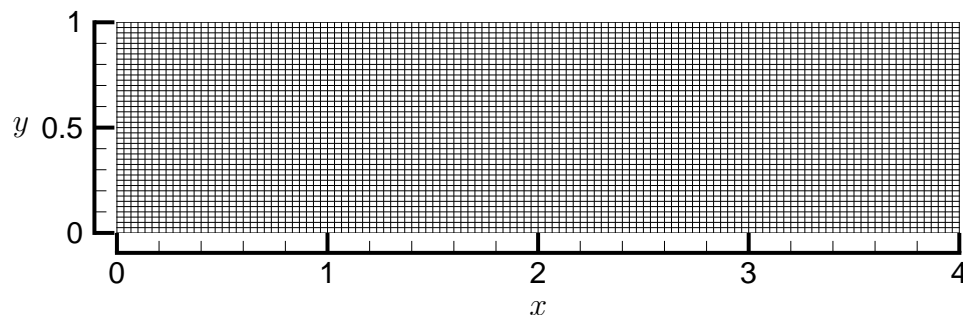

Figure 5.2: Coarse mesh used for the shock reflection on a flat plate problem

Due to the presence of shocks, the time–conservative finite–volume method needs to have certain numerical dissipation. Thus, this dissipation is introduced using the weighting procedure given by eqs. (4.33) and (4.34). The development of incident and reflected shocks for the distribution of computed pressure on the fine mesh can be seen in Figs. 5.3 and 5.4, respectively.
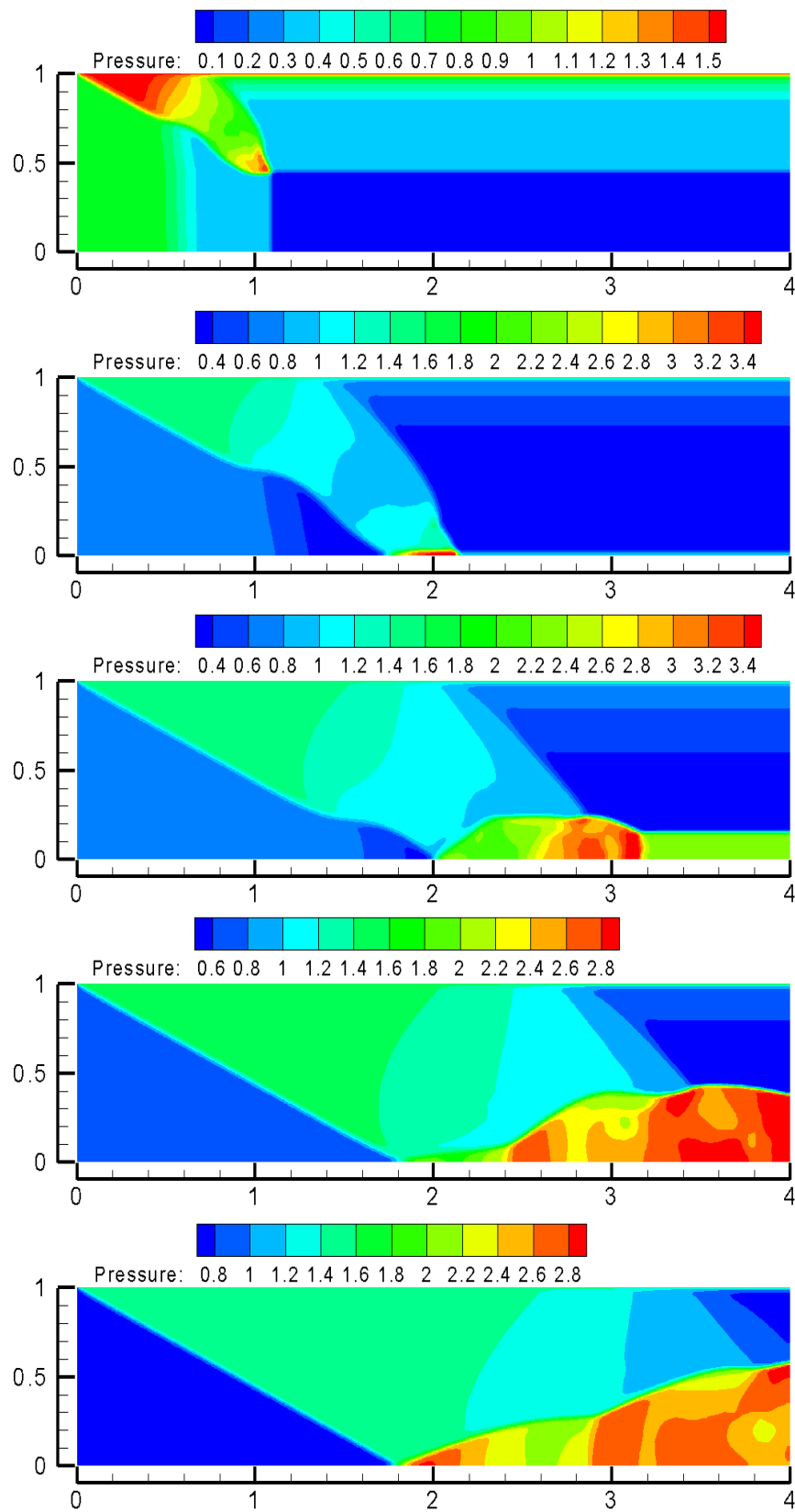
Figure 5.3: Development of incident shock for the distribution of computed pressure on the fine mesh at $t = 0.025, 0.05, 0.075, 0.1$ and 0.125 from *(upper)* to *(lower)*
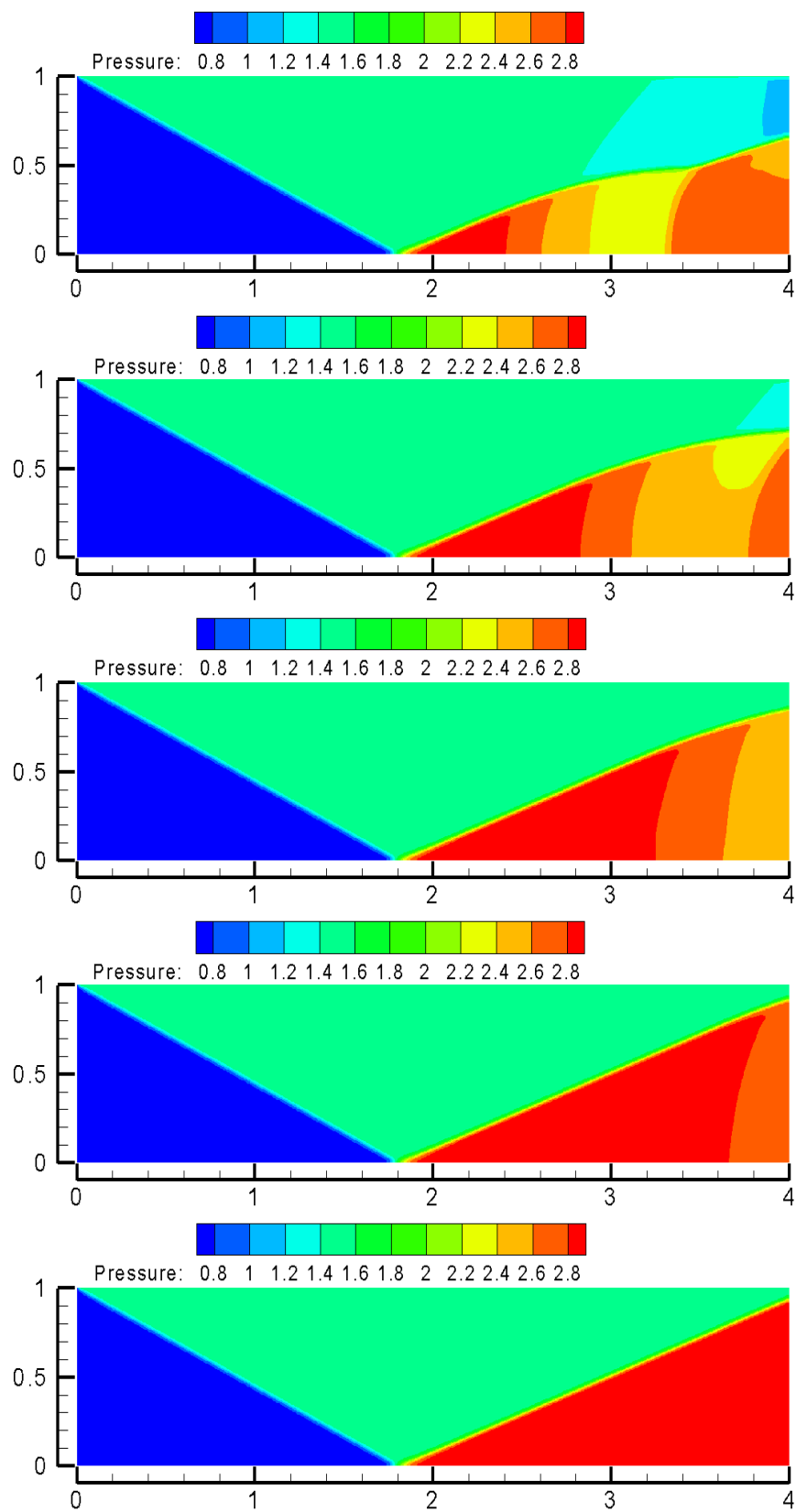
Figure 5.4: Development of reflected shock for the distribution of computed pressure on the fine mesh at $t = 0.15, 0.175, 0.2, 0.225$ and 0.25 from *(upper)* to *(lower)*

A comparison of the resulting steady–state pressure and Mach number contours with isolines on the coarse and fine meshes is depicted in Figs. 5.5 and 5.6, respectively. The improvement in shock resolution by using a finer mesh (241×81) can be seen in these figures. The distribution of the pressure coefficient (C_p) along the mid–section of the computational domain $(y = 0)$ is defined by

$$C_p = \frac{2}{\gamma M_\infty^2} \left(\frac{P}{P_\infty} - 1 \right) \tag{5.2}$$

where $\gamma = 1.4$, $M_\infty = 2.9$ and $P_\infty = 0.71428$.

In Fig. 5.7, the computed values of the pressure coefficient distribution on the coarse and fine meshes are compared with the exact solution. The computed C_p values agree very well with the exact solution. A reduction in grid spacing shows an improvement in flow resolution as expected. The numerical resolution of the reflected shock is identical to that of the incident shock. No numerical oscillations are detected near either the incident or the reflected shocks.
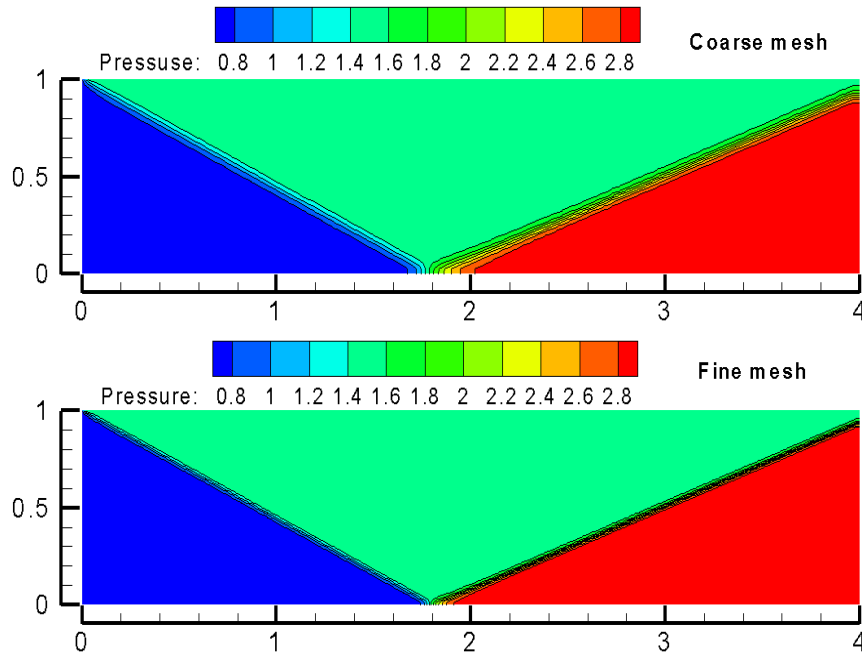
Figure 5.5: Distribution of pressure and isolines, as computed on the coarse *(upper)* and fine *(lower)* meshes
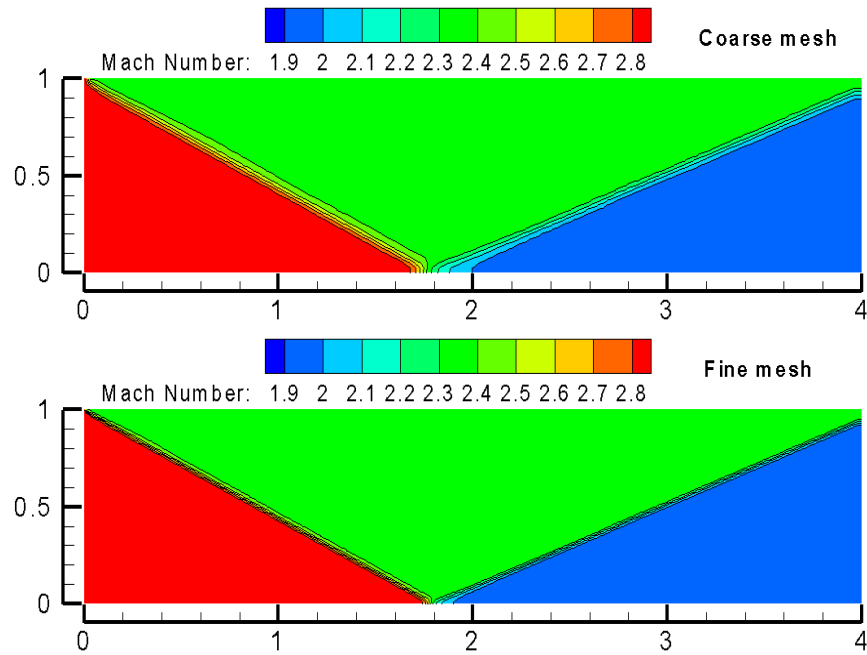
Figure 5.6: Distribution of computed Mach number and isolines, on the coarse *(upper)* and fine *(lower)* meshes
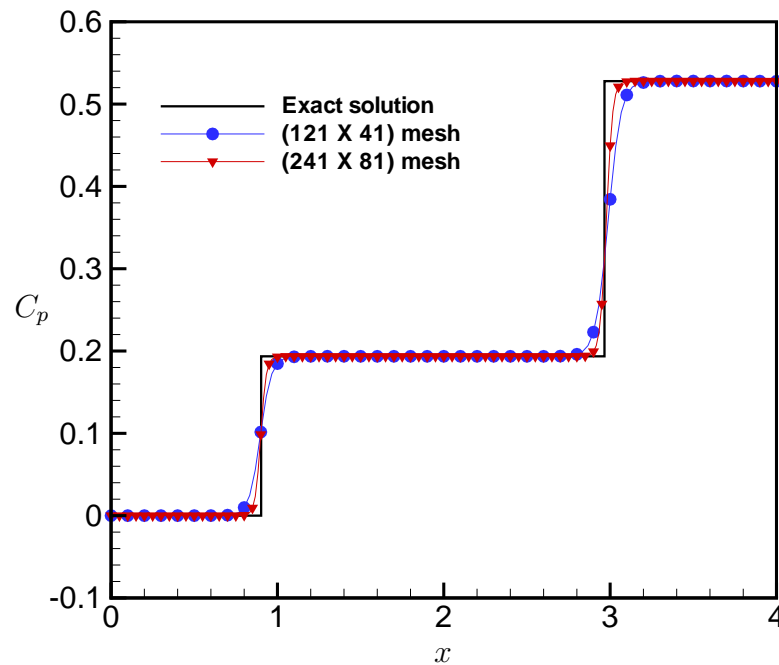

Figure 5.7: Pressure coefficient distribution along the mid–section of the computational domain $(y = 0.5)$

5.1.2 Shock Capturing Case for a Convergent–Divergent Nozzle

Steady flow with formation of a normal shock wave in the divergent section of a convergent–divergent nozzle is considered here. The flow at the inlet to the nozzle comes from a reservoir where the stagnation pressure and temperature are p_0 and T_0, respectively. The flow is subsonic in the convergent portion of the nozzle, sonic at the throat and supersonic at the divergent section, as shown in Fig. 5.8. A normal shock wave may form in the divergent section of the nozzle depending on the pressure at the outlet (see Fig. 5.8) (Anderson, 1995).
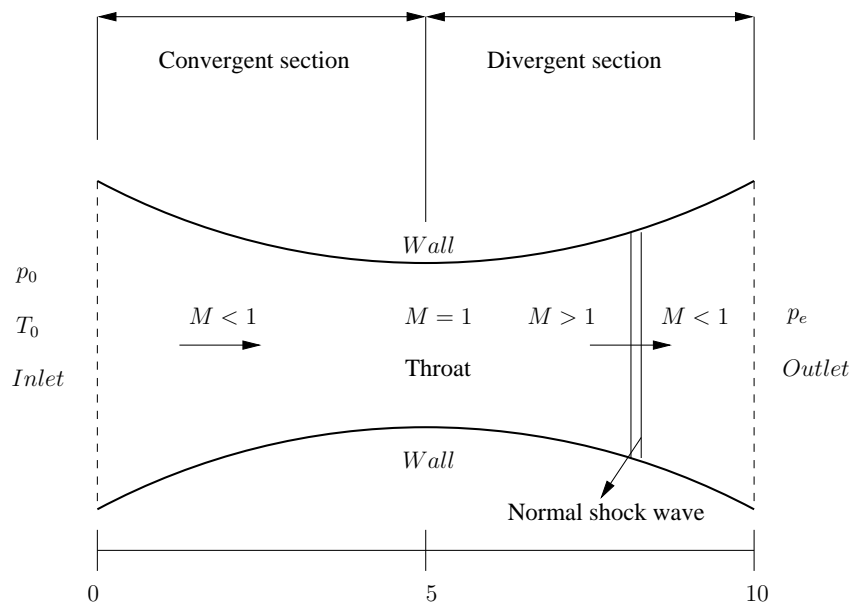
Figure 5.8: Schematic view of the convergent–divergent nozzle with a normal shock wave in the divergent section

The Mach number distribution through the nozzle is governed by the area–Mach number relation. This relation is given by (Anderson, 1995)

$$\left(\frac{A}{A^*}\right)^2 = \frac{1}{M^2}\left[\frac{2}{\gamma+1}\left(1+\frac{\gamma-1}{2}M^2\right)\right]^{\frac{(\gamma+1)}{(\gamma-1)}} \tag{5.3}$$

where γ is the ratio of specific heats, A is the cross–sectional area and A^* is the area of the sonic throat.

The variation of pressure, density and temperature as a function of Mach number

is given by

$$\frac{p}{p_0} = \left(1 + \frac{\gamma - 1}{2} M^2\right)^{\frac{-\gamma}{\gamma - 1}} \tag{5.4}$$

$$\frac{\rho}{\rho_0} = \left(1 + \frac{\gamma - 1}{2} M^2\right)^{\frac{-1}{\gamma - 1}} \tag{5.5}$$

$$\frac{T}{T_0} = \left(1 + \frac{\gamma - 1}{2} M^2\right)^{-1} \tag{5.6}$$

where $\gamma = 1.4$ and p_0 is the stagnation pressure.

The dimensions of the computational domain are: $10\ m$ (streamwise)$\times\ 1.5\ m$ (wall–normal). The area ratio between the inlet and the sonic throat is 1.5. The throat of the nozzle is at $x = 5.0\ m$. The convergent section occurs $x < 5.0\ m$ and the divergent section occurs for $x > 5.0\ m$ (see Fig. 5.8). The mesh consists of 151×25 grid points in the streamwise and wall–normal directions, respectively (see Fig. 5.9).
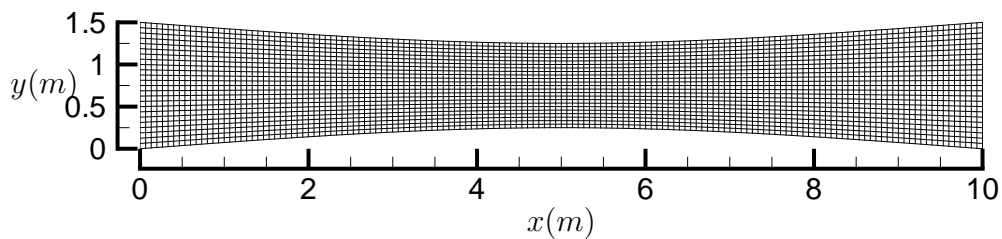

Figure 5.9: (151×25) mesh for the convergent–divergent nozzle problem

The stagnation pressure and temperature are set to $10^5\ Pa$ and $300\ K$, respectively. These flow conditions are imposed as inflow boundary condition. The slip boundary condition is implemented at the upper and lower walls. The spatial derivatives of the flow variables are set to zero at the inlet and outlet boundaries. On the other hand, the gradients at the walls were evaluated from an interior node closest to this boundary. Exit pressure, p_e, is set to 80,000 Pa. The convergent–divergent nozzle becomes choked at this pressure value. A normal shock wave will form somewhere in the divergent section of the nozzle. The flow becomes subsonic immediately behind the normal shock. The area–Mach number expression, eq. (5.3), is only valid for isentropic flow. The flow properties between the inlet and ahead of the shock can

be determined by the area–Mach number and isentropic relations given by eqs. (5.4) to (5.6). The total pressure is constant between the inlet and the normal shock wave due to constant entropy (i.e., an isentropic flow). However, the total pressure decreases across the shock due to entropy increase. Therefore, the expression for the area–Mach number given by eq. (5.3) can not be used across the normal shock wave (Anderson, 1995). In order to evaluate the flow properties behind the shock wave, the normal shock relations need to be used. The exact location of the normal shock wave is calculated at $x = 7.61\ m$ using these relations. The Mach number in front of the shock and the Mach number immediately behind the shock wave are calculated as 1.49 and 0.705, respectively.
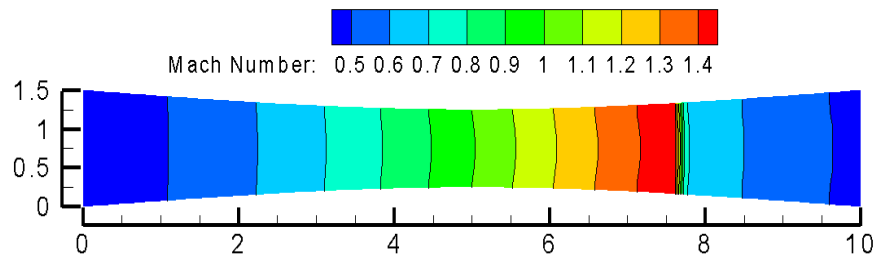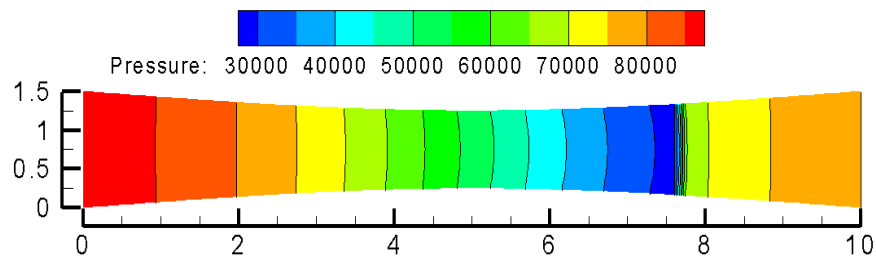

**Figure 5.10:** Mach number contours with isolines on the (151×25) mesh
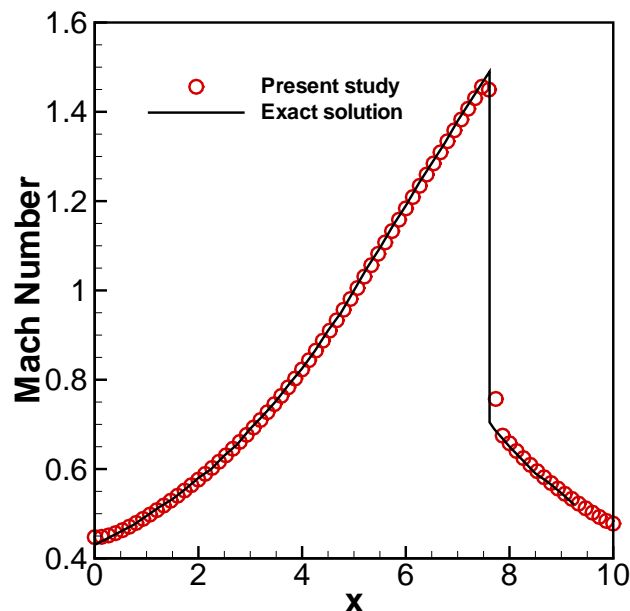
Figure 5.11: Distribution of Mach number along the mid–section of the convergent–divergent nozzle

The distribution of computed Mach numbers and pressure with isobars are depicted in Fig. 5.10 and Fig. 5.12, respectively. The subsonic flow behind the normal shock wave and increase in pressure can be observed from these figures. Comparison of Mach number and pressure distribution against the exact solution along the mid–section of the nozzle are shown in Fig. 5.11 and Fig. 5.13, respectively. The simulation results are agree very well with the exact solution. The shock is resolved with a few grid points and no numerical oscillations are detected in the vicinity of the normal shock wave. The steady–state flow field in the convergent–divergent nozzle and the location of the shock were predicted accurately by the present two–dimensional Euler solver.


Figure 5.12: Pressure contours with isolines on the (151×25) mesh
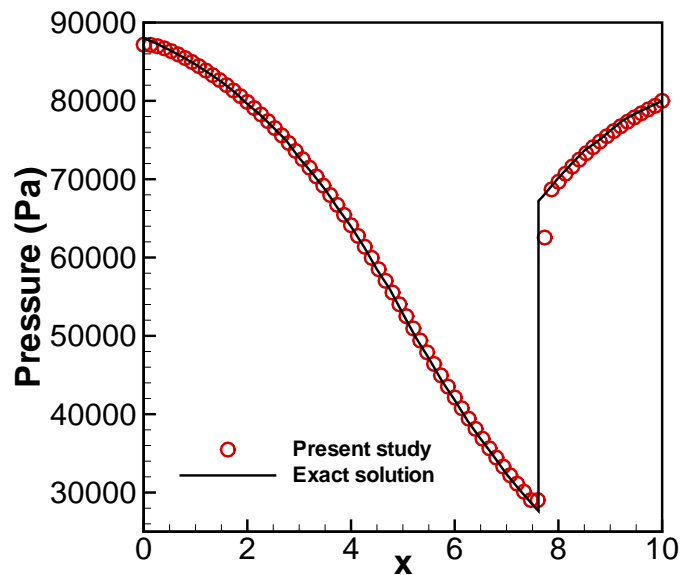
Figure 5.13: Distribution of pressure along the mid–section of the convergent–divergent nozzle

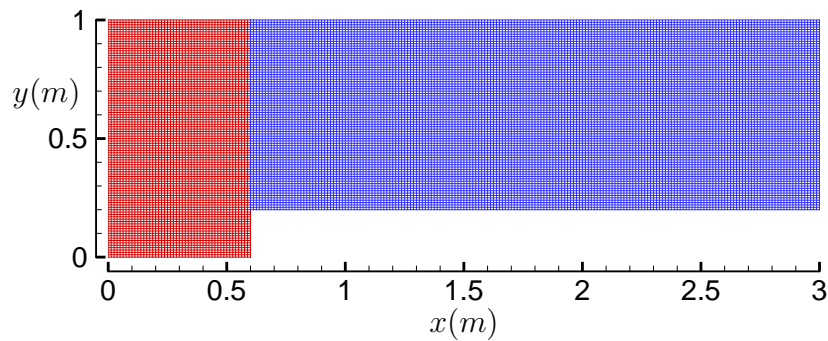### 5.1.3   Supersonic Flow Over a Forward–Facing Step

Accurate simulation of flows with strong shocks is a challenging topic. A two–dimensional simulation of supersonic flow over a forward–facing step is carried out, which is a standard benchmark problem in literature. This benchmark case was used by Woodward and Colella (1984); Giannakouros and Karniadakis (1994) to compare the accuracy of different numerical methods. This problem was also considered by Chang et al. (1999); Zhang, Z.C. and Yu (1999).
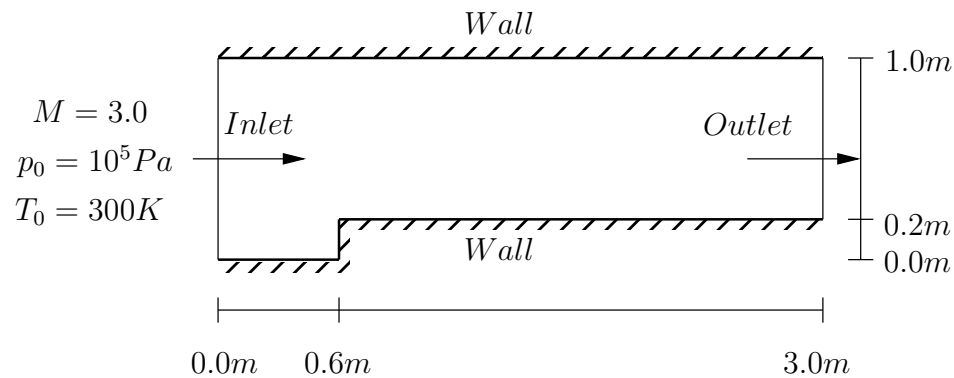
Figure 5.14: Computational domain and boundary conditions of a supersonic flow over a forward–facing step

Fig. 5.14 shows the computational domain and the boundary conditions of the supersonic flow over a forward–facing step problem. The domain extends from $x = 0$ to $x = 3.0\ m$ and from $y = 0$ to $y = 1.0\ m$. The free stream Mach number is 3.0, the stagnation pressure is $10^5\ Pa$ and the stagnation temperature is $300\ K$. These flow conditions are imposed on the left–hand boundary as supersonic inlet boundary condition. The reflecting boundary condition is applied to the walls. The outlet boundary condition has no influence on the flow, since the exit velocity is always supersonic. The condition at the outlet is extrapolated from an interior node closest to this boundary. The domain is decomposed into 2 subdomains and the mesh used for this problem can be seen in Fig. 5.15. A quadrilateral mesh is used with 0.0125 m and 0.01 m grid spacing in the x and y–directions, respectively. The multiblock flow solver is used first for this benchmark case (Aybay and He, 2007).

The corner of the step is the centre of a rarefaction fan and hence is a singular point of the flow (Woodward and Colella, 1984; Chang et al., 1999). According

Figure 5.15: Quadrilateral mesh used for the supersonic flow over a forward–facing step problem with equal grid spacing

to Woodward and Colella (1984), without applying special numerical treatment at the singular point the flow is seriously affected by large numerical errors in the vicinity of this singular point. In order to reduce the numerical errors, an additional boundary condition near the step corner was imposed by Woodward and Colella (1984). Chang et al. (1999); Zhang, Z.C. and Yu (1999) did not apply any special numerical treatment at the step corner and presented very good results. However, they tried to avoid placing a grid point at this singular point. In the present study, the calculations are carried out without employing any special treatment at the corner of the step and due to the new definitions of the control volume (see Section 4.1) a grid point is used at the upper corner of the step. According to Woodward and Colella (1984), the density distribution is the most difficult to compute for this problem due to the weak contact discontinuity caused by the Mach reflection of the bow shock at the upper wall. Here, the simulation is carried out with a Courant number of 0.8. Formation of the expansion fan at the step corner, the Mach stem on the lower wall and the interaction between the reflected shock with rarefaction waves are depicted using the density distribution in Fig. 5.16. The step corner shock on the upper wall is formed with a right length as presented by Woodward and Colella (1984) when the reflected shock passes exactly through the upper corner at the outlet boundary of the computational domain (see Fig. 5.16 *(lower)*).

The density distribution (with 30 contours) at $t = 4 \times 10^{-2}$ s is shown in Fig. 5.17. The agreement is excellent with the high–resolution results of Woodward and Colella (1984); Chang et al. (1999). In conclusion, flow field features of the forward–facing
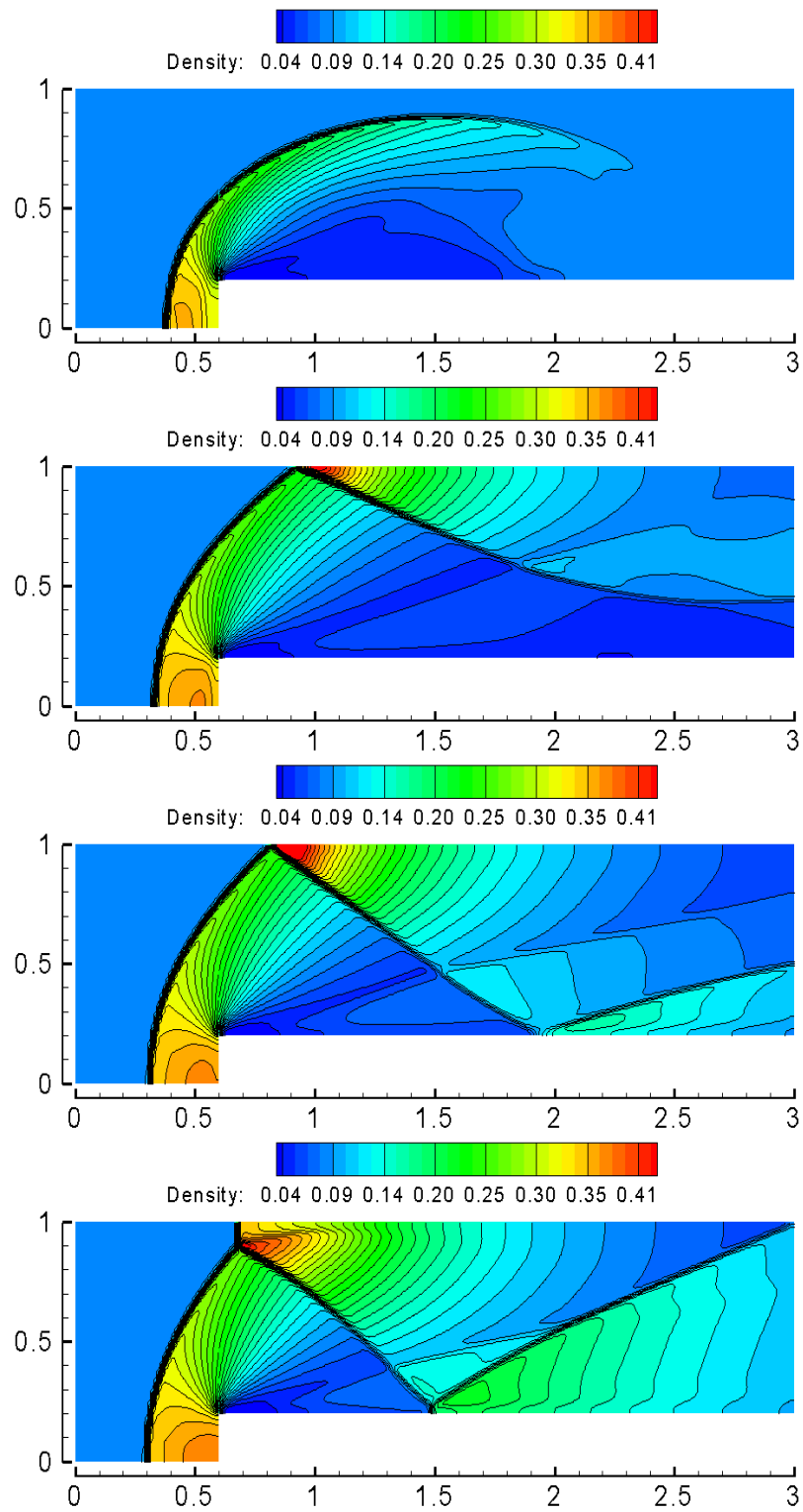
Figure 5.16: Density contours of the supersonic flow over a forward–facing step problem at $t = 1 \times 10^{-2}$ s, 1.5×10^{-2} s, 2×10^{-2} s and 2.5×10^{-2} s from *(upper)* to *(lower)*

step problem are predicted accurately with high–fidelity by the time–conservative finite–volume method without using any special numerical treatment at the upper corner of the step. The multiblock methodology is validated here also. Then, this methodology is used for the implementation of the flow solver on a parallel computer by means of domain decomposition.
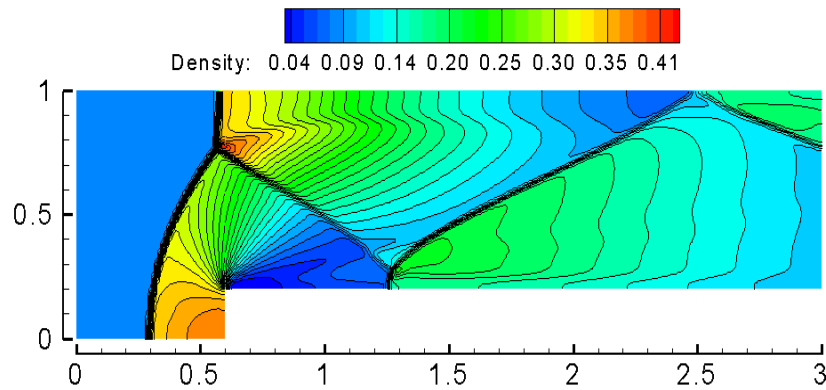
Figure 5.17: Distribution of computed density with 30 contours at $t = 4 \times 10^{-2}$ s

5.2 Viscous Laminar Flows

The Navier–Stokes equations consist of the Euler equations, the viscous shear stresses and the heat conduction effects. The Navier–Stokes solver is an extension of the Euler solver. The viscous and heat flux terms are added to the Euler solver. The only change that the inviscid solver is required to discretize the additional viscous and heat flux terms. These terms are represented by second order derivatives and both being diffusion type terms (Hirsch, 2007). Details about discretization of the viscous fluxes can be found in Section 4.2. The compressible Navier–Stokes equations in Cartesian coordinates, in absence of external forces and heat addition is already provided in Section 3.1 using eq. (4.1). One of the major differences that occurs when solving the Navier–Stokes equations, compared to the Euler equations, is the solid wall boundary condition, where all the velocity components have to vanish. For this reason the velocity and temperature profiles can vary rapidly over a short distance in the near–wall regions (Hirsch, 2007). In order to properly resolve thin viscous layers in the near–wall regions high density grids with large aspect ratio

are required. In many cases this requirement will lead to a substantial amount of computing time including data storage issues. When the aspect ratio of grid cells becomes larger, numerical schemes typically produce larger truncation error resulting in slower convergence (Tannehill et al., 1997). The number of iterations can be reduced by the addition of the multigrid technique. In order to accelerate the convergence of the Navier–Stokes solver, the direct–flux based multigrid method (see Section 4.5.1) is implemented. Influence of this multigrid method on the convergence speed of the solution scheme is represented in Sections 5.2.1 and 5.2.2.

5.2.1 Laminar Flow Over a Flat Plate

The laminar boundary layer development along a flat plate is one of the fundamental applications of laminar viscous flows. Laminar flow over a flat plate is often used as a standard validation case for a Navier-Stokes solver. Despite its simple geometry, the main advantage of this case is the availability of an exact solution, obtained by solving the Blasius equation. A detailed description of the Blasius solution can be found in Schlichting (1979).

The computational domain is selected between the leading edge and the trailing edge of the flat plate. Although this selection might create a nonrealistic flow field near the leading edge of the flat plate, it is used here for its simplicity. A nonuniform quadrilateral mesh used for the laminar viscous flow over a flat plate case is depicted in Fig. 5.18. The mesh consists of (101×61) grid points in the streamwise (x) and wall–normal (y) directions. The thickness of the first grid cell in the wall–normal direction is about 0.00156 times the plate length and this results in more than 10 grid cells in the boundary layer. The boundary in the far–field (i.e., upper boundary) is located at a distance of half the flat plate length. Far from the flat plate the flow is almost uniform and allows coarser grid cells. The maximum grid spacing around the far–field boundary is about 50 times the thickness of the first grid cell. The grid spacing in the streamwise direction is kept constant, whereas an exponential stretching is applied in the wall–normal direction.
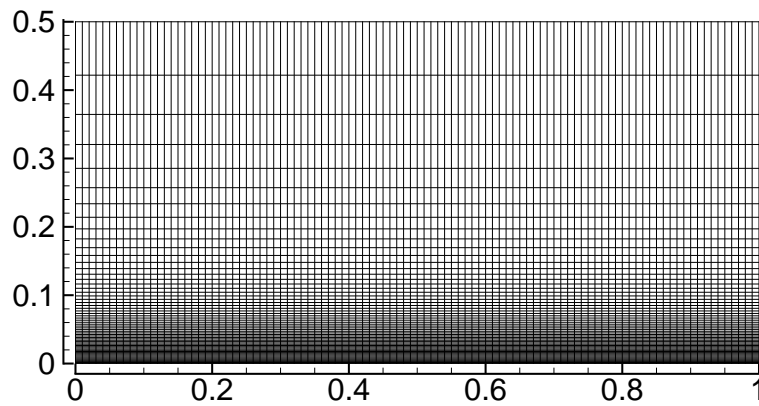
Figure 5.18: Mesh used for the laminar viscous flow over a flat plate case

A free stream Mach number of 0.3 and a Reynolds number of 2,000, based on the free stream velocity and the flat plate length, are used at the inlet. The inlet stagnation pressure and stagnation temperature are fixed to 10^5 Pa and 300 K, respectively. These flow conditions are imposed at the inlet boundary with a uniform flow assumption. The outflow boundary is applied on the right–hand boundary using the (Type–II) non–reflecting boundary condition. The lower boundary is a viscous wall, where a no–slip boundary condition is imposed. The upper boundary is represented by a far–field boundary condition, where the flow variables are set to free stream values and the spatial derivatives of the flow variables are extrapolated from the interior.
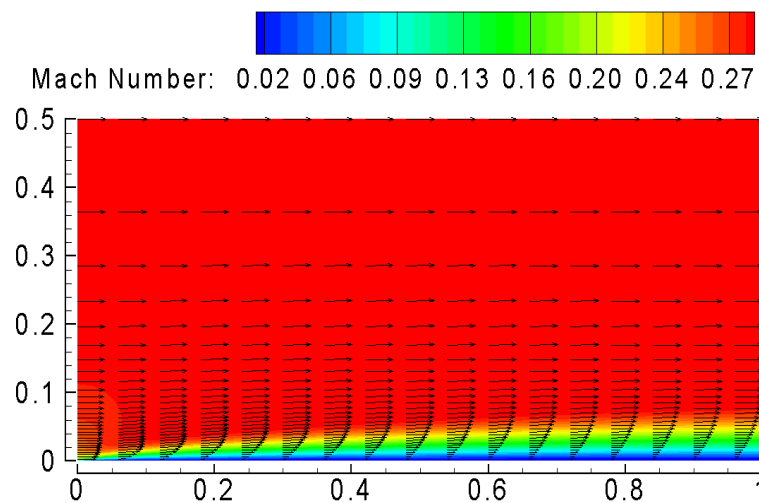
Figure 5.19: Distribution of computed Mach number with velocity vectors

In Fig. 5.19, the distribution of computed Mach number with velocity vectors is represented. The laminar boundary layer development with velocity vectors along the flat plate can be seen also in Fig. 5.19. No deterioration of the boundary layer is observed along the flat plate. The laminar boundary layer profile seems to be as expected. Influence of the computational domain selection using a uniform flow assumption at the inlet boundary can be seen by the velocity vectors near the leading edge of flat plate.

Computed streamwise (i.e., axial) velocity profiles are displayed in Fig. 5.20 including computation for the two–level multigrid method. The distribution of computed streamwise velocity profiles at 40 %, 50 %, 60 % and 70 % of the flat plate are compared with the analytical solution of Blasius (Hirsch, 2007) using

$$\eta = \frac{y}{x}\sqrt{Re} \quad \text{and} \quad Re = \frac{\rho V L}{\mu}. \tag{5.7}$$

where η is a non–dimensional coordinate normal to the flat plate and L is a characteristic length. It appears that, with a sufficient number of grid cells in the boundary layer the Navier–Stokes solver is able to reproduce the analytical distribution of streamwise velocities at 40 %, 50 %, 60 % and 70 % of the flat plate. Computed streamwise velocity profiles are in very good agreement with the analytical solution not only for the single–grid results but also for the two–level multigrid results (see Fig. 5.20 *(right)*).

The variation of computed friction coefficient (C_f) along the flat plate is depicted in Fig. 5.21. Comparison of the friction coefficient distribution with the analytical solution ($C_f = 0.664/\sqrt{Re}$ (Hirsch, 2007)) is carried out using the single–grid and two–level multigrid technique. The local friction coefficient is defined by

$$C_f = \frac{\tau_w}{0.5\rho_\infty U_\infty^2} \quad \text{and} \quad \tau_w = \mu \frac{\partial u}{\partial y}\mid_{y=0} . \tag{5.8}$$

Similarly, for the distribution of computed friction coefficient along the plate, a very good agreement is observed between the analytical solution and computed results (see Fig. 5.21).

The convergence history of the x–momentum equation is provided in Fig. 5.22. The x–momentum residual is decreased by about 5 orders of magnitude. The two–level multigrid method is associated to a more rapid convergence, as shown
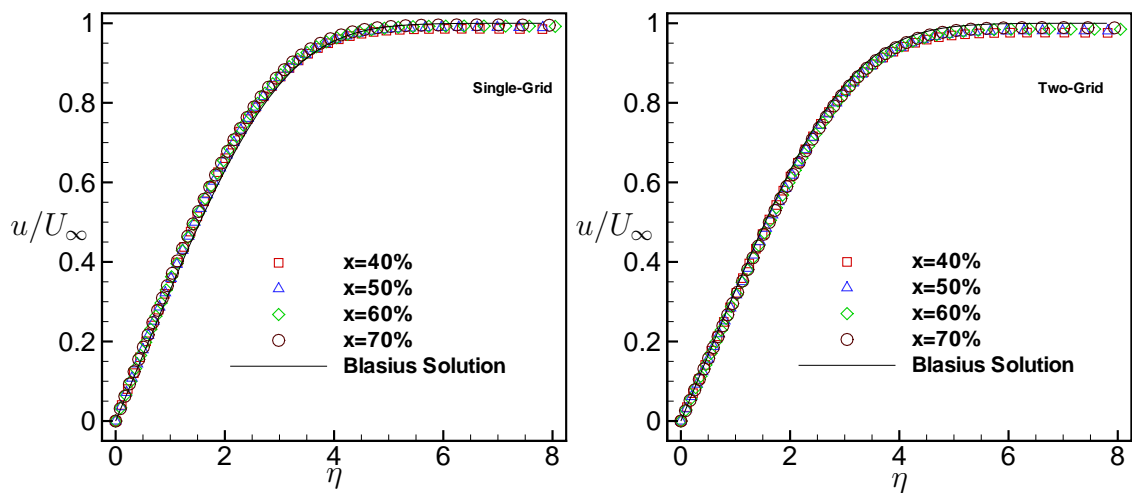
Figure 5.20: Axial velocity distribution at 40 %, 50 %, 60 % and 70 % of the flat plate including computation for the two–level multigrid technique *(right)*
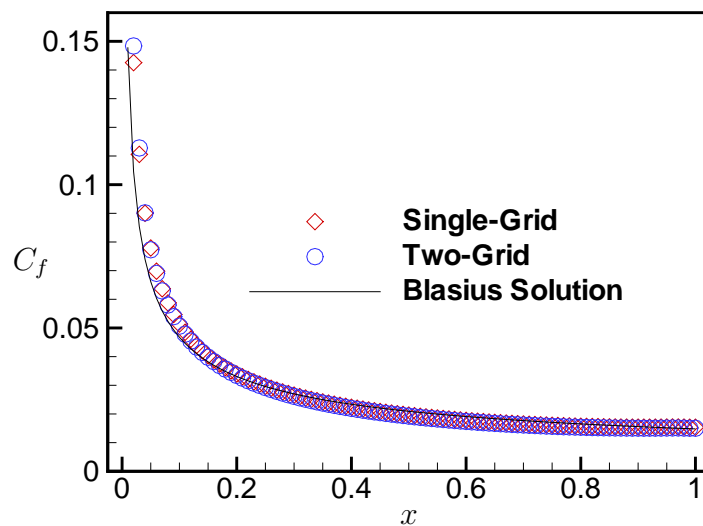
Figure 5.21: Distribution of friction coefficient along the flat plate

in Fig. 5.22, due to the use of the larger time step. An improvement by employing multigrid acceleration technique with respect to a single–grid calculation can be seen clearly. The number of iterations is considerably reduced by the addition of multigrid technique and the steady state flow condition can be quickly reached without losing any significant accuracy. These results validate the accuracy of the Navier–Stokes solver including the implementation of the direct–flux based multigrid method.
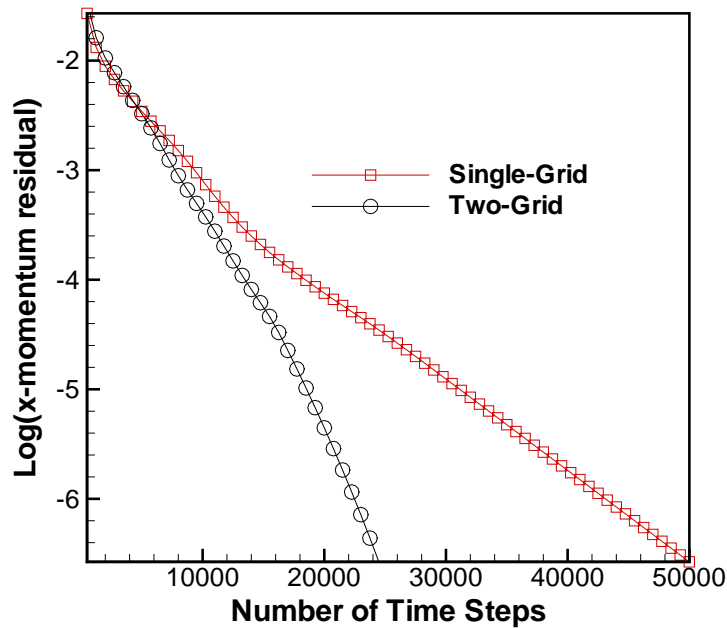
Figure 5.22: Convergence history of the x–momentum residual

5.2.2   Lid Driven Cavity Flow

The lid driven cavity flow in a square cavity is used as a second validation case
for the Navier–Stokes solver. The direct flux–based multigrid method is employed
here again at two–level in order to reduce the run–time requirement of the simu-
lation. Ghia et al. (1982) and Schreiber and Keller (1983) were among the first to
publish data on the lid driven flow in a square cavity case. These classical papers
are frequently referenced by the other researchers in order to validate their Navier–
Stokes solver or to test the performance of multigrid technique. In the present
study, all computed results were validated against the results published by Ghia
et al. (1982). This benchmark problem was considered by Guo et al. (2004); Zhang,
M. et al. (2004); Venkatachari et al. (2008) to validate their two–dimensional Navier–
Stokes solver based on the space–time conservation element and solution element
(CE/SE) method. Although the cavity geometry is simple, the driven cavity flow
exhibits a number of interesting physical features and several complex flow phe-
nomena, such as flow separation from the stationary wall, the existence of viscous
corner eddies in the rigid 90° corners, primary (longitudinal) vortices and interaction
between vortices depending on the Reynolds number.

A nonuniform quadrilateral mesh consists of (129×129) grid points in the x and y–directions. An exponential grid stretching is applied from the boundaries of the cavity until the cavity centre (see Fig. 5.23). Therefore a packed grid topology is obtained in order to resolve the corner eddies accurately. The flow conditions are Mach number of 0.1 and a Reynolds number of 400 based on the speed of the upper (i.e., moving) boundary and the height of the cavity. The stagnation pressure and stagnation temperature are fixed to 10^5 Pa and 300 K, respectively. These flow conditions are imposed at the upper boundary of the cavity as a moving boundary condition. The other boundaries are stationary (i.e. viscous) walls where a no-slip boundary condition is imposed.
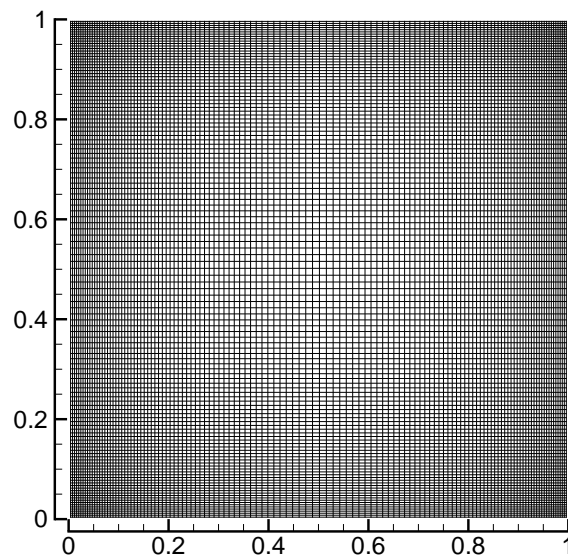

Figure 5.23: A nonuniform quadrilateral mesh used for the lid driven cavity problem

Two–dimensional compressible Navier–Stokes equations are solved to demonstrate the capability of the viscous flow solver and to test the performance of the direct–flux based multigrid technique. In Fig. 5.24, the distribution of computed u–velocity along the vertical line through the cavity centre *(left)* and the distribution of computed v–velocity along the horizontal line through the cavity centre *(right)* are represented for the single–grid and two–level multigrid method. The computed results are compared with those obtained by Ghia et al. (1982) for the same Reynolds number. A primary vortex inside the cavity and two smaller reverse–rotating vortices at both corners of the lower wall can be seen including the distribution of

computed Mach number and the streamlines, as shown in Fig. 5.25. The lower left–hand corner secondary vortex is resolved slightly different by the multigrid method (see Fig. 5.25 *(right)*) with respect to the single–grid computation. In general, the results obtained through the developed solver based on the time–conservative finite–volume method are in close agreement with the available numerical results.
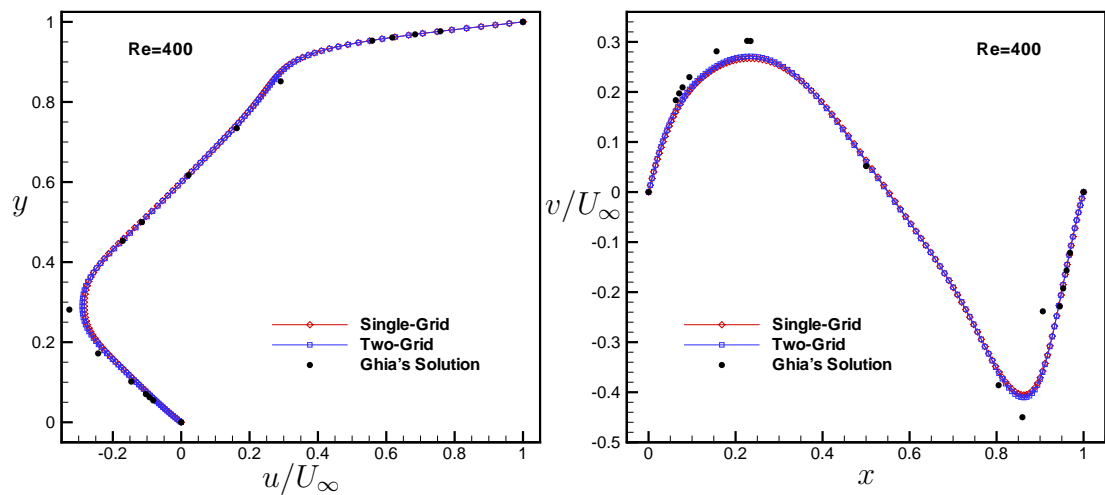
Figure 5.24: Distribution of the u–velocity along the vertical line through the cavity centre *(left)* and distribution of the v–velocity along the horizontal line through the cavity centre *(right)* at Re = 400
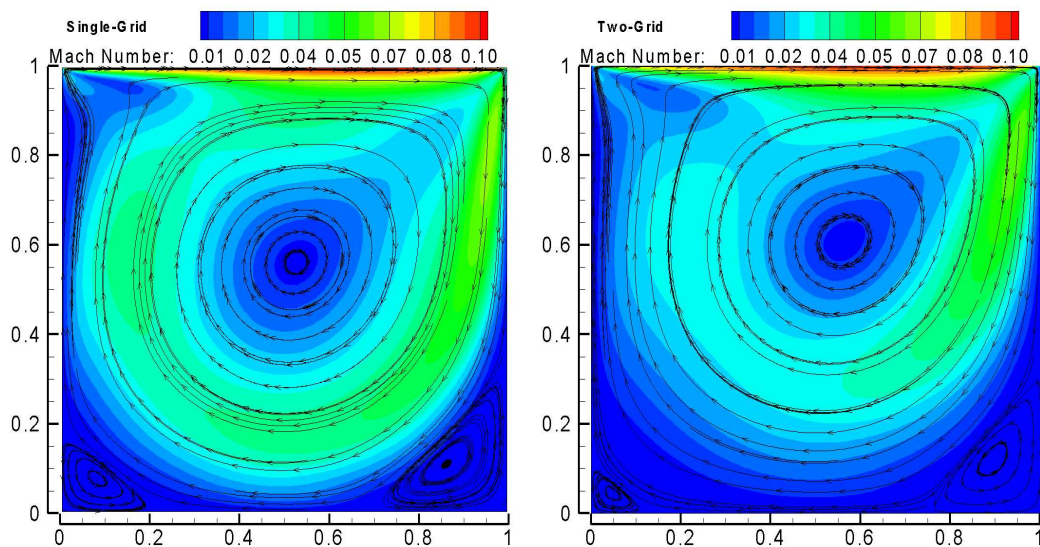
Figure 5.25: Distribution of computed Mach number and streamlines for single–grid *(left)* and two–level multigrid *(right)* at Re = 400
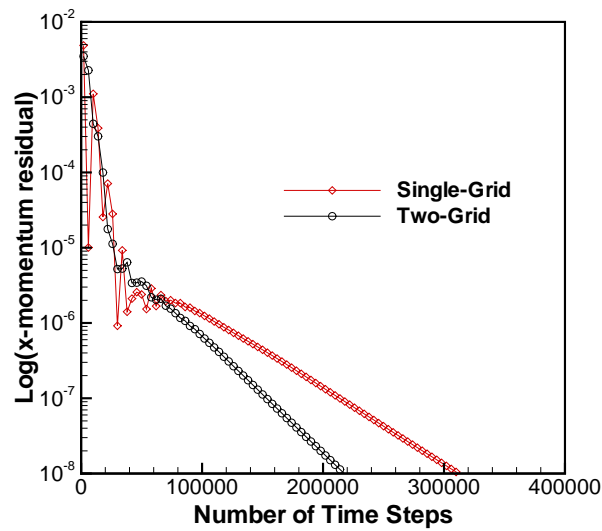
Figure 5.26: Convergence history of the x–momentum residual for the lid driven cavity problem at Re = 400

In Fig. 5.26, the convergence history of the x–momentum equation for the lid driven cavity flow is displayed. The x–momentum residual is decreased by about 6 orders of magnitude. A more rapid convergence rate is obtained by the two–level multigrid technique due to the use of the larger time step. The number of iterations are too high for this benchmark problem due to the low subsonic Mach number regime. The computation time is reduced by the implementation of the multigrid technique without a significant reduction in accuracy. Influence of the multigrid method becomes more visible after the x–momentum residual is decreased by about 4 orders of magnitude. The lid driven cavity flow is investigated at different Reynolds numbers using the same mesh and boundary conditions. In Figs. 5.27 to 5.32, the computed results are in a very good agreement with those obtained by Ghia et al. (1982). An upstream eddy in the upper left–hand corner begins to grow in size and strength as the Reynolds number increases. The flow field at different Reynolds numbers is calculated accurately by the present flow solver.

In general, it can be concluded that from these validation studies, the accuracy of the present Navier–Stokes solver based on the new definitions of cell interface and control volume (see Section 4.1) including the discretization of the viscous fluxes as well as the implementation of multigrid method are validated successfully.
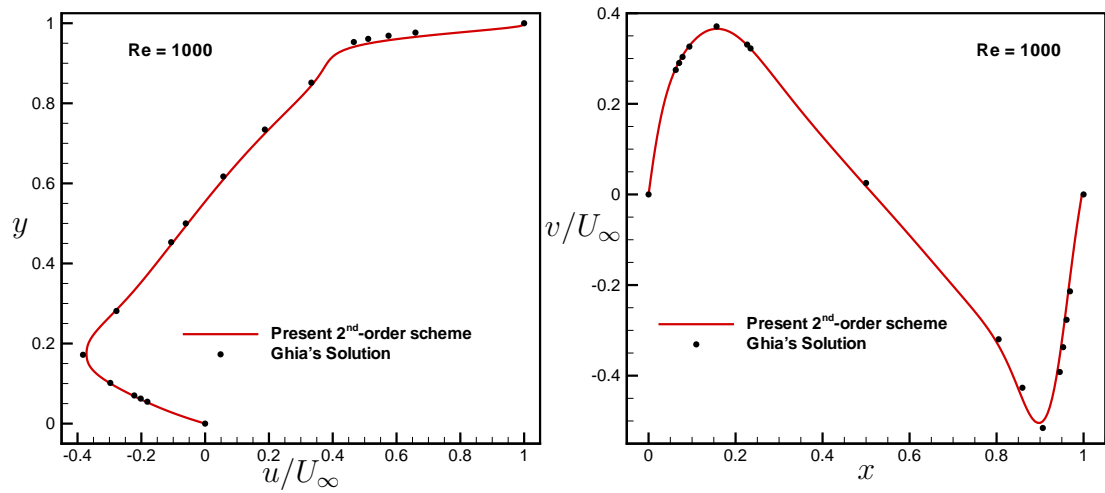
Figure 5.27: Distribution of the u–velocity along the vertical line through the cavity centre *(left)* and distribution of the v–velocity along the horizontal line through the cavity centre *(right)* at Re = 1000
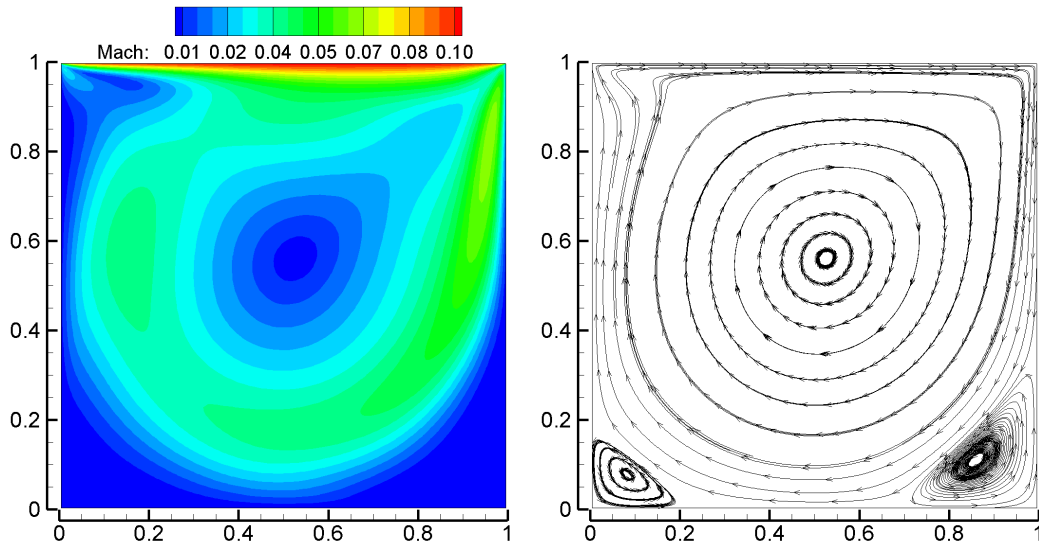
Figure 5.28: Distribution of computed Mach number *(left)* and streamlines *(right)* at Re = 1000

Figure 5.29: Distribution of the u–velocity along the vertical line through the cavity centre *(left)* and distribution of the v–velocity along the horizontal line through the cavity centre *(right)* at Re = 3200

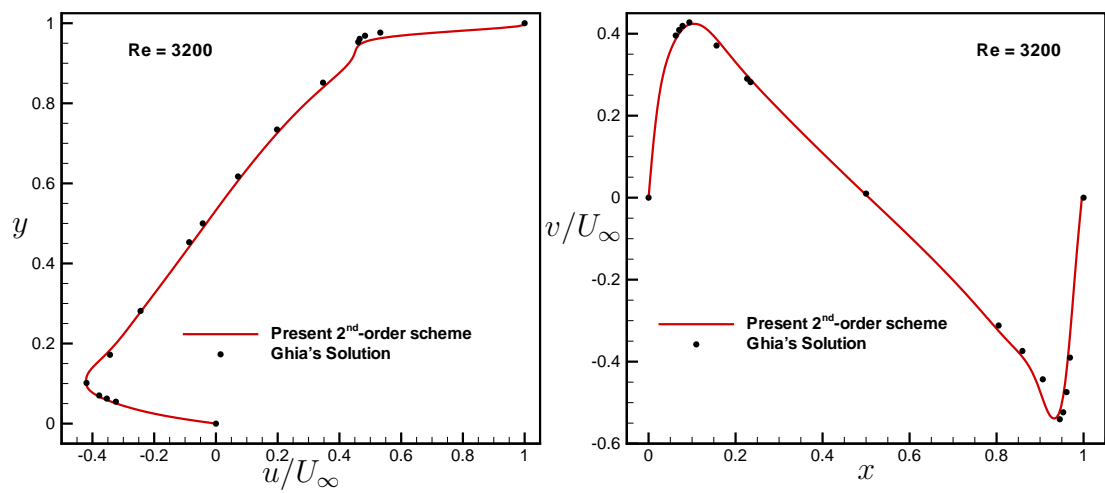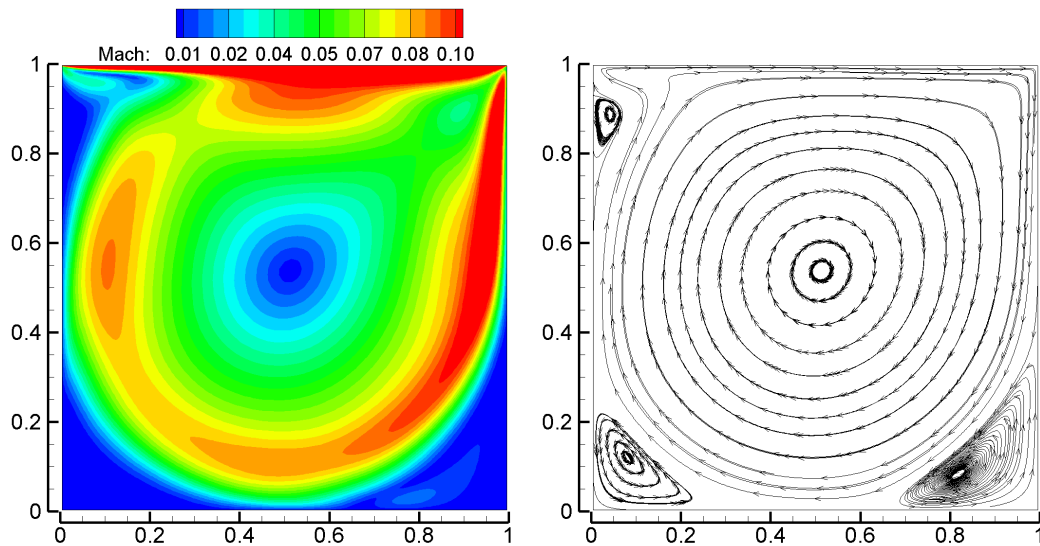**Figure 5.30:** Distribution of computed Mach number *(left)* and streamlines *(right)* at Re = 3200

Figure 5.31: Distribution of the u–velocity along the vertical line through the cavity centre *(left)* and distribution of the v–velocity along the horizontal line through the cavity centre *(right)* at $Re = 5000$
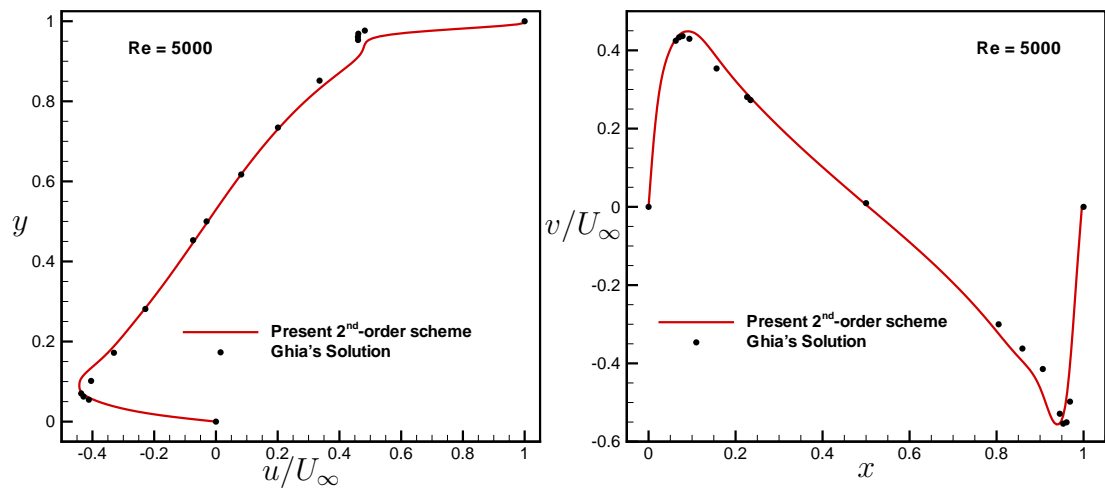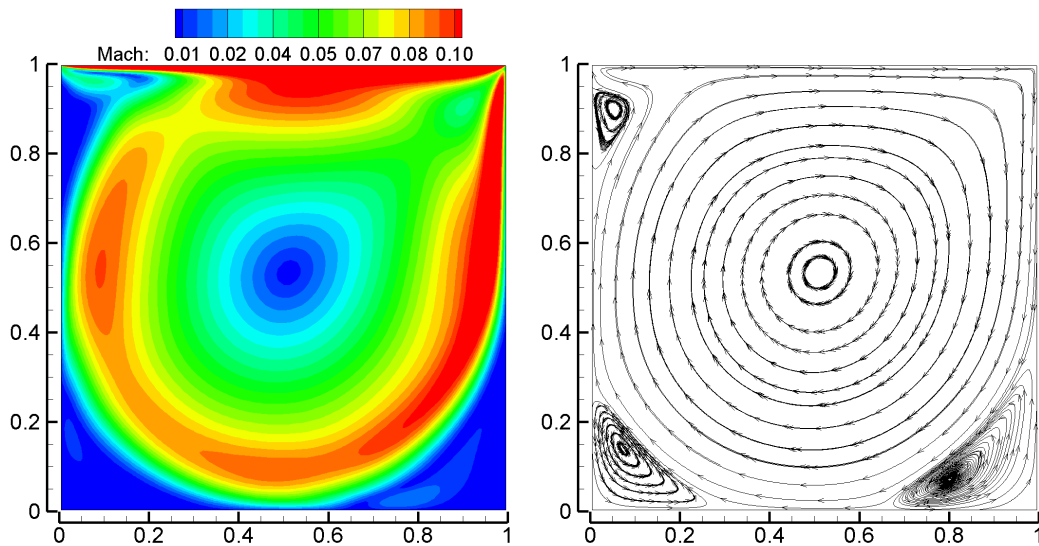

Figure 5.32: Distribution of computed Mach number *(left)* and streamlines *(right)* at $Re = 5000$

5.3   Viscous Turbulent Flows

Aeroacoustic problems are highly time dependent. All technically relevant aeroacoustic problems are governed by turbulent flows. An overview of different techniques, namely, DNS, LES, RANS as well as hybrid LES–RANS methods to simulate turbulent flows and compute their effect on the aerodynamic noise generation and propagation are already mentioned briefly in Section 2.1. In the present study, the large–eddy simulation technique is used in order to simulate the turbulent flow field features with high–fidelity as well as to predict the near–field aerodynamic noise directly. Details of the subgrid–scale modeling for the compressible filtered Navier–Stokes equations with the Smagorinsky model constants can be found in Section 3.3.1. The implemented LES technique is tested by solving three different two–dimensional problems, before carrying out full three–dimensional aeroacoustic simulations. The geometry and the flow configuration of the problems are defined in the subsequent sections including the details of the grids and boundary conditions.

5.3.1   Large–Eddy Simulation of a Mixing Layer

Planar shear layers and sound generation mechanisms by vortex pairing have been studied numerically by Rogers and Moser (1994), Colonius et al. (1997), Bogey et al. (1999), Bogey (2000a), Bogey et al. (2000b), Uzun (2003) and Ribault (2005). Here, a two–dimensional spatially evolving mixing layer problem is solved. This test case is the same as the one studied by Bogey (2000a) and Uzun (2003).

The hyperbolic tangent inflow profile for the mean streamwise velocity is defined by

$$\overline{U}(y) = \frac{U_1 + U_2}{2} + \frac{U_2 + U_1}{2} \tanh\left(\frac{2y}{\delta_{w0}}\right) \qquad (5.9)$$

where $U_1 = 50 \ m/s$ and $U_2 = 100 \ m/s$ are the low–speed and high–speed streams, respectively. δ_{w0} is the initial vorticity thickness that is defined as (Uzun, 2003)

$$\delta_{w0} = \frac{U_2 - U_1}{\left|\frac{\partial U}{\partial y}\right|_{max}} \qquad (5.10)$$

The mean transverse velocity $(\overline{V}(y))$ is set to zero. According to Uzun (2003), to simulate a naturally developing shear layer, a random perturbation may be used at

the inflow boundary. The random perturbation is given as

$$v'(y) = \epsilon \alpha \left(\frac{U_1 + U_2}{2} \right) \exp \left(\frac{-y^2}{\Delta y_0^2} \right) \tag{5.11}$$

where $\alpha = 0.0045$, Δy_0 is the minimum grid spacing in the y–direction and ϵ is a random number between -1 and 1. Similar random perturbation approach was used by Bogey (2000a) also.

The convective Mach number which measures the intrinsic compressibility of a mixing layer is defined by (Ribault, 2005)

$$M_c = \frac{U_2 + U_1}{2c_\infty} = 0.074 \tag{5.12}$$

where c_∞ is the speed of sound in the free stream. The Reynolds number based on the initial vorticity thickness (δ_{w0}) and velocity difference across the shear layer is

$$Re_w = \frac{\delta_{w0}(U_2 - U_1)}{\nu} = 5333 \tag{5.13}$$

In Fig. 5.33, the mesh used for the spatially evolving mixing layer problem is depicted. The mesh consists of 625×301 grid points in the x and y–directions, respectively. The computational domain lies between $0 \le x \le 250\delta_{w0}$ and $-100\delta_{w0} \le y \le 100\delta_{w0}$. The mesh is uniform in the streamwise direction whereas in the transverse direction an exponential grid stretching is applied. The minimum grid spacing is about $0.16\delta_{w0}$ at $y = 0$ and the maximum grid spacing around the lower and upper boundaries is $3\delta_{w0}$. The physical domain is decomposed into 16 subdomains for parallel computing. The results are compared with those obtained by using the 6th–order tri–diagonal compact scheme (Uzun, 2003). For comparison, the grid of Uzun (2003) consists of 720×576 grid points in the x and y–directions, respectively. He also applied grid stretching toward the upper and lower boundaries using the same exponential grid stretching. His domain extends up to $400\delta_{w0}$ in the streamwise direction and from $y = -300\delta_{w0}$ to $y = 300\delta_{w0}$ in the transverse direction. In order to diminish the reflecting effect from the outlet boundary he used a sponge region in his simulation, the physical region was extended up to $x = 250\delta_{w0}$. The first 625 grid points in the x–direction were used in the physical region and the remaining 95 grid points formed the sponge region.
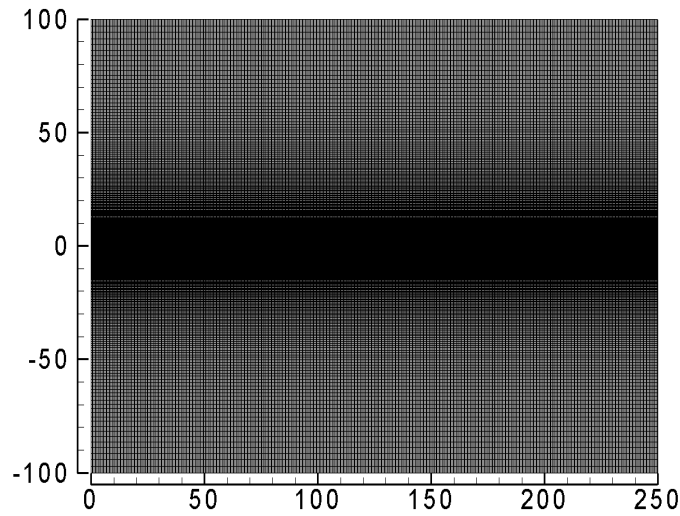
Figure 5.33: (625×301) mesh used for the mixing layer problem

In the present study, a smaller computational domain in both streamwise and transverse directions is used with no sponge zone due to the effective non–reflecting boundary condition. The hyperbolic tangent profile (eq. 5.9) with the random per-turbation (eq. 5.11) is used as the inflow boundary. The non–reflecting boundary condition (Type–II) is imposed at the upper, lower and outlet boundaries.

In Fig. 5.34, an instantaneous snapshot of vorticity magnitude is displayed. The vortex pairing at various locations in the domain can be observed clearly in the same figure.
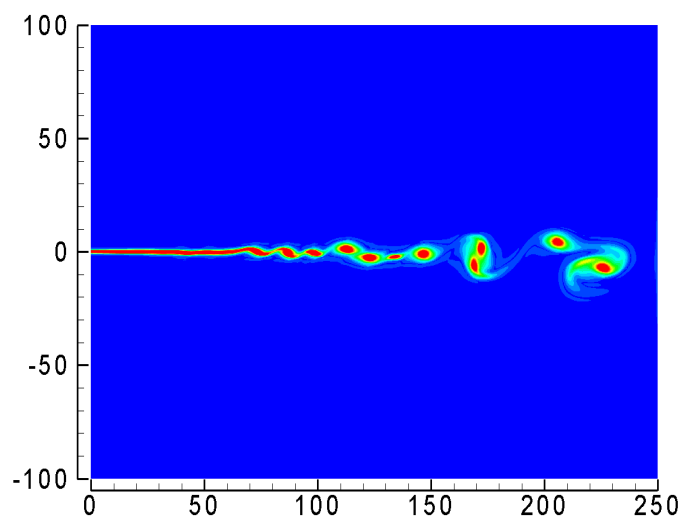
Figure 5.34: Instantaneous snapshot of vorticity magnitude

In Fig. 5.35, an instantaneous snapshot of streamwise velocity *(left)* and the distribution *(right)* of mean streamwise velocity are shown. Near the pairing locations, increase in the shear layer thickness can be seen from the mean streamwise contours in Fig. 5.35 *(right)*. The statistical data and the mean flow variables are obtained by time–averaging the flow field variables after passing the initial transient period.
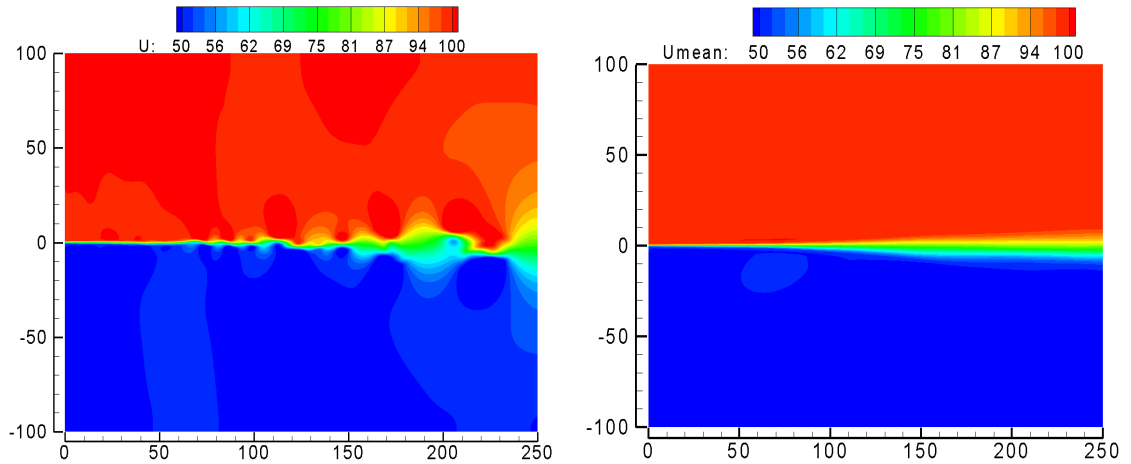
Figure 5.35: Instantaneous snapshot of streamwise velocity *(left)* and distribution of mean streamwise velocity *(right)*

The vorticity thickness evaluation is shown in Fig. 5.36. After the initial transients, the vorticity thickness grows linearly. The spreading rate parameter is given by (Pope, 2000)

$$S = \frac{0.5(U_1 + U_2)}{U_2 + U_1} \frac{\partial \delta_w(x)}{\partial x} = 0.09 \tag{5.14}$$

The range of reported experimental results for the parameter S is changing from 0.06 to 0.11. The parameter S predicted by the present 2–D LES solver is within the range of experimental values.

The normalized Reynolds stresses are defined as

$$\sigma_{xx} = \frac{\langle u'u' \rangle}{(U_2 - U_1)^2} \quad \text{and} \quad \sigma_{yy} = \frac{\langle v'v' \rangle}{(U_2 - U_1)^2}. \tag{5.15}$$

where $\langle \rangle$ denotes time–averaging. In Fig. 5.37, the turbulence intensities are compared with the normalized Reynolds stress distribution obtained by Uzun (2003). For comparison the transversal direction is non–dimensionalized by the vorticity thickness $\delta_w(x)$. In conclusion, although a smaller computational domain is used

with no sponge zone for the present computation, the 2–D simulation of the mixing
layer problem is capable of obtaining the vorticity thickness growth fairly. The com-
puted turbulence intensities are in reasonably good agreement with those using the
6th–order tri–diagonal compact scheme of Uzun (2003) whereas the present scheme
is just 2nd–order accurate in space and time.
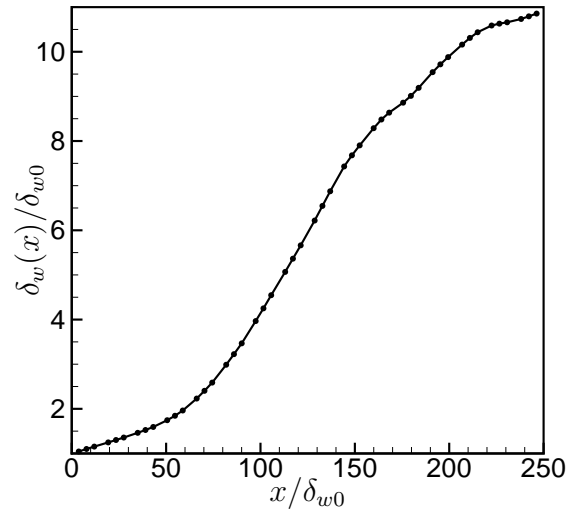
Figure 5.36: Vorticity thickness growth in the mixing layer
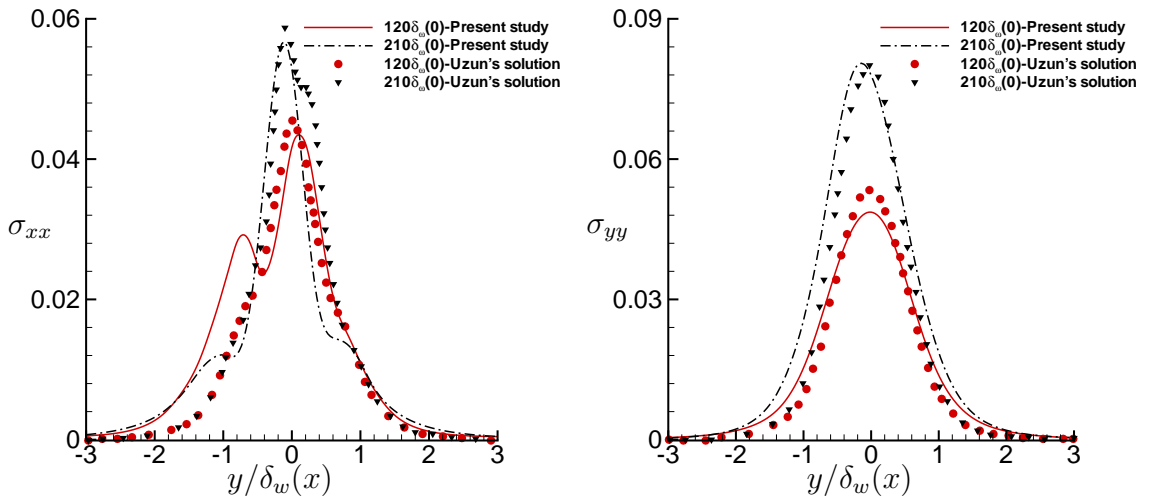
Figure 5.37: Normalized Reynolds normal stress σ_{xx} *(left)* and σ_{yy} *(right)* profiles

5.3.2   2–D Cavity Flow Noise

The flow field generated by a two–dimensional open cavity in a transonic flow is investigated here. The present 2–D LES solver is used to perform numerical simulation on a rectangular cavity at a Mach number of 0.85. Physical description of different mechanisms for generating cavity flow noise and a review of previous studies are already provided in Section 2.4. The 2–D cavity case computed here is the same as the one studied by Chen et al. (2007). Two–dimensional LES results of the present scheme are compared with those of high–order numerical scheme (Chen et al., 2007) as well as experimental data (Peshkin, 2002; Henshaw, 2000) for the flow over a rectangular cavity.

The cavity geometry with a length–to–depth (L/D) ratio of 5 exhibiting flow in shear layer mode, so called because the separated shear layer at the cavity leading edge does not attach to the cavity floor. This geometry is adapted here to carry out a 2–D simulation from the M219 cavity configurations given by Peshkin (2002). Its length L and the depth D are equal to 508 mm and 101.6 mm, respectively. The dimensions of the computational domain are: $11D$ (streamwise) $\times 4D$ (wall–normal) as shown in Fig. 5.38. In the present study, the size of computational domain and the grid configuration are same as the one given by Chen et al. (2007). The grid consists of $400 \times 130 \approx 5.2 \times 10^4$ CVs above the cavity and $250 \times 80 \approx 2.0 \times 10^4$ CVs inside the cavity. Total grid consists of 72,000 CVs. The physical domain is decomposed into 16 subdomains for parallel computations. Each subdomain is represented by red line boundary, as shown in Fig. 5.38.
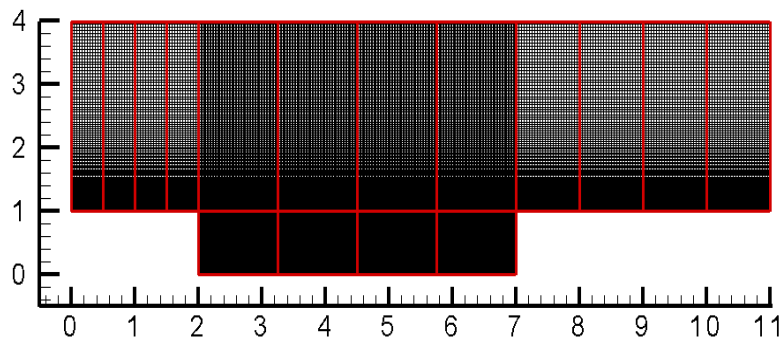
Figure 5.38: Mesh and subdomains used for the two–dimensional open cavity problem

The flow conditions correspond to a free–stream Mach number of 0.85, a Reynolds number of 1.36 million based on the cavity depth, the stagnation pressure of 99,600 Pa and the stagnation temperature of 305 K are imposed as inflow boundary condition and the spatial derivatives of the flow variables are taken as zero. The inflow boundary is set to 2 times the cavity depth upstream of the cavity whereas the outflow (right–hand) boundary is set to 4 times the cavity depth downstream of the cavity. In order to achieve an unsteady turbulent boundary at the leading edge of the cavity a steady turbulent boundary layer profile is implemented at the inflow. Hence the boundary layer thickness at the leading edge of the cavity is found to be similar to the experimental value of 10.16 mm (Nayyar et al., 2005). In order to trigger cavity flow oscillations, small perturbations are added. When the self–sustained oscillations inside the cavity started, the perturbations are turned off to prevent the spectral analysis from numerical artifacts. Similar random perturbation approach was used by Chen et al. (2007) also. The periodic boundary condition in spanwise and the no–slip boundary condition at the walls of the cavity are imposed. The non–reflecting boundary condition (Type–II) are applied to the outflow (right–hand) and far–field (upper section of the domain) boundaries. The schematic view of the open cavity dimensions and the imposed boundary conditions are displayed in Fig. 5.39.
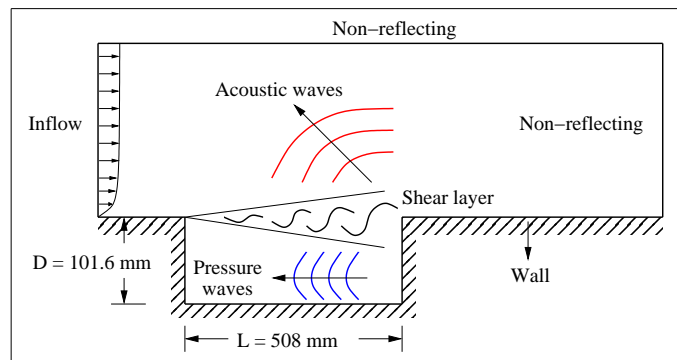

Figure 5.39: Schematic view of the open cavity dimensions and boundary conditions

Fig. 5.40 *(left)* represents the history of pressure fluctuations for a time interval of 0.2 s at $x/L = 0.95$ and $y/L = 0$. The simulation is carried out with a time step of 7.0×10^{-7} s and the pressure signals are numerically sampled every 238 time

steps corresponding to a sampling rate of ≈ 6 kHz which is in accordance with the experimentally used value. The simulation is performed for $0.25\ s$ and the first 0.05 s of the pressure signals are truncated to discard the initial transient. The sound pressure level (SPL) of pressure fluctuations is compared with the experimental data, as shown in Fig. 5.40 *(right)*. The SPLs are related to the energy carried by the sound wave, defined by

$$SPL(dB) = 20 \log_{10} \frac{P_{rms}}{P_{ref}} \tag{5.16}$$

where the P_{rms} is the root–mean–square values of the pressure fluctuations and $P_{ref} = 2.0 \times 10^{-5}\ Pa$.
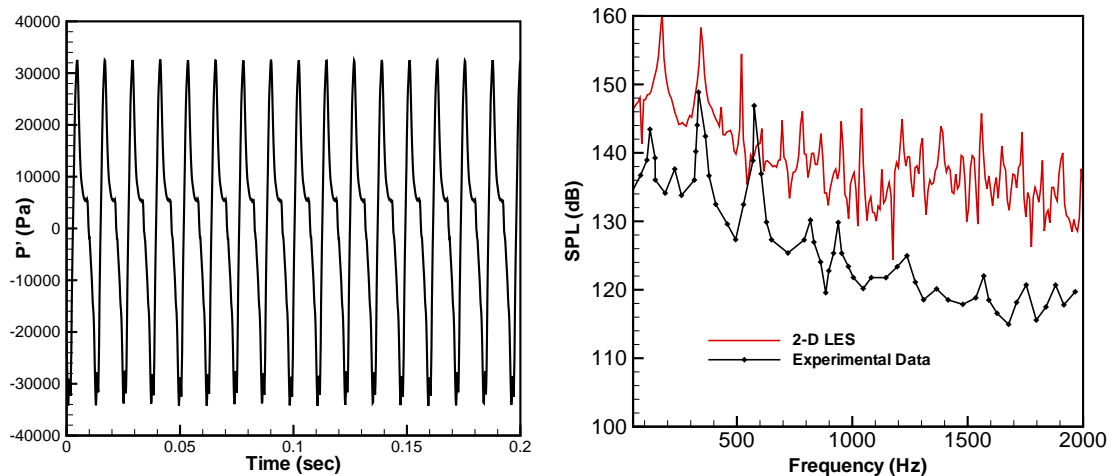
Figure 5.40: History of pressure fluctuations *(left)* and SPL spectrum *(right)* close to the cavity rare wall, at $x/L = 0.95$ and $y/L = 0$

An instantaneous snapshot of vorticity magnitude is displayed Fig. 5.41. Comparison of the root–mean–square (RMS) values of the pressure fluctuations along the cavity floor with the experimental data and the numerical solution obtained by Chen et al. (2007) is depicted in Fig. 5.42. As a result, the deviations to the measurements are clearly visible in Fig. 5.40 *(right)*, the computed SPL spectrum is not in good agreement with the measurements. In Fig. 5.42, the discrepancy between the computed RMS values of pressure fluctuations and the experimental one is significant due to the 3–D nature of the problem. On the other hand, the computed RMS values from the present 2nd–order accurate scheme are in close agreement with the 4th–order central finite–difference scheme given by Chen et al. (2007). The 2–D

LES results are incapable of successfully capturing the near–field flow behavior of the open cavity problem. However, similar behaviour is observed also by Chen et al. (2007) using the high–order numerical scheme. Therefore, a 3–D simulation for the open cavity case at Mach number of 0.85 is required to clarify the above–mentioned points (see Section 6.1).
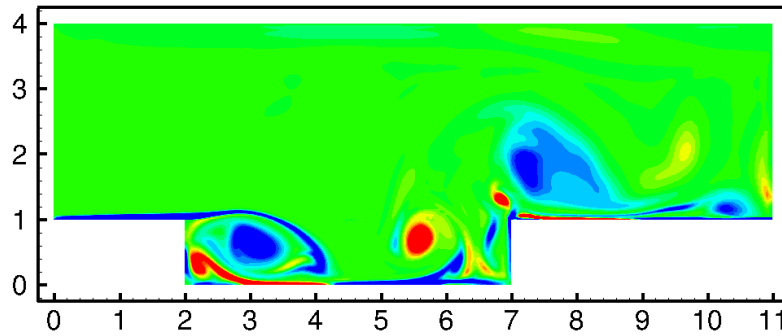

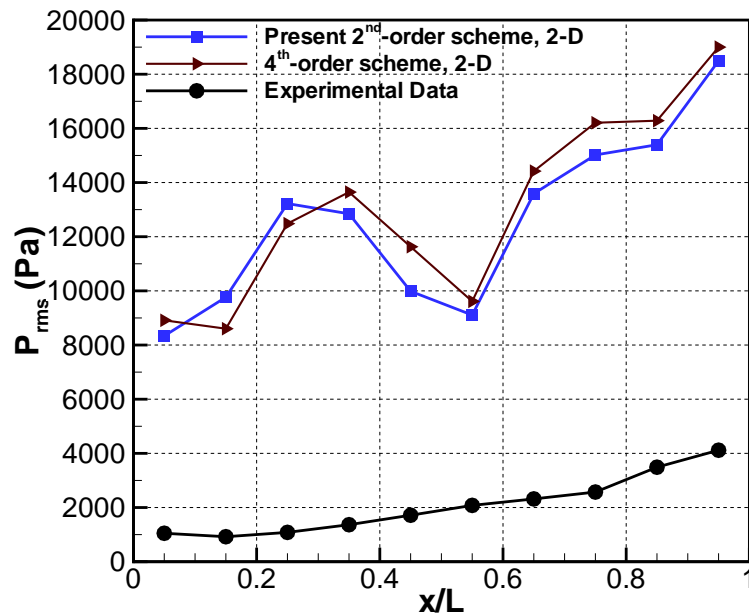**Figure 5.41:** Instantaneous snapshot of vorticity magnitude

Figure 5.42: Comparison of RMS values of the pressure fluctuations along the cavity floor (4th–order scheme (Chen et al., 2007))

5.3.3   2–D Screech Noise

The generation of screech tones in an underexpanded jet and shock–induced acoustic waves owing to the interaction of flow instabilities originate from the nozzle lip with the quasi–periodic shock–cell structure are investigated in 2D here. The present 2–D parallel LES solver is used for numerical simulation of rectangular underexpanded jet problem. The jet operates at a fully expanded Mach number of 1.55. Description of the three basic components of the supersonic jet noise, namely, discrete frequencies, the broadband shock–associated noise and the turbulent mixing noise, as well as a review of previous experimental, theoretical and numerical studies can be found in Section 2.5. The 2–D screech generation in a planar supersonic jet problem studied here is adapted from the one computed by Berland et al (2007) for a 2–D simulation. Two–dimensional LES results of the present time–conservative finite–volume scheme are compared with the experimental data (Raman and Rice, 1994; Panda et al., 1997) and the analytical solution of (Tam, 1988) for the rectangular supersonic jets.
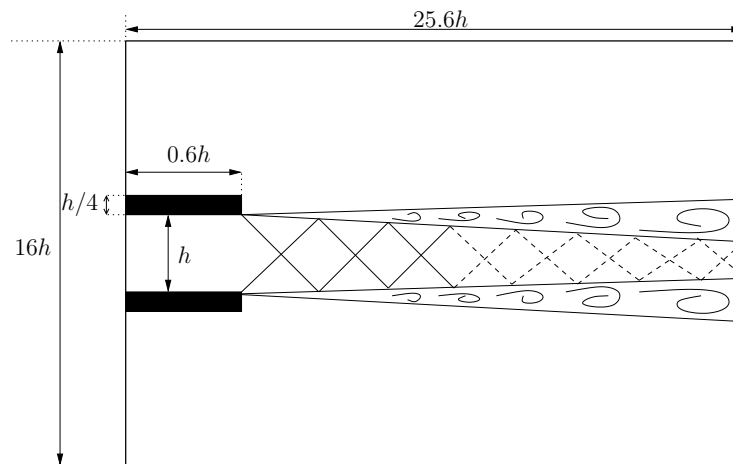
Figure 5.43: Schematic view of the computational domain for the two–dimensional screech noise problem

In Fig 5.43, the schematic of the computational domain is displayed. The jet height is 3 mm and the nozzle lip thickness is $h_l = h/4$ similar to that used in the experiments of Raman and Rice (1994). The dimensions of the computational domain are: 25.6h (streamwise) ×16h (wall–normal), with a nozzle extending

over $0.6h$ inside the domain, as shown in Fig. 5.43. A Cartesian grid consists of $520 \times 260 \approx 1.35 \times 10^5$ CVs. The smallest mesh size $\Delta_m = h/40$ allows to use 40 grid points within the jet height and approximately ten grid nodes inside the boundary layer. The physical domain is decomposed into 64 subdomains to perform parallel computing. Each subdomain is represented by red line boundary, as shown in Fig. 5.44.
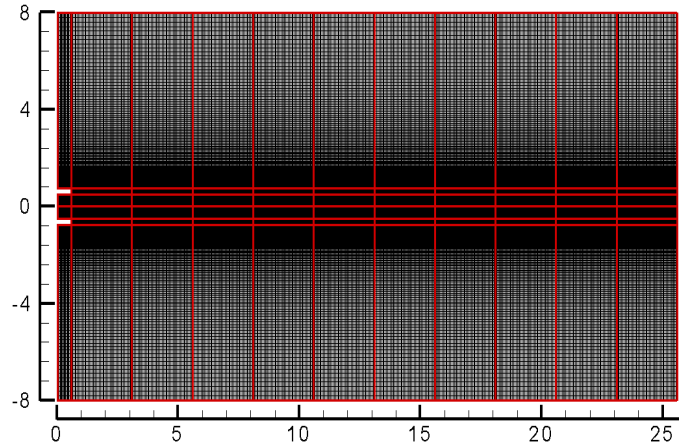
Figure 5.44: Mesh and subdomains used for the 2–D planar underexpanded jet problem

The jet assumed to be supplied by a convergent nozzle whose designed Mach number M_d is equal to 1. The ambient region surrounding the flow is at rest. An ambient pressure (P_∞) and density (ρ_∞) are set to 10^5 Pa and 1.22 kg/m^3, respectively. Temperature of reservoir T_r is set to 288 K and an elevated pressure $p_e/p_\infty = 2.09$ is imposed inside the nozzle so that the jet operates at underexpanded conditions. The fully expanded jet Mach number M_j is defined by (Berland et al, 2007)

$$M_j = \left\{ \frac{2}{\gamma - 1} \left[\left(1 + \frac{\gamma - 1}{2} M_d^2 \right) \left(\frac{p_e}{p_\infty} \right)^{(\gamma-1)/\gamma} - 1 \right] \right\}^{1/2} = 1.55 \qquad (5.17)$$

Flow variables are uniform inside the nozzle except in the near–wall regions, where a no–slip boundary condition is required. Therefore, boundary layer profiles are imposed in the vicinity of the solid surfaces (i.e., between nozzle lips) using an approximation of the laminar Blasius solution, expressed as (Berland et al, 2007)

$$\frac{u}{U_e} = \begin{cases} \eta(2 - 2\eta^2 + \eta^3), & \text{if } \eta < 1 \\ 1, & \text{if } \eta \geq 1 \end{cases} \qquad (5.18)$$

where η is the distance to the wall normalized by the boundary layer thickness δ, and the designed nozzle velocity, U_e, is set to $310 \; m/s$.

The inflow density profile is provided by using the Crocco–Busemann relation as (Berland et al, 2007)

$$\rho = \left[\frac{1}{\rho_w} - \left(\frac{1}{\rho_w} - \frac{1}{\rho_e} \right) \frac{u}{U_e} - \frac{\gamma - 1}{2} M_d^2 \left(\frac{u}{U_e} - 1 \right) \frac{u}{U_e} \right] \qquad (5.19)$$

where the density on the walls, ρ_w, can be evaluated by using the ideal gas relation given by eq. (3.13). A Reynolds number of 6×10^4 based on the jet height and velocity, where $U_j = M_j c_j$ and $c_j = 278 \; m/s$, is used here. The no–slip wall boundary condition is imposed only at the inner section of nozzle lips. The non–reflecting boundary condition (Type–I) is applied to the far–field (left–hand, upper and lower boundaries) and the non–reflecting boundary condition (Type–II) is imposed at the outlet owing to the substantial gradients in the y–directions. The schematic view of the 2–D planar underexpanded jet dimensions and the boundary conditions are shown in Fig. 5.45.
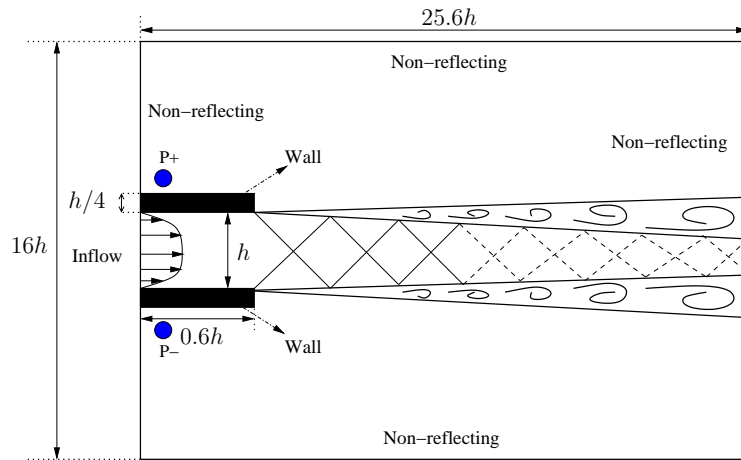
Figure 5.45: Schematic view of the 2–D planar underexpanded jet dimensions and boundary conditions

An instantaneous snapshot of the streamwise velocity *(upper)* and the distribution of mean streamwise velocity *(lower)* in the whole computational domain are represented in Fig. 5.46. Two shock–cell structures are apparent in the jet plume for $x/h < 6$ then these shock–cells are breaking down, as shown in Fig. 5.46 *(upper)*, and releasing energy. Owing to this energy release the resolved turbulent kinetic

energy increases in the downstream direction for $x/h > 6$ (see Fig. 5.47). On the other hand, in Fig. 5.46 *(lower)*, four shock–cell structures exhibiting the distinctive bow–shaped structure are clearly visible in the jet plume ($x/h < 10$) for the computed mean streamwise velocity due to the overpressure at the nozzle exit. The streamwise velocity decreases and a weakening of the shock strength in the downstream direction can be observed in Fig. 5.46. Similar flow field features are observed by Berland et al (2007) also. A snapshot of the numerical Schlieren (density gradient modulus) *(upper)* and the distribution of computed mean density gradient *(lower)* are depicted in Fig. 5.48. The shock–cell structures in the jet plume are clearly demonstrated in these figures.
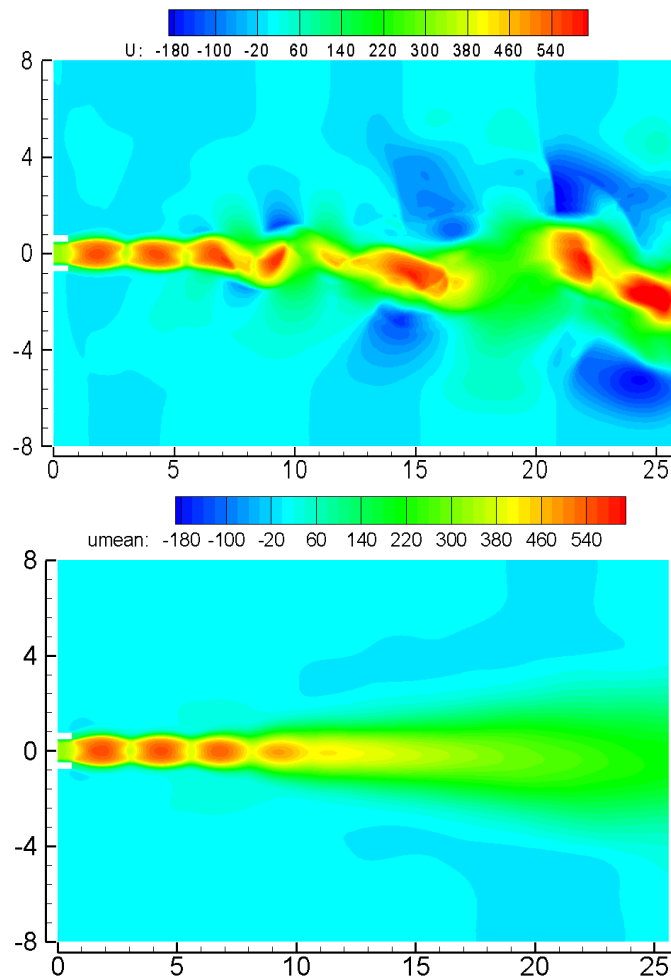
Figure 5.46: Instantaneous streamwise velocity *(upper)* and distribution of mean streamwise velocity *(lower)* for the 2–D planar underexpanded jet
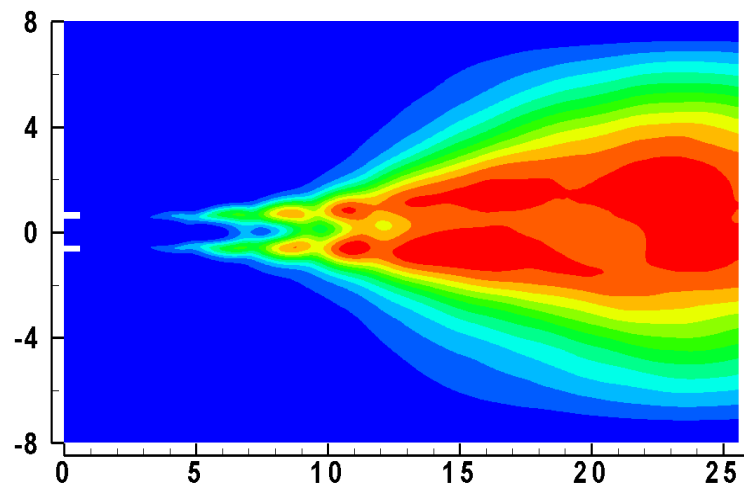
Figure 5.47: Distribution of resolved turbulent kinetic energy for the 2–D planar under-expanded jet
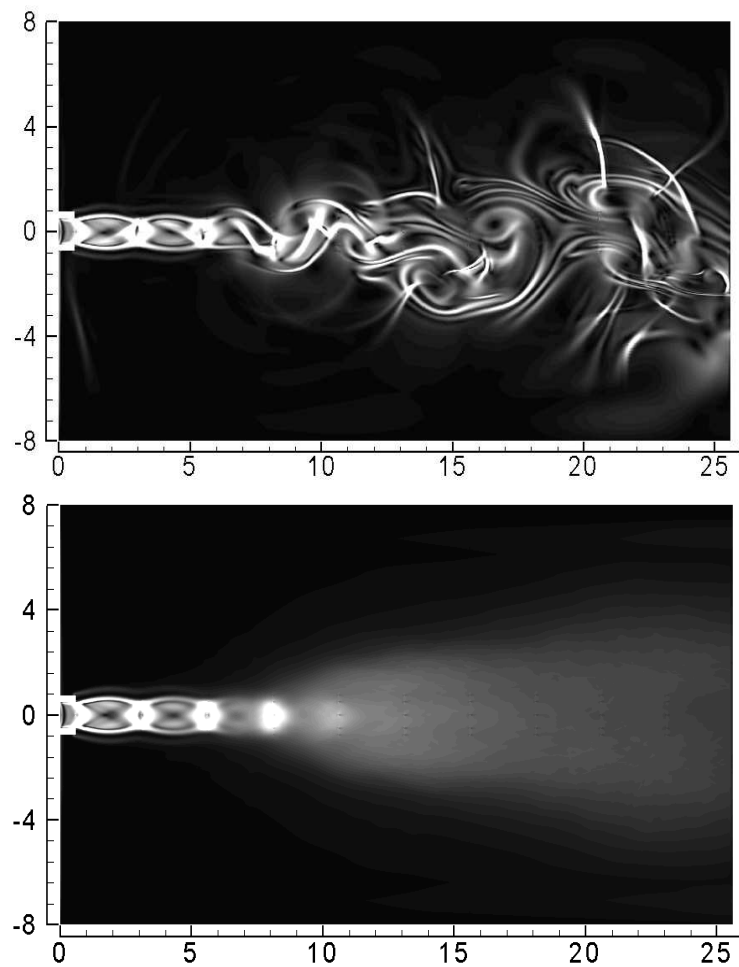
Figure 5.48: Instantaneous numerical Schlieren *(upper)* and distribution of time–averaged numerical Schlieren *(lower)*
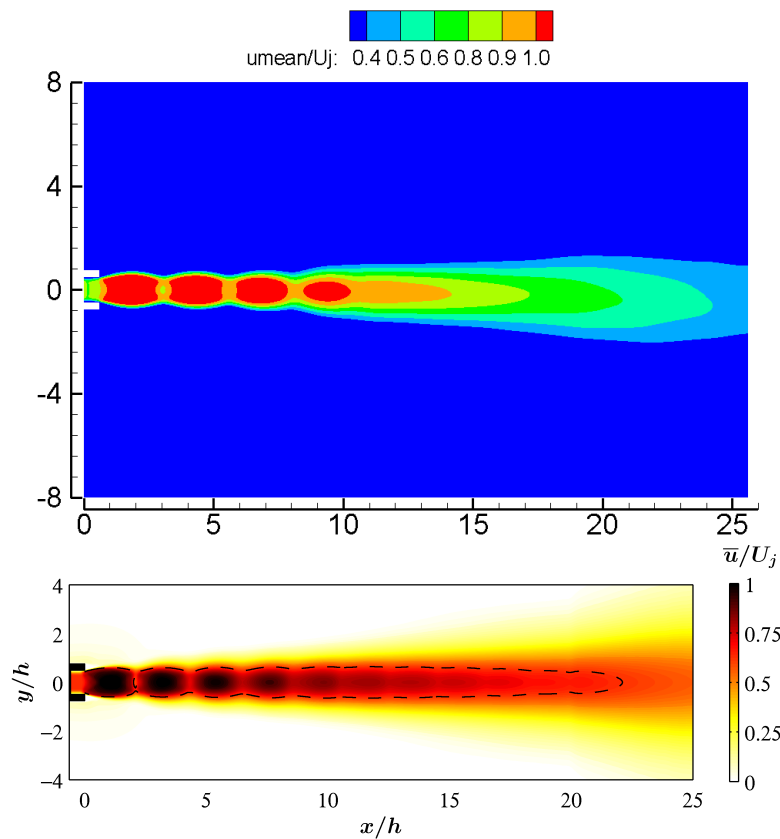
Figure 5.49: Distribution of mean streamwise velocity present study *(upper)* and Berland et al (2007) *(lower)*

In Fig. 5.49, the normalized mean streamwise velocity is compared with the 3–D LES result obtained by Berland et al (2007) *(lower)*. Though the present results are 2–D, the shock–cell spacing (L_s/h) is in a very good agreement with the experimental data and the analytical solution of Tam (1988), as shown in Fig. 5.50. The pressure signals are numerically sampled at the upstream location (0.2h, 0.85h) and (0.2h, -0.85h) represented by points P^+ and P^- in Fig. 5.45, respectively. The 2–D LES is performed for 0.07 s with a time step of $2.0 \times 10^{-7}s$. The time evolution of the pressure signals close to the nozzle lip and SPLs of pressure fluctuations as a function of Strouhal number are depicted in Figs. 5.51 and 5.52, respectively. Though the shock–cell spacing is predicted very well by the 2–D LES solver, SPLs of pressure perturbations clearly show that the dominant screech tone and its subharmonics are not captured by the flow solver. The 2–D LES solver is incapable of predicting the three basic components of a supersonic jet, namely, the turbulent mixing noise, the

screech tones and the broadband shock–associated noise. It will be shown later from the 3–D simulation of underexpanded jet (see Section 6.2) these supersonic jet noise components can be predicted reliably by the 3–D LES solver.
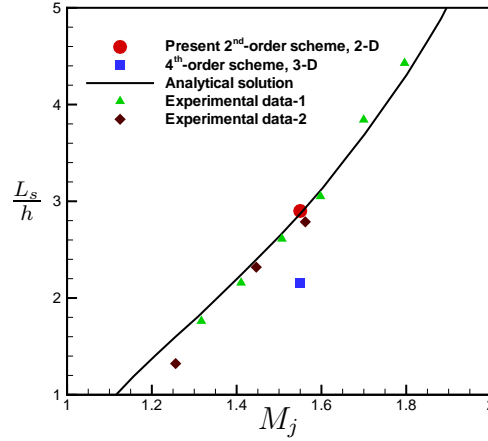
Figure 5.50: Shock–cell spacing (L_s/h) based on the fully expanded jet Mach number (M_j). 4th–order scheme (Berland et al, 2007), analytical solution (Tam, 1988), experimental data–1 (Panda et al., 1997), experimental data–2 (Raman and Rice, 1994)
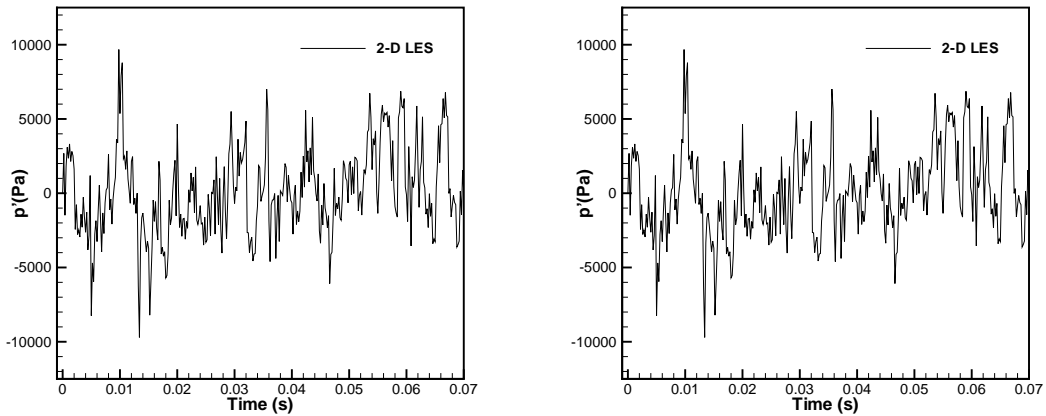
Figure 5.51: History of pressure fluctuations at P^+ (0.2h, 0.85h) *(left)* and P^- (0.2h, -0.85h) *(right)*
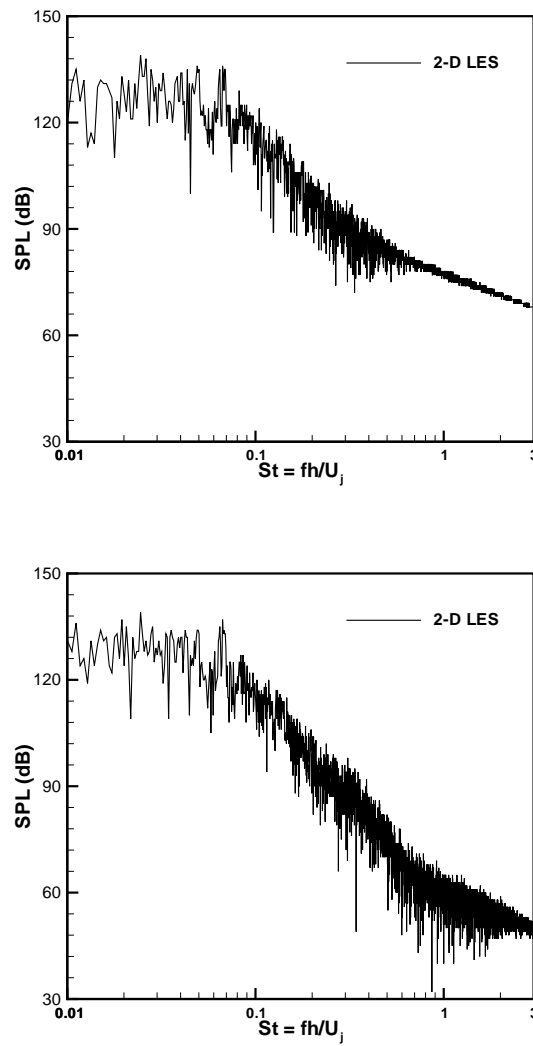
Figure 5.52: SPLs of pressure fluctuations as a function of Strouhal number at P^+ (0.2h, 0.85h) *(upper)* and P^- (0.2h, -0.85h) *(lower)*

Chapter 6

Applications and Results of the 3–D LES for Aeroacoustics

The two–dimensional Euler, Navier–Stokes and LES solvers are validated in the previous chapter. The present three–dimensional parallel LES solver is developed from its two–dimensional counterpart. In order to investigate its suitability to practically relevant acoustic problems, two challenging acoustic problems are considered here, namely, near–field cavity aeroacoustics (Section 6.1) and shock–induced noise by a planar underexpanded jet (Section 6.2). Their two–dimensional counterparts (the open cavity flow and the screech noise problem) are already investigated in Sections 5.3.2 and 5.3.3, respectively.

6.1 Near–Field Cavity Aeroacoustics

The 3–D parallel LES solver is used in order to predict narrowband and broadband flow noise in a rectangular cavity. Numerical investigations into the flow physics of the M219 cavity at Mach number of 0.85 were performed also by Mendonça et al. (2003), Allen and Mendonça (2004), Nayyar et al. (2005), Chen et al. (2007) and Caraeni et al. (2009). In Section 2.4, physical description of different mechanisms for generating cavity flow noise and a review of previous studies can be found. The results are compared with the LES results of high–order numerical schemes (Chen et al., 2007; Nayyar et al., 2005) and the experimental data (Peshkin,

2002; Henshaw, 2000) for the flow over the M219 cavity. The method proposed here provides the acoustic–resonance frequencies and the acoustic (natural) modes. This specific case was provided by AGARD (Henshaw, 2000) as a benchmark problem and experiments were carried out by QinetiQ as part of the project on Turbulence Modeling for Military Application Challenges (Peshkin, 2002). In Fig. 6.1, the test rig dimensions and the location of the Kulite transducers are displayed.
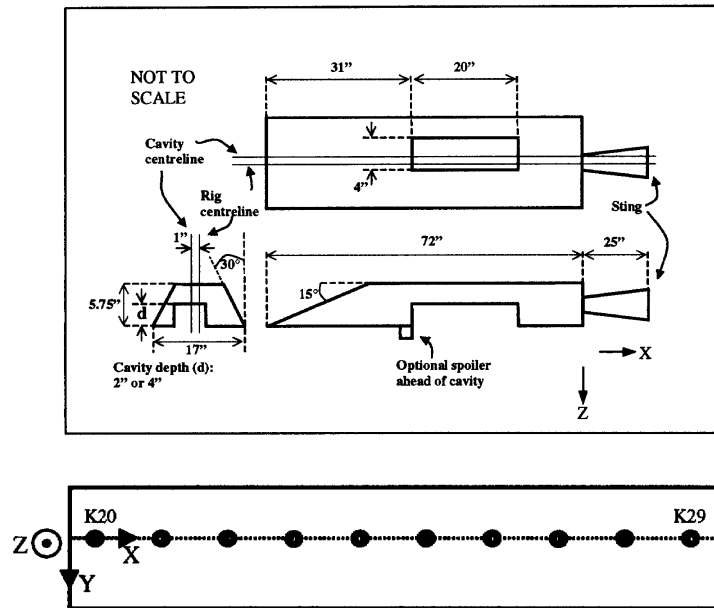
Figure 6.1: Test rig and dimensions including position of the pressure transducers (dimensions are in inches) (Henshaw, 2000)

The cavity geometry with a length–to–depth (L/D) ratio of 5 and a width–to–depth (W/D) ratio of 1 exhibiting flow in shear layer mode so called, since the separated shear layer at the cavity leading edge does not attach to the cavity floor. This geometry is taken from the M219 cavity configurations (Peshkin, 2002). Its length L is 508 mm, the width W and the depth D are equal to 101.6 mm. The dimensions of the computational domain are: $11D$ (streamwise) $\times 4D$ (wall–normal) $\times 2D$ (spanwise). The domain is decomposed into 64 subdomains for parallel computations, as shown in Fig. 6.2. The grid consists of $415 \times 130 \times 60 \approx 3.24 \times 10^6$ CVs above the cavity and $260 \times 80 \times 30 \approx 0.625 \times 10^6$ CVs inside the cavity. The distribution of mesh in the x–y (left) and y–z (right) planes are illustrated in Fig. 6.3.
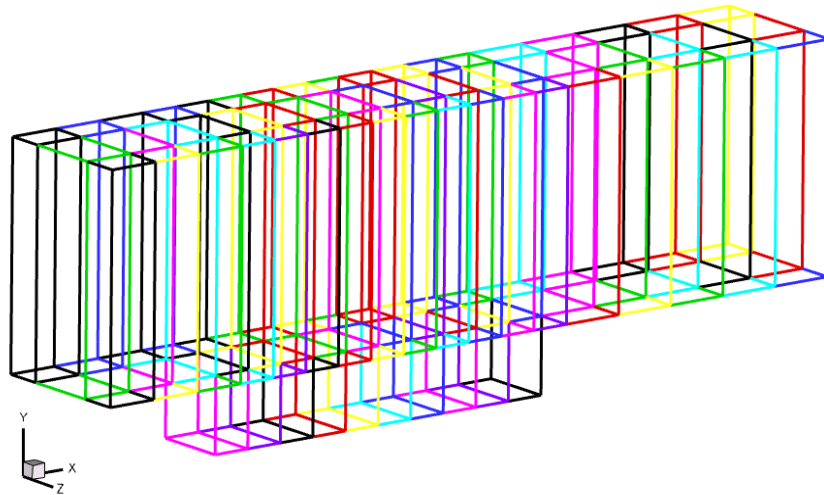
Figure 6.2: Decomposition of the M219 cavity domain into 64 subdomains
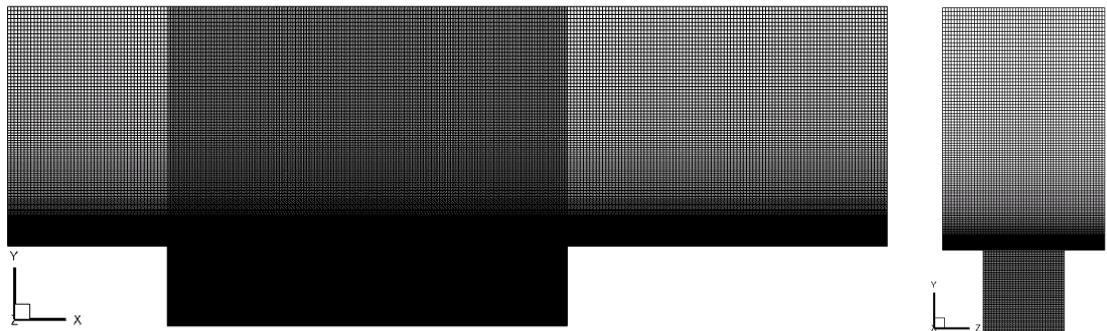
Figure 6.3: Mesh distribution in the x–y *(left)* and y–z *(right)* planes

A free–stream Mach number of 0.85, a Reynolds number of 1.36 million based on the cavity depth, the stagnation pressure of 99,600 Pa and the stagnation temperature of 305 K are imposed as inflow boundary condition and the spatial derivatives of the flow variables are taken as zero similar to the 2–D open cavity case (see Section 5.3.2). The inflow boundary is set to 2 times the cavity depth upstream of the cavity whereas the outflow (right–hand) boundary is set to 4 times the cavity depth downstream of the cavity. A steady turbulent boundary layer profile is implemented at the inflow to achieve an unsteady turbulent boundary at the leading edge of the cavity. Hence the boundary layer thickness at the leading edge of the cavity is 10.16 mm. In order to trigger cavity flow oscillations, unsteady 3–D disturbances are added. When the self–sustained oscillations inside the cavity started,

the perturbations are turned off again to prevent spectral analysis from unwanted numerical artifacts. The periodic boundary condition in spanwise and the no–slip boundary condition at the walls are imposed. The non–reflecting boundary condition (Type–II) is applied to the outflow (right) and far–field (upper) boundaries. The summary of the M219 cavity dimensions and the boundary conditions in 3D are shown in Fig. 6.4.
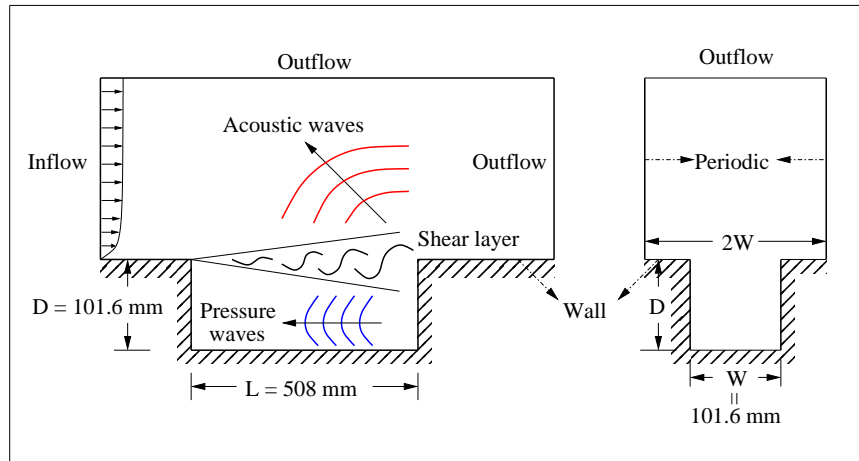
Figure 6.4: Schematic view of the M219 cavity dimensions and boundary conditions

Computed results are compared with those obtained by using a 4th–order central finite–difference scheme (Chen et al., 2007) and the numerical method based on a cell–centered finite–volume method where MUSCL interpolation is used to provide 3rd–order accuracy (Nayyar et al., 2005). For comparison, a wider computational domain, $15D$ (streamwise) $\times 7D$ (wall–normal) $\times 2D$ (spanwise), was used by Chen et al. (2007). The grid consists of $450 \times 150 \times 72 \approx 4.86 \times 10^6$ CVs above the cavity and $250 \times 80 \times 4 \approx 0.88 \times 10^6$ CVs inside the cavity (Chen et al., 2007) and finer grid consists of $\approx 8.4 \times 10^6$ CVs was used by Nayyar et al. (2005) for the LES of the M219 cavity.

In the present study, the simulation is carried out with a time step of $5.0 \times 10^{-7}s$ and the pressure signals are sampled every 330 time steps corresponding to a sampling rate of ≈ 6 kHz. The experimental signal is sampled at 6 kHz so the numerical results are sampled at the same rate for proper comparison. After the initial transients exited the computational domain, the simulation is carried out for

$0.25s$ and the first $0.05s$ of the pressure signals are truncated in order to discard the initial transient and to prevent the spectral analysis from unwanted numerical artifacts.

Fig. 6.5 represents a snapshot of the magnitude of the vorticity on the central plane of the domain *(upper)*. After the development of the shear layer, vortices break down before the middle of the cavity and grow larger in size whereas they propagate in the streamwise direction. This phenomenon can be observed also from the instantaneous iso–surfaces of the vorticity magnitude in Fig. 6.5 *(lower)*. Instantaneous magnitude of the vorticity contours at different positions in the streamwise and spanwise directions are displayed in Figs. 6.6 to 6.7.
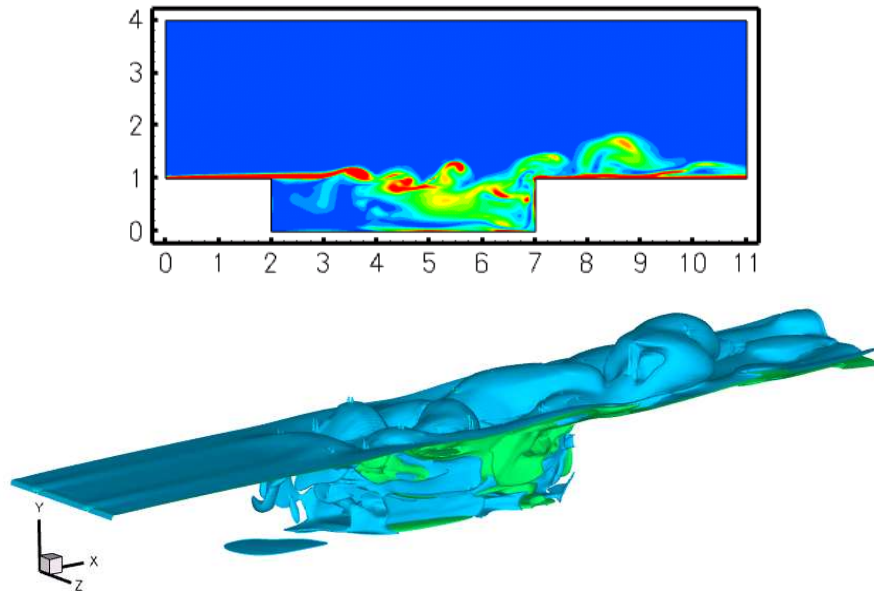
Figure 6.5: Instantaneous snapshot of the magnitude of the vorticity at $z/W = 0.5$ *(upper)* and iso–surfaces of the vorticity magnitude *(lower)*

Fig. 6.8 *(left)* represents the history of pressure fluctuations for a time interval of $0.2\ s$ at the K29 position. The noise spectrum of cavity contains both tonal noise due to the feedback loop and broadband noise, introduced by the turbulence in the shear layer. The computed pressure spectrum decomposed into Rossiter modes (low frequency tones) and broadband noise which are depicted in Fig. 6.8 *(right)*.

A comparison of modal frequencies, i.e. low frequency tones, at the Kulite location K29 is given in Table 6.1. The computed 1st mode frequency is slightly
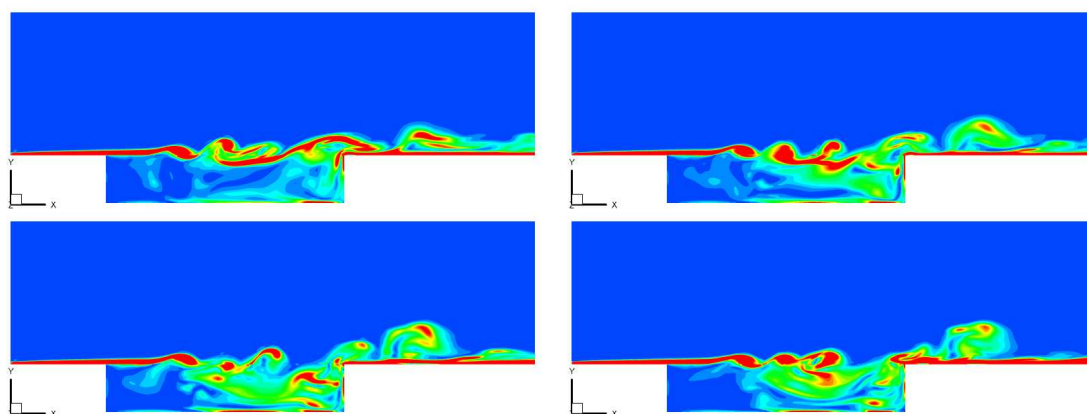
Figure 6.6: Instantaneous snapshot of vorticity contours at $z/W = 0.2$ *(upper left)*, $z/W = 0.4$ *(upper right)*, $z/W = 0.6$ *(lower left)* and $z/W = 0.8$ *(lower right)* in the spanwise direction
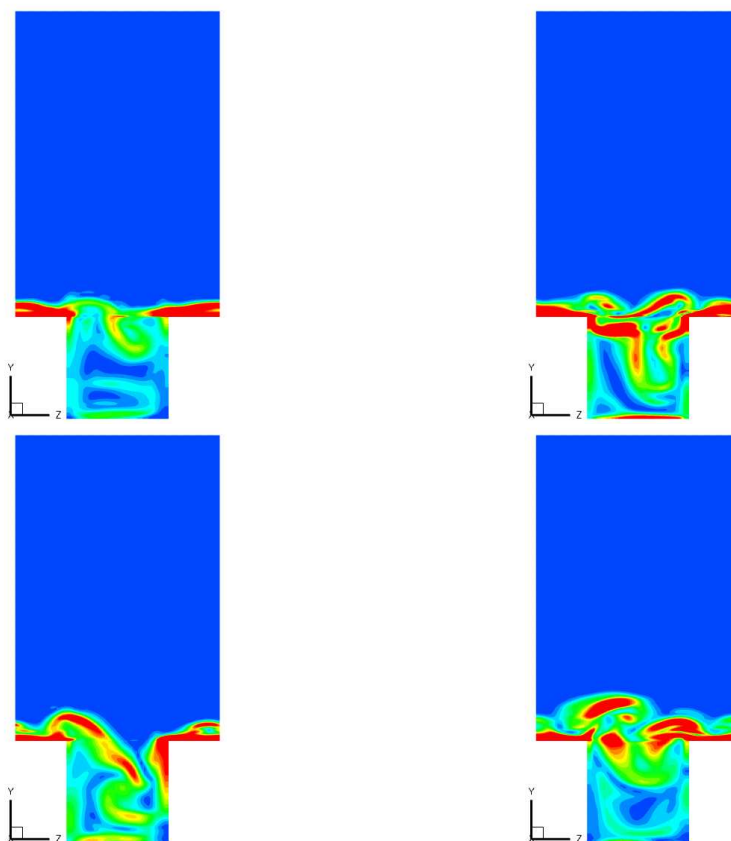
Figure 6.7: Instantaneous snapshot of vorticity contours at $x/L = 2$ *(upper left)*, $x/L = 3$ *(upper right)*, $x/L = 4$ *(lower left)* and $x/L = 4.9$ *(lower right)* in the streamwise direction
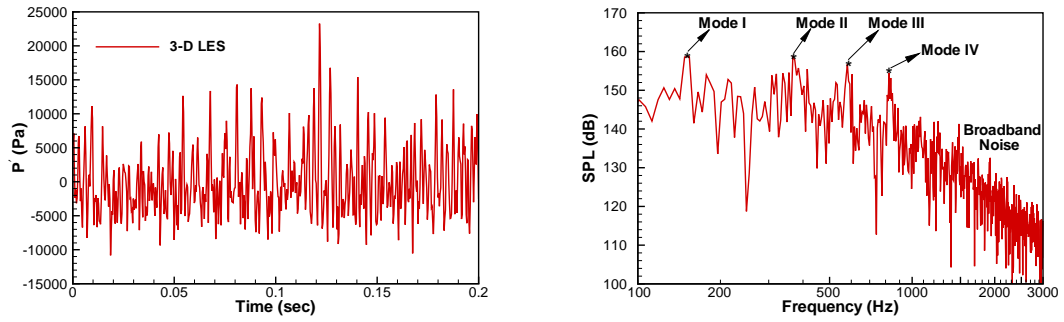
Figure 6.8: History of pressure fluctuations *(left)* and SPL spectrum *(right)* at K29

Table 6.1: Comparison of modal frequencies at K29

Mode	*I*	*II*	*III*	*IV*
Rossiter's Formula	159 Hz	371 Hz	582 Hz	794 Hz
Experiment (Peshkin, 2002)	151 Hz	370 Hz	605 Hz	773 Hz
4th–order Scheme (Chen et al., 2007)	131 Hz	332 Hz	553 Hz	794 Hz
Present 2nd–order Scheme	154 Hz	367 Hz	580 Hz	823 Hz

over–predicted compared to the experimental data with an error of about $+2\%$ whereas the 2nd and 3rd mode frequencies are under–predicted by about -1% and -4%, respectively. Lastly, the 4th mode frequency is over–predicted with an error of about $+6.5\%$. Consequently, all modal frequencies are well predicted and within 7% error in comparison to the experimental data. Rossiter's semi–empirical predictions of the modal frequencies (Rossiter, 1964) defined by

$$f_n = \frac{U_\infty}{L} \frac{n - \gamma}{M_\infty + \frac{1}{\kappa}} \qquad (6.1)$$

where U_∞ and M_∞ are the free–stream velocity and Mach number, respectively. L is the length of the cavity and n is the mode number. $\kappa = 0.57$ and $\gamma = 0.25$ are empirical constants corresponding to the average convection speed of the vortical perturbations in the shear layer and a phase delay, respectively.

In Fig. 6.9, the intensity of the noise generation inside the cavity can be seen from the comparison of SPL spectrum along the cavity floor with the measurements
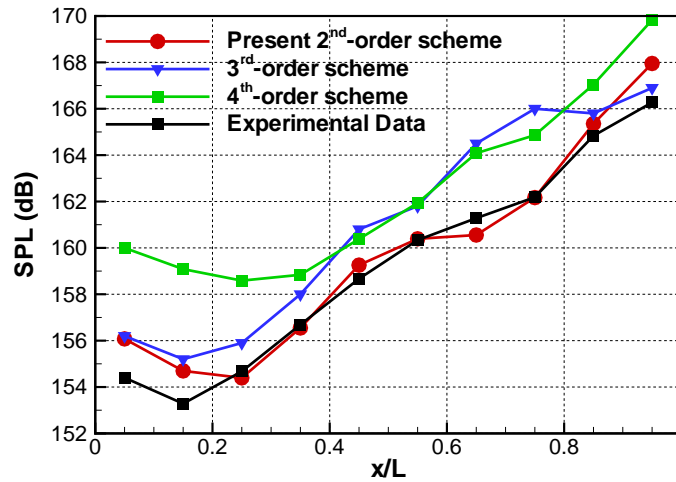
Figure 6.9: Comparison of SPL spectrum along the cavity floor (3rd–order scheme (Nayyar et al., 2005), 4th–order scheme (Chen et al., 2007))

as well as results of other numerical schemes available in the literature (Nayyar et al., 2005; Chen et al., 2007). Fig. 6.9 clearly shows that the SPL curve increases in streamwise direction in the cavity due to the spreading of the energy from the shear layer after it breaks down. The rear wall region experiences the most intensive pressure fluctuations due to the the frequent flow impingement. The computed SPLs by the present time–conservative scheme along the cavity floor are in very good agreement with the experimental data (Henshaw, 2000; Peshkin, 2002). Compared to other numerical results using either an LES technique on a finer grid ($\approx 8.4 \times 10^6$ CVs) (Nayyar et al., 2005) or the fourth–order accurate scheme (Chen et al., 2007) the deviations to the measurements are much smaller.

A significant discrepancy between 2–D LES results and the experimental data for the RMS values of pressure fluctuations are shown in Fig. 5.42. The prediction of 3–D LES solver is more accurate than its 2–D counterpart as shown in Fig. 6.10. The prediction of the RMS values of the pressure fluctuations along the cavity floor are in a very good agreement with the measurements.

In Figs. 6.11 to 6.19, the computed history of pressure fluctuations *(upper–left)* and the measurements *(upper–right)* are depicted for different Kulite locations K20 to K28 including the SPL spectrum *(lower–left)* as well as power spectral density against the Strouhal number *(lower–right)*.
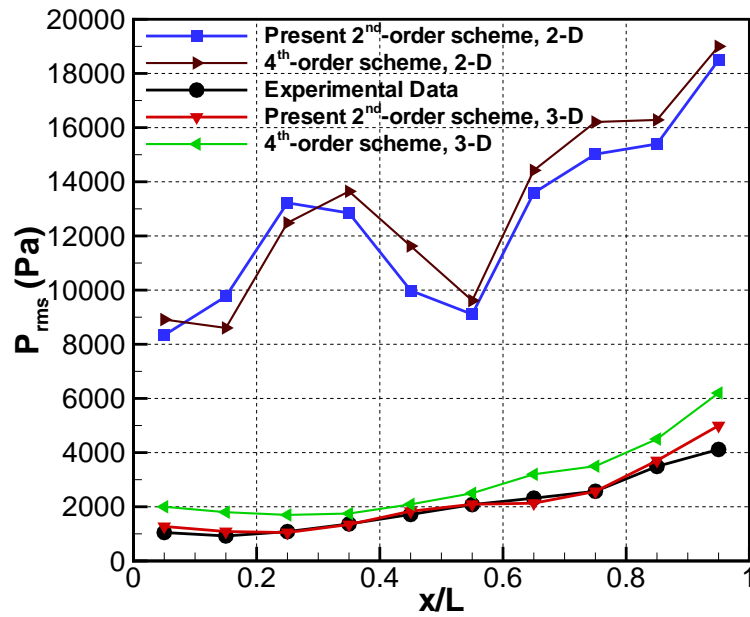
Figure 6.10: Comparison of RMS values of the pressure fluctuations along the cavity floor (4th–order scheme (Chen et al., 2007))
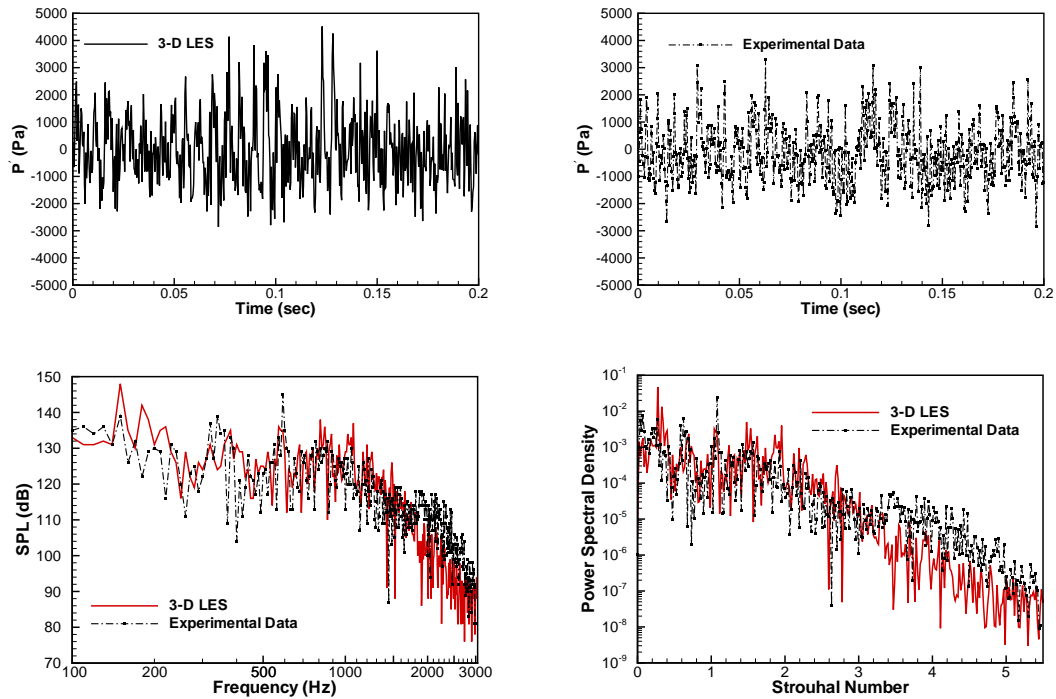
Figure 6.11: History of pressure fluctuations *(upper)* and spectral analysis *(lower)* at K20
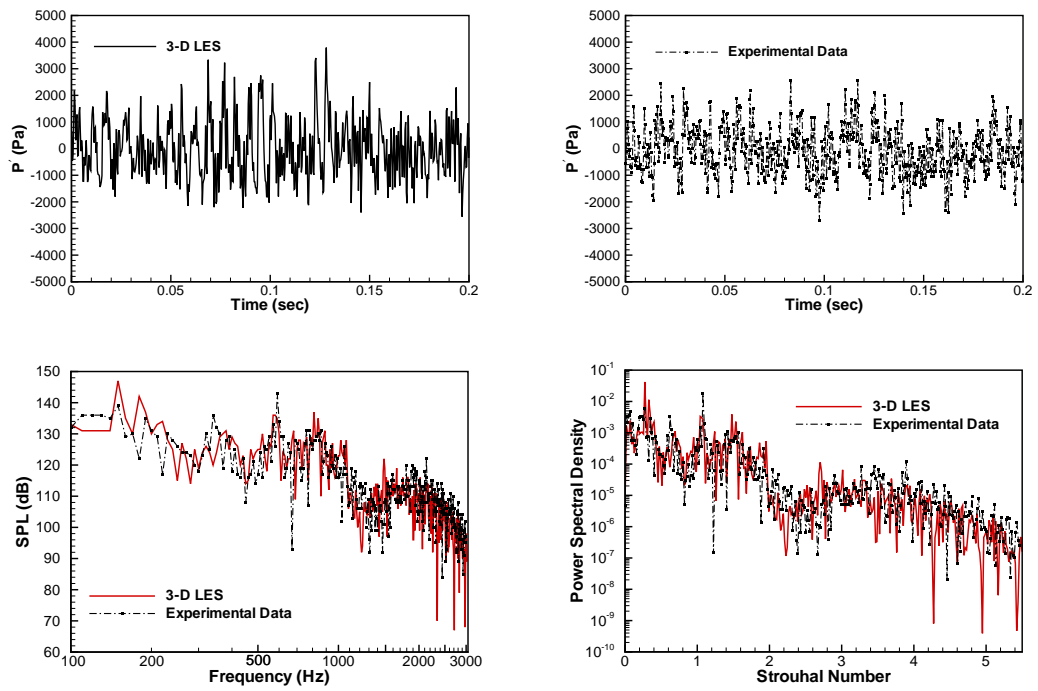
Figure 6.12: History of pressure fluctuations *(upper)* and spectral analysis *(lower)* at K21
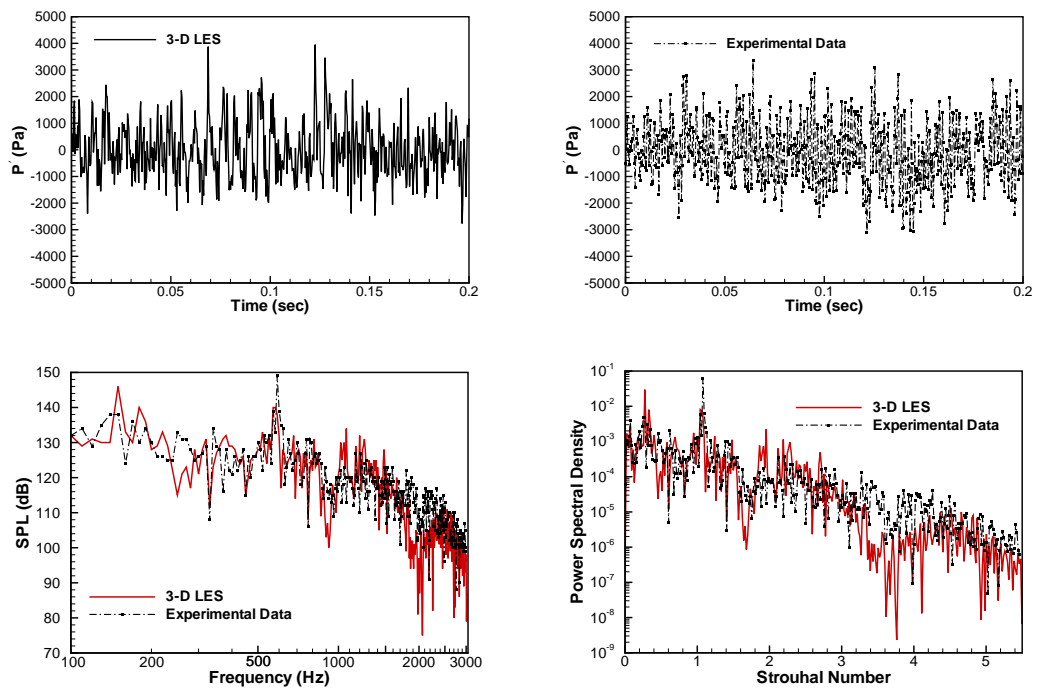
Figure 6.13: History of pressure fluctuations *(upper)* and spectral analysis *(lower)* at K22
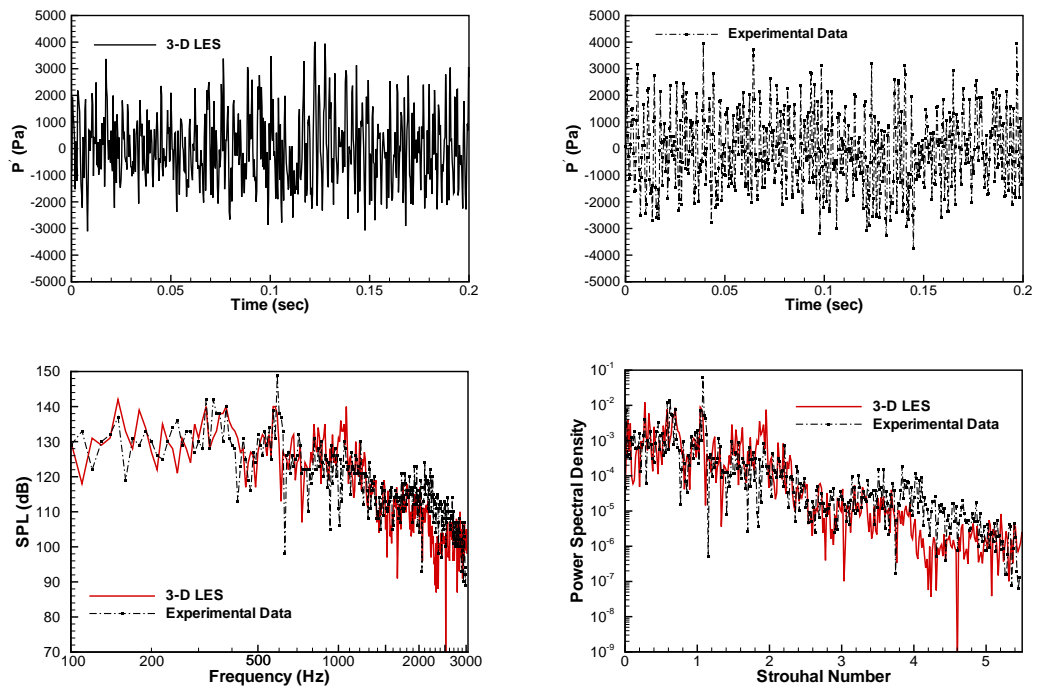
Figure 6.14: History of pressure fluctuations *(upper)* and spectral analysis *(lower)* at K23
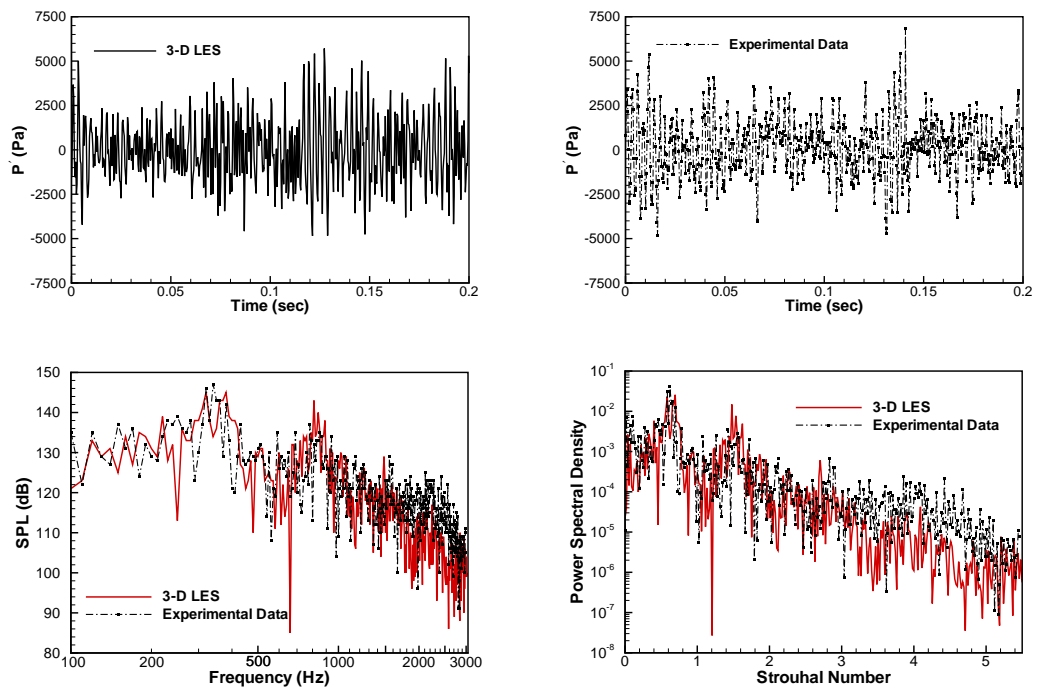
Figure 6.15: History of pressure fluctuations *(upper)* and spectral analysis *(lower)* at K24
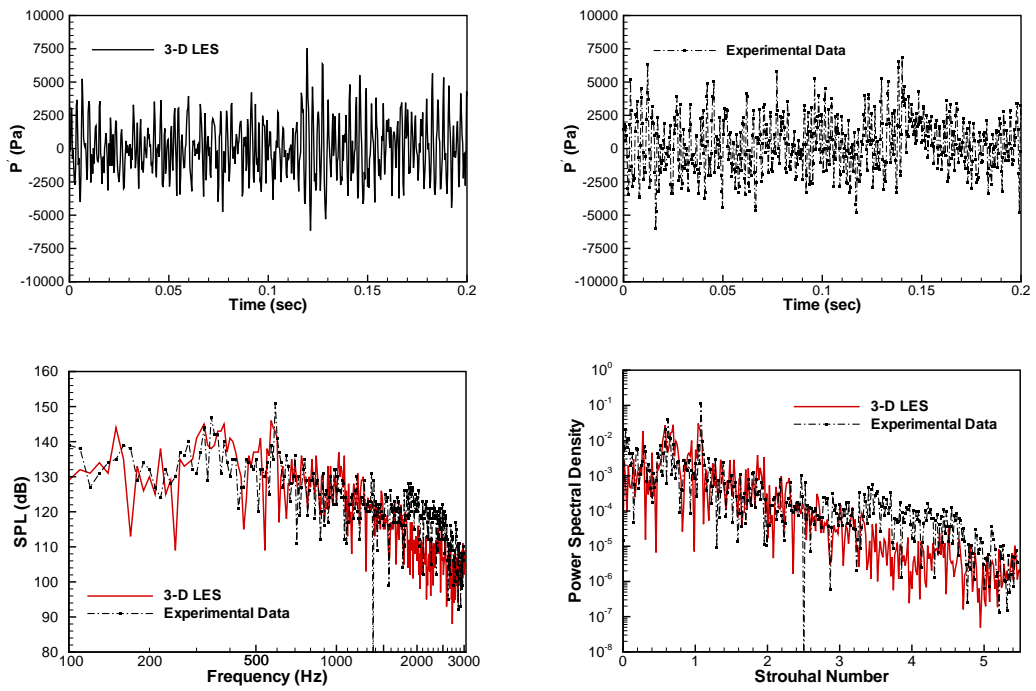
Figure 6.16: History of pressure fluctuations *(upper)* and spectral analysis *(lower)* at K25
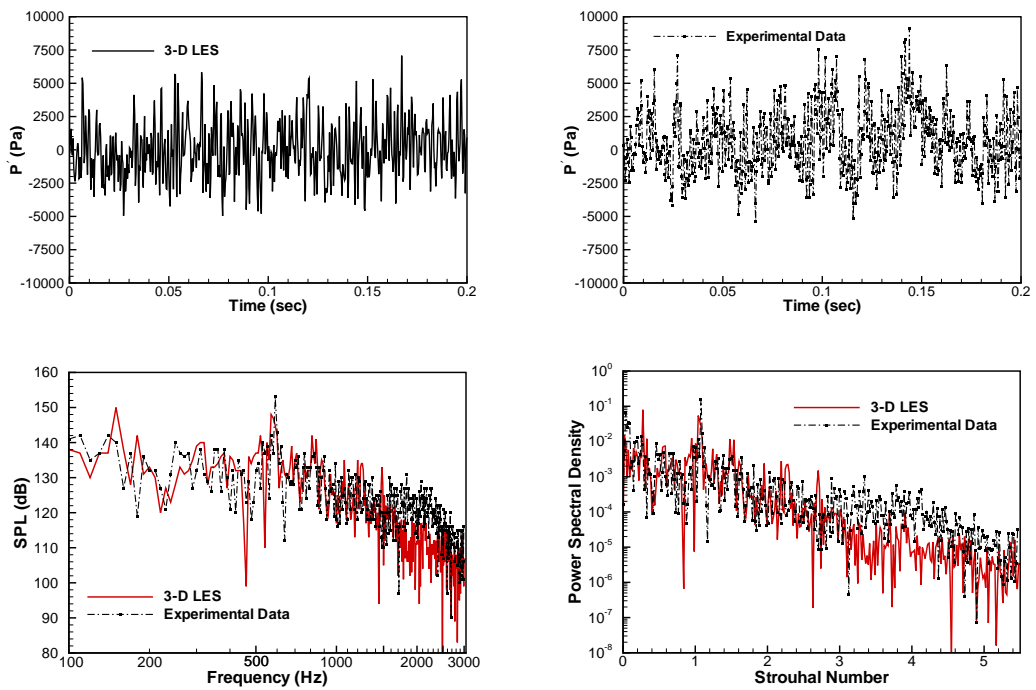
Figure 6.17: History of pressure fluctuations *(upper)* and spectral analysis *(lower)* at K26
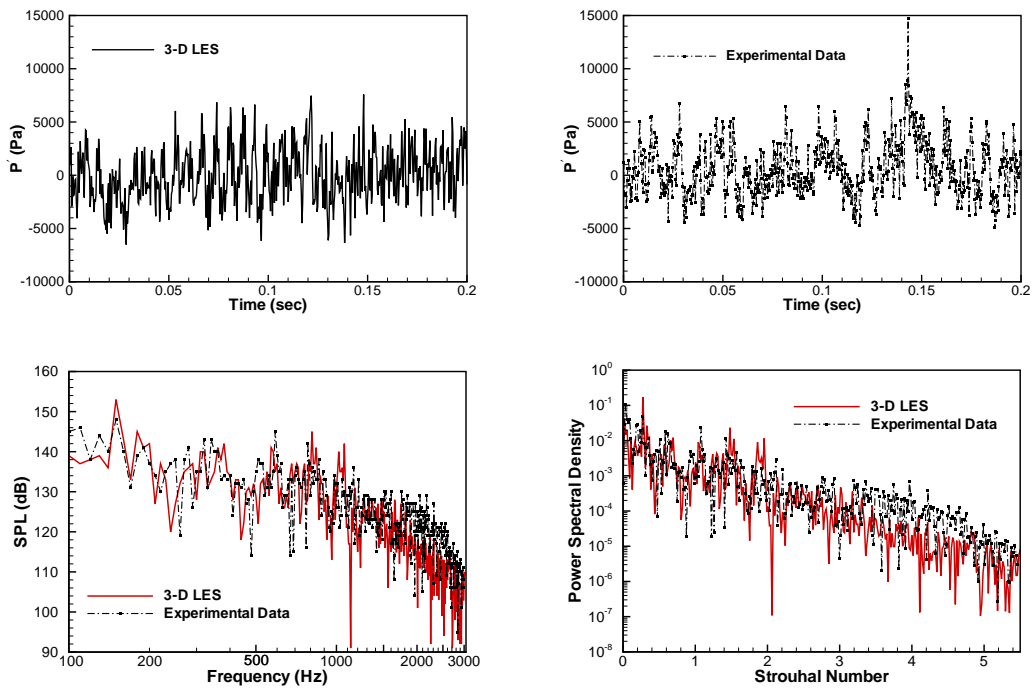
Figure 6.18: History of pressure fluctuations *(upper)* and spectral analysis *(lower)* at K27
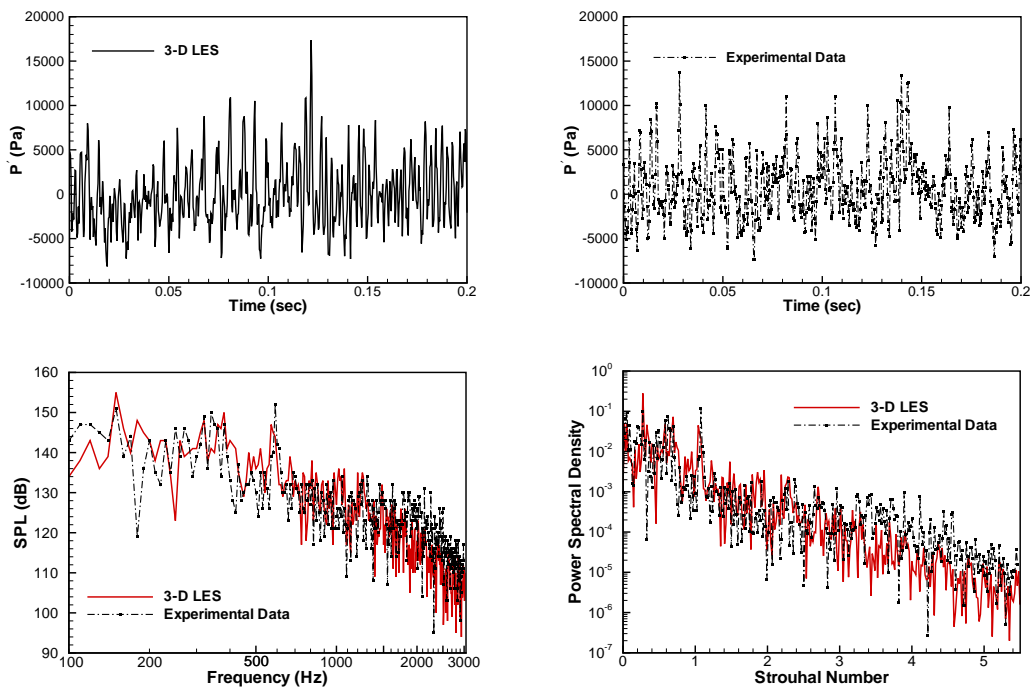
Figure 6.19: History of pressure fluctuations *(upper)* and spectral analysis *(lower)* at K28

Fig. 6.20 shows band–limited RMS pressures along the cavity floor. Band–limited RMS pressures reveal the contribution from each Rossiter mode to cavity noise in more detail. Each modal band is calculated by processing the PSD data. The LES solver captures all mode shapes very well, particularly the dominant second Rossiter mode, but over–predicts the weakest fourth mode.

In conclusion, the 3–D simulation of the open cavity flow is essential for the correct prediction of near acoustic field. The 3–D parallel LES solver is capable of successfully capturing the near–field flow features of the open cavity flow with high–accuracy.
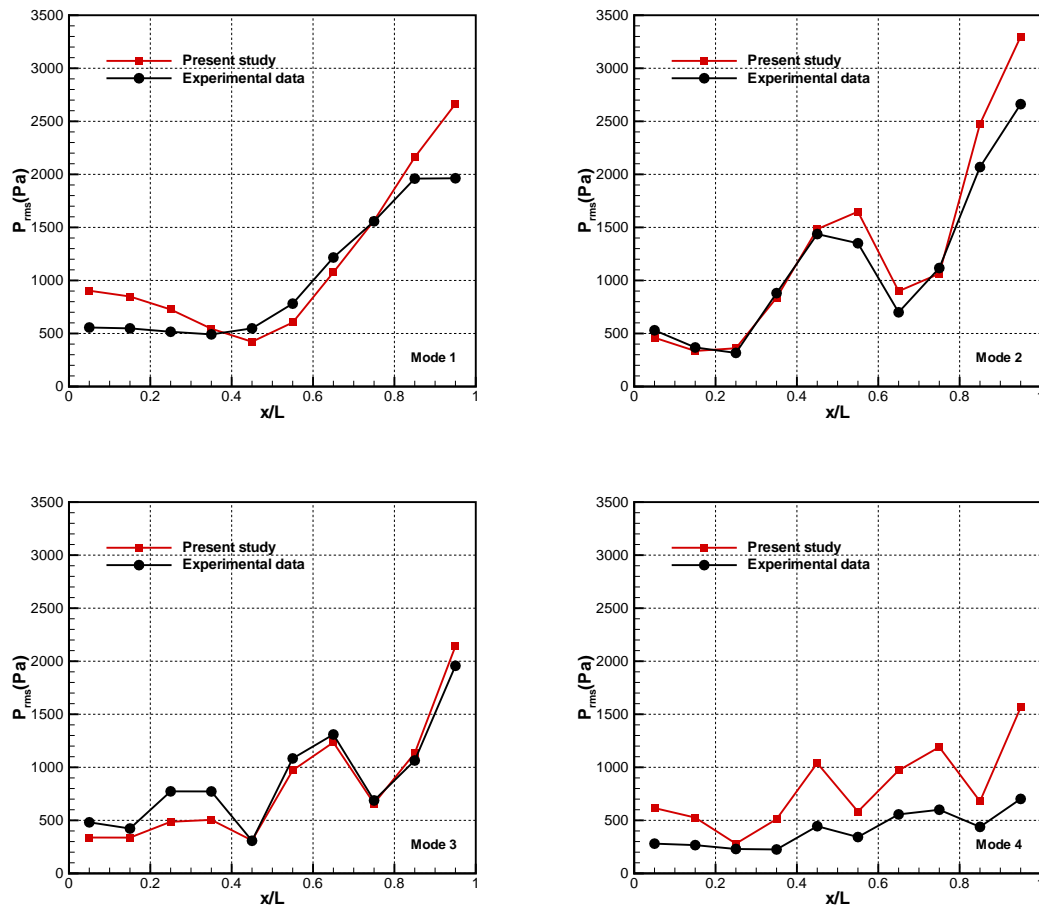
Figure 6.20: Band–limited RMS pressures along the cavity floor

6.2 Shock–Induced Noise by a Planar Underexpanded Jet

Shock–induced noise by a 3–D rectangular underexpanded jet is investigated using the present 3–D parallel LES solver and its 2–D counterpart is computed in Section 5.3.3. The streamwise growing instability waves naturally occurring in the jet shear layer interact with this shock–cell structure then generate broadband shock–associated noise and under certain operating conditions screech tones develop through a feedback loop. Details of the characteristics of this feedback loop and a review of previous studies are provided in Section 2.5. Numerical investigations of the screech noise at fully expanded Mach number were performed by Loh et al. (2000a), Loh et al. (2000b), Loh et al. (2001c) Loh and Hultgren (2002), Shen and Tam (2002), Rona and Zhang (2004), Berland et al (2007) and, Schulze et al. (2009). The 3–D screech generation in a planar supersonic jet problem studied here is similar to the one computed by Berland et al (2007). Three–dimensional LES results of the present scheme are compared with the results of high–order numerical scheme (Berland et al, 2007) and the experimental data (Raman and Rice, 1994; Panda et al., 1997) as well as the analytical solution of (Tam, 1988).
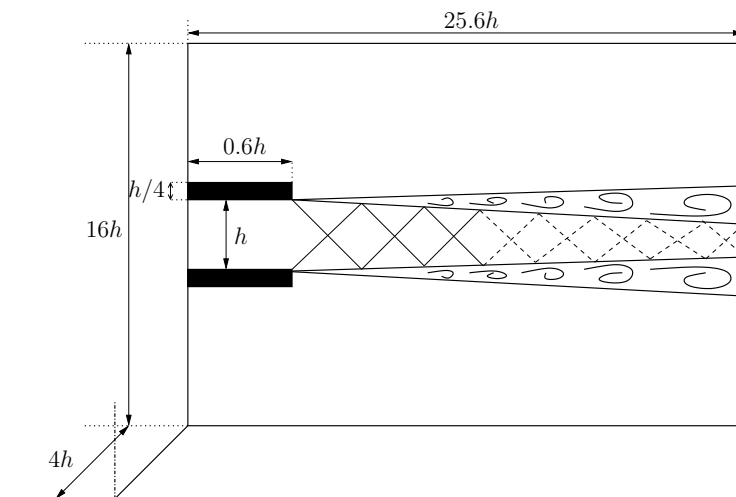
Figure 6.21: Schematic view of the computational domain for the three–dimensional screech noise problem

In Fig 6.21, the schematic of the computational domain is displayed. The jet height (h) is 3 mm and the nozzle lip thickness is $h_l = h/4$ similar to that used in the experiments of Raman and Rice (1994). The dimensions of the computational domain are: $25.6h$ (streamwise) $\times 16h$ (wall–normal) $\times 4h$ (spanwise), with a nozzle extending over $0.6\ h$ inside the domain, as shown in Fig. 6.21. A Cartesian grid consists of $520 \times 260 \times 50 \approx 6.76 \times 10^6$ CVs. The smallest mesh size $\Delta_m = h/40$ allows to use 40 grid points within the jet height and approximately ten grid nodes inside the boundary layer (same as the 2-D case). The distribution of mesh in the x–y and y–z planes are illustrated in Fig. 6.22. The physical domain is decomposed into 124 subdomains for parallel computations, as shown in Fig. 6.23.
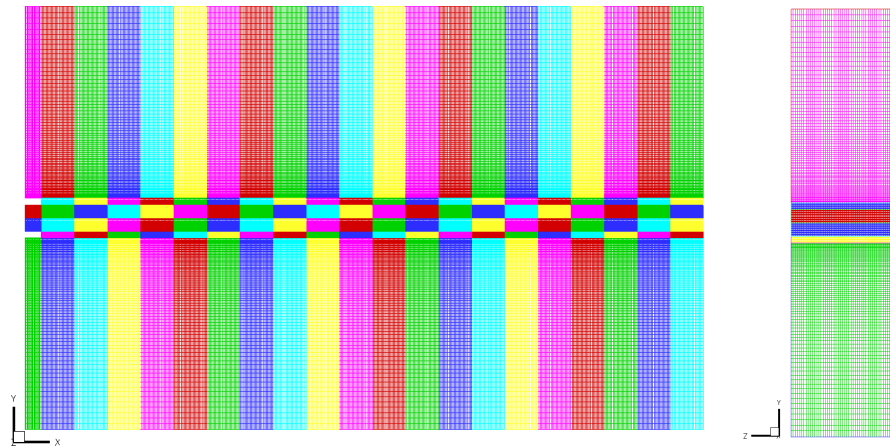
Figure 6.22: Mesh distribution in the x–y *(left)* and y–z *(right)* planes
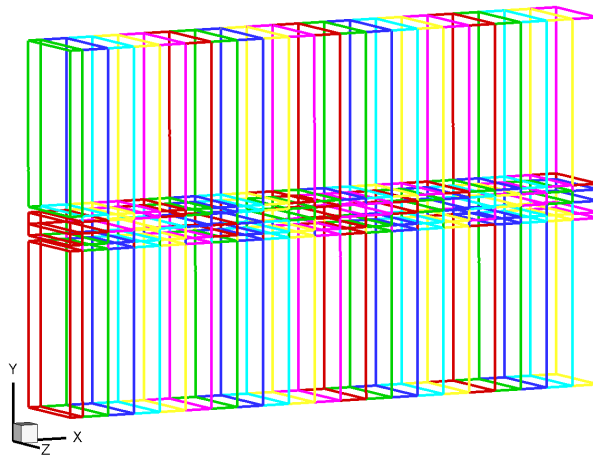
Figure 6.23: 124 subdomains used for the 3–D rectangular underexpanded jet problem

PSfrag
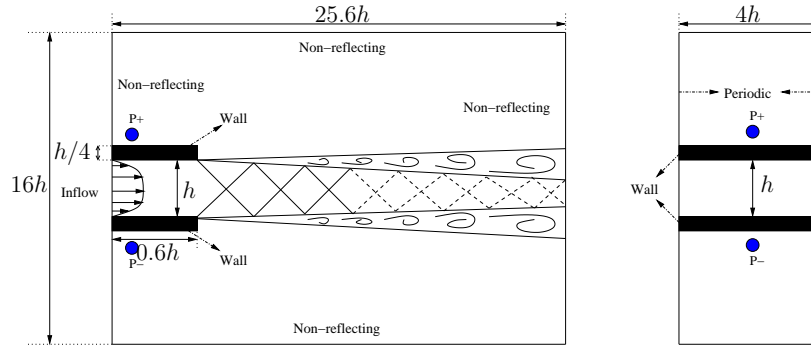
Figure 6.24: Schematic view of the 3–D planar underexpanded jet dimensions and boundary conditions

Boundary layer profiles based on the laminar Blasius solution, eq. (5.18), and the inflow density profile using the Crocco–Busemann relation, eq. (5.19), are already provided in Section 5.3.3. These conditions are imposed at the inlet between the nozzle lips. A Reynolds number of 6×10^4 based on the jet height and velocity. The no–slip wall boundary condition is imposed only at the inner section of nozzle lips. The periodic boundary condition is used in spanwise. The non–reflecting boundary condition (Type–I) is applied to the far–field (left–hand, upper and lower boundaries) and the non–reflecting boundary condition (Type–II) is imposed at the outlet owing to the substantial gradients in the y and z–directions. The schematic view of the 3–D planar underexpanded jet dimensions and the boundary conditions are shown in Fig. 6.24.

The present simulation results are compared with those obtained by using the 4th–order finite–difference scheme (Berland et al, 2007). For comparison, a computational domain, $25.6h$ (streamwise) $\times 16h$ (wall–normal) $\times 5h$ (spanwise), was used by Berland et al (2007). The grid consists of $525 \times 257 \times 121 \approx 16.3 \times 10^6$ points.

An instantaneous snapshot of the streamwise velocity *(upper)* and the distribution of mean streamwise velocity *(lower)* in the whole computational domain are displayed in Fig. 6.25. In the jet plume, four shock–cell structures are apparent for $x/h < 10$ then these shock–cells are breaking down, as shown in Fig. 6.25 *(upper)*. In Fig. 6.25 *(lower)*, five shock–cell structures exhibiting the distinctive bow–shaped structure are clearly visible in the jet plume ($x/h < 12$) for the computed mean streamwise velocity due to the overpressure at the nozzle exit. The streamwise

velocity decreases and a weakening of the shock strength in the downstream direction can be observed in Fig. 6.25 as well. Similar flow field features are observed by Berland et al (2007) and the 2–D counterpart of this simulation. A snapshot of the numerical Schlieren (density gradient modulus) *(left)* and the distribution of computed mean density gradient *(right)* are depicted in Fig. 6.26. The shock–cell structures in the jet plume can be seen clearly in these figures also. Instantaneous snapshots of the vorticity magnitude at different locations in the spanwise direction are shown in Fig. 6.27. Similarly, snapshots of spanwise vorticity iso–surfaces at different time steps are depicted in Figs. 6.28 to 6.30. A large range of turbulence scales can be observed in these figures.

Comparison of the normalized mean streamwise velocity with the 3–D LES result obtained by Berland et al (2007) using $\approx$ 16.3 million grid points *(lower)* is displayed in Fig. 6.31. The shock–cell spacing (L_s/h) is in a very good agreement with the experimental data and the analytical solution of Tam (1988), as shown in Fig. 6.32. The pressure signals are sampled at the upstream location (0.2h, 0.85h, 2h) and (0.2h, -0.85h, 2h) represented by points P^+ and P^- in Fig. 6.24, respectively. The 3–D LES is performed for 0.0275 s with a time step of $5.0 \times 10^{-8}s$. The first 0.0075 s of the pressure signals are truncated to prevent the spectral analysis from unwanted numerical artifacts. The time evolution of the pressure fluctuations close to the nozzle lip and SPLs of pressure perturbations as a function of Strouhal number are shown in Figs. 6.33 and 6.34, respectively. The dominant screech tone is observed at $St = 0.138$ and subharmonics of the screech tone are predicted also (see Fig. 6.34). The Strouhal number of the screech tone as a function of the fully expanded jet Mach number is displayed in Fig. 6.35. The computed Strouhal number of the fundamental discrete frequency is slightly over–predicted in comparison to experimental and analytical results. As a result, three basic components of a supersonic jet, namely, the turbulent mixing noise, the screech tones and the broadband shock–associated noise are predicted very well. The 3–D parallel LES solver is capable of successfully capturing the upstream acoustic field of underexpanded rectangular jet and the shock–cell structure in the jet plume with high–fidelity.
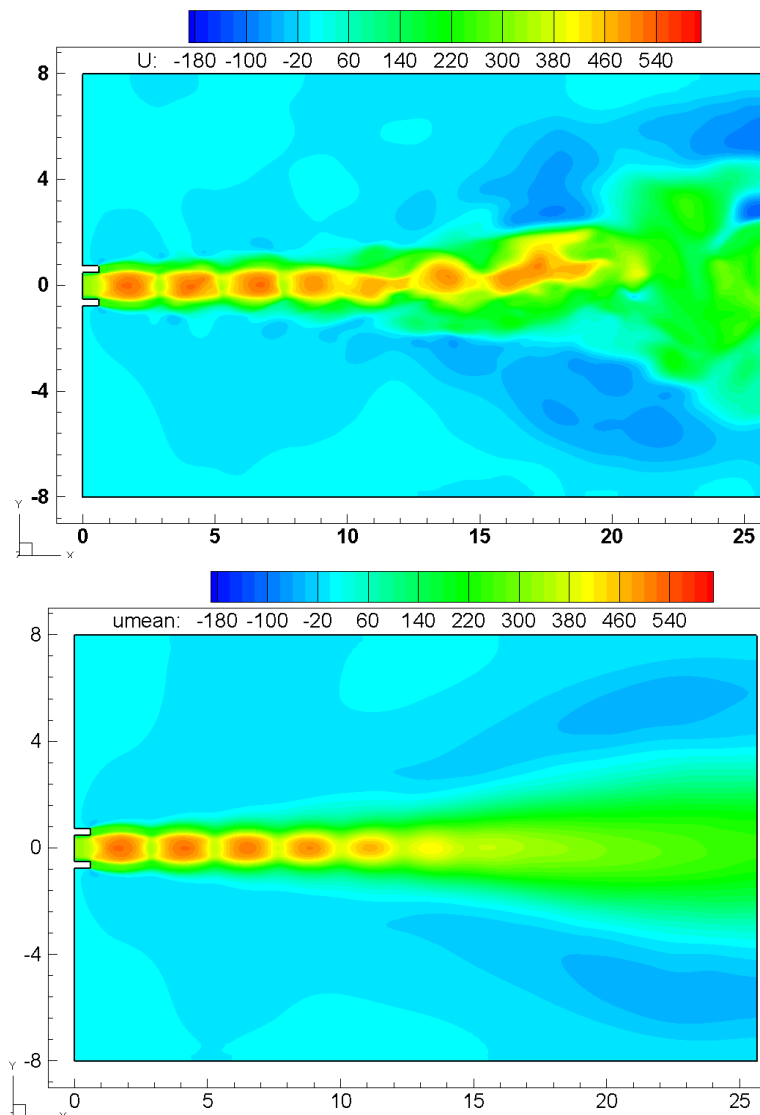
Figure 6.25: Instantaneous snapshot of streamwise velocity and mean streamwise velocity contours
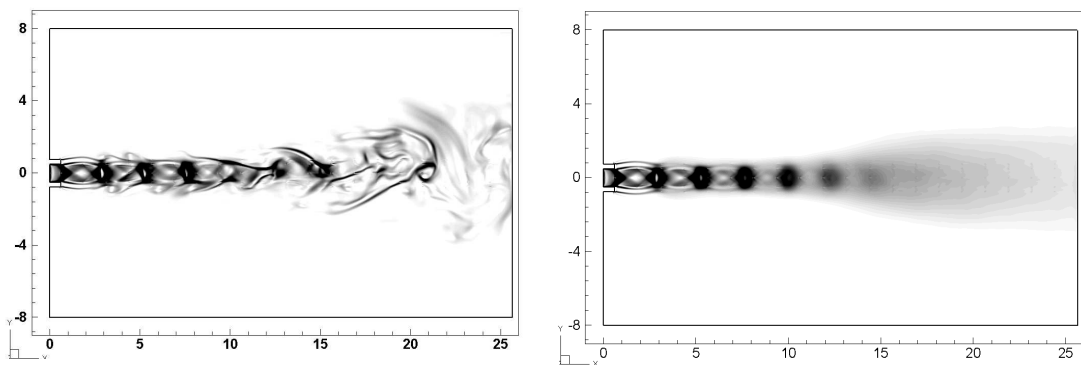
Figure 6.26: Instantaneous snaphot of density gradient and mean density gradient
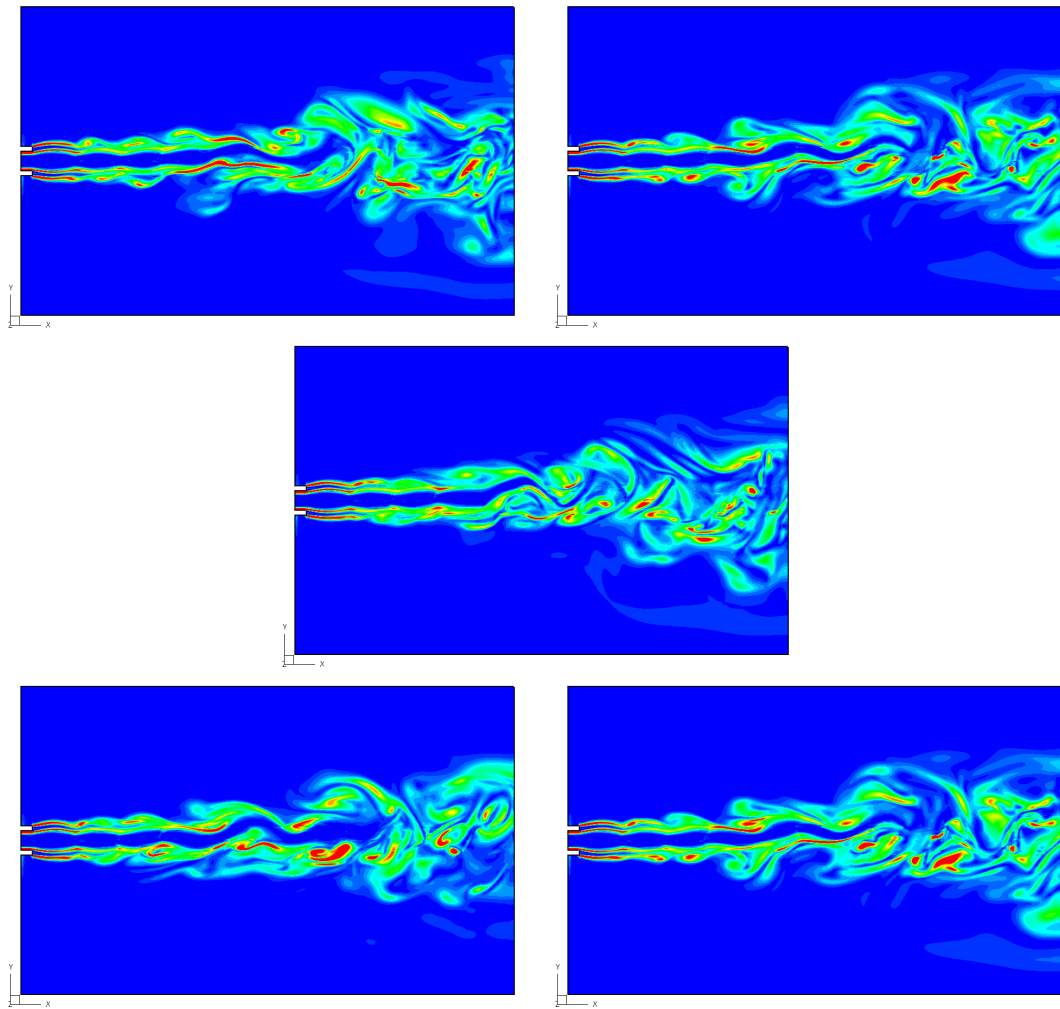
Figure 6.27: Instantaneous snapshots of vorticity magnitude at $z/h = -2$ *(upper left)*, $z/h = -1$ *(upper right)*, $z/h = 0$ *(middle)*, $z/h = 1$ *(lower left)*, $z/h = 2$ *(lower right)*
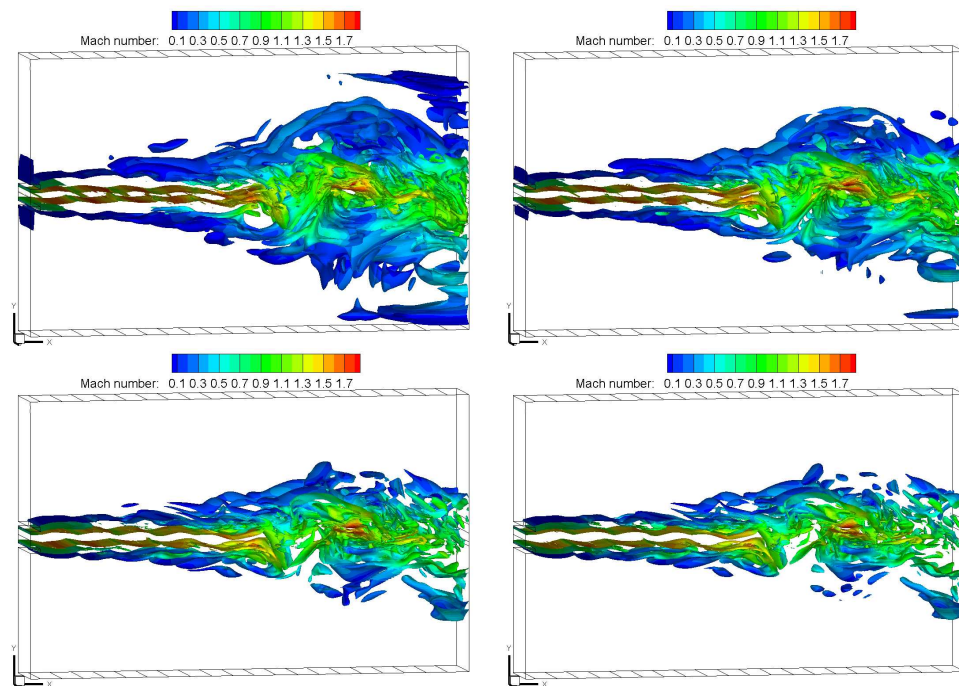
Figure 6.28: Iso–surfaces of spanwise vorticity colored by Mach number at $t = 0.01s$
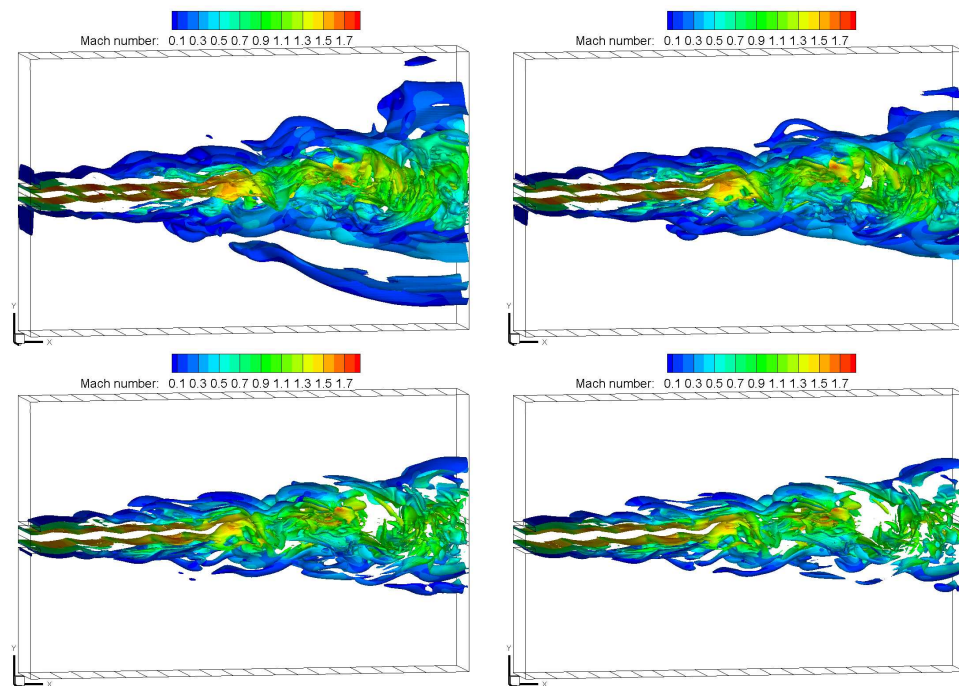
Figure 6.29: Iso–surfaces of spanwise vorticity colored by Mach number at $t = 0.02s$
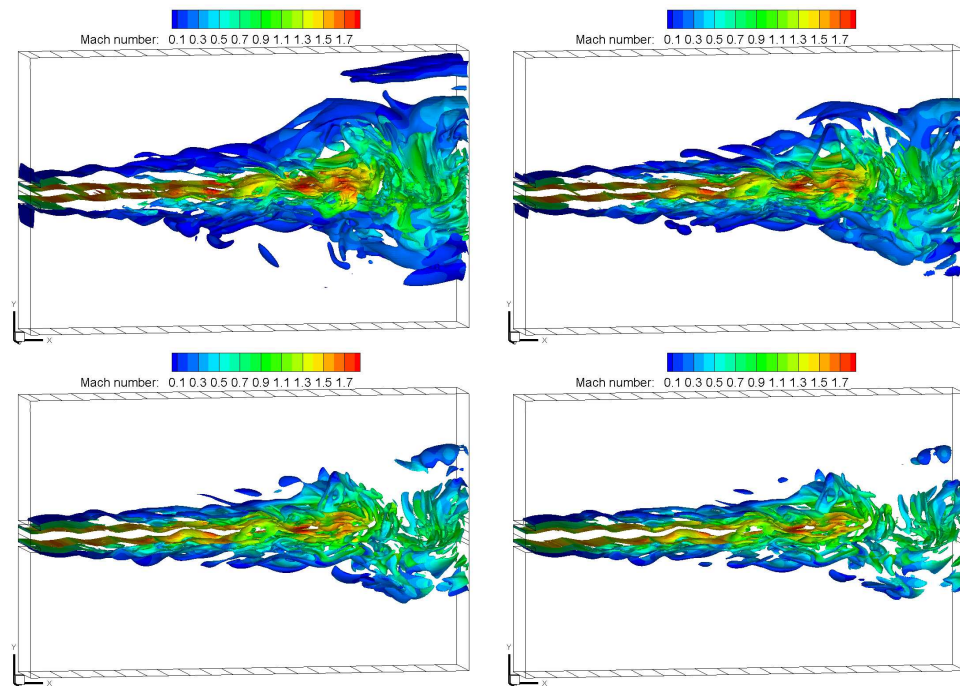
Figure 6.30: Iso–surfaces of spanwise vorticity colored by Mach number at $t = 0.0275s$
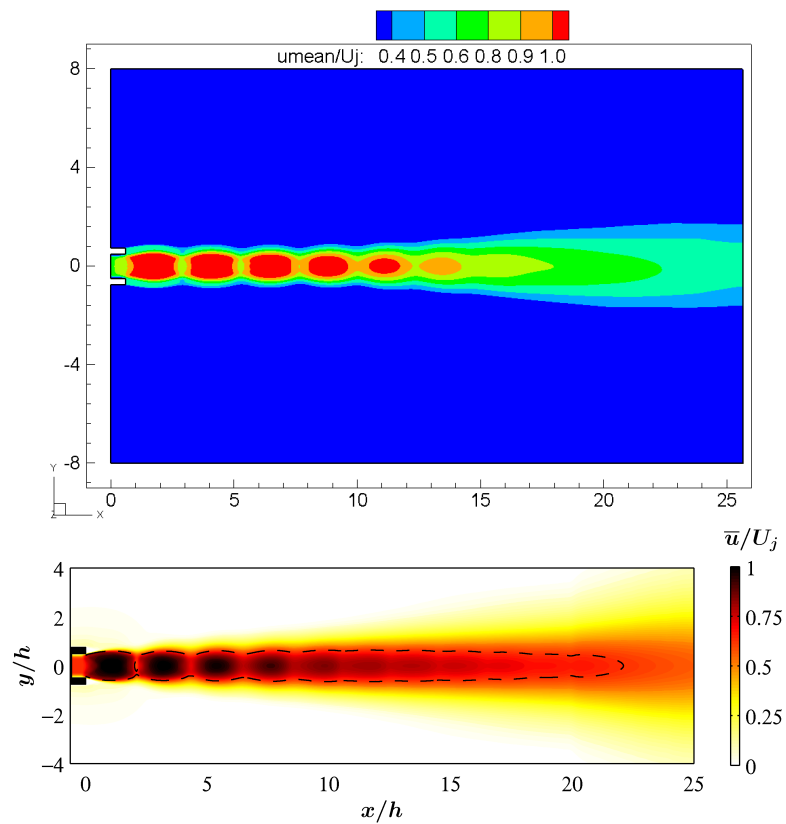
Figure 6.31: Distribution of mean streamwise velocity present study *(upper)* and Berland et al (2007) *(lower)*
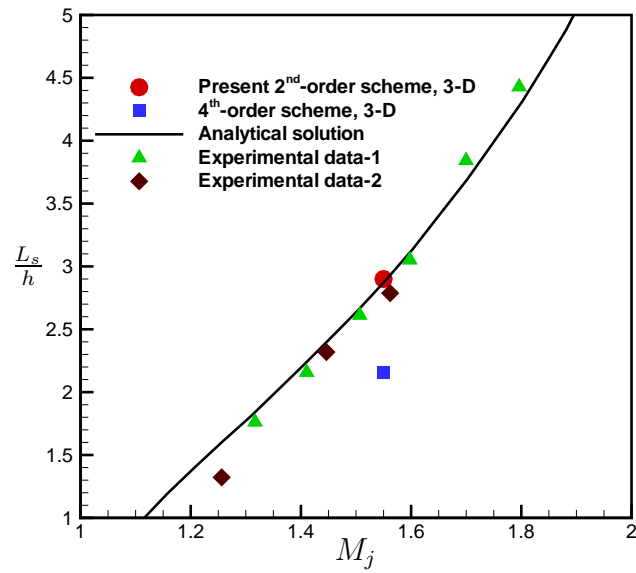
Figure 6.32: Shock–cell spacing
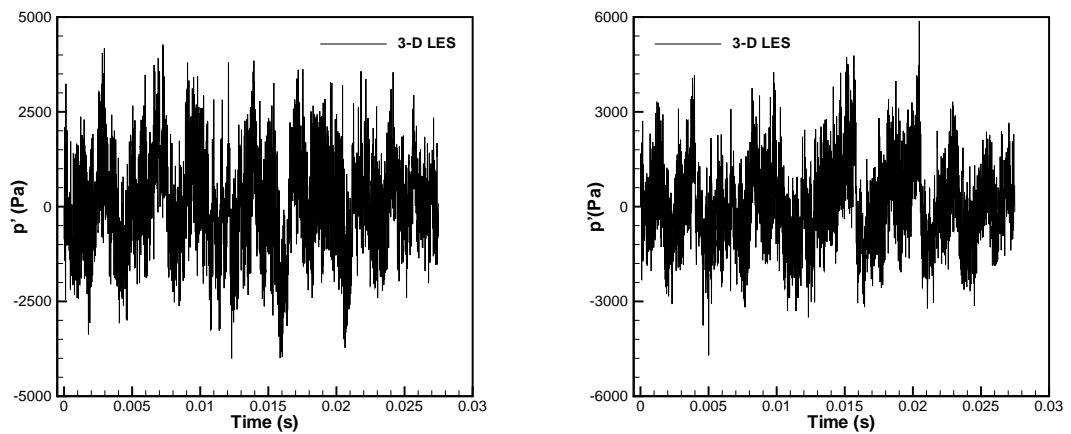
Figure 6.33: History of pressure fluctuations at P^+ (0.2h, 0.85h, 2h) *(left)* and P^- (0.2h, -0.85h, 2h) *(right)*
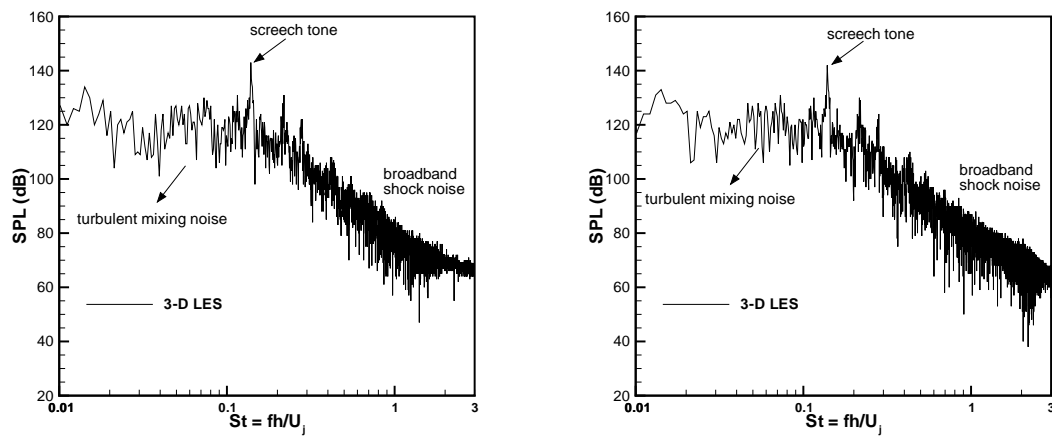
Figure 6.34: SPLs of pressure fluctuations as a function of Strouhal number at P^+ (0.2h, 0.85h, 2h) *(left)* and P^- (0.2h, -0.85h, 2h) *(right)*
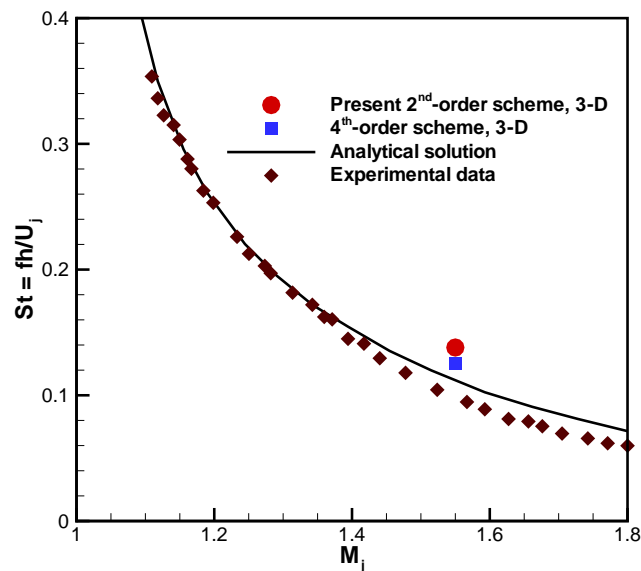
Figure 6.35: Strouhal number of the screech tone against the fully expanded jet Mach number. 4th–order scheme (Berland et al, 2007), analytical solution (Tam, 1988), experimental data (Panda et al., 1997)

Chapter 7

Conclusions and Recommendations for Future Work

7.1   Conclusions

The main research objectives have been successfully accomplished. One is the successful development of the advanced, high–resolution and low dissipation second–order numerical scheme based on the time–conservative finite–volume approach. Other aims are the implementation of the large–eddy simulation technique to directly predict the near acoustic field and to simulate the turbulent flows with high–fidelity as well as similar accuracy as higher–order schemes.

The 3–D parallel LES solver is developed from scratch by the author. The present solver is used to carry out near–field acoustic simulations and to investigate technically relevant aeroacoustic problems. The two–dimensional Euler solver is developed first, based on the new definitions of cell interface and control volume. The objectives of these new definitions were twofold: to ensure the flux conservation in the vicinity of the domain boundaries and to simplify the implementation of the multiblock technique in order to deal with complex geometries and to split up the computational domain by means of domain decomposition for parallel computing. The evaluation of fluxes along the boundaries is simplified and the flux conservation

is ensured by the new definitions of control volume and cell interface, which is the first of the kind in literature, to the best knowledge of the author.

Three inviscid flow cases are solved to validate and to verify the accuracy of the Euler solver. The first case is the shock reflection on a flat plate. Here, the accuracy and the shock–capturing capabilities of the solver are illustrated. The results are found to be in a very good agreement with the analytical solution. The resolution of the reflected shock is found to be identical to that of the incident shock with no oscillation near the shocks. The second inviscid flow case is the shock capturing case for a convergent–divergent nozzle. A normal shock wave is formed somewhere in the divergent section of the nozzle due to a certain exit pressure value. The location of the normal shock in the divergent section of the nozzle and the steady–state flow field features along the convergent–divergent nozzle are predicted accurately. The last case is attempted to demonstrate the ultimate shock–capturing capability of the time–conservative finite–volume scheme. The computation of a supersonic flow over a forward–facing step is carried out without using any kind of ad hoc techniques (i.e., special numerical treatment) particularly at the corner of the step. Formation of the expansion fan at the step corner and the Mach stem on the lower wall as well as the interaction between the reflected shock with rarefaction waves are presented with an excellent agreement in comparison to high–resolution results.

In order to perform viscous laminar flow simulations, the Navier–Stokes solver is developed by extending the Euler solver. The standard validation cases for a Navier–Stokes solver are carried out. The laminar boundary layer development along a flat plate is considered first, due to its simple geometry and the availability of an analytical solution, obtained by solving the Blasius equation. The lid driven cavity flow is used as a second validation benchmark case for the Navier–Stokes solver. In order to accelerate the convergence rate of the Navier–Stokes solver, the direct–flux based multigrid method is implemented. To the best knowledge of the author, the implementation of this flux based multigrid technique into the time–conservative finite–volume method is carried out for the first time in the present study. The accuracy of the Navier–Stokes solver including the discretization of the viscous fluxes as well as the implementation of the multigrid method are validated

successfully by solving these benchmark problems.

The large–eddy simulation (LES) technique is implemented in order to simulate the turbulent flow field features and to predict the near–field aerodynamic noise. The subgrid–scale turbulent fluctuations approximated by the Smagorinsky subgrid–scale (SGS) model. The growth of the small scales in the near–wall regions is reduced by using Van Driest damping function. A two–dimensional spatially evolving mixing layer problem, an open cavity flow and the generation of screech tones in an underexpanded jet are investigated by using the 2–D parallel LES solver. The results are found in reasonably good agreement with the other well–established results. On the other hand, large deviations are observed compared to the available experimental data due to the three–dimensional nature of these problems. The 2–D parallel LES solver is incapable of successfully capturing the near–field flow features. Therefore, 3–D simulations of the open cavity flow and the screech tones in an underexpanded jet are carried out using the 3–D parallel LES solver. In order to reduce the cost of the practical acoustic calculations, the 3–D LES solver as well as the 2–D counterpart are parallelized by domain decomposition with explicit message passing via MPI.

The prediction of narrowband and broadband flow noise in a rectangular cavity is performed by using the 3–D parallel LES solver. The results are compared with those obtained by high–order numerical schemes as well as with the experimental data. The computed Rossiter modes, i.e. low frequency tones, and broadband noise results are found to be in very good agreement with the measurements. In comparison to other numerical results obtained by using the high–order schemes, the deviations to the experimental data are much smaller in the present study. The generation of screech tones in an underexpanded jet due to the interaction of flow instabilities originate from the nozzle lip with the quasi–periodic shock–cell structure in the jet plume are investigated in order to demonstrate the capability of the time–conservative finite–volume approach resolving strong shocks and small disturbances (e.g., acoustic pressure fluctuations) simultaneously. The turbulent mixing noise, the screech noise with subharmonic tones and the broadband shock–associated noise with a set of closely related frequencies are accurately predicted by

using the 3–D parallel LES solver. The shock–cell structures in the jet plume are demonstrated with high–resolution and the results are found to be in a very good agreement in comparison to those obtained by the high–order numerical scheme and the available experimental data as well as the analytical solution.

The present method is efficient and yields high–resolution, low dissipation results similar to those of high–order numerical schemes. The time–conservative finite–volume method offers an accurate way to compute the most relevant frequencies and acoustic modes for aeroacoustic calculations. The proposed time–conservative method can meet future engineering simulation challenges reliably with its unique and non–traditional features. The second–order time–conservative finite–volume method can accurately solve practically relevant aeroacoustic problems with high–fidelity which is an exception to the conventional second–order schemes commonly regarded as inadequate for computational aeroacoustic (CAA) applications.

7.2   Recommendations for Future Work

In this research work, the 3–D parallel LES solver based on the time–conservative finite–volume method is used to investigate only the near acoustic field. Though the flow solver can accurately produce near–field results with high–fidelity, it is unable to investigate sound propagation mechanisms for far–field. The time–accurate LES near–field data can be coupled with an integral formulation for far–field sound calculations. Hence, it is worthwhile to investigate the possibility of coupling the LES solver with an acoustic analogy (e.g., the Lighthill's acoustic analogy (Lighthill, 1952), Ffowcs Williams and Hawkings (FWH) acoustic analogy (Ffowcs Williams and Hawkings, 1969) or Kirchhoff integral method (Freund et al., 1996)) to predict sound propagation into the far–field. Therefore, the coupling of the LES solver with one of the acoustic analogy will make the present CAA methodology a powerful tool not only for identification of noise mechanisms but also for noise reduction and control.

In LES implementation, the subgrid–scale turbulent fluctuations are approximated by the Smagorinsky subgrid–scale (SGS) model. Despite the Smagorinsky subgrid–scale model being very simple, it has several disadvantages. One main disadvantage of the Smagorinsky SGS model is that the SGS eddy–viscosity is usually adjusted with a damping function to take into account the reduction of the subgrid–scale length in the immediate vicinity of walls. This makes the application of the present SGS model to complex geometries very difficult. This drawback can be relieved by using a Wall–Adapting Local–Eddy Viscosity (WALE) SGS model. The WALE SGS model was proposed by Nicoud and Ducros (1999) and uses a novel form of the velocity gradient tensor. The main advantage of the WALE SGS model is that it does not require any form of near–wall damping. This model also produces the correct scaling in the vicinity of the wall without using the local wall distance. There is still room for improvement of the SGS model. Therefore, the coupling of the present methodology with a future SGS model can improve the quality of the near acoustic field results.

The specification of realistic inlet boundary condition can have a strong influence not only in the vicinity of the inlet boundary but also for the entire flow development in large–eddy simulations of spatially developing flows. The synthetic–eddy–method (SEM) to generate inflow conditions for large–eddy simulations was proposed by Jarrin et al. (2006). The SEM method retains the conceptual basis of the vortex method. According to Jarrin, the implementation of the SEM method is easy and the model performs well on any kind of geometry for any flow regimes. This method can be implemented into the flow solver to generate the instantaneous velocity field required at inflow boundaries by LES computations and then new simulations can be carried out in order to investigate the influence of inflow boundary conditions for the prediction of sound.

Appendix A

Derivation of Diffusive Thermal Fluxes

The thermal fluxes are defined as

$$q_x = -k\frac{\partial T}{\partial x}, \qquad q_y = -k\frac{\partial T}{\partial y}, \quad \text{and} \quad q_z = -k\frac{\partial T}{\partial z}. \tag{A.1}$$

where

$$k = \frac{\mu}{Pr}\frac{\gamma R}{(\gamma - 1)} \tag{A.2}$$

using ideal gas relation

$$T = \frac{p}{\rho R} \tag{A.3}$$

$$q_x = \frac{\mu}{Pr}\frac{\gamma}{(\gamma - 1)}\frac{\partial(p/\rho)}{\partial x} \tag{A.4}$$

using eq. (3.15) the diffusive thermal fluxes can be written in the following modified form

$$p = (\gamma - 1)\left(U_5 - \frac{1}{2}\rho\left(u^2 + v^2 + w^2\right)\right) \tag{A.5}$$

$$q_x = \gamma\frac{\mu}{Pr}\frac{\partial}{\partial x}\left[\frac{U_5}{U_1} - \frac{1}{2}\left(\left(\frac{U_2}{U_1}\right)^2 + \left(\frac{U_3}{U_1}\right)^2 + \left(\frac{U_4}{U_1}\right)^2\right)\right] \tag{A.6}$$

$$
\begin{aligned}
q_x = {} & \gamma\frac{\mu}{Pr}\left[\frac{1}{U_1}\frac{\partial U_5}{\partial x} - \frac{U_5}{(U_1)^2}\frac{\partial U_1}{\partial x}\right] \\
& - \frac{\gamma}{2}\frac{\mu}{Pr}\left[\left((U_2)^2 + (U_3)^2 + (U_4)^2\right)\left(-2\frac{U_1}{(U_1)^4}\right)\frac{\partial U_1}{\partial x}\right] \\
& - \frac{\gamma}{2}\frac{\mu}{Pr}\left[\frac{2}{(U_1)^2}\left(U_2\frac{\partial U_2}{\partial x} + U_3\frac{\partial U_3}{\partial x} + U_4\frac{\partial U_4}{\partial x}\right)\right]
\end{aligned}
\tag{A.7}
$$

149

Therefore the x component of the heat flux can be written as functions of $(U_m, U_{m,x}, U_{m,y}, U_{m,z})$

$$
\begin{aligned}
q_x &= \gamma \frac{\mu}{Pr} \left[\frac{U_{5,x}}{U_1} - \frac{U_5 U_{1,x}}{U_1^2} + \frac{U_2^2 + U_3^2 + U_4^2}{U_1^3} U_{1,x} \right] \\
&\quad - \gamma \frac{\mu}{Pr} \left[\frac{U_2 U_{2,x} + U_3 U_{3,x} + U_4 U_{4,x}}{U_1^2} \right]
\end{aligned}
\tag{A.8}
$$

Other components of the heat flux can be derived similarly (see eqs. (3.25) and (3.26))

Appendix B

Full Set of the Viscous Fluxes

$$F_{v1} = 0 \tag{B.1}$$

$$F_{v2} = \frac{2}{3}\mu \left(2\frac{U_{2,x}}{U_1} - 2\frac{U_2 U_{1,x}}{U_1^2} - \frac{U_{3,y}}{U_1} + \frac{U_3 U_{1,y}}{U_1^2} - \frac{U_{4,z}}{U_1} + \frac{U_4 U_{1,z}}{U_1^2} \right) \tag{B.2}$$

$$F_{v3} = \mu \left(\frac{U_{2,y}}{U_1} - \frac{U_2 U_{1,y}}{U_1^2} + \frac{U_{3,x}}{U_1} - \frac{U_3 U_{1,x}}{U_1^2} \right) \tag{B.3}$$

$$F_{v4} = \mu \left(\frac{U_{2,z}}{U_1} - \frac{U_2 U_{1,z}}{U_1^2} + \frac{U_{4,x}}{U_1} - \frac{U_4 U_{1,x}}{U_1^2} \right) \tag{B.4}$$

$$
\begin{aligned}
F_{v5} \;=\;\; & \frac{U_2}{U_1}\frac{2}{3}\mu \left(2\frac{U_{2,x}}{U_1} - 2\frac{U_2 U_{1,x}}{U_1^2} - \frac{U_{3,y}}{U_1} + \frac{U_3 U_{1,y}}{U_1^2} - \frac{U_{4,z}}{U_1} + \frac{U_4 U_{1,z}}{U_1^2} \right) \\
& + \frac{U_3}{U_1}\mu \left(\frac{U_{2,y}}{U_1} - \frac{U_2 U_{1,y}}{U_1^2} + \frac{U_{3,x}}{U_1} - \frac{U_3 U_{1,x}}{U_1^2} \right) \\
& + \frac{U_4}{U_1}\mu \left(\frac{U_{2,z}}{U_1} - \frac{U_2 U_{1,z}}{U_1^2} + \frac{U_{4,x}}{U_1} - \frac{U_4 U_{1,x}}{U_1^2} \right) \\
& + \gamma\frac{\mu}{Pr} \left[\frac{U_{5,x}}{U_1} - \frac{U_5 U_{1,x}}{U_1^2} + \frac{U_2^2 + U_3^2 + U_4^2}{U_1^3}U_{1,x} \right] \\
& - \gamma\frac{\mu}{Pr} \left[\frac{U_2 U_{2,x} + U_3 U_{3,x} + U_4 U_{4,x}}{U_1^2} \right]
\end{aligned}
\tag{B.5}
$$

$$G_{v1} = 0 \tag{B.6}$$

$$G_{v2} = \mu \left(\frac{U_{2,y}}{U_1} - \frac{U_2 U_{1,y}}{U_1^2} + \frac{U_{3,x}}{U_1} - \frac{U_3 U_{1,x}}{U_1^2} \right) \tag{B.7}$$

$$G_{v3} = \frac{2}{3}\mu \left(2\frac{U_{3,y}}{U_1} - 2\frac{U_3 U_{1,y}}{U_1^2} - \frac{U_{2,x}}{U_1} + \frac{U_2 U_{1,x}}{U_1^2} - \frac{U_{4,z}}{U_1} + \frac{U_4 U_{1,z}}{U_1^2} \right) \tag{B.8}$$

$$G_{v4} = \mu \left(\frac{U_{3,z}}{U_1} - \frac{U_3 U_{1,z}}{U_1^2} + \frac{U_{4,y}}{U_1} - \frac{U_4 U_{1,y}}{U_1^2} \right) \tag{B.9}$$

$$
\begin{aligned}
G_{v5} \;\; = \;\; & \frac{U_2}{U_1}\mu\left(\frac{U_{2,y}}{U_1} - \frac{U_2 U_{1,y}}{U_1^2} + \frac{U_{3,x}}{U_1} - \frac{U_3 U_{1,x}}{U_1^2}\right) \\
& + \frac{U_3}{U_1}\frac{2}{3}\mu\left(2\frac{U_{3,y}}{U_1} - 2\frac{U_3 U_{1,y}}{U_1^2} - \frac{U_{2,x}}{U_1} + \frac{U_2 U_{1,x}}{U_1^2} - \frac{U_{4,z}}{U_1} + \frac{U_4 U_{1,z}}{U_1^2}\right) \\
& + \frac{U_4}{U_1}\mu\left(\frac{U_{3,z}}{U_1} - \frac{U_3 U_{1,z}}{U_1^2} + \frac{U_{4,y}}{U_1} - \frac{U_4 U_{1,y}}{U_1^2}\right) \\
& + \gamma\frac{\mu}{Pr}\left[\frac{U_{5,y}}{U_1} - \frac{U_5 U_{1,y}}{U_1^2} + \frac{U_2^2 + U_3^2 + U_4^2}{U_1^3}U_{1,y}\right] \\
& - \gamma\frac{\mu}{Pr}\left[\frac{U_2 U_{2,y} + U_3 U_{3,y} + U_4 U_{4,y}}{U_1^2}\right]
\end{aligned}
\tag{B.10}
$$

$$
H_{v1} = 0 \tag{B.11}
$$

$$
H_{v2} = \mu\left(\frac{U_{2,z}}{U_1} - \frac{U_2 U_{1,z}}{U_1^2} + \frac{U_{4,x}}{U_1} - \frac{U_4 U_{1,x}}{U_1^2}\right) \tag{B.12}
$$

$$
H_{v3} = \mu\left(\frac{U_{3,z}}{U_1} - \frac{U_3 U_{1,z}}{U_1^2} + \frac{U_{4,y}}{U_1} - \frac{U_4 U_{1,y}}{U_1^2}\right) \tag{B.13}
$$

$$
H_{v4} = \frac{2}{3}\mu\left(2\frac{U_{4,z}}{U_1} - 2\frac{U_4 U_{1,z}}{U_1^2} - \frac{U_{2,x}}{U_1} + \frac{U_2 U_{1,x}}{U_1^2} - \frac{U_{3,y}}{U_1} + \frac{U_3 U_{1,y}}{U_1^2}\right) \tag{B.14}
$$

$$
\begin{aligned}
H_{v5} \;\; = \;\; & \frac{U_2}{U_1}\mu\left(\frac{U_{2,z}}{U_1} - \frac{U_2 U_{1,z}}{U_1^2} + \frac{U_{4,x}}{U_1} - \frac{U_4 U_{1,x}}{U_1^2}\right) \\
& + \frac{U_3}{U_1}\mu\left(\frac{U_{3,z}}{U_1} - \frac{U_3 U_{1,z}}{U_1^2} + \frac{U_{4,y}}{U_1} - \frac{U_4 U_{1,y}}{U_1^2}\right) \\
& + \frac{U_4}{U_1}\frac{2}{3}\mu\left(2\frac{U_{4,z}}{U_1} - 2\frac{U_4 U_{1,z}}{U_1^2} - \frac{U_{2,x}}{U_1} + \frac{U_2 U_{1,x}}{U_1^2} - \frac{U_{3,y}}{U_1} + \frac{U_3 U_{1,y}}{U_1^2}\right) \\
& + \gamma\frac{\mu}{Pr}\left[\frac{U_{5,z}}{U_1} - \frac{U_5 U_{1,z}}{U_1^2} + \frac{U_2^2 + U_3^2 + U_4^2}{U_1^3}U_{1,z}\right] \\
& - \gamma\frac{\mu}{Pr}\left[\frac{U_2 U_{2,z} + U_3 U_{3,z} + U_4 U_{4,z}}{U_1^2}\right]
\end{aligned}
\tag{B.15}
$$

Appendix C

Jacobian Matrices

$$F_{11} = 0, \qquad F_{12} = 1, \qquad F_{13} = 0, \qquad F_{14} = 0, \qquad F_{15} = 0. \qquad \text{(C.1)}$$

$$F_{21} = \frac{\gamma - 1}{2} \left(\frac{U_3}{U_1} \right)^2 + \frac{\gamma - 1}{2} \left(\frac{U_4}{U_1} \right)^2 - \frac{3 - \gamma}{2} \left(\frac{U_2}{U_1} \right)^2, \qquad \text{(C.2)}$$

$$F_{22} = (3 - \gamma) \frac{U_2}{U_1}, \qquad F_{23} = -(\gamma - 1) \frac{U_3}{U_1},$$

$$F_{24} = -(\gamma - 1) \frac{U_4}{U_1}, \qquad F_{25} = (\gamma - 1).$$

$$F_{31} = -\frac{U_2 U_3}{(U_1)^2}, \qquad F_{32} = \frac{U_3}{U_1}, \qquad \text{(C.3)}$$

$$F_{33} = \frac{U_2}{U_1}, \qquad F_{34} = 0, \qquad F_{35} = 0.$$

$$F_{41} = -\frac{U_2 U_4}{(U_1)^2}, \qquad F_{42} = \frac{U_4}{U_1}, \qquad \text{(C.4)}$$

$$F_{43} = 0, \qquad F_{44} = \frac{U_2}{U_1}, \qquad F_{45} = 0.$$

$$F_{51} = -\gamma \frac{U_2 U_5}{(U_1)^2} + (\gamma - 1) \left(\frac{U_2}{U_1} \right)^3 + (\gamma - 1) \frac{U_2 (U_3)^2}{(U_1)^3} + (\gamma - 1) \frac{U_2 (U_4)^2}{(U_1)^3}, \qquad \text{(C.5)}$$

$$F_{52} = \gamma \frac{U_5}{U_1} - \frac{(\gamma - 1)}{2} \left[\left(\frac{U_2}{U_1} \right)^2 + \left(\frac{U_3}{U_1} \right)^2 + \left(\frac{U_4}{U_1} \right)^2 \right] - (\gamma - 1) \left(\frac{U_2}{U_1} \right)^2,$$

$$F_{53} = -(\gamma - 1) \frac{U_2 U_3}{(U_1)^2}, \qquad F_{54} = -(\gamma - 1) \frac{U_2 U_4}{(U_1)^2}, \qquad F_{55} = \gamma \frac{U_2}{U_1}.$$

$$G_{11} = 0, \qquad G_{12} = 0, \qquad G_{13} = 1, \qquad G_{14} = 0, \qquad G_{15} = 0. \qquad \text{(C.6)}$$

$$G_{21} = -\frac{U_2 U_3}{(U_1)^2}, \qquad G_{22} = \frac{U_3}{U_1}, \qquad \text{(C.7)}$$

$$G_{23} = \frac{U_2}{U_1}, \qquad G_{24} = 0, \qquad G_{25} = 0.$$

$$G_{31} = \frac{(\gamma - 1)}{2}\left(\frac{U_2}{U_1}\right)^2 + \frac{(\gamma - 1)}{2}\left(\frac{U_4}{U_1}\right)^2 - \frac{(3 - \gamma)}{2}\left(\frac{U_3}{U_1}\right)^2, \qquad \text{(C.8)}$$

$$G_{32} = -(\gamma - 1)\frac{U_2}{U_1}, \qquad G_{33} = (3 - \gamma)\frac{U_3}{U_1},$$

$$G_{34} = -(\gamma - 1)\frac{U_4}{U_1}, \qquad G_{35} = (\gamma - 1).$$

$$G_{41} = -\frac{U_3 U_4}{(U_1)^2}, \qquad G_{42} = 0, \qquad \text{(C.9)}$$

$$G_{43} = \frac{U_4}{U_1}, \qquad G_{44} = \frac{U_3}{U_1}, \qquad G_{45} = 0.$$

$$G_{51} = -\gamma\frac{U_3 U_5}{(U_1)^2} + (\gamma - 1)\frac{U_3(U_2)^2}{(U_1)^3} + (\gamma - 1)\left(\frac{U_3}{U_1}\right)^3 + (\gamma - 1)\frac{U_3(U_4)^2}{(U_1)^3}, \qquad \text{(C.10)}$$

$$G_{52} = -(\gamma - 1)\frac{U_3 U_2}{(U_1)^2},$$

$$G_{53} = \gamma\frac{U_5}{U_1} - \frac{(\gamma - 1)}{2}\left[\left(\frac{U_2}{U_1}\right)^2 + \left(\frac{U_3}{U_1}\right)^2 + \left(\frac{U_4}{U_1}\right)^2\right] - (\gamma - 1)\left(\frac{U_3}{U_1}\right)^2,$$

$$G_{54} = -(\gamma - 1)\frac{U_3 U_4}{(U_1)^2}, \qquad G_{55} = \gamma\frac{U_3}{U_1}.$$

$$H_{11} = 0, \qquad H_{12} = 0, \qquad H_{13} = 0, \qquad H_{14} = 1, \qquad H_{15} = 0. \qquad \text{(C.11)}$$

$$H_{21} = -\frac{U_2 U_4}{(U_1)^2}, \qquad H_{22} = \frac{U_4}{U_1}, \qquad \text{(C.12)}$$

$$H_{23} = 0, \qquad H_{24} = \frac{U_2}{U_1}, \qquad H_{25} = 0.$$

$$H_{31} = -\frac{U_3 U_4}{(U_1)^2}, \qquad H_{32} = 0, \qquad \text{(C.13)}$$

$$H_{33} = \frac{U_4}{U_1}, \qquad H_{34} = \frac{U_3}{U_1}, \qquad H_{35} = 0.$$

$$H_{41} = \frac{(\gamma - 1)}{2}\left[\left(\frac{U_2}{U_1}\right)^2 + \left(\frac{U_3}{U_1}\right)^2\right] - \frac{(3 - \gamma)}{2}\left(\frac{U_4}{U_1}\right)^2, \qquad \text{(C.14)}$$

$$H_{42} = -(\gamma - 1)\frac{U_2}{U_1}, \qquad H_{43} = -(\gamma - 1)\frac{U_3}{U_1},$$

$$H_{44} = (3 - \gamma)\frac{U_4}{U_1}, \qquad H_{45} = (\gamma - 1).$$

$$H_{51} = -\gamma\frac{U_4 U_5}{(U_1)^2} + (\gamma - 1)\frac{U_4(U_2)^2}{(U_1)^3} + (\gamma - 1)\frac{U_4(U_3)^2}{(U_1)^3} + (\gamma - 1)\left(\frac{U_4}{U_1}\right)^3, \qquad \text{(C.15)}$$

$$H_{52} = -(\gamma - 1)\frac{U_4 U_2}{(U_1)^2}, \qquad H_{53} = -(\gamma - 1)\frac{U_4 U_3}{(U_1)^2},$$

$$H_{54} = \gamma \frac{U_5}{U_1} - \frac{(\gamma - 1)}{2} \left[\left(\frac{U_2}{U_1} \right)^2 + \left(\frac{U_3}{U_1} \right)^2 + \left(\frac{U_4}{U_1} \right)^2 \right] - (\gamma - 1) \left(\frac{U_4}{U_1} \right)^2,$$

$$H_{55} = \gamma \frac{U_4}{U_1}.$$

Appendix D

Space–Time Flux Evaluation
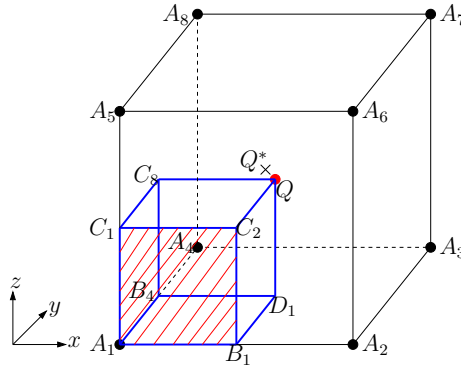
Figure D.1: Flux evaluation on the quadrilateral defined by $A_1B_1C_2C_1$

The quadrilateral defined by $A_1B_1C_2C_1$ is depicted Fig. D.1, its surface vector is $s_{A_1B_1C_2C_1} = \frac{\Delta t}{2}((y_{C_2} - y_{A_1})(z_{C_1} - z_{B_1}) - (z_{C_2} - z_{A_1})(y_{C_1} - y_{B_1}), (z_{C_2} - z_{A_1})(x_{C_1} - x_{B_1}) - (x_{C_2} - x_{A_1})(z_{C_1} - z_{B_1}), (x_{C_2} - x_{A_!})(y_{C_1} - y_{B_1}) - (y_{C_2} - y_{A_1})(x_{C_1} - x_{B_1}), 0)$ and the coordinates of its centroid are $(C_{x_2}, C_{y_2}, C_{z_2}, t^n + \frac{\Delta t}{4})$. The flux leaving the

surface $A_1B_1C_2C_1$ is

$$
\begin{aligned}
(FLUX_m)_{A_1B_1C_2C_1} \;=\;\; & \frac{\Delta t}{2}[(y_{C_2}-y_{A_1})(z_{C_1}-z_{B_1})-(z_{C_2}-z_{A_1})(y_{C_1}-y_{B_1})] \\[4pt]
& [(F_m)^n_{A_1^*}+(C_{x_2}-x_{A_1^*})(F_{m,x})^n_{A_1^*}+(C_{y_2}-y_{A_1^*})(F_{m,y})^n_{A_1^*} \\[4pt]
& + (C_{z_2}-z_{A_1^*})(F_{m,z})^n_{A_1^*} \\[4pt]
& + \frac{\Delta t}{4}(F_{m,t})^n_{A_1^*}-F_{vm}^{A_1B_1C_2C_1}] \\[4pt]
& + \frac{\Delta t}{2}[(z_{C_2}-z_{A_1})(x_{C_1}-x_{B_1})-(x_{C_2}-x_{A_1})(z_{C_1}-z_{B_1})] \\[4pt]
& [(G_m)^n_{A_1^*}+(C_{x_2}-x_{A_1^*})(G_{m,x})^n_{A_1^*}+(C_{y_2}-y_{A_1^*})(G_{m,y})^n_{A_1^*} \\[4pt]
& + (C_{z_2}-z_{A_1^*})(G_{m,z})^n_{A_1^*} \\[4pt]
& + \frac{\Delta t}{4}(G_{m,t})^n_{A_1^*}-G_{vm}^{A_1B_1C_2C_1}] \\[4pt]
& + \frac{\Delta t}{2}[(x_{C_2}-x_{A_!})(y_{C_1}-y_{B_1})-(y_{C_2}-y_{A_1})(x_{C_1}-x_{B_1})] \\[4pt]
& [(H_m)^n_{A_1^*}+(C_{x_2}-x_{A_1^*})(H_{m,x})^n_{A_1^*}+(C_{y_2}-y_{A_1^*})(H_{m,y})^n_{A_1^*} \\[4pt]
& + (C_{z_2}-z_{A_1^*})(H_{m,z})^n_{A_1^*} \\[4pt]
& + \frac{\Delta t}{4}(H_{m,t})^n_{A_1^*}-H_{vm}^{A_1B_1C_2C_1}]
\end{aligned}
\tag{D.1}
$$

where the viscous fluxes $F_{vm}^{A_1B_1C_1}$, $G_{vm}^{A_1B_1C_2C_1}$ and $H_{vm}^{A_1B_1C_2C_1}$ are obtained from the flow variables at the centroid of surface $A_1B_1C_2C_1$ as well as $(U_{m,x})^n_{A_1^*}$, $(U_{m,y})^n_{A_1^*}$ and $(U_{m,z})^n_{A_1^*}$.

Figure D.2: Flux evaluation on the quadrilateral defined by $A_1B_1D_1B_4$

The quadrilateral defined by $A_1B_1D_1B_4$ is given Fig. D.2, its surface vector is

$s_{A_1B_1D_1B_4} = \frac{\Delta t}{2}((y_{A_1}-y_{D_1})(z_{B_4}-z_{B_1})-(z_{A_1}-z_{D_1})(y_{B_4}-y_{B_1}),(z_{A_1}-z_{D_1})(x_{B_4}-x_{B_1})-(x_{A_1}-x_{D_1})(z_{B_4}-z_{B_1}),(x_{A_1}-x_{D_1})(y_{B_4}-y_{B_1})-(y_{A_1}-y_{D_1})(x_{B_4}-x_{B_1}),0)$

and the coordinates of its centroid are $(C_{x_3}, C_{y_3}, C_{z_3}, t^n + \frac{\Delta t}{4})$. The flux leaving the surface $A_1 B_1 D_1 B_4$ is

$$
\begin{aligned}
(FLUX_m)_{A_1 B_4 C_8 C_1} &= \frac{\Delta t}{2}[(y_{A_1} - y_{D_1})(z_{B_4} - z_{B_1}) - (z_{A_1} - z_{D_1})(y_{B_4} - y_{B_1})] \\
&\quad [(F_m)_{A_1^*}^n + (C_{x_3} - x_{A_1^*})(F_{m,x})_{A_1^*}^n + (C_{y_3} - y_{A_1^*})(F_{m,y})_{A_1^*}^n \\
&\quad + (C_{z_3} - z_{A_1^*})(F_{m,z})_{A_1^*}^n \\
&\quad + \frac{\Delta t}{4}(F_{m,t})_{A_1^*}^n - F_{vm}^{A_1 B_1 D_1 B_4}] \\
&\quad + \frac{\Delta t}{2}[(z_{A_1} - z_{D_1})(x_{B_4} - x_{B_1}) - (x_{A_1} - x_{D_1})(z_{B_4} - z_{B_1})] \\
&\quad [(G_m)_{A_1^*}^n + (C_{x_3} - x_{A_1^*})(G_{m,x})_{A_1^*}^n + (C_{y_3} - y_{A_1^*})(G_{m,y})_{A_1^*}^n \\
&\quad + (C_{z_3} - z_{A_1^*})(G_{m,z})_{A_1^*}^n \\
&\quad + \frac{\Delta t}{4}(G_{m,t})_{A_1^*}^n - G_{vm}^{A_1 B_1 D_1 B_4}] \\
&\quad + \frac{\Delta t}{2}[(x_{A_1} - x_{D_1})(y_{B_4} - y_{B_1}) - (y_{A_1} - y_{D_1})(x_{B_4} - x_{B_1})] \\
&\quad [(H_m)_{A_1^*}^n + (C_{x_3} - x_{A_1^*})(H_{m,x})_{A_1^*}^n + (C_{y_3} - y_{A_1^*})(H_{m,y})_{A_1^*}^n \\
&\quad + (C_{z_3} - z_{A_1^*})(H_{m,z})_{A_1^*}^n \\
&\quad + \frac{\Delta t}{4}(H_{m,t})_{A_1^*}^n - H_{vm}^{A_1 B_1 D_1 B_4}]
\end{aligned}
\tag{D.2}
$$

where the viscous fluxes $F_{vm}^{A_1 B_1 D_1 B_4}$, $G_{vm}^{A_1 B_1 D_1 B_4}$ and $H_{vm}^{A_1 B_1 D_1 B_4}$ are obtained from the flow variables at the centroid of surface $A_1 B_1 D_1 B_4$ as well as $(U_{m,x})_{A_1^*}^n$, $(U_{m,y})_{A_1^*}^n$ and $(U_{m,z})_{A_1^*}^n$.

$$
\begin{aligned}
(flux_m)_2^n &= (FLUX_m)_{A_2 B_2 D_1 B_1 C_3 C_4 Q C_2} + (FLUX_m)_{A_2 B_2 C_4 C_3} \\
&\quad + (FLUX_m)_{A_2 C_3 C_2 B_1} + (FLUX_m)_{A_2 B_2 D_1 B_1}
\end{aligned}
\tag{D.3}
$$

$$
\begin{aligned}
(flux_m)_3^n &= (FLUX_m)_{A_3 B_3 D_1 B_2 C_5 C_6 Q C_4} + (FLUX_m)_{A_3 C_5 C_4 B_2} \\
&\quad + (FLUX_m)_{A_3 B_3 C_6 C_5} + (FLUX_m)_{A_3 B_3 D_1 B_2}
\end{aligned}
\tag{D.4}
$$

$$
\begin{aligned}
(flux_m)_4^n &= (FLUX_m)_{A_4 B_4 D_1 B_3 C_7 C_8 Q C_6} + (FLUX_m)_{A_4 B_3 C_6 C_7} \\
&\quad + (FLUX_m)_{A_4 B_4 C_8 C_7} + (FLUX_m)_{A_4 B_4 D_1 B_3}
\end{aligned}
\tag{D.5}
$$

$$
\begin{aligned}
(flux_m)_5^n &= (FLUX_m)_{A_5 B_5 D_2 B_8 C_1 C_2 Q C_8} + (FLUX_m)_{A_5 B_5 C_2 C_1} \\
&\quad + (FLUX_m)_{A_5 B_8 C_8 C_1} + (FLUX_m)_{A_5 B_5 D_2 B_8}
\end{aligned}
\tag{D.6}
$$

$$(flux_m)_6^n = (FLUX_m)_{A_6 B_6 D_2 B_5 C_3 C_4 Q C_2} + (FLUX_m)_{A_6 C_3 C_4 B_6}$$
$$+ (FLUX_m)_{A_6 B_5 C_2 C_3} + (FLUX_m)_{A_6 B_6 D_2 B_5} \tag{D.7}$$

$$(flux_m)_7^n = (FLUX_m)_{A_7 B_7 D_2 B_6 C_5 C_6 Q C_4} + (FLUX_m)_{A_7 B_7 C_6 C_5}$$
$$+ (FLUX_m)_{A_7 B_6 C_4 C_5} + (FLUX_m)_{A_7 B_7 D_2 B_6} \tag{D.8}$$

$$(flux_m)_8^n = (FLUX_m)_{A_8 B_8 D_2 B_7 C_7 C_8 Q C_6} + (FLUX_m)_{A_8 B_8 C_8 C_7}$$
$$+ (FLUX_m)_{A_8 B_7 C_6 C_7} + (FLUX_m)_{A_8 B_8 D_2 B_7} \tag{D.9}$$

Bibliography

Anderson, J.D. (1995) *Computational Fluid Dynamics: The Basics with Applications*, McGraw–Hill Singapore.

Allen, R. and Mendonça, F. (2004) DES Validations of Cavity Acoustics over the Subsonic to Supersonic Range, *AIAA Paper*, 2004–2862.

Aybay, O. and He, L. (2007) Time–Conservative Finite–Volume Method for Large–Eddy Simulation, *Proc. of the World Congress on Engineering 2007*, **2**, pp. 1198–1203.

Aybay, O. and He, L. (2008a) Development of a High–Resolution Time–Conservative Finite–Volume Method for Large–Eddy Simulation, *Engineering Letters*, **16**(1), pp. 96–103.

Aybay, O. and He, L. (2008b) Development of Time–Conservative Finite–Volume Method for Large–Eddy Simulation, *Current Themes in Engineering Science 2007*, (ed.) Korkunsky, A.M., American Institute of Physics, pp. 31–41.

Aybay, O., Breuer, M., and He, L. (2009a) Large–Eddy Simulation of Three–Dimensional Cavity Flow Using a Time–Conservative Finite–Volume Method, *New Results in Numerical and Experimental Fluid Mechanics VII* (eds.) Dillmann, A., Heller, G., Klass, M., Kreplin, H.–P., Nitsche, W. and Schröder, W., Notes on Numerical Fluid Mechanics and Multidisciplinary Design, Vol. 112, Springer, 2010. (Presented at 16. DGLR Symposium of STAB, RWTH Aachen University, Nov. 3–4, Germany).

Aybay, O., Breuer, M. and He, L. (2009b) Large–Eddy Simulation of Cavity Aeroacoustics Based on a Time–Conservative Finite–Volume Method, *EUROMECH–Colloquium 504: Large–Eddy Simulation for Aerodynamics and Aeroacoustics*, Technical University of Munich, March 23–25, Germany.

Bailly, C., Lafon, P. and Candel, S. (1997) Subsonic and Supersonic Jet Noise Predictions from Statistical Source Models, *AIAA Journal*, **35**(11), pp. 1688–1696.

Bardina, J., Ferziger, J.H. and Reynolds, W.C. (1980) Improved Subgrid–Scale Models for Large–Eddy Simulation, *AIAA Paper*, 1980–1357.

Blazek, J. (2005) *Computational Fluid Dynamics: Principles and Applications*, 2nd ed. Oxford:Elsevier.

Berland, J., Bogey, C. and Bailly, C. (2007) Numerical Study of Screech Generation in a Planar Supersonic Jet, *Physics of Fluids*, **19**(7), pp. 1–14.

Bertier, N., Courbet, B., Dutoya, D. and Vuillot, F. (2004) Large–Eddy Simulation of a Subsonic Flow over a Cavity on General Unstructured Grids, *AIAA Paper*, 2004–0679.

Bodony, D.J. and Lele, S.K. (2003) Large–Eddy Simulation of Jet Engine Exhaust Noise, *ERCOFTAC Bulletin, Theme Issue: Aeroacoustics*, **58**, 21–24.

Bodony, D.J. and Lele, S.K. (2004) Jet Noise Prediction of Cold and Hot Subsonic Jets Using Large–Eddy Simulation, *AIAA Paper*, 2004–3022.

Boersma, B.J. and Lele, S.K. (1999) Large–Eddy Simulation of Compressible Turbulent Jets, *Annual Research Briefs 1999*, Center for Turbulence Research, Stanford University, 365–376.

Bogey, C., Bailly, C. and Juvé D. (1999) Computation of Mixing Layer Noise Using Large–Eddy Simulation, *AIAA Paper*, 1999–1871.

Bogey, C. (2000a) Calcul Direc du Bruit Aérodynamique et Validation de Modèles Acoustiques Hybrides, PhD thesis, Laboratoire de Mécanique des Fluides at d'Acoustique, École Centrale de Lyon, France.

Bogey, C., Bailly, C. and Juvé, D. (2000b) Numerical Simulation of Sound Generated by Vortex Pairing in a Mixing Layer, *AIAA Journal*, **38**(12), pp. 2210–2218.

Bogey, C., Bailly, C. and Juvé, D. (2000c) Computation of the Sound Radiated by a 3–D Jet Using Large–Eddy Simulation, *AIAA Paper*, 2000–2009.

Bogey, C. and Bailly, C. (2006) Computation of a High Reynolds Number Jet and its Radiated Noise using LES based on Explicit Filtering, *Computers and Fluids*, **35**(10), pp. 1344–1358.

Boris, J.P., Grinstein, F.F., Oran, E.S. and Kolbe, R.J. (1992) New Insights into Large–Eddy Simulation, *Fluid Dynamics Research*, **10**, pp. 199–228.

Brandt, A. (1992) Guide to Multigrid Development, Multigrid Methods *I*, *Lecture Notes in Mathematics*, **960**, Springer Verlag, New York.

Breuer, M. (1998) Large–Eddy Simulation of the Subcritical Flow Past a Circular Cylinder: Numerical and Modeling Aspects, *Int. Journal for Numerical Methods in Fluids*, **28**, pp. 1281–1302.

Breuer, M. (2007) Direct Numerical Simulation and Large–Eddy Simulation of Turbulent Flows, 10th *School of Computational Fluid Dynamics*, Roscoff, France.

Breuer, M., Jaffrézic, B. and Arora, K. (2008) Hybrid LES–RANS Technique Based on a One–Equation Near–Wall Model, *Journal of Theoretical and Computational Fluid Dynamics*, **22**, pp. 157–187.

Breuer, M., Aybay, O., Jaffrézic, B., Visonneau, M., Deng, G., Guilmineau, E. and Chikhaoui, O. (2009) Hybrid LES–RANS–Coupling for Complex Flows with Separation, *Notes on Numerical Fluid Mechanics and Multidisciplinary Design*, (eds.) Brun, C., Juve, D., Manhart, M. and Munz, C.D., **104**, pp. 201–229, Springer Berlin, Heidelberg.

Brés, G.A. and Colonius, T. (2007a) Three–Dimensional Linear Stability Analysis of Cavity Flows, *AIAA Paper*, 2007–1126.

Brés, G.A. and Colonius, T. (2007b) Direct Numerical Simulation of Three–Dimensional Cavity Flows, *AIAA Paper*, 2007–3405.

Brés, G.A. and Colonius, T. (2008) Three–Dimensional Instabilities in Compressible Flow over Open Cavities, *Journal of Fluid Mechanics*, **599**, pp. 309–339.

Caraeni, M., Devaki, R.K., Aroni, M., Oswald, M., Srikanth, K.V.S.S. and Caraeni, D. (2009) Efficient Acoustic Modal Analysis for Industrial CFD, *AIAA Paper*, 2009–1418.

Carati, D., Ghosal, S. and Moin, P. (1995) On the Representation of Backscatter in Dynamic Localization Models, *Physics of Fluids*, **7**, pp. 606–616.

Chang, S.C. (1995) The Method of Space–Time Conservation Element and Solution Element – A New Approach for Solving the Navier–Stokes and Euler Equations, *Journal of Computational Physics*, **119**, pp. 295–324.

Chang, S.C., Wang, X.Y. and Chow, C.Y. (1999) The Space–Time Conservation Element and Solution Element Method A New High–Resolution and Genuinely Multidimensional Paradigm for Solving Conservation Laws, *Journal of Computational Physics*, **156**, pp. 89–136.

Chang, S.C., Himansu, A., Loh, C.Y., Wang, X.Y. and Yu, S.T. (2003) Robust and Simple Nonreflecting Boundary Conditions for the Euler Equations – A New Approach Based on the Space–Time CE/SE Method, *NASA/TM*, 2003–212495.

Chang, S.C. (2007) The $a(4)$ Scheme A High–Order Neutrally Stable CE/SE Solver, *43rd AIAA Joint Propulsion Conference*, Cincinnati, July 11, USA.

Chen, X., Sandham, N.D. and Zhang, X. (2007) Cavity Flow Noise Predictions, University of Southampton, Report No. AFM–07/05, pp. 1–51.

Chollet, J.P. and Lesieur, M. (1981) Parameterization of Small Scales of Three–Dimensional Isotropic Turbulence Utilizing Spectral Closures, *Journal of the Atmospheric Sciences*, **38**, pp. 2747–2757.

Colonius, T., Lele, K.S. and Moin, P. (1997) Sound Generation in a Mixing Layer, *Journal of Fluid Mechanics*, **330**, pp. 375–409.

Colonius, T. and Lele, K.S. (2004) Computational Aeroacoustics: Progress on Nonlinear Problems of Sound Generation, *Progress in Aerospace Sciences*, **40**, pp. 345–416.

Curle, N. (1955) The Influence of Solid Boundaries upon Aerodynamical Sound, *Proc. of the Royal Society of London, Series A: Mathematical and Physical Sciences*, **231**, pp. 505–514.

Davidson, L. and Peng, S.H. (2003) A One–Equation SGS Model Combined with a $k - \omega$ Model for Predicting Recirculating Flows, *Int. Journal for Numerical Methods in Fluids*, **43**, pp. 1003–1018.

De Stefano, G. and Vasilyev O.V. (2004) "Perfect" Modeling Framework for Dynamic SGS Model Testing in Large Eddy Simulation, *Theoretical and Computational Fluid Dynamics*, **18**, pp. 27–41.

Deardorff, J.W. (1970) A Numerical Study of Three–Dimensional Turbulent Channel Flow at Large Reynolds Numbers, *Journal of Fluid Mechanics*, **41**, pp. 453–480.

Envia, E., Wilson, A.G. and Huff, D.L. (2004) Fan Noise: A Challenge to CAA, *Int. Journal of Computational Fluid Dynamics*, **18**(6), pp. 315–333.

Erlebacher, G., Hussaini, M.Y., Speziale, C.G. and Zang, T.A. (1992) Toward the Large–Eddy Simulation of Compressible Turbulent Flows, *Journal of Fluid Mechanics*, **238**, pp. 155–185.

Ewert, R., Zhang, Q., Schröder, W. and Delfs, J. (2003) Computation of Trailing Edge Noise of a 3D Lifting Airfoil in Turbulent Subsonic Flow, *AIAA Paper*, 2003–3114.

Ewert, R. and Schröder, W (2004) On the Simulation of Trailing Edge Noise with a Hybrid LES/APE Method, *Journal of Sound and Vibration*, **270**, pp. 509–524.

Ferziger, J.H. and Perić, M. (2002) *Computational Methods for Fluid Dynamics*, 3rd ed. Berlin:Springer–Verlag.

Ffowcs Williams, J.E. and Hawkings, D.L. (1969) Sound Generation by Turbulence and Surfaces in Arbitrary Motion, *Proc. of the Royal Society of London, Series A: Mathematical and Physical Sciences*, **264**, pp. 321–342.

Freund, J.B., Lele, S.K. and Moin, P. (1996) Calculation of the Radiated Sound Field Using an Open Kirchhoff Surface, *AIAA Journal*, **34**(5), pp. 909–1016.

Freund, J.B., Lele, S.K. and Moin, P. (2000) Direct Numerical Simulation of a Mach 1.92 Turbulent Jet and its Sound Field, *AIAA Journal*, **38**(11), pp. 2023–2031.

Freund, J.B. (2001) Noise Sources in a Low–Reynolds–Number Turbulent Jet at Mach 0.9, *Journal of Fluid Mechanics*, **438**, pp. 277–305.

Fröhlich, J. and Rodi, W. (2002) Introduction to Large–Eddy Simulation of Turbulent Flows, *Closure Strategies for Turbulent and Transitional Flows*, (eds.) Launder, B.E. and Sandham, N.D., Cambridge University Press, pp. 267–298.

Fureby, C. and Grinstein, F.F. (1999) Monotonically Integrated Large–Eddy Simulation of Free Shear Flows, *AIAA Journal*, **37**(5), pp. 544–556.

Fureby, C. and Grinstein, F.F. (2000) Large–Eddy Simulation of High Reynolds–Number Free and Wall–Bounded Flows, *AIAA Paper*, 2000–2307.

Garnier, E., Mossi, M., Sagaut, P., Comte, P. and Deville, M. (1999) On the Use of Shock–Capturing Schemes for Large–Eddy Simulation, *Journal of Computational Physics*, **153**, pp. 273–311.

Germano, M., Piomelli, U., Moin, P. and Cabot, W. (1991) A Dynamic Subgrid–Scale Eddy Viscosity Model, *Physics of Fluids A*, **3**(7), pp. 1760–1765.

Ghosal, S., Lund, T.S., Moin, P. and Akselvoll, K. (1995) A Dynamic Localization Model for Large–Eddy Simulation of Turbulent Flows, *Journal of Fluid Mechanics*, **286**, pp. 229–255.

Ghia, U., Ghia, K.N. and Shin, C.T. (1982) High–Re Solutions for Incompressible Flow Using the Navier–Stokes Equations and a Multigrid Method, *Journal of Computational Physics*, **48**, pp. 387–411.

Giannakouros, J. and Karniadakis, G.E. (1994) A Spectral Element–FCT Method for the Compressible Euler Equations, *Journal of Computational Physics*, **115**, pp. 65–85.

Gloerfelt, X., Bogey, C. and Bailly, C. (2007) *Large–Eddy Simulation for Acoustics*, (eds.) Wagner, C., Hüttl, T. and Sagaut, P., Cambridge University Press.

Gullbrand, J. and Chow, F.K. (2003) The Effect of Numerical Errors and Turbulence Models in Large–Eddy Simulations of Channel Flow, with or without Explicit Filtering, *Journal of Fluid Mechanics*, **495**, pp. 323–341.

Guo, Y., Hsu, A.T., Wu, J., Yang, Z. and Oyediran, A. (2004) Extension of CE/SE Method to 2D Viscous Flows, *Computers and Fluids*, **33**, pp. 1349–1361.

Hamba, F. (2003) A Hybrid RANS–LES Simulation of Turbulent Channel Flow, *Theoretical and Computational Fluid Dynamics*, **16**, pp. 387–403.

He, L. and Denton, J.D. (1994) Three–Dimensional Time–Marching Inviscid and Viscous Solutions for Unsteady Flows Around Vibrating Blades, *Journal of Turbomachinery*, **116**, pp. 469–476.

Hedges, L.S., Travin, A.K. and Spalart, P.R. (2002) Detached–Eddy Simulations Over a Simplified Landing Gear, *Journal of Fluids Engineering*, **124**, pp. 413–423.

Henderson, J., Babcock, K. and Richards, B.E. (2000) Subsonic and Transonic Transitional Cavity Flows, *AIAA Paper*, 2000–1996.

Henshaw, M.J. de C. (2000) Verification and Validation Data for Computational Unsteady Aerodynamics, RTO–TR–26, AC/323(AVT)TP/19, pp. 473–480.

Hinterberger, C., Garcia–Villalba, M. and Rodi, M. (2003) LES of Flow Around the Ahmed Body: Lecture Notes in Applied Mechanics, *Proc. of the UEF Conference*

on "The Aerodynamics of Heavy Vehicles: Trucks, Buses and Trains, Monterey, CA, 2002, Springer–Verlag.

Hirsch, C. (2007) *Numerical Computation of Internal and External Flows: The Fundamentals of Computational Fluid Dynamics*, 2nd ed. Oxford:Elsevier.

Howard, R.J.A. and Pourquie, M. (2002) Large–Eddy Simulation of the Ahmed Reference Model, *Journal of Turbulence*, **42**(3), pp. 1–18.

Howe, M.S. (2000) Analytical Representations of Fluid–Structure Interaction Noise for Large–Eddy Simulations, Report–AM–00–003, Boston University, College of Engineering.

Hughes, T.J.R., Mazzei, L., Oberai, A.A. and Wray, A.A. (2001) The Multiscale Formulation of Large–Eddy Simulation: Decay of Homogeneous Isotropic Turbulence, *Physics of Fluids*, **13**(2), pp. 505–512.

Ihme, M. and Breuer, M. (2002) Sound Prediction for a Turbulent Co–flowing Jet Based on LES, Int. Workshop on LES for Acoustics, DLR Göttingen, Germany, (eds.) Hüttl, T., Wagner, C. and Delfs, J., DGLR–Report 2002–03.

Inagaki, M., Murata, O., Kondon, T. and Abe, K. (2002) Numerical Prediction of Fluid–Resonant Oscillation at Low Mach Number, *AIAA Journal*, **40**(9), pp. 1823–1908.

Jaffrézic, B. and Breuer, M. (2008) Application of an Explicit Algebraic Reynolds Stress Model within a Hybrid LES–RANS Method, *Journal of Flow, Turbulence and Combustion*, **81**, pp. 415–448.

Jameson, A. (1983) Solution of the Euler Equations by a Multigrid Method, *Applied Mathematics and Computation*, **13**, pp. 327–356.

Jarrin, N., Benhamadouche, S., Laurence,D. and Prosser, R. (2006) A synthetic–Eddy–Method for Generating Inflow Conditions for Large–Eddy Simulations, *International Journal of Heat and Fluid Flow*, **27**(4), pp. 585–593.

Jorgenson, P.C.E. and Loh, C.Y. (2002) Computing Axisymmetric Jet Screech Tones Using Unstructured Grids, *AIAA Paper*, 2002–3889.

Kim, J.W. and Lee, D.J. (2001) Adaptive Nonlinear Artificial Dissipation Model for Computational Aeroacoustics, *AIAA Journal*, **39**(5), pp. 810–818.

Kurbatskii, K.A. and Mankbadi, R.R. (2004) Review of Computational Aeroacoustics Algorithms, *Int. Journal of Computational Fluid Dynamics*, **18**(6), pp. 533–546.

Kobayashi, T. (2006) Large–Eddy Simulation for Engineering Applications, *Fluid Dynamics Research*, **38**, pp. 84–107.

Kuwahara, K. and Komurasaki, S. (2000) Semi–Direct Simulation of a Flow Around a Subsonic Airfoil, *AIAA Paper*, 2000–2656.

Lafon, P., Caillaud, S., Devos, J.P. and Lambert, C. (2003) Shallow Cavity Noise Aeroacoustical Coupling and its Structural Effects on a Piping Stream Line, *Journal of Fluids and Structures*, **18**, pp. 695–713.

Lai, H. and Luo, K.H. (2007) A Three–Dimensional Hybrid LES–Acoustic Analogy Method for Predicting Open–Cavity Noise, *Journal of Flow, Turbulence and Combustion*, **79**, pp. 55–82.

Larchevêque, L., Sagaut, P., Mary, I. and Labbé, O. (2003) Large–Eddy Simulation of a Compressible Flow Past a Deep Cavity, *Physics of Fluids*, **15**(1), pp. 193–210.

Lele, S.K. (1992) Compact Finite–Difference Schemes with Spectral–Like Resolution, *Journal of Computational Physics*, **103**(1), pp. 16–42.

Leonard, A. (1974) Energy Cascade in Large–Eddy Simulations of Turbulent Fluid Flows, *Advances in Geophysics*, (eds.) Frankiel, F.N. and Munn, R.E., **18A**(1), pp. 237–248, Academic, New York.

Li, Q., Page, G.J. and McGuirk, J.J. (2007) Large–Eddy Simulation of Twin Impinging Jets in Cross–Flow, *The Aeronautical Journal*, **111**, pp. 195–206.

Lighthill, M.J. (1952) On Sound Generated Aerodynamically, I: General Theory, *Proc. of the Royal Society of London, Series A: Mathematical and Physical Sciences*, **211**, pp. 564–587.

Lighthill, M.J. (1953) On Sound Generated Aerodynamically, II: Turbulence as a Source of Sound, *Proc. of the Royal Society of London, Series A: Mathematical and Physical Sciences*, **222**, pp. 1–32.

Lilly, D.K. (1967) The Representation of Small–Scale Turbulence in Numerical Simulation Experiments, *Proc. IBM Scientific Computing Symp. on Environmental Sciences*, (ed.) Goldstein, H.H., pp. 195–210, Yorktown Heights, NY:IBM.

Lockard, D.P. (1999) An Overview of Computational Aeroacoustic Modeling at NASA Langley, 10th *Thermal and Fluids Analysis Workshop*, September 13–17, 1999.

Loh, C.Y., Chang, S.C., Scott, J.R. and Yu, S.T. (1996) The Space–Time Conservation Element Method – A New Numerical Scheme for Computational Aeroacoustics, *AIAA Paper*, 1996–0276.

Loh, C.Y., Hultgren, L.S., Chang, S.C. and Jorgenson, P.C.E. (2000) Noise Computation of a Shock–Containing Supersonic Axisymmetric Jet by the CE/SE Method, *AIAA Paper*, 2000–0475.

Loh, C.Y., Hultgren, L.S., Wang, X.Y., Chang, S.C. and Jorgenson, P.C.E. (2000) Aeroacoustics Computation for Nearly Fully Expanded Supersonic Jets Using the CE/SE Method, *AIAA Paper*, 2000–2010.

Loh, C.Y., Wang, X.Y., Chang, S.C. and Jorgenson, P.C.E. (2000) Computation of Feedback Aeroacoustic System by the CE/SE Method, *NASA/TM*, 2000–210479.

Loh, C.Y. (2001) Computational Aeroacoustics by the Space–Time CE/SE Method, *NASA/CR*, 2001–210680.

Loh, C.Y., Hultgren, L.S. and Chang, S.C. (2001a) Wave Computation in Compressible Flow Using Space–Time Conservation Element and Solution Element Method, *AIAA Journal*, **39**(5), pp. 794–801.

Loh, C.Y., Hultgren, L.S. and Jorgenson, P.C.E. (2001b) Near–Field Noise Computation for an Underexpanded Supersonic Jet by the CE/SE Method, *NASA/TM*, 2001–210958.

Loh, C.Y., Himansu, A., Wang, X.Y. and Jorgenson, P.C.E. (2001c) Computation of an Underexpanded 3–D Rectangular Jet by the CE/SE Method, *AIAA Paper*, 2001–0986.

Loh, C.Y. and Hultgren, L.S. (2002) Computing Jet Screech – A Complex Aeroacoustic Feedback System, *NASA/TM*, 2002–211807.

Loh, C.Y. (2003a) Nonlinear Aeroacoustics Computations by the CE/SE Method, *NASA/CR*, 2003–212388.

Loh, C.Y. (2003b) On a Non–Reflecting Boundary Condition for Hyperbolic Conservation Laws, *AIAA Paper*, 2003–3975.

Loh, C.Y. (2005) Computation of Tone Noise From Supersonic Jet Impinging on Flat Plates, *NASA/CR*, 2005–213426.

Loh, C.Y. and Hultgren, L.S. (2005) Near–Field Noise Computation for a Supersonic Circular Jet, *NASA/TM*, 2005–213816.

Loh, C.Y. and Jorgenson, P.C.E. (2005) A Robust Absorbing Boundary Condition for Compressible Flows, *AIAA Paper*, 2005–4716.

Lund, T.S. (1997) On the Use of Discrete Filters for Large Eddy Simulation, *Center for Turbulence Research, Annual Research Briefs*, pp. 83–95.

Lyrintzis, A.S. (2003) Integral Acoustic Methods: From the (CFD) Near–Field to the (Acoustic) Far–Field, *Int. Journal of Aeroacoustics*, **2**(2), pp. 95–128.

Manning, T.A. and Lele, S.K. (2000) A Numerical Investigation of Sound Generation in Supersonic Jet Screech, *AIAA/CEAS Paper*, 2000–2081.

Marvin, E.G. (1976) *Aeroacoustics*, McGraw–Hill.

Mendonça, F., Allen, R., Charentenay, J. and Lewis, M. (2002) Towards Understanding LES and DES for Industrial Aeroacoustic Predictions, *International Workshop on 'LES for Acoustics'*, DLR Göttingen, October 7–8, Germany.

Mendonça, F., Allen, R. and Charentenay, J. (2003) CFD Prediction of Narrowband and Broadband Cavity Acoustics at M = 0.85, *AIAA Paper*, 2003–3303.

Menter, F.R. and Kuntz, M. (2002) Adaptation of Eddy–Viscosity Turbulence Models to Unsteady Separated Flow Behind Vehicles, *The Aerodynamics of Heavy Vehicles*, (eds.) McCallen, R., Browand, F., Ross, J., Monterey, December 2–6, USA, Springer, Berlin (2004).

Mihăescu, M. (2005) Computational Aeroacoustics Based on Large–Eddy Simulation and Acoustic Analogies, PhD thesis, Lund Institute of Technology, Sweden.

Mitchell, B.E., Lele, S.K. and Moin, P. (1995) Direct Computation of the Sound from a Compressible Co–rotating Vortex Pair, *Journal of Fluid Mechanics*, **285**, pp. 181–202.

Möhring, W. (1979) Modeling Low Mach Number Noise, *Mechanics of Sound Generation in Flows*, (ed.) Müller, E.-A., Springer, Berlin.

Moin, P. and Kim, J. (1982) Numerical Investigation of Turbulent Channel Flow, *Journal of Fluid Mechanics*, **118**, pp. 341–377.

Moin, P., Squires, K., Cabot, W. and Lee, S. (1991) A Dynamic Subgrid–Scale Model for Compressible Turbulence and Scalar Transport, *Physics of Fluids A*, **3**(11), pp. 2746–2757.

Nayyar, P., Barakos, G.N. and Badcock, K.J. (2005) Analysis and Control of Weapon Bay Flows, RTO–MP–AVT–123, NATO–RTO.

Nicoud, F. and Ducros, F. (1999) Subgrid–Scale Stress Modeling Based on the Square of the Velocity Gradient Tensor, *Journal of Flow, Turbulence and Combustion*, **62**, pp. 183–200.

Nikitin, N.V., Nicoud, F., Wasistho, B., Squires, K.D. and Spalart, P.R. (2000) An Approach to Wall Modeling in Large–Eddy Simulations, *Physics of Fluids*, **12**(7), pp. 1629–1632.

Panda, J., Raman, G. and Zaman, K.B.M.Q (1997) Underexpanded Screeching Jets from Circular, Rectangular and Elliptic Nozzles, *AIAA Paper*, 1997–1623.

Panda, J. (1998) Shock Oscillation in Underexpanded Screeching Jets, *Journal of Fluid Mechanics*, **363**, pp. 173–198.

Panda, J. (1999) An Experimental Investigation of Screech Noise Generation, *Journal of Fluid Mechanics*, **378**, pp. 71–96.

Peshkin, D.A. (2002) TurMMAC Application Challenge Test Case Specification: M219 Cavity, QINETIQ/FST/CAT/WP020905.

Piomelli, U., Moin, P. and Ferziger, J.H. (1988) Model Consistency in Large–Eddy Simulation of Turbulent Channel Flows, *Physics of Fluids*, **31**(7), pp. 1884–1891.

Piomelli, U. and Liu, J. (1995) Large–Eddy Simulation of Rotating Channels Flows Using a Localized Dynamic Model, *Physics of Fluids*, **7**, pp. 839–848.

Piomelli, U. and Balaras, E. (2002) Wall–Layer Models for Large–Eddy Simulations, *Annual Review of Fluid Mechanics*, **34**, pp. 349–374.

Pope, S.B. (2000) *Turbulent Flows*, Cambridge University Press, New York, USA.

Powell, A. (1953) On the Mechanism of Choked Jet Noise, *Proceedings of the Physical Society Section B*, **66**, pp. 1039–1056.

Powell, A. (1964) Theory of Vortex Sound, *Journal of Acoust. Soc. Am.*, **36**(1), pp. 177–195.

Raichel, D.R. (2006) *The Science and Applications of Acoustics*, 2nd ed. Springer.

Raman, G. and Rice, E.J. (1994) Instability Modes Excited by Natural Screech Tones in a Supersonic Rectangular Jet, *Physics of Fluids*, **6**, pp. 3999–4008.

Ribault, C. Le (2005) Large–Eddy Simulation of Compressible Mixing Layers, *Int. Journal of Computational Fluid Dynamics*, **1**(1), pp. 87–111.

Rodi, W. (2006) DNS and LES of Some Engineering Flows, *Fluid Dynamics Research*, **38**, pp. 145–173.

Rogallo, R.S. and Moin P. (1984) Numerical Simulation of Turbulent Flows, *Annual Review of Fluid Mechanics*, **16**, pp. 99–137.

Rona, A. and Zhang X. (2004) Time Accurate Numerical Study of Turbulent Supersonic Jets, *Journal of Sound and Vibration*, **270**, pp. 297–321.

Rogers, M.M. and Moser R.D. (1994) Direct Simulation of a Self–Similar Turbulent Mixing Layer, *Physics of Fluids*, **6**, pp. 903–923.

Rossiter, J.E. (1964) Wind Tunnel Experiments on the Flow Over Rectangular Cavities at Subsonic and Transonic Speeds, *Reports and Memoranda*, **3438**, Aeronautical Research Council.

Sagaut, P. (2006) *Large–Eddy Simulation for Incompressible Flows*, 3rd ed. Springer.

Schlichting, H. (1979) *Boundary–Layer Theory*, McGraw–Hill, New York.

Schreiber, R. and Keller H.B. (1983) Driven Cavity Flows by Efficient Numerical Techniques, *Journal of Computational Physics*, **49**, pp. 310–333.

Schulze, J., Sesterhenn, J., Schmid, P., Bogey, C., Cacqueray, N., Berland, J. and Bailly, C. (2009) Numerical Simulation of Supersonic Jet Noise, *Notes on Numerical Fluid Mechanics and Multidisciplinary Design*, **104**, pp. 29–46.

Schumann, U. (1975) Subgrid–Scale Model for Finite–Difference Simulations of Turbulent Flows in Plane Channels and Annuli, *Journal of Computational Physics*, **18**, pp. 376–404.

Shen, H. and Tam, C.K.W. (2002) Three–Dimensional Numerical Simulation of the Jet Screech Phenomenon, *AIAA Journal*, **40**(1), pp. 33–41.

Shieh, C.M. and Morris, P.J. (1999) Parallel Numerical Simulation of Subsonic Cavity Noise, *AIAA Paper*, 1999–1891.

Smagorinsky, J.S. (1963) General Circulation Experiments with the Primitive Equations, *Monthly Weather Review*, **91**(3), pp. 99–165.

Spalart, P.R., Jou, W.-H., Strelets, M. and Allmaras, S.R. (1997) Comments on the Feasibility of LES for Wings, and on a Hybrid RANS/LES Approach, Advances in DNS/LES, (eds.) Liu, C. and Liu, Z., Proc. 1st AFOSR Int. Conf. on DNS/LES, Aug. 4–8, Greyden Press, Columbus, OH.

Spalart, P.R., Deck, S., Shur, M.L., Squires, K.D., Strelets, M. and Travin, A. (2006) A New Version of Detached–Eddy Simulation Resistant to Ambiguous Grid Densities, *Journal of Theoretical and Computational Fluid Dynamics*, **20**, pp. 181–195.

Spalart, P.R. (2009) Detached–Eddy Simulation, *Annual Review of Fluid Mechanics*, **41**, pp. 181–202.

Stolz, S. and Adams, N.A. (1980) An Approximate Deconvolution Procedure for Large–Eddy Simulation, *Physics of Fluids A*, **11**(7), pp. 1699–1701.

Stromberg, J.L., McLaughlin D.K. and Troutt, T.R. (1980) Flow Field and Acoustic Properties of a Mach Number 0.9 Jet at a Low Reynolds Number, *Journal of Sound and Vibration*, **72**(2), pp. 159–176.

Suzuki, T. and Lele, S.K. (2003) Shock Leakage Through an Unsteady Vortex–Laden Mixing Layer: Application to Jet Screech, *Journal of Fluid Mechanics*, **490**, pp. 139–167.

Tam, C.K.W. (1988) The Shock–Cell Structures and Screech Tone Frequencies of Rectangular and Non–Axisymmetric Supersonic Jets, *Journal of Sound and Vibration*, **121**(1), pp. 135–147.

Tam, C.K.W. and Webb, J.C. (1993) Dispersion–Relation–Preserving Finite Difference Schemes for Computational Acoustics, *Journal of Computational Physics*, **107**, pp. 262–282.

Tam, C.K.W. (1995) Supersonic Jet Noise, *Annual Review of Fluid Mechanics*, **27**, pp. 17–43.

Tam, C.K.W. (2001) Computational Aeroacoustics:An Overview, *Aging Mechanisms and Control: Part A– Developments in Computational Aero– and Hydro– Acoustics*, Manchester, Oct. 8–11, UK.

Tam, C.K.W. (2004) Computational Aeroacoustics: An Overview of Computational Challenges and Applications, *Journal of Computational Fluid Dynamics*, **18**(6), pp. 547–567.

Tannehill, J.C., Anderson, D.A. and Pletcher, R.H. (1997) *Computational Fluid Mechanics and Heat Transfer*, 2nd ed. Taylor and Francis.

Temmerman, L., Hadziadbic, M., Leschziner, M. and Hanjalić, K. (2005) A Hybrid Two–Layer URANS–LES Approach for Large–Eddy Simulation at High Reynolds Numbers, *Int. Journal of Heat and Fluid Flow*, **26**, pp. 173–190.

Uzun, A., Blaisdell, G.A. and Lyrintzis, A.S. (2002) Recent Progress Towards a Large–Eddy Simulation Code for Jet Aeroacoustics, *AIAA Paper*, 2002–2598.

Uzun, A. (2003) 3D Large–Eddy Simulation for Jet Aeroacoustics, PhD thesis, Purdue University, USA.

Vergne, S., Auger, J.–M., G'Styr, N. and Périé, F. (2002) Simulation of Cavity Aero–Elastic Noise Induced by an External Turbulent Flow Perturbed by a Small Ruler, *International Workshop on 'LES for Acoustics'*, DLR Göttingen, October 7–8, Germany.

(eds.) Wagner, C., Hüttl, T. and Sagaut, P. (2007) *Large–Eddy Simulation for Acoustics*, Cambridge University Press.

Wallin, S. and Johansson, A.V. (2000) An Explicit Algebraic Reynolds Stress Model for Incompressible and Compressible Turbulent Flows, *Journal of Fluid Mechanics*, **403**, pp. 89–132.

Wang, M., Freund, J.B. and Lele, S.K. (2006) Computational Prediction of Flow–Generated Sound, *Annual Review of Fluid Mechanics*, **38**, pp. 483–512.

Wilcox, D.C. (1994) *Turbulence Modeling for CFD*, DCW Industries, Inc.

Woodward, P. and Colella, P. (1984) The Numerical Simulation of Two–Dimensional Fluid Flow with Strong Shock, *Journal of Computational Physics*, **54**, pp. 115–173.

Van Driest, E. (1956) On Turbulent Flow Near a Wall, *Journal of Aeronautical Science*, **23**, pp. 1007–1011.

Van Dyke, M. (1982) An Album of Fluid Motion, *The Parabolic Press*, Stanford, California, USA.

Venkatachari, B.S., Cheng, G.C., Soni, B.K. and Chang, S.C. (2008) Validation and Verification of Courant Number Insensitive CE/SE Method for Transient Viscous Flow Simulations, *Mathematics and Computers in Simulation*, **78**, pp. 653–670.

Yee, H.C., Warming, R.F. and Harten, A. (1983) Implicit Total Variation Diminishing (TVD) Scheme for Steady–State Calculations, *AIAA Paper*, 1983–1902.

Yoshizawa, A. (1986) Statistical Theory for Compressible Turbulent Shear Flows with Applications to Subgrid Modeling, *Physics of Fluids*, **29**(7), pp. 2152–2164.

Zhang, M., Yu, S.T. and Chang, S.C. (2004) Solving the Navier–Stokes Equations by the CE/SE Method, *AIAA Paper*, 2004–0075.

Zhang, X., Rona, A. and Edwards, J.A. (1998) The Effect of Trailing Edge Geometry on Cavity Flow Oscillation Driven by a Supersonic Shear Layer, *AIAA Journal*, **102**, pp. 129–136.

Zhang, Z.C. and Yu, S.T. (1999) Shock Capturing without Riemann Solver - A Modified Space–Time CE/SE Method for Conservation Laws, *AIAA Paper*, 1999–0904.

Zhang, Z.C., Yu, S.T. and Chang, S.C. (2002) A Space–Time Conservation Element and Solution Element Method for Solving the Two and Three–Dimensional Unsteady Euler Equations using Quadrilateral and Hexahedral Meshes, *Journal of Computational Physics*, **175**, pp. 168–199.